Durability Studies Relevant to Marine Equipment

By

Dimitris Mantzavinos

Vol. I

A thesis submitted to

The Department of Mechanical Engineering

University of Glasgow

UNIVERSITY
of
GLASGOW

in fulfilment of the requirement for

The Degree of Doctor of Philosophy

ABSTRACT

The corrosion behaviour of two copper-nickel alloys, namely Cu-30%Ni and Cu-10%Ni, commercially pure titanium and two titanium alloys (Ti-6Al-4V and Ti:5111) has been examined in environments of relevance to desalination and other marine equipment. The investigation was focused on two extremes of environments, pure water and high-velocity (with and without suspended solids) saline water. These represent conditions in which operational problems have been experienced or are anticipated and in relation to which very little information on basic durability is available. This work contained only brief experiments in quiescent seawater which has been studied in abundance previously; such tests were included in this research for background and comparison purposes only. The study involved exposure of specimens to distilled water (1.5-7 μS/cm) at 20° – 80°C with and without injected carbon dioxide. At 20°C upon initial exposure to distilled water, the 10%Ni alloy exhibited somewhat active corrosion behaviour during anodic polarisation potentiodynamic scans, but after a few days' exposure, more-passive behaviour of both alloys was indicated with the 30%Ni material demonstrating better corrosion resistance than the lower-nickel alloy. This relative behaviour was replicated in comparative tests conducted in 3.5% NaCl at 20°C in which the corrosion resistance of Cu-30%Ni was clearly greater than that displayed by the lower-Ni alloy. However, at higher temperatures in distilled water, the superiority of the 30%Ni alloy was less evident especially in the presence of dissolved carbon dioxide. Microscopical examination of specimens revealed a susceptibility to general corrosion with 'etched' surfaces and also pitting attack which seemed to have a lesser effect on Cu-10%Ni than Cu-30%Ni. Certainly at short exposure times, titanium, titanium alloys and UNS S31603 stainless steel (used for comparison purposes) exhibited considerably superior corrosion resistance than the copper-nickel alloys over the entire range of distilled water conditions studied.

The erosion-corrosion characteristics of commercially pure titanium, the two titanium alloys, UNS S32760 and UNS S31603 stainless steels were assessed under an impinging jet of 3.5% NaCl solution at a velocity of 71.1 m/s free from solids at both 20° and 50°C, and also at a velocity of 12.6 m/s containing solids up to 1800 ppm at

20°C. Under zero-solid liquid erosion-corrosion conditions at 20°C, UNS S31603 stainless steel and the three Ti-base materials exhibited excellent erosion-corrosion resistance. At 50°C UNS S31603 stainless steel showed some weight loss but the Ti-base materials retained their excellent erosion-corrosion resistance. After anodic polarisation tests in zero-solid liquid erosion-corrosion at 20°C, the three Ti-base materials were covered rather evenly by films of various thicknesses, apparently formed due to hydrodynamic effects. That was also the case for zero-solid liquid erosion-corrosion tests at 50°C with and without polarisation.

In the presence of solids, all the materials suffered some deterioration. Quite interestingly, in terms of material loss, pure titanium's erosion-corrosion resistance was found to be no better than the one exhibited by UNS S32760 stainless steel. The relative contribution to overall erosion-corrosion damage, from pure erosion, pure corrosion and interactive synergistic processes were quantified and some complex features of the disposition and mechanisms of erosion-corrosion became apparent through tests on concentric specimens. Microscopical examination after solid/liquid erosion-corrosion tests revealed drill holes in the centre of the specimens (region directly under the jet) and signs of plastic deformation ('skid' marks) further out for all four materials. UNS S31603 also showed evidence of damage due to pitting attack.

In terms of the mechanisms of attack by the contributory processes, whilst the detailed mechanisms of the synergistic component was not unambiguously identified, it was clearly evident that the pure corrosion component of the erosion-corrosion deterioration involves rapid periodic depassivation/repassivation events. The pure erosion damage was observed to be associated with microdrilling and plastic deformation processes.

CONTENTS

LIST OF FIGURES

Figure 4.1.8b. General corrosion and intergranular attack on Cu-10%Ni when anodically polarised after 2 day exposure in seawater at 20°C.

Figure 4.1.9a. Uniform layer of general corrosion on Cu-10%Ni after 7 day exposure in seawater at 20°C.

Figure 4.1.9b. General corrosion and "etched" surface on Cu-10%Ni after 7 day exposure in seawater at 20°C.

Figure 4.1.10a. Pitting attack on the surface of Cu-10%Ni when anodically polarised after 7 day exposure in seawater at 20°C.

Figure 4.1.10b. Signs of pitting and intergranular corrosion on Cu-10%Ni when anodically polarised after 7 day exposure in seawater.

Figure 4.1.11a. Etched appearance on Cu-10%Ni after anodic polarisation upon initial exposure to distilled water at 20°C.

Figure 4.1.11b. Close-up view of the above features.

Figure 4.1.12a. General corrosion and clean patches on Cu-10%Ni after 2 day exposure in distilled water at 20°C.

Figure 4.1.12b. At high magnification the clean patches appear to be full of numerous particles.

Figure 4.1.13a. Etched appearance and general attack with shallow pitting on Cu-10%Ni when anodically polarised after 2 day exposure in distilled water at 20°C.

Figure 4.1.13b. At high magnification the dark regions on the above picture appear to be uniform.

Figure 4.1.14a. Bright surface with regions of thicker corrosion products on Cu-10%Ni after 7 day exposure in distilled water at 20°C.

Figure 4.1.14b. High magnification reveals numerous particles on the bright surface.

Figure 4.1.15a. Pitting attack and circular regions consisting of individual particles on Cu-10%Ni when anodically polarised after 7 day exposure in distilled water at 20°C.

Figure 4.1.15b. Pits were noted to have a centred depth.

Figure 4.1.16a. General corrosion and pitting attack on Cu-10%Ni after 60 day exposure in distilled water at 20°C.

Figure 4.1.16b. At high magnification pits are shown to be shallow.

Figure 4.1.17a. Pitting and general attack on Cu-10%Ni when anodically polarised after 60 day exposure in distilled water at 20°C.

Figure 4.1.17b. Small shallow pits were also present on Cu-10%Ni when anodically polarised after 60 day exposure in distilled water at 20°C.

Figure 4.1.18a. Regions of intergranular corrosion and few dark patches on Cu-10%Ni when anodically polarised in distilled water at 50^0C.

Figure 4.1.18b. Crevice corrosion on Cu-10%Ni when anodically polarised in distilled water at 50^0C.

Figure 4.1.19a. Etched appearance of Cu-10%Ni when anodically polarised in distilled water at 20°C with CO_2 injection.

Figure 4.1.19b. At high magnification the surface shown in the previous photograph is full of tiny particles.

Figure 4.1.20a. General corrosion on Cu-10%Ni when anodically polarised in distilled water at 50^0C with CO_2 injection.

Figure 4.1.20b. Regions of revealed metal grain structure with minor pitting on Cu-10%Ni when anodically polarised in distilled water at 50^0C with CO_2 injection.

Figure 4.2.1a. Anodic polarisation tests of Cu-30%Ni in artificial seawater at 20°C after 1 hour immersion except where stated.

Figure 4.2.1b. Anodic polarisation tests of Cu-30%Ni in artificial seawater at 20°C after 1 hour immersion except where stated.

Figure 4.2.2a. Anodic polarisation curves of Cu-30%Ni in distilled water at 20°C in comparison to artificial seawater at 20°C after 1 hour of immersion except where stated. Dotted lines = seawater, full lines = distilled water.

Figure 4.2.2b. Anodic polarisation curves of cross-section Cu-30%Ni specimens and outer surface Cu-30%Ni specimens in distilled water at 20°C after 1 hour of immersion except where stated. Dotted lines = outer surface specimens, full lines = cross-section specimens.

Figure 4.2.3a. Anodic polarisation curves of Cu-30%Ni after 1 hour of immersion in distilled water at 50°C in comparison to distilled water at 20°C. Dotted lines = 20°C, full lines = 50°C.

Figure 4.2.3b. Anodic polarisation curves of Cu-30%Ni after 1 hour of immersion in distilled water at 50°C in comparison to distilled water at 20°C. Dotted lines = 20°C, full lines = 50°C.

Figure 4.2.4a. Anodic polarisation curves of Cu-30%Ni after 1 hour of immersion in distilled water at 20°C with injected CO_2, in comparison to distilled water at 20°C. Dotted lines = 20°C, full lines = 20°C + CO_2.

Figure 4.2.4b. Anodic polarisation curves of Cu-30%Ni after 1 hour of immersion in distilled water at 20°C with injected CO_2, in comparison to distilled water at 20°C. Dotted lines = 20°C, full lines = 20°C + CO_2.

Figure 4.2.5a. Anodic polarisation curves of Cu-30%Ni after 1 hour of immersion in distilled water at 50°C with injected CO_2, in comparison to distilled water at 50°C. Dotted lines = 50°C, full lines = 50°C + CO_2.

Figure 4.2.5b. Anodic polarisation curves of Cu-30%Ni after 1 hour of immersion in distilled water at 50°C with injected CO_2, in comparison to distilled water at 50°C. Dotted lines = 50°C, full lines = 50°C + CO_2.

Figure 4.2.6a. Thin film and patches of thicker corrosion products and pitting attack on Cu-30%Ni when anodically polarised after initial exposure to seawater at 20°C.

Figure 4.2.6b. High magnification reveals tiny particles over the entire surface of Cu-30%Ni when anodically polarised after initial exposure to seawater at 20°C.

Figure 4.2.7a. General corrosion on Cu-30%Ni after 2 day exposure in seawater at 20°C.

Figure 4.2.7b. At high magnification general corrosion is noted to be uniform on Cu-30%Ni after 2 day exposure in seawater at 20°C.

Figure 4.2.8a. General corrosion on Cu-30%Ni when anodically polarised after 2 day exposure in seawater at 20°C.

Figure 4.2.8b. High magnification shows general corrosion to be uniform on Cu-30%Ni when anodically polarised after 2 day exposure in seawater at 20°C.

Figure 4.2.9a. General attack and crevice corrosion on Cu-30%Ni after 7 day exposure in seawater at 20°C.

Figure 4.2.9b. Pitting attack on Cu-30%Ni after 7 day exposure in seawater at 20°C.

Figure 4.2.10. General attack and crevice corrosion on Cu-30%Ni when anodically polarised after 7 day exposure in seawater at 20°C.

Figure 4.2.11a. Cu-30%Ni after anodic polarisation upon initial exposure to distilled water at 20°C.

Figure 4.2.11b. High magnification reveals shallow pitting on Cu-30%Ni when anodically polarised after initial exposure to distilled water at 20°C.

Figure 4.2.12a. Light general corrosion on Cu-30%Ni after 2 day exposure in distilled water at 20°C.

Figure 4.2.12b. Formation of particles noted on the inside edge of Cu-30%Ni after 2 day exposure in distilled water at 20°C.

Figure 4.2.13a. Pitting corrosion on Cu-30%Ni when anodically polarised after 2 day exposure in distilled water at 20°C.

Figure 4.2.13b. Large pits were also present on Cu-30%Ni when anodically polarised after 2 day exposure in distilled water at 20°C.

Figure 4.2.14a. General corrosion and few small pits on Cu-30%Ni after 7 day exposure in distilled water at 20°C.

Figure 4.2.14b. Group of numerous shallow pits attack on Cu-30%Ni after 7 day exposure in distilled water at 20°C.

Figure 4.2.15a. Severe pitting attack and dark general corrosion on Cu-30%Ni when anodically polarised after 7 day exposure in distilled water at 20°C.

Figure 4.2.15b. Pitting corrosion and numerous tiny particles on Cu-30%Ni when anodically polarised after 7 day exposure in distilled water at 20°C.

Figure 4.2.16a. Uniform general corrosion and pitting attack on Cu-30%Ni after 60 day exposure in distilled water at 20°C.

Figure 4.2.16b. Pits were noted to be rather deep on Cu-30%Ni after 60 day exposure in distilled water at 20°C.

Figure 4.2.17a. Severe pitting attack and uniform general corrosion on Cu-30%Ni when anodically polarised after 60 day exposure in distilled water at 20°C.

Figure 4.2.17b. Quite severe and extensive pitting attack on another part of the specimen shown in the previous figure.

Figure 4.2.18a. General corrosion and pitting on the outer surface of Cu-30%Ni when anodically polarised after initial exposure to distilled water at 20°C.

Figure 4.2.18b. Region of general corrosion with "etched" appearance on the outer surface of Cu-30%Ni when anodic polarised after initial exposure to distilled water at 20°C.

Figure 4.2.19. Thin layer of general corrosion on the outer surface of Cu-30%Ni after 60 day exposure to distilled water at 20°C.

Figure 4.2.20a. Pitting attack on the outer surface of Cu-30%Ni when anodically polarised after 60 day exposure in distilled water at 20°C.

Figure 4.2.20b. Pits were noted to be rather deep on the outer surface of Cu-30%Ni when anodically polarised after 60 day exposure in distilled water at 20°C.

Figure 4.2.21a. Region of general corrosion and minor pitting on Cu-30%Ni when anodically polarised upon initial exposure to distilled water at 50^0C.

Figure 6.2.28. Part of the surface outside the central region of the Ti:G2 specimen shown in figure 6.2.25. Scratches reveal bare metal underneath.

Figure 6.2.29. Bare patches ,where the film was damaged, in the impinging region of the Ti:G2 specimen shown in figure 6.2.25.

Figure 6.2.30. 316L when anodically polarised after 12 hours of liquid erosion-corrosion at 50°C and 71.1 m/s impinging jet velocity.

Figure 6.2.31. Severe pitting in the centre of the 316L specimen shown in figure 6.2.30.

Figure 6.2.32. Non-uniform surface on the region directly under the jet of a Ti:5111 specimen when anodically polarised after 12 hours of liquid erosion-corrosion at 50°C and 71.1 m/s (S.E.M. image).

Figure 6.2.33. Uniform surface just outside the impinging target (i.e. on first dark ring in dark-blue colour also shown in figure 6.2.27) of a Ti:5111 specimen when anodically polarised after 12 hours of liquid erosion-corrosion at 50°C and 71.1 m/s (S.E.M. image).

Figure 6.2.34. Surface of high roughness on the outer edge of the first dark ring around the impinging target of a Ti:5111 specimen when anodically polarised after 12 hours of liquid erosion-corrosion at 50°C and 71.1 m/s (S.E.M. image).

Figure 6.2.35. Non-uniform surface on the outer edge of the light-coloured ring (also shown in figure 6.2.27) of a Ti:5111 specimen when anodically polarised after 12 hours of liquid erosion-corrosion at 50°C and 71.1 m/s (S.E.M. image).

Figure 6.2.36. Film on the region directly under the jet (shown in a tilted position) of a Ti:G2 specimen when anodically polarised after 12 hours of liquid erosion-corrosion at 50°C and 71.1 m/s (S.E.M. image).

Figure 6.2.37. Film on the region directly under the jet (shown in a tilted position) of a Ti:5111 specimen when anodically polarised after 12 hours of liquid erosion-corrosion at 50°C and 71.1 m/s (S.E.M. image).

Figure 6.3.1. Weight loss versus time for Ti:G2, Ti:5111, Ti-6Al-4V and 316L under solid-liquid erosion-corrosion at 12.4 m/s and 1500-1600 ppm.

Figure 6.3.2. Scar depth versus time for Ti:G2, Ti:5111, Ti-6Al-4V and 316L under solid-liquid erosion-corrosion at 12.4 m/s and 1500-1600 ppm.

Figure 6.3.3. Surface profile of Ti:G2 after 72 hours of solid/liquid erosion-corrosion at 12.4 m/s and 1500-1600 ppm.

Figure 6.3.4. Surface profile of Ti:5111 after 72 hours of solid/liquid erosion-corrosion at 12.4 m/s and 1500-1600 ppm.

Figure 7.3.1. Anodic polarisation curve of a composite Ti:G2 specimen under static conditions (**A**), compared to the anodic polarisation curve of the outer concentric Ti:G2 specimen under solid/liquid erosion-corrosion (**B**).

LIST OF TABLES

Table 7.2.1. Previous data on liquid erosion-corrosion for Ti and Ti-6Al-4V.

Table 7.2.2. Degree of roughness and extent of each separate zone of film on the surface of a Ti:5111 specimen that was anodically polarised after 12 hours of liquid erosion-corrosion at 50°C and 71.1 m/s (r = radius of extent from stagnation point, d = diameter of nozzle = 1 mm).

Table 7.3.1. i_{corr} values and oscillating/steady mean current density values for inner concentric, outer concentric and composite specimen (note that the 0.5 $\mu A/cm^2$ is the i_{corr} of the outer specimen as approximated on the anodic polarisation curve of the outer specimen in figure 6.3.37).

Table 7.3.2. Scar depths of 5 cm^2 and 8 cm^2 Ti:G2 specimens after 16 hours of solid/liquid erosion-corrosion at comparable sand loadings.

ACKNOWLEDGEMENTS

Above all I would like to thank Dr Trevor Hodgkiess for his knowledge, guidance and constructive supervision, without which this work would not have been possible to carry out. I would also like to thank him for his help to me outside this project. Full acknowledgement goes to Prof. J. Hancock for the provision of a scholarship for this research. Thanks to the technicians of this department for sharing some of that struggle for maintenance on the rigs with me. To Paul Kennedy who still hasn't realised exactly how much money I've earned out of marking his scripts; if it wasn't Paul and his engineering drawing course I would never have survived through my fourth year. Many thanks to George Vassiliou for all the great fun we have shared in the last nine years but also for providing his kitchen to me to sleep in for three months. To Fiona for helping me out with accommodation and finding me a roof to sleep under for two weeks (maybe three). To Dave, an ex-flatmate; standing by his side in the pubs has made me an alcoholic, cheers mate! To Alex, a true clubbing enthusiast but above all very good friend. I also need to give many thanks to 'The Windows'; the acoustic band with the very inimitable sound basically consisting of me and Alex; we never made it as rock stars (although we should have sent that tape to EMI) but our fans and disturbed neighbours will remember us for the rest of their lives, thanks guys. To Guinness and the so unique sensation of drinking till you drop and then drink some more! Loads of credit goes to all those people I was out with or happened to be out with on alcohol adventures. I would also like to thank some other stuff which I better not go into. Finally I'd like to express my total appreciation to the whole city of Glasgow for making my staying here such a pleasant one.

LIST OF PUBLICATIONS

"Corrosion of copper-nickel alloys in pure water", T. Hodgkiess, D. Mantzavinos. *Desalination* 126 (1999) 129-137.

"Corrosion of condenser tube materials in distilled water", D. Mantzavinos[a], T. Hodgkiess[b*], S. L. Lai[c]. *Desalination* 138 (2001) 365-370.

1. INTRODUCTION AND OUTLINE OF THESIS

1.1. Introduction

This research project has comprised a study of the durability of copper-nickel (Cu-Ni) alloys and titanium (Ti) and alloys. A particular focus initially was the use of these materials in desalination plant but the study developed into investigations on Ti alloys with a much wider marine technology relevance.

In detail, the project was targeted on issues of current interest with regard to the two classes of materials studied. The first of these concern the corrosion behaviour of Cu-Ni alloys in condensing-water situations in thermal desalination plant and the second relates to an assessment of the potential of Ti and alloys for use in equipment (including desalination plant) which is subjected to impingement of high-velocity seawater with and without the presence of suspended solids.

Cu-Ni alloys have served for decades as the standard material for a range of marine components including seawater piping systems, heat exchangers in naval ships, offshore platforms, industrial plants. Although such alloys have provided good performance in many sections of these seawater-handling systems, these materials do possess some well-documented limitations particularly under erosion-corrosion conditions [1-4] and in the presence of certain contaminants such as sulphides [5-9] and ammonia [10].

A rather less documented and investigated aspect of the performance of Cu-Ni alloys is that in recent years there have been a number of reported instances [11-14] of serious vapour-side corrosion problems of copper-nickel alloy tubes in the high-temperature stages of Multistage Flash Desalination units. Failures due to vapour-side corrosion have occurred in distillers in Kuwait, Qatar, Saudi Arabia and Abu Dhabi [3], so the problem is not confined to one particular area or group of distillers. However, information is lacking in ascertaining the actual cause of vapour-side corrosion and virtually nothing seems to have been published on the corrosion

behaviour of copper-nickel alloys in distilled water. Consequently, part of the research described in this thesis presents a fundamental investigation focused on this latter topic.

Alternative strategies include consideration of other practical materials for seawater service. Common candidate materials include aluminium, stainless steels, high nickel alloys, glass-reinforced plastics (GRP) and titanium. Service and laboratory experience has demonstrated that aluminium and common stainless steels are quite susceptible to crevice and pitting corrosion in seawater. Although improved resistance is exhibited by certain high chromium + molybdenum austenitic duplex and ferritic stainless steels, total corrosion reliability in seawater can not be assured, and alloy cost is significantly increased. Reasonably good seawater corrosion performance can be achieved with certain high molybdenum-chromium nickel-based alloys, but at a very high cost penalty. Although GRP offers excellent seawater resistance below 90°C, it is not highly fire-resistant, possesses poor thermal conductivity for heat exchanger service and may exhibit unacceptable joint integrity [15]. Thus, most of the common materials possess one or more major limitations for service in seawater systems such as piping systems and heat exchanger service. This process of elimination leaves titanium for consideration.

Titanium industries around the world are booming at the moment. Recent rapid growth of the demand for titanium in materials for building, personal items and sports goods is remarkable. Automotive parts, marine construction, food industries, medical and dental materials, fishery, desalination plants at coastal cities and waste water and waste gas treatment plants are areas where titanium is currently being used and are expected to become even more promising markets in the future [16].

As indicated earlier in this section, the research described in this thesis was conducted in two phases:

1. A study of the corrosion behaviour of Cu-Ni base alloys in distilled water at a range of temperatures. This work relates to problems, currently encountered in thermal desalination plant, of corrosion failures of these materials on the condensing-water side of the heat-transfer tubes.

2. An investigation of the durability of Ti and two of its alloys. This included some attention to corrosion resistance in distilled water but with a major emphasis on erosion-corrosion behaviour in saline water in the absence of and presence of added suspended solids. This work was undertaken against a background of a lack of information on this aspect of the durability of Ti and its alloys in marine environments, and included some experiments on two stainless steel alloys for comparison purposes.

1.2. Outline of thesis

The structure of this thesis is such that Chapter 2 reviews the current literature on the corrosion behaviour of Cu-Ni alloys. It continues by giving a review of titanium and titanium alloys addressing their corrosion and, in more detail, erosion-corrosion resistance.

Chapter 3 details the experimental equipment, techniques and procedures used in this thesis. Analysis of the composition of the alloys studied is also included.

Chapter 4 introduces the two Cu-Ni alloys studied in this research: Cu-10%Ni and Cu-30%Ni. The results of all static corrosion tests carried out on each alloy are presented here.

Chapter 5 provides a discussion of all the results on the two Cu-Ni alloys presented, drawing on major findings and comparing with results in the literature.

Chapter 6 introduces titanium and two titanium alloys studied in this research. The results of static tests in distilled water together with the results of all erosion-corrosion tests, with or without solids, carried out on titanium and its two alloys are presented here. Some related studies that were also carried out on two stainless steels for comparison purposes are also included.

Chapter 7 provides a discussion of all the results on titanium and its alloys and the two stainless steels presented drawing on major findings and comparing with results in the literature.

Chapter 8 lists the main conclusions from the work presented in this thesis and suggests some topics where further work could be useful.

2. LITERATURE REVIEW

2.1. Basic corrosion principles [146]

Aqueous corrosion is an electrochemical phenomenon. It involves reactions in which both charge transfer and mass transfer occur spontaneously across metal surfaces. The reactions are called **"electrode reactions"** and the metal surfaces are called **"electrodes"**.

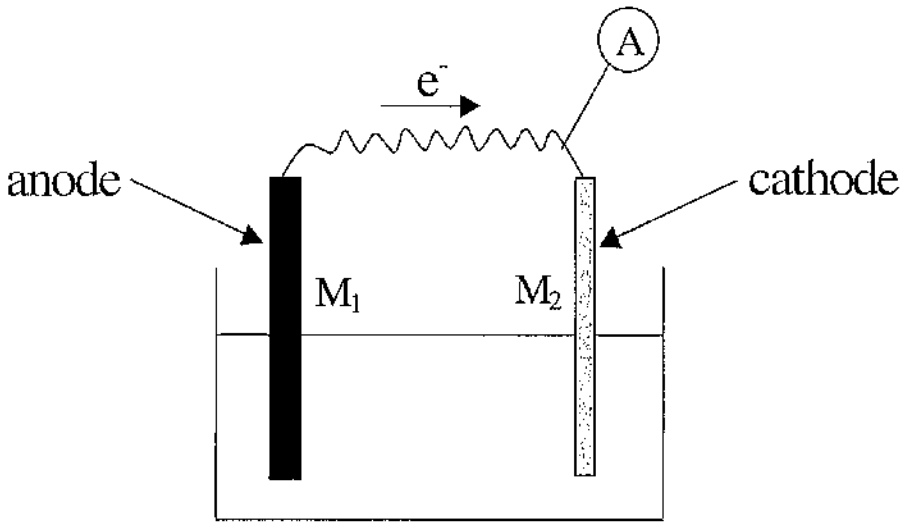

Figure 2.1.1. Electrochemical Cell involving two different metals (schematic).

The electrochemical mechanism of corrosion can be demonstrated in the set-up shown in Figure 2.1.1 which shows an electrochemical cell which consists of two different metals connected externally and immersed in a common solution. There is clearly an association between corrosion on M_1 and flow of current which can be measured through an ammeter. M_1 acts as anode (supports electron producing reactions) and M_2 acts as cathode (supports electron consuming reactions). The larger the current flow is, the more severe is corrosion on M_1.

Considering the above description, aqueous corrosion can now be specified as an electrochemical process in which the actual metal loss occurs by dissolution of charged metal ions M^{n+}, and the production of electrons as follows,

$$M = M^{n+} + ne^-$$

For example in the case of Fe:

$$Fe = Fe^{2+} + 2e^-$$

Any reaction which 'releases' electrons as above is called **"anodic reaction"**.

The electrons released by the anodic reaction must be consumed by **"cathodic reactions"** occurring simultaneously over the metal surface which involve substances or chemical species present in the surrounding aqueous environment. The two most relevant cathodic reactions in corrosion reactions are:

a) In acidic environment (pH below 7)

$$2H^+ + 2e^- = 2H_{ads} \begin{cases} \nearrow H_{2(g)} \\ \searrow 2H_{(m)} \end{cases}$$

Where H_{ads} represents a hydrogen atom adsorbed on the metal surface and the two arrows are meant to indicate two alternative "routes" for the adsorbed hydrogen atoms. Thus one possibility is that the latter can combine to yield a hydrogen molecule ($H_{(g)}$) which is released from the metal surface either as a gas molecule dissolved in the aqueous environment or combines with other adsorbed hydrogen atoms to form gas bubbles. The alternative is for the adsorbed hydrogen atoms to diffuse into the interior of the metal (indicated by $H_{(m)}$) and where in certain circumstances with some metals, they can cause embrittlement of the metal.

b) In alkaline or neutral conditions (i.e. pH around or above 7) the cathodic reaction involves the reduction of oxygen molecules dissolved in the aqueous environment as follows,

$$O_2 + 2H_2O + 4e^- = 4(OH)^-.$$

In most instances of the corrosion of metals, both anodic and cathodic reactions occur on the surface of a single component. The corroding metal acts like a short-circuited electrochemical cell with the aqueous environment completing the circuit between anodic and cathodic sites (Figure 2.1.2).

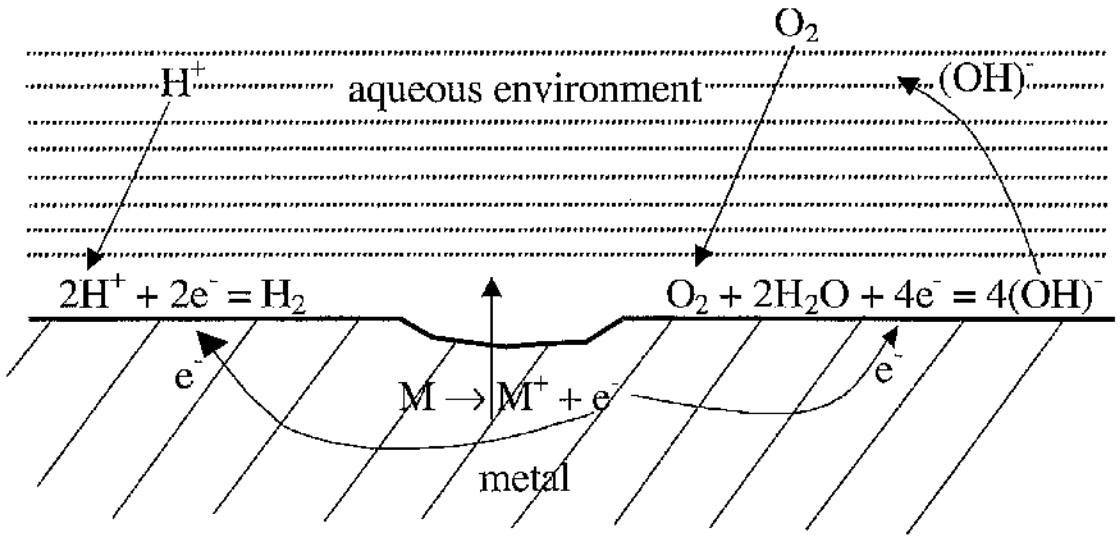

Figure 2.1.2. Schematic diagram of anodic and cathodic reactions on a metal surface.

A major consequence of this electrochemical mechanism of corrosion is that the rate of metal loss (in say mm of thickness lost per year) is directly proportional (via Faraday's law of electrolysis) to the magnitude of the electrical current flowing in the surface of the corroding metal. Faraday's law can be stated in the following manner.

The passage of one Faraday (96500 Coulomb) of electrical charge across the metal will cause the liberation or consumption of 1/n moles of chemical species, where "n" is the number of electrons involved in the electron reaction. Thus during the corrosion of iron, $Fe = Fe^{2+} + 2e^-$, the passage of 1 Faraday will dissolve ½ mole = 55.85/2 gram of iron, since the atomic mass number of Fe equals 55.85.

The rate of electron reaction is the dissolution rate after the passage of 1F/sec. For iron the dissolution rate will be 55.85/2 = 27.93 g/sec.

Electrode Potential

During aqueous corrosion, charge is being transferred across the metal surface according to the anodic and cathodic sites. This will lead to a charge separation across the metal surface (Figure 2.1.3) on which the anodic reaction $M = M^{n+} + ne^-$ is occurring.

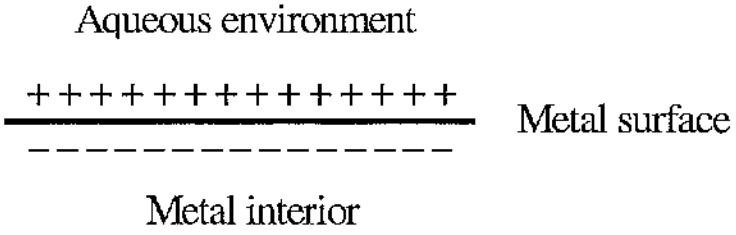

Figure 2.1.3. Charge separation across the metal surface.

This charge separation is called the **"electrode potential"** and can be easily measured by connecting the metal via a high impedance voltmeter to a reference electrode (Figure 2.1.4).

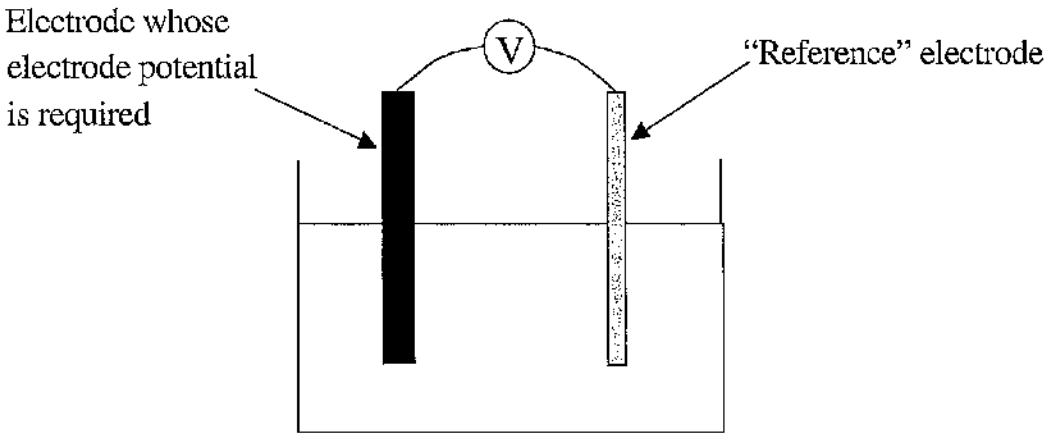

Figure 2.1.4. Representation of measurement of electrode potential.

The indicated voltage is then taken as the electrode potential relative to that of the reference electrode used, and is expressed as:

"x volts to the SHE scale" if a standard hydrogen reference electrode has been used

or

"y volts on the SCE scale" if a saturated calomel reference electrode has been used.

Equilibrium Electrode Potential

As the metal dissolution reaction $M = M^{n+} + ne^-$ progresses, the charge separation across the surface increases in magnitude. Eventually the electric field will have built up to such a level that any further metal dissolution will be prevented.

This situation is called "equilibrium condition" and the value of the potential difference across the metal's surface is called the **"equilibrium electrode potential"**, E_o.

As shown in Figure 2.1.5, if the existing electrode potential, E, across the metal surface is more positive than the equilibrium value, E_o, then the dissolution reaction $M = M^{n+} + ne^-$ is driven spontaneously in the anodic direction, $M \longrightarrow M^{n+} + ne^-$.

If the existing electrode potential, E, across the metal surface is less positive than the equilibrium value, E_o, then the reaction is driven spontaneously in the cathodic direction, $M^{n+} + ne^- \longrightarrow M$.

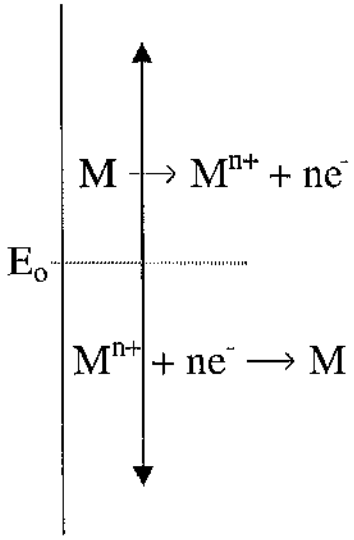

Figure 2.1.5. Schematic representation of the directions of anodic and cathodic reactions.

Mixed Potential

It was indicated that a metal tends to come to an equilibrium state in which there is no net reaction occurring. This represents what happens if only one electrode reaction can occur on the surface of a metal. However, in general the basic mechanism of aqueous corrosion is based on the occurrence of at least two reactions on a metal.

Consider a piece of pure iron immersed in an acidic aqueous solution (say pH=4) which contains dissolved Fe^{2+} ions at a very low concentration. One reaction that can occur is:

$$Fe = Fe^{2+} + 2e^-.$$

The value of E_o can be calculated using the 'Nernst' equation:

$$E_o = E_o^o + \frac{RT}{nF} \ln \frac{C_{M^{n+}}}{C_M}$$

Where E_o^o : The 'standard equilibrium electrode potential'

R : General gas constant

T : Absolute temperature

C_{Mn+} : Concentration of metal ion in the aqueous solution

C_M : Concentration of metal ion in the solid metal

For a given concentration of Fe^{2+} ions in the aqueous solution of say 1×10^{-6} mol/l, at 25^0C, E_o = -0.62 V (SHE).

Another possible reaction is $2H^+ + 2e^- = H_2$.

The equilibrium electrode potential for this reaction will be -0.24 V.

So there appear to be two electrode reactions tending to impose different potential differences across the metal surface. A uniform piece of a specific metal exposed to a homogeneous environment cannot exist at two different electrode potentials. It attains an intermediate value which is called **"mixed potential"** (Figure 2.1.6).

By reference to Figure 2.1.6, it can be deduced that at the mixed potential (often called the corrosion potential, E_{corr}) the spontaneous reactions are:

$$Fe \longrightarrow Fe^{2+} + 2e^- \quad \text{(anodic)}$$
$$2H^+ + 2e^- \longrightarrow H_2 \quad \text{(cathodic)}$$

i.e. Fe will be spontaneously corroding.

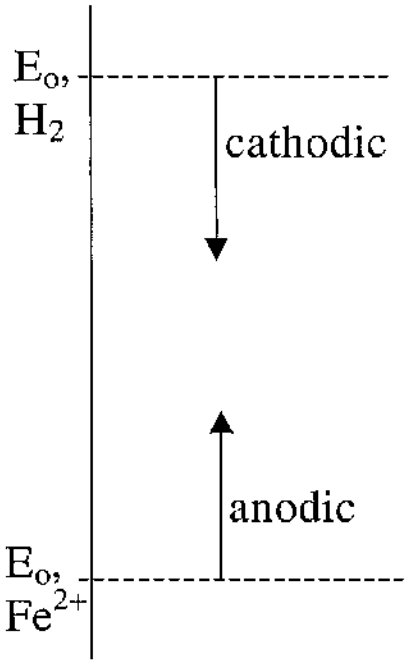

Figure 2.1.6. Schematic representation of the mixed potential.

Types of Corrosion Damage

General corrosion

General attack, at a more or less uniform rate, over large areas of the surface of a component, is the most common form of corrosion. The rates of this type of corrosion can vary over very wide ranges. If the product (say M^{n+} ions) of the anodic reaction, $M = M^{n+} + ne^-$ go into solution in the immediately adjacent environment, then the rate of metal loss may be high – thus leading to serious operational problems.

On the other hand, there may become established on the metal surface an insoluble film (often an oxide or hydroxide). This may be an air-formed film or it may be produced upon exposure to the aqueous environment and, if it is protective, i.e. if it forms as an adherent, non-porous film on the metal surface, it can protect the metal from rapid corrosion. This kind of behaviour, when a protective film forms on the surface, is known as "passivity".

Galvanic corrosion

When two dissimilar metals are in contact (connected by an external wire or by welding or bonding) in the presence of an aqueous environment (Figure 2.3.) a battery effect is created, current flows and one of the metals corrode. In considering bimetallic couple, it is important to know which of the two metals is more anodic (less noble). Any metal in the galvanic series will tend to have corrosion accelerated when it is coupled, in the presence of an aqueous environment, with a metal of more positive equilibrium electrode potential. The corrosion of the metal with positive or less negative potential will tend to be reduced, or even avoided.

Pitting corrosion

Pitting occurs when the protective film of a metal breaks down at small isolated spots. Once started, the attack may accelerate because of differences in electrode potential between large area of passive surface (large cathode) versus the active pit small anode). Typical events leading to the initiations of pits on a free surface are:

a) Localised mechanical or chemical damage to a protective oxide film in circumstances preventing its reformation.
b) Localised damage to, or poor application of, a paint coating.

Crevice corrosion

This type of corrosion results from local differences in oxygen concentration associated with deposits on the metal surface (typically weld deposits), gaskets, joints of a bolted assembly etc. where small amounts of water can collect and become stagnant. Once attack begins within the crevice, its progress is very rapid, and it is frequently more intense in chloride environments. Mechanisms of initiation of corrosion under crevices are associated with changes in local chemistry (such as acidification, oxygen depletion, depletion of inhibitors) compared to the bulk solution outside the crevice.

Intergranular corrosion

The grain boundaries in a material are sometimes attacked by a corrodent preferentially to the interior of the grain. The attack is usually related to the segregation of specific elements or the formation of a compound in the boundary.

Corrosion then occurs by preferential attack on the grain-boundary phase, or in a zone adjacent to it that has lost an element necessary for adequate corrosion resistance. In a severe case of grain-boundary corrosion, entire grains may be dislodged due to complete deterioration of their boundaries. In any case the mechanical properties of the structure will be seriously affected.

De-alloying or Selective leaching

In some, relatively rare, circumstances (but often involving copper-base alloys) corrosion on an alloy component may take the observed form of one of the major alloying constituents being seemingly "selectively dissolved" leaving other alloy components behind as a kind of spongy mass on the component surface. The detailed mechanisms involved to produce this phenomenon may be rather more complex than simple selective dissolution.

Stress corrosion cracking (SCC)

SCC is caused by the combined effects of tensile stress and corrosion. Materials can fail in certain environments after being subjected for periods of time to stresses which they could support indefinitely in air. The stresses involved in SCC need not necessarily be applied stresses; they may be residual stresses produced during manufacture. The detailed mechanism involved to produce this mode of failure consist of three stages. First there is an induction or initiation period which consists of slow corrosive attack. This produces a pit or other form of stress concentration which can develop into a recognisable crack. Second there is a stage of slow crack growth during which the combined effects of stress and corrosion promote propagation. Third when the remaining sound metal cannot support the applied stress, rapid failure occurs.

2.2. Copper-nickel alloys

2.2.1. Relevance to marine industrial situation

MSF operational principal

Multi stage flash distillation is highly developed and the most widely used of the distillation processes, for producing potable water from seawater. As described in [17], an MSF Evaporator is made of a massive block of carbon steel which consists of a number of stages. As shown in Figure 2.2.1.1, an MSF plant consists of three sections, heat input, heat recovery and heat reject. The heat recovery section is enclosed in a single vessel, which is divided into compartments and separated by internal walls. The flash chambers are designed to withstand pressure differentials.

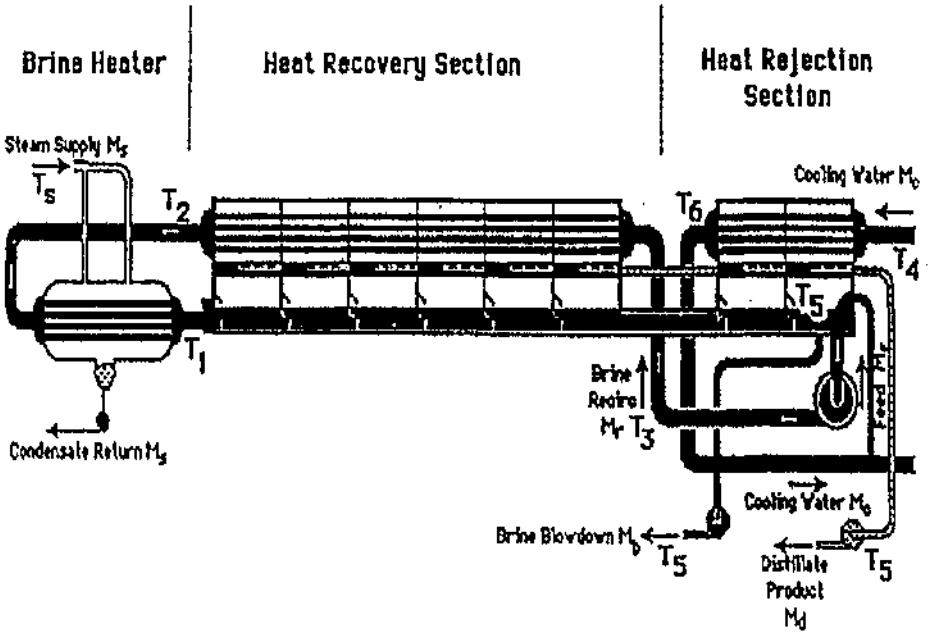

Figure 2.2.1.1. A lay out of an MSF evaporator plant [1]

Each stage consists of condenser, flash chamber, deflecting plates, demister pads, flow guide vane, product tray, and distillate storage and non-condensable gas extraction pipes with all those components welded together. The flash chamber, which is located at the lower part of each stage, is the most important part of the evaporator. This is where brine flashes and distillate is produced (Figure 2.2.1.2).

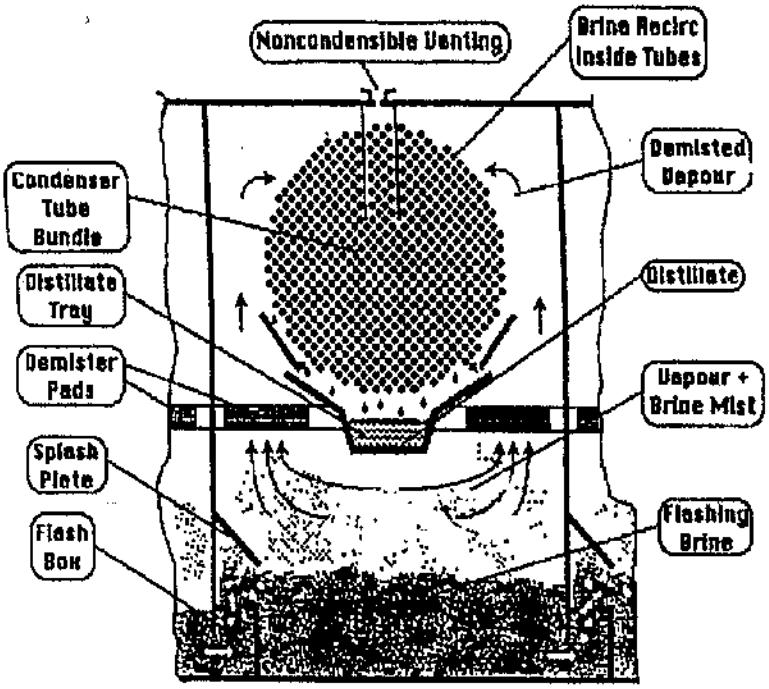

Figure 2.2.1.2. MSF evaporator recovery stage [1]

Pretreated seawater from a common seawater header is pumped to the inlet of the last stage of the evaporator reject section. It flows through the condenser tubes of all reject stages, where water is preheated by vapours generated in flash chambers and passed through demister pads. The vapour condenses on the outside of the condenser tubes and the resulting liquid water is collected on distillate trays. On leaving the final stage of the heat reject section the cooling water, except for a portion equal to seawater feed make-up, is rejected to the sea. Make up seawater is chemically treated and then passed through either internal or external dearators to reduce corrosion caused by oxygen and carbon dioxide.

Feed make up is then introduced into the flash chamber of the last heat reject section where it mixes with concentrated brine. Part of this brine is rejected as blow down and the rest is introduced as a coolant into the condenser of the last stage of the multistage flash evaporator heat recovery section.

Recirculated brine temperature within the heat recovery section increases as it gains latent heat of condensation from the last to the first stage of recovery. From the outlet of the first stage of heat recovery section, recirculated hot brine flows into the heat input section where its temperature increases by a few degrees using low pressure steam until it reaches its required top end temperature. The heated seawater is then passed to the first stage of the recovery section flash chamber. Part of the hot brine introduced into the first stage flash chamber flashes into vapour and condenses on the condenser tubes. In this way liberated heat is used to preheat the recirculating brine.

An air ejector is used to maintain the required vacuum at each stage of the process and to remove non-condensable gases. The pressure in every stage is controlled so that incoming heated brine flashes instantaneously. After flashing, the temperature of the circulating brine reduces and passes into the next lower pressure stage where further flashing takes place. The maximum temperature in the top flash chamber is usually chosen to be somewhere between 95° – 115°C while the minimum temperature in the bottom end flash chamber is typically about 5°C above ambient temperature (dependent on the location of the MSF plant). The corresponding pressures are in the range of ~1 bar (for maximum temperature) and 0.03 – 0.07 bar (for minimum temperature of 25° to 40°C respectively). This operation continues at lower temperature and pressure until circulating brine reaches the last stage of the heat reject section where it is mixed with feed make-up seawater. The brine then flows into the brine recirculating pump and the process is repeated.

Distillate from each stage of both recovery and reject section is collected in a common product water tray. As the product proceeds from a higher to a lower pressure stage it flashes and consequently cools down. Vapours from distillate flashing condense on the condenser tubes and drop back as liquid into the product tray. This process of brine and distillate passing in parallel continues until they reach the last stage of the evaporator reject section where distillate is pumped out. Heat is rejected as the

temperature of the circulating brine and distillate is reduced to the temperature of the incoming feed at the last stage of the evaporator reject section.

Corrosion problems

Corrosion is a factor with very important consequences on the life of any process plant and in particular on the efficiency of water production of MSF desalination plants. Corrosion is a common problem in MSF distillation plants with many components, pumps, pipework, main shell and flash chambers, commonly experiencing corrosion problems. Additionally corrosion can have a major impact on the heat exchangers (condenser tubes) where problems are expected both on the brine side of tube (tube inlet [18] and internal surface of the tube) and the vapour side of tube (outside surface of the tube). The research work described herein is addressed to corrosion on the heat exchanger tubes and thus this particular issue is discussed later in more detail.

The main factors determining the choice of materials for heat exchanger tubes in MSF (and other) plants are cost, corrosion resistance and thermal conductivity. Copper-base alloys have wide application in industrial heat exchangers on account of their high thermal conductivities, reasonable cost and acceptable corrosion resistance in many circumstances. For the conditions in MSF plants aluminium brass has been found to be rather vulnerable to corrosion damage. Hence copper-nickel alloys have found increasing application in MSF plants on account of their generally superior corrosion resistance. In fact the thermal conductivity of the copper-nickel alloys is less than that of most other copper alloys. However, the overall heat transfer from the vapour outside the tubes to the liquid inside is dependent not only on the conductivity of the tube material but also on the films and deposits which form on the metal surfaces.

Brine side

In recent years [19], Cu-10 %Ni and Cu-30 %Ni have seen increasing application as the material most commonly used for heat exchanger tubes in MSF plants. These

copper-base alloys depend for their corrosion resistance upon the formation of an oxide film and, when tube failures occur, they are most usually associated with local breakdown of the protective film by pitting attack. Such localised attack is most prevalent in high-velocity water and often involves impingement and/or erosion-corrosion mechanisms. The precise value of the velocity at which the protective film breaks down depends upon a number of factors including alloy composition, aggressiveness of the water and presence of suspended solids.

Flow rates through tubes in MSF plants are in the range 1.5 – 2.5 m/s. In any case, local flow rates may significantly exceed 'plant-design values' causing breakdown of the protective oxide film due to localised turbulence caused by poor inlet-end design and deposition of debris. The water velocity can be increased three times locally by such restrictions. On the other hand pitting can occur under 'stagnant' water conditions (below about 1 m/s for the copper-nickel alloys), especially where deposits can settle on the tube wall to allow locally aggressive conditions. It is also mentioned in [19] that the largest proportion of tube failures occur in the highest temperature stages of the heat recovery section.

Vapour side

Corrosion can also occur on the condensing side of tubes [19]. Experience in recent years indicates [11,12,13] that corrosion from this source occurs to a greater extent than perhaps had been recognised. A particular cause of corrosion from the steam side is inadequate venting of non-condensable gases. The detailed events involved in this phenomenon are as follows. CO_2 is released in the high-temperature flash chambers by thermal decomposition of bicarbonate present in the feed:

$$2(HCO_3)^- = (CO_3)^{2-} + CO_2 + H_2O$$

The liberated CO_2 can lead to the formation of carbonic acid when in contact with the condensing water film on the tubes

$$H_2O + CO_2 = H_2CO_3.$$

This can stimulate corrosion on the tubes in the high-temperature stages by lowering the pH of the condensate film as follows:

$$H_2CO_3 = H^+ + (HCO_3)^-$$
$$\text{and } (HCO_3)^- = H^+ + (CO_3)^{2-}.$$

The authors of [18] have summarised the service problems linked to vapour side corrosion in MSF plant located in Abu Dhabi as follows:

- Copper oxide deposit of thickness 2-3 mm covered the distillate system i.e. trays, corridors, and distillate pumps. This problem is a vapour side corrosion and some of the tubes in the high temperature region had reached a critical limit and lost 50 % of the thickness.
- High concentration of copper in the distillate product during and after the start-up of the MSF units is in the range 0.3 to 0.4 ppm. It was observed that the high initial rise of copper concentration is related to the outage period of the distiller.

Vapour-side corrosion of condenser tubes can also be associated with other gases such as Cl_2 and Br_2 but these problems are of relatively rare occurrence.

2.2.2. General comments on the corrosion behaviour of Cu and Cu-base materials.

Copper is a very versatile material and its properties both with regard to corrosion and mechanical strength can be easily improved by alloying. Most copper base alloys show a satisfactory performance in seawater. However, they can undergo serious damage under conditions of high flow velocities and polluted seawater, particularly by sulphides and ammonia. There are hundreds of copper alloys with different properties and these are grouped in a limited number of families [20] and the most important of these are discussed below.

Copper

The term "copper" here is meant to describe materials which have a designated minimum copper content equal to or higher than 99.3 %. These materials occupy a noble position to some extent in the seawater galvanic series and in many marine environments, including total immersion. Their corrosion resistance is good as they are attacked evenly and slowly provided the velocity of water does not exceed 1 m/s. The corrosion rate seriously increases in waters with speeds above this value. Water containing substantial amounts of carbon dioxide, often found in water from evaporators, may attack copper. Oxidation of copper by pure deoxygenated water under the formation of hydrogen is not thermodynamically feasible as described in [21]. No hydrogen evolution by corrosion of pure copper in deoxygenated distilled water was observed during an exposure period of 61 days. Because of their high thermal conductivity, some coppers are used in condensers and heat exchanger tube, in evaporators, in distiller tubings and in air conditioning and refrigeration units.

A major use for "copper" is for pipework in domestic and industrial plumbing systems. Copper usually performs satisfactorily but, over several recent decades, pitting corrosion problems of copper pipes have been experienced in many countries [22]. Such problems are often associated with specific water composition and many aspects of this matter have been discussed in relevant investigations [23-25].

The brasses

Brasses are basically binary alloys of copper and zinc. Small amounts of other elements might be included to enhance some special properties. According to their crystallographic structure, brasses are generally divided into the following categories:

a) Single phase (alpha) brasses with up to 37 % Zn.
b) Two phase (alpha + beta) brasses which start to form at about 37.5 % Zn.
c) Single phase (beta) brasses which contain about 46 % Zn.
d) Two phase (beta + gamma) brasses containing above 50 % Zn.

The *alpha* brasses are very similar to copper. Their strength improves with the increase of the zinc content. Alpha brasses suffer considerably from the selective dissolution of zinc and the phenomenon is known as dezincification. The loss of zinc reduces the mechanical properties of the material since the dezincified portions are weak and porous. Nowadays the use of alpha brasses must be limited to the inhibited types (containing arsenic). Inhibited alpha brasses are successfully used in small seawater cooled condensers, provided the flow velocities are low and the water is clean.

The *alpha-beta* brasses are two-phases alloys whose zinc content lies within the limit 37.5 to 45 %. Alpha-beta brasses suffer severely from dezincification when in contact with seawater. To date no reliable method of inhibiting the dezincification of the two phase brasses has been discovered. Despite this fact, some two phase brasses are used in desalination plants and ship building. Although the alloys seem to function properly, their success is not due to good corrosion properties, but rather to gross over-design in very thick sections. They must be continually inspected and treated by patching and painting. As a rule alpha-beta brasses should not be used in contact with seawater.

The *beta brasses*, containing 50 % of each of copper and zinc, should not used in contact with seawater. They suffer rapid dezincification which is in the form of intercrystalline cracking.

Similarly, *gamma brasses*, with less than 45% Cu, possess neither the mechanical nor the corrosion properties necessary for the construction of plants operating with seawater.

Small additions (2.5 %) of aluminium to alpha brasses greatly improve their corrosion resistance. The material known as Aluminium Brass owes its excellent resistance to impingement attack to a self-healing, thin protective surface film. Aluminium brasses are used in seawater and brackish water at velocities up to 2.2 m/s. Al-brass alloy has been used as tubes in the brine heater of MSF plants because of its often good resistance to high temperature brine. A further improvement of the erosion-corrosion resistance of Al-brasses involved the addition of 0.2 to 0.5 % silicon.

The bronzes

Bronzes are basically copper-tin alloys, containing up to 8 % tin. The higher the tin content of theses alloys the more resistant they are to corrosion by seawater. Care must, however, be paid that the heat treatment of the high-tin alloys does not produce tin-reach segregates since that will lower the corrosion resistance in sea water.

Generally bronzes exhibit a better corrosion resistance than brasses. It was shown in [26] that after 24h dipping in the aqueous solution of copper chloride (12.7 g $CuCl_2 \cdot 2H_2O$/1000 ml H_2O) dezincification was more or less recognised for three specimens of brass, but not for bronze specimens at all. The test results agreed well with the field experiences in that bronzes are superior to brasses in corrosion resistance.

Alloys of copper containing up to 10 % aluminium, referred to as aluminium bronzes, have proved to be very useful as their corrosion resistance in sea water is very high. This type of copper alloy owes its good corrosion characteristics to the presence of a very thin transparent film on its surface which heals very rapidly when damaged. However, dealloying of aluminium bronze has repeatedly shown to be a problem [27,28]. Although additions of nickel has found to improve its character, severe selective phase corrosion can occur near the heat affected zone of welded cast of nickel-aluminium bronze during exposure to seawater environment.

Copper-nickel alloys are another important range of copper-base engineering materials with corrosion resistance, especially in marine conditions, usually superior to brasses and bronzes [29,30]. But since copper-nickel alloys form the basis of this research, their corrosion behaviour is described and discussed separately later.

Ferrous sulphate as a treatment for copper alloys

The possibility of being able to control corrosion behaviour of copper alloy condenser tubes more precisely than by relying on the formation of iron corrosion products in the system is described in [31]. According to the author small regular additions of ferrous sulphate ($FeSO_4$) to the cooling water can have great effects on limiting the deterioration of copper base condenser tubes.

The points of interest concerning ferrous sulphate treatment to prevent corrosion of copper base condenser tubes can be summarised as follows [32]:

a) It is most important to inject freshly made up ferrous sulphate solution directly into the condenser waterbox, or at a point in the cooling water intake pipe close to the condenser. Experience suggests that the further from the condenser the point of injection is, the less effective the treatment will be.
b) Substances based on ferrous sulphate are claimed to increase effectiveness in corrosion resistance.
c) There is some evidence that chlorination can cause increased risk of corrosion at higher than normal levels and that ferrous sulphate can prevent the damaging effects.
d) With copper-nickel alloy tubes ferrous sulphate treatment is normally unnecessary. However, there have been instances where corrosion has developed in increased levels and the treatment has proved beneficial with such tubes.
e) Although ferrous sulphate treatment is normally used in seawater situations, beneficial effects has also been observed with fresh waters.
f) Studies of the films forming as a result of ferrous sulphate treatment indicate that lepidocrocite FeO.OH is sometimes present. North and Pryor [33] showed that this film provides corrosion resistance to copper surfaces.

Erosion-Corrosion

It is well known [1-4] that copper-base alloys are rather susceptible to erosion-corrosion attack at relatively low velocities (say compared to stainless steels). The different alloys possess varying resistances to erosion-corrosion and this leads to the specification of maximum permissible flow rates in various conditions (see later in relevance to desalination plant).

Some work, directed to erosion-corrosion of copper alloys in domestic water systems involved a study, [26], of a number of brass and bronze alloys using a vibratory cavitation test with eccentric stationary specimen for cavitation erosion-corrosion and also a jet-in-slit test for flow induced localised corrosion. The appearance of damaged surfaces after cavitation erosion-corrosion test were quite similar to each other. Damage depth was adopted as the index of cavitation erosion-corrosion damage. The most important feature was the linear relationship between the depth and exposure time. This test method was judged to have failed since the results obtained indicated the superiority of brasses over bronzes, which is contrary to the field experience. After the 420 min test in the jet-in-slit apparatus every surface of bronze specimen was covered with a relatively thick layer of corrosion products. In contrast to this, dezincification (as identified by the change in colour) as well as flow induced localised corrosion (as identified by the ring shaped groove) had occurred on the surface of brass specimens. Over the whole range of measurements the bronze specimens exhibit smaller amounts of mass loss and lower corrosion rates than the brass specimens. The test results agreed in all aspects with the field experience and the superiority of bronzes over brasses in the erosion–corrosion resistance was clear.

2.2.3. Copper-nickel alloys in seawater

This section covers a general review of copper-nickel alloys when in contact with seawater, and the relevant industrial situation where copper-nickel alloys are widely being used.

General review

Much valuable and detailed work on copper-nickel alloys in seawater was done in 1970's and 1980's and during this period a number of review papers appeared [1,2,10,34-36], the main features of which are now summarised.

Effect of iron in the composition of copper-nickel alloys

The beneficial effect of incorporating iron in the copper-nickel alloys has long been known and this addition is essential to obtain adequate corrosion resistance by assisting in protective film formation [10,20]. It has been established that the main component of the protective film forming on these alloys in seawater is cuprous oxide (Cu_2O) with the protective value enhanced by the incorporation in the film of nickel and iron causing decrease in both ionic and electronic conductivity [2,36]. Small additions of iron to copper-nickel alloys are also known to improve their resistance to erosion-corrosion [37]. However, at velocities above 7.6 m/s the corrosion rate of a Cu-30%Ni containing 0.6 % Fe has been reported to be greater than that for a 0.06 % iron alloy. At velocities less than 7.6 m/s the addition of 0.6 % Fe appeared to be increasingly beneficial [34]. Again, under high velocity (7.5 m/s) conditions causing film breakdown, the rate of impingement attack for Cu-10%Ni was marginally higher with the 2 % iron alloy than with 1.1 % - 1.4 % iron alloys, but still a good deal less than with alloys with 0.7 % iron or less [36].

Nature of the protective film

It is well established that under stagnant or low velocity conditions, at least, corrosion rates obtained for short periods of exposure of copper-nickel alloys are generally very much higher than for long periods of exposure [3,34,38,39]. The decrease in corrosion

rate with time is due to the formation of partially protective films of corrosion products at the metal surface. As time passes, this film can thicken and offer increasing protection against further corrosion. For instance one of the reviews reported that copper-nickel alloys had significantly lower long-term corrosion rates after 18 months compared to those specimens measured only after 6 months of exposure to seawater [1]. Again over a 30-day period in natural and artificial seawater [40], corrosion rates of Cu-10%Ni and Cu-30%Ni decreased continuously. It was noted in [39] that the corrosion rate of copper-nickel alloys, as measured by weight loss, continues to decrease in quiet and flowing seawater well beyond three months up to, at least, 7 years.

It has been noted [2] that after one week's exposure of Cu-10%Ni there was a slight accumulation of iron and nickel at the surface. After 6 to 8 weeks exposure, by which time the protective layer appeared to be stabilised, there was a definite accumulation of iron and nickel at the alloy's protective film. The film formed in clean saline water has been identified to be largely cuprous oxide (Cu_2O), as inner layer, with cuprous hydroxychloride [$Cu_2(OH)_3Cl$] and cupric oxide (CuO), as outer layer, being present in significant amounts. The inner film is normally reddish. The outer film may be greenish, brown or yellow-brown. Although cuprous and cupric oxides are the principal components of the films, the lattice usually includes other metallic ions, iron, nickel, aluminium, calcium, sometimes silicon and sometimes other species. Principal anions include chlorides, hydroxides and carbonates, bicarbonates and oxides. Despite variations in compositions, this oxide type film offers a high degree of protection when formed in clean seawater [1,39,40]. It is known, as reported in [41], that the protective mechanism of the Cu-30%Ni alloy is the formation of a strong, adherent, protective, passive layer. On the other hand, Cu-10%Ni corrodes uniformly at a low rate, and resists localised attack and biofouling to a greater extent.

Effect of temperature

Temperature has a significant effect on corrosion of copper-nickel alloys, but does not, as might be predicted, result in a general increase in corrosion with increasing temperature. Generally, the corrosion of copper-base alloys in deaerated seawater flowing from 0.9 to 2.7 m/s increases as the seawater is heated to 63^0C. Maximum corrosion occurs at the intermediate temperatures 54 to 71^0C. As the seawater

temperature increases to high temperatures (~107^{0}C), a significant decrease in corrosion is noted [3].

The main effect at higher temperatures is the very fast formation of an efficient protective corrosion product layer [38,39]. In aerated seawater, as the temperature is increased from 10 to 40^{0}C, the protective layer of corrosion products is more readily formed. Moreover, the protective quality also seems to increase with increasing temperature. At 40^{0}C an efficient protective corrosion product film is formed within a few days of exposure. On the contrary, at lower temperatures increasingly more time is needed to obtain a corrosion product layer which, moreover, is less protective than that formed at 40^{0}C. For instance, as reported in [39], at 16^{0}C it took three months before a reasonable mature film covered specimens of Cu-10%Ni. Accordingly, substantially lower average corrosion rates are found for the same alloy exposed at 40^{0}C as compared with those found at lower temperatures [38].

Effect of velocity

Seawater moving over a surface creates a shear stress between that surface and the layer of seawater closest to the metal surface. As velocity increases the corrosion rate will at first increase slowly, as a result of increased oxygen supply (cathodic depolarisation) and decreased concentration (anodic) polarisation. Eventually the degree of turbulence and the shear stress will be such that the protective film is locally removed and at this "breakdown" velocity the rate of attack will increase dramatically [2]. It is shown that the shear stress at the inlet end of a condenser tube is about double that further down the tube. This explains why inlet-end erosion-corrosion is such a common occurrence and also explains the preference for the copper-nickel alloys that have been developed because of their greater velocity tolerance [1]. It was reported in [34] that Cu-30%Ni has a breakdown velocity of about 5 m/s when seawater flows through smooth pipes, but that this can drop to about 3 m/s when the degree of turbulence increases on the inner surface of the pipe.

Cu-30%Ni seems to be more resistant in low seawater velocities than Cu-10%Ni. According to [2] Cu-10%Ni suffered attack at velocities running from 2.5 to 3.5 m/s, but Cu-30%Ni was resistant at 4.5 m/s. However, Cu-10%Ni exhibited a significantly

lower corrosion rate than Cu-30%Ni at velocities of 7.9 to 8.8 m/s although the Cu-30%Ni alloy has a somewhat greater resistance to inlet-end erosion-corrosion in condensers and heat exchangers than Cu-10%Ni [1]. General experience is that Cu-10%Ni, with iron content of about 1.5 %, is used successfully in condensers and heat exchangers with water velocities up to about 2.5 m/s [35,36].

Under impingement conditions the corrosion resistance of Cu-30%Ni seems to be superior to Cu-10%Ni. At impingement velocity of 6.1 m/s Cu-30%Ni is more resistant than Cu-10%Ni [7,9].

Excessively low water velocities can be undesirable for copper-nickel alloys. At water velocities less than about 1 m/s, solid deposits in the water streams tend to settle on the metal surface. Some deposits can cause crevice or deposit attack. In addition deposits may stimulate impingement attack, e.g., where a lodged shell fragment in small diameter tubing divert flow against the tube wall. Maximum seawater velocity for Cu-10%Ni to avoid impingement attack and pitting is given at about 2.6 m/s [10].

Effect of pH

As pH decreases the corrosion rate increases. Low pH levels prevent copper-base alloys in general from developing or maintaining protective films (which, as mentioned earlier, consist of corrosion products at the metal surface) and thus, high corrosion rates are sustained. It has been shown, as reported in [39], that there was no film formation in seawater on Cu-10%Ni and Cu-30%Ni below pH 6 even though there was adequate oxygen, 5.5-7.5 mg/l, present. The unfilmed corrosion rates were high since high oxygen levels in combination with low pH further accelerate corrosion [3]. At higher pH's where some oxygen was present, corrosion rates were low and normal.

Furthermore, lowering the pH of either fresh water or sea water increases the rate of erosion-corrosion. If the pH of warm (35^{0}C) seawater flowing at about 2.7 m/s is adjusted to 3.6, no protective film forms on the surface of Cu-10%Ni [34].

Effect of oxygen content of water on corrosion rate

Corrosion of copper-nickel alloys is either eliminated or greatly reduced when the seawater has been deaerated [34]. According to [1] the corrosion rates of Cu-10%Ni and Cu-30%Ni remain low in the 20 to 200 ppb oxygen range (say in comparison to aluminium brass). Moreover higher dissolved oxygen (200 to 600 ppb) content does not significantly reduce the corrosion resistance of copper-nickel alloys at high temperatures (>77^{0}C) [3]. This explains the preference of these two alloys in desalination applications. It has also been reported that at a temperature test of 110^{0}C both Cu-10%Ni and Cu-30%Ni showed significantly reduced corrosion rates as the oxygen content was reduced from about 75 ppb O_2 to 5 ppb O_2 [34].

The effect of varying oxygen contents on the corrosion of copper-nickel alloys is also seen in flowing seawater. For flowing conditions of 1.6 m/s and for oxygen concentrations up to that corresponding to the air saturated value, Cu-30%Ni was more resistant than the Cu-10%Ni but at higher oxygen concentrations the two alloys behaved similarly [2]. Analysis of the films showed the main constituents to be copper, nickel, oxygen and chlorine.

Corrosion in polluted seawater

Copper-nickel alloys corrode at increased rates in polluted waters, particularly when sulphides or other sulphur compounds are present [1,2,10]. It is noted that sulphides in saline waters are not particularly detrimental to copper alloys unless dissolved oxygen is also present or unless exposure to oxygen-free sulphide-polluted seawater is followed by exposure to aerated seawater [1,2,5,35,36]. Generally the corrosion rate of both Cu-10%Ni and Cu-30%Ni alloys increases with increasing concentrations of dissolved sulphide [8]. It has been indicated that Cu-30%Ni is less severely attacked than Cu-10%Ni after exposure to sulphide concentrations. This behaviour difference is attributed to the more stable passive film that forms on the Cu-30%Ni alloy [2,8]. This comes into agreement with [7] where it is noted that sulphide is very deleterious to the alloys with low nickel content. In addition to that it is concluded that the higher the nickel content the more severe the susceptibility to pitting attack. However, increasing the sulphide pollutant in the seawater reduces the severity of pitting

tendency. For alloys with lower nickel content (Cu-10%Ni), the extent of localised attack seems to be slight.

An investigation on the corrosion of copper-nickel alloys in flowing (1.6 m/s) seawater containing sulphide, polysulphides or sulphur is reviewed in [2]. Under these conditions, cuprous oxide (Cu_2O) forms as the principal corrosion product causing damage to the protective film on the metal surface and hence lack of passivity. It is stated that if during the early life of condenser tubes clean seawater passes through, good protective films will form which are likely to withstand most adverse conditions. If, however, polluted waters are encountered during the early life, the films formed on the condenser tubes will likely not be fully protective and the risk of premature failure will be considerably increased [10].

It is also reported, [36], that all copper-nickel alloys are liable to deep attack in jet impingement tests with contaminated seawater, particularly when the water contains hydrogen sulphide. Under these conditions the behaviour of Cu-30%Ni is again superior to Cu-10%Ni [7,9]. This comes in contrast to [41] where it is claimed that Cu-10%Ni is more resistant than Cu-30%Ni under the same conditions. However, at high impingement velocity, corrosion of copper-nickel alloys decrease with increasing sulphide concentration. This is due to the formation of a copper sulphide layer that acts as a physical barrier to further corrosion [41]. The corrosion susceptibilities (as measured by polarisation resistance) of copper-nickel alloys in sulphide polluted seawater, whether aerated or deaerated, under a jet impingement velocity of 6.1 m/s were found [9] to be lower than those in unpolluted seawater under the same conditions.

Biofouling

Copper-nickel alloys are more resistant to the attachment of biofouling organisms than steels and most of the other common materials for construction. They are also resistant to the microfouling that occurs within condenser and heat exchanger tubing. The resistance to biofouling is an inherent characteristic of copper alloys in general and appears to be associated with copper ion formation within the corrosion product film [1]. It is reported in [35] that copper base alloys posses fouling resistance due to

the formation of the cuprous oxide (Cu_2O) corrosion product in their protective film which is toxic to the organisms.

Dealloying

The nickel content determines the corrosion behaviour over a wide range of nickel concentration. Increasing the nickel content reduces dissolution of the copper matrix, and even a small percentage of nickel significantly decreases the corrosion rate of copper-nickel alloys. For nickel contents < 50% (alloys Cu-30%Ni and Cu-10%Ni) there is simultaneous dissolution of both components with eventual redeposition of copper [6]. It is also observed [5] that the presence of sulphides in aerated seawater enhances the average mean corrosion rate of the highest nickel content alloy (Cu-30%Ni) by promoting copper preferential dissolution. The authors of [40] observed that dealloying of copper-nickel alloys only occurred in natural seawater (long term exposure >1 month) which suggested that it was due to the action of micro-organisms. No evidence of dealloying was noted in artificial seawater.

Effect of suspended particles

Sand is common in seawater from open channels in shallow waters. High sand loadings can be detrimental to copper alloy tubing and can damage the protective film, exposing bare metal to high unfilmed corrosion rates. For any given sand loading damage increases with the size and sharpness of the sand present. Fine beach sands which are the most likely to be encountered are less damaging than larger angular particles. Periodic exposure to even higher loadings is not necessarily damaging, particularly when fully mature films have formed. In general, Cu-30%Ni is more resistant than Cu-10%Ni in the presence of sand [39].

Chloride ion concentration

Corrosion behaviour in fresh, brackish and higher salinity waters is quite similar to performance in seawater. Experience indicates that velocity and turbulence damage may be a little less in brackish waters than in seawater. Copper alloys seem to perform much the same in low as well as high chloride waters. It is the other factors (pH, aeration, velocity, temperature, pollution) rather than chloride ion concentration that appear to control performance [39].

Industrial situation

Copper-nickel alloys have found extensive applications in desalination plants as heat exchanger materials due to their good antifouling characteristics, excellent heat transfer properties, their economic viability and, in general, satisfactory corrosion resistance. They exhibit good resistance both at high liquid velocity (erosion-corrosion) and at low liquid velocity (pitting attack), ammonia contamination, suspended solid etc [42,43].

Long term researches and actual field experiences have proven the suitability of copper-nickel alloys for tubing in the range of service conditions which are foreseen for a desalination plant. In spite of all knowledge, however, desalination plants do experience sometimes unexpected corrosion, the reasons, [44], being generally connected to:

a) improper surface of the tubes
b) corrosive conditions as occur during start-up or shut-down and still periods, leading to localised corrosion
c) malfunctioning of control instrumentation or omission of chemical analyses, resulting in an increase of the general corrosion.

Corrosive conditions can occur during start-up or shut-down and still periods leading to localised corrosion. For instance in the MSF desalination plant of Abu Dhabi it was observed [12] that the copper content of the distillate product of any distiller increased above the permissible limits when the distiller was brought back into operation following an outage. The results of the investigation followed, showed that the wear of copper oxide film during the shut-down of the desalination plant can be safely related to the corrosive humid atmosphere inside the desalinator. Under these conditions the oxidation of copper forms either cuprous hydroxide, CuOH, or hydrated cuprous oxide $Cu_2O.\times H_2O$ instead of the unhydrated oxide. These hydrated forms are assumed to be imperfect and hence less protective than the unhydrated oxide. Furthermore the hydrated films will be much thicker and probably less adherent. Hence, with the extension of the times of outages, more of the metal will be

oxidised. As the distiller is put again into operation a certain lapse of time will be needed to remove the unprotective film and to built a more compact one.

Furthermore another form of attack, which is improbable during continuous operation but very probable during still periods, is deposit attack caused by sand or fine particles carried by sea water that settled on tube surface. This situation can be very critical in heat reject stages. Once all causes of local corrosion are eliminated and the plant has been given a good start-up, the tubes will experience general corrosion at very low level provided the physico-chemicals parameters are kept under control [44].

Non-uniform corrosion and pitting corrosion are two most common attacks which can seriously affect a tube and which are linked with stagnant waters inside the tubes and high oxygen concentration above the permissible limits. In general, the presence of oxygen is detrimental to tube life and efficient deaeration is essential for successful desalting plant operation with copper alloys. The presence of seawater on copper alloy surfaces when oxygen is not controlled causes a differential aeration mechanism to be operative, especially when tubes are not wholly filled [44,45].

The higher metal losses are observed in the heat recovery exchanger, caused by the high oxygen concentration in the incoming seawater [45]. The feed from the heat reject section to the heat recovery section of many MSF desalination plants is deaerated, hence corrosion in the heat recovery section was not normally expected. However, the flash chambers of the heat recovery section are under vacuum and air is sucked in. In practice there seems always to be sufficient oxygen present due to the oxygen content of heat recovery section feed and to in-leakage of air, to support some corrosion of copper-nickel alloys [39].

Velocity of seawater has several effects in MSF plants [39]. At velocities below 0.9 m/s, sediments settle on the inside of pipes and tubing. Unless removed periodically, under-sediment corrosion in the form of pitting attack may occur. Slime layers are also built up at low velocities giving the chance to biofouling organisms to attach and grow. At normal heat exchanger tube velocities much of the biofouling is swept away because it is so lightly attached to the slime layer, which is one factor tending to keep the tubes clean and heat transfer capability in an acceptable range.

Erosion-corrosion is the major cause of copper-nickel alloy condenser tube deterioration and is most frequently encountered as either inlet end attack or as the result of lodged obstructions in the tube bore [39,42]. At normal design velocities of 1.5-2.4 m/s turbulence around debris lodged in copper-nickel alloy tubes, partially blocking flow, has led to pinhole type failures of the tubes downstream of such lodgements. The critical velocity at which the protective film is stripped away by flow for the tube alloys is 4.5 m/s and 4.1 m/s for Cu-10%Ni and Cu-30%Ni respectively. The extreme turbulence that occurs around lodgements explain why pinhole type penetrations occur downstream of debris lodgements and underline the need for good screens and good screen maintenance.

Cu-10%Ni is a reliable material for the heat recovery section of the desalination plants. Its performance is quite satisfactory since it does not undergo pitting and crevice corrosion under conditions of stagnancy which are encountered during shut-down. Inside these heat exchanger tubes, seawater is deaerated and virtually oxygen-free and therefore there is no chance of corrosion but damage due to erosion is not uncommon. Cu-30%Ni is an appropriate choice for brine heaters and heat rejection tubes and it is also used for tubing in the heat recovery section [43].

2.2.4. Copper-nickel alloys in distilled water

So far the effects of vapour side environments in MSF plants are not exactly clear. However, it is stated in the final report of the Dow Freeport program, as mentioned in [39], that unless CO_2 is effectively removed from the feed to the heat recovery section it will form low pH carbonic acid in the vapour zone and lead to increased vapour side corrosion of copper nickel tubing. As the pH drops low enough due to the presence of CO_2, corrosion of copper nickel alloys should be expected [46] provided sufficient air is also present. In the absence of air, CO_2 even at low pH would not corrode copper nickel [14].

In general Cu-10%Ni has performed exceedingly well in the heat recovery section, except in a few plants where inadequate venting of CO_2 in the first stage has led to high copper content in the distillate and external corrosion failures of a few tubes.

The latter is discussed in [20] on the failure of 66/30/2/2 cupro-nickel tubes in the first few high temperature stages of many MSF plants. Failures have occurred in distillers in Kuwait, Qatar, Saudi Arabia and Abu Dhabi, so the problem is not confined to one particular area of group of distillers.

More specifically in a utility with 24 large distillers, high temperature stage tube failures were detected in 14 units. A low pH and a higher than normal copper content in the distillate of the remaining 10 units indicated that failures will happen with them also. Failures are characterised by a sudden rise in distillate conductivity requiring an immediate shut down for tube plugging.

Earlier investigations [47] of low performance ratios and unequal flashing conditions in stages of many of the distillers in the group of 24 indicated that the vent flow rates were insufficient to extract the non-condensable gas. Although improvements in venting gave good performance benefits, they were not sufficient to reduce the tube failure rates to acceptable levels. The inner surfaces of all tubes in heat recovery sections were in excellent condition and no tube failures were due to erosion or tube bore fitting. All failures were attributed to vapour side corrosion.

It was concluded that tube damage was due to carbon dioxide. Since damage was remote from the vent positions, it was also concluded that flowing steam/carbon dioxide was not a problem and that vent flow was sufficient to avoid excessive gas concentrations at the vent extraction. The position of damaged tubes and the probable low vapour velocities at that point indicated that the problem was due to pockets of stagnant CO_2 gas.

When first considering this problem, it had been assumed that CO_2 would not dissolve in the distillate as it had been released from brine at virtually the same temperature and pressure. However, since CO_2 is not effectively extracted, a pocket of gas surrounding several tubes will blank them from condensing vapour. If the gas pocket

is of sufficient size the gas will cool to the temperature of the water flowing in the tubes. In this instance the gas temperature could be 7^0C less than saturation. Distillate dropping from upper row tubes would also be cooled by contact with the cold tubes. Gas could then redissolve in the distillate, leading to a lowering of pH. The aggressive solution obtained with up to 7 degrees of under-cooling will damage the protective oxide film of the tubes, leading to high copper content in the distillate. The installation of an auxiliary vent to reduce the size of the gas pocket allowed significant increase of the pH and reduction in dissolved copper.

Similarly, in initial stages of distillers of the MSF desalination plant of Jeddah, Saudi Arabia [13], there is a sharp rise in CO_2 if venting is not done properly. As a result CO_2 gets released into the vapour and attack the protective oxide film on the condenser tube surface. Most of the CO_2 is released in the high temperature stages.

The release rate of CO_2 is determined by two linked processes: decomposition of HCO_3^- in the flashing chambers,

$$2HCO_3 \longrightarrow CO_2\uparrow + CO_3^{2-} + H_2O,$$

and mass transport of CO_2 from brine to vapour. CO_2 evolved reacts with water and carbonic acid is formed as follows:

$$CO_2 + H_2O \longrightarrow H_2CO_3$$

If the steam and evolved gases are trapped somewhere in the evaporator or ventilation is not very effective then the condensation of the trapped vapours is quite possible. In consequence, acidic vapour side condensate will cause corrosion in presence of an oxidant, like oxygen which is conveniently available [13].

Analysis of the problem of vapour side corrosion of cupro nickels (Cu-10%Ni and Cu-30%Ni) in MSF plants is also given in [12]. After 15,700 hours of running the distillate pump No. 11 distillers 4 and 5 of UAN (E) plant, the pumps were inspected. The following observations were made:

- All rotating elements of the pumps were covered with a thick reddish brown powder in a thickness of 2-3 mm.
- Inner casing and diffusers were covered with the same deposit to a thickness of 1-2 mm.
- The cutless rubber bearing was completely damaged and sealed with the same deposits.

Chemical analysis of the deposit collected from the various pump section showed it to be formed mainly of cuprous oxide, Cu_2O, (94-97 %), while the rest was invariably iron oxide, Fe_2O_3. Apparently the Cu_2O originated from the corrosion of the vapour side of the condenser tubes.

The two distillers concerned were inspected in some detail and the results obtained were compared with those of a third distiller (unit No.6 of the same plant) whose pump did not show thick Cu_2O deposits. The study involved the determination of the copper ion content, the conductivity and the pH value of distillates of Cell Nos. 1, 2, 3, 9 and 16 of the three distillers. The measurements were taken over a period of three months. Inspection of the data revealed the following:

- With the exception of Cell Nos. 1 and 3 the copper content of the distillate of the three distillers was practically one and the same and ranged between 0.03 and 0.1 ppm. Cell Nos. 1 and 3 on the other hand exhibited comparatively larger copper content (0.2 to 0.55 ppm Cu^{2+}). This suggests that corrosion occurred principally in these two cells.
- The conductivity of all cells was practically one and the same. It ranged between 1.5 and 9 μS/cm.
- In all cells the distillate had a comparatively low pH, 6.2 to 6.8, denoting its contamination with some acidic gases which were not removed through the vacuum of the venting system.
- There was no relationship between the conductivity and the pH value of the distillate and its copper ion content.

The fact that corrosion was obvious in Cell Nos. 1 and 3 compared to the other cells strongly suggests that it was related to the design and/or operation of the distillers under consideration. Examination of the distillers showed that the vacuum system under which flashing occurs starts at Cell No. 2. The discharge of acidic non-condensable gases (CO_2, Cl_2, Br_2, etc.) will be maximum in this cell. On the other hand in Cell Nos. 1 and 3 poor ventilation of these gases is expected to prevail. The gases will have a better chance to dissolve in the vapour and to attack the protective oxide film on the tube surface. This will lead to the increased copper content of the distillate of the two cells compared to the Cell No. 2, as found experimentally. Moreover, analysis of the temperature in the concerned cells strongly supported that in Cell Nos. 1 and 3, the removal of non-condensable gases was not sufficient.

Two complementary steps were suggested here. A curative step which will take care of the already present defects, and a preventive step with the aim to reduce the rate of attack.

The curative step involves:

a) The careful survey of the design diagrams of the distillers
b) Correction of the working deficiencies of cells
c) Removal of the existing copper oxides deposits
d) Adding sodium sulphite to the feedwater to scavenge any remaining chlorine/bromine
e) Passivation of the stainless steel tray and corridor to prevent deposition of copper.

The preventive step involves removal of all stagnant gas pockets by ensuring effective ventilation.

The vapour-side corrosion of Cu-30%Ni condenser tubes in MSF distillers is also recognised in [14]. Attack takes place at the inlets of tubes in the first high temperature cells and is located mainly at the lower part of the tube bundle. Recent failed tubes have shiny surfaces and a clear reduction of their wall thickness from the vapour side. Failure takes two distinct forms: The first is a circumferential attack at

the point of junction of the tube with either the tube plate or the tube support. The second form of attack involves longitudinal perforations along the tube differing in their size, depending on the progress of attack.

According to A. M. Shams El Din and R. A. Mohammed [14], corrosion is not due to assault on tube material by CO_2 resulting from the thermal decomposition of HCO_3^- and CO_3^{2-} ions of seawater. Corrosion involves the primary oxidation of the metal by air leaking through flanges, glands and/or gaskets, followed by dissolution in CO_2-loaded vapours condensing on the colder ends of the tubes.

For corrosion to occur in CO_2-loaded vapours, an oxidant must be present simultaneously. Two agents might be thought of. The first is chlorine which is added to seawater to a concentration of 0.20 to 0.25 ppm to discourage marine fouling inside the distiller. The second most likely agent to be consider is oxygen gas. This can originate either from the brine or from leakages. The O_2 in the flash chambers comes, most probably, from leakage through flanges, glands and/or glass sights. The entry of the gas is promoted by the vacuum inside the chambers.

Therefore it is concluded that the presence of both O_2 and CO_2 in the atmosphere of the cells is essential for the active dissolution of condenser tubes. When the two gases are present simultaneously, attack is 10-40% higher than the sum of that caused by individual gases.

In an attempt to support the above given assumptions, the authors devised a simple experimental set-up which simulated -to a reasonable extent- the conditions prevailing in the high temperature cells of an MSF distiller. The principle of the tests was to follow the change in weight of Cu-30%Ni test coupons as a function of time of exposure to water vapour at 100°C. A special adjustable glass guide ensured that water drops fell on the middle of specimens of a certain group. In that way the effect of bombardment with water droplets falling from an upper tube on a lower one could be also established.

Consideration of the test results allowed the following conclusions to be drawn:

1. The copper alloy is not affected by pure water vapour. Over a period 240 day exposure to steam, no detectable change in the coupon's weight was recorded. Since no trial was made to exclude air from the vapour, the excellent performance of the alloy was attributed to the formation on the surface of the metal of a protective oxide film. The film was also resistant to the hammering action of the falling water droplets. Over the same test period, the change in the coupon weight was less than 1 mg/coupon.
2. The Cu-Ni alloy is not affected by CO_2-loaded steam, whether alone or under bombardment with water droplets.
3. The inclusion of air (oxygen) in CO_2-saturated vapour greatly increases the corrosion rate of the alloy. In experiments where the metal was subjected to the combined action of the two gases through the thin skin of condensed water, the coupon experienced at the beginning a steady, linear loss in weight of 1.25 mg/dm^2 per day.
4. Coupons subjected to the action of falling water droplets in an O_2/CO_2 atmosphere exhibited a high rate of corrosion. The high corrosion rate, which amounted to some five times that measured in the absence of droplet bombardment, was evidently the result of the conjoint mechanical/erosive action of the droplets.

Experiments that included the hammering effect of falling water droplets were carried out to find a reasonable explanation to the fact that vapour side corrosion of condenser tubes is mainly confined to the lower part of tube bundle. The results obtained revealed that condensate droplets falling from tubes at the top of the condenser accelerate the wear of tubes at lower levels. Apparently a single impact will have no detectable effects. However, thousands of such droplets hitting the same spot will undermine the metal oxides as fast as they are formed.

2.3. Basic erosion-corrosion principles

Introduction

The need to maximise efficiency and minimise costs in handling fluids demands higher flow rates with the inherent risk of flow-dependent corrosion of engineering equipment [48]. Flow-dependent corrosion occurs on pumps especially as impeller speeds are increased, on pipes where high intensity turbulence exists in unstreamlined geometry changes or where the flow direction is suddenly changed and on valve seats where high velocities are induced during throttling [49-52].

Many of the types of problems alluded to above are commonly referred to as erosion-corrosion. However, in the general literature, there exist many different detailed definitions and interpretations of the term erosion-corrosion and of general materials degradation in flowing liquids.

Flow-induced corrosion can be defined as a complex form of material deterioration by an electrochemical corrosion reaction, which is accelerated by the relative movement (flow hydrodynamics) between a corrosive fluid and the metal surface [53]. The increased corrosion rate caused by a high-velocity fluid is associated with the transport of species to and from the metal surface, stimulating in that way the oxygen-reduction cathodic reaction.

Rapidly flowing water can have additional mechanical effects, in causing the tearing away of corrosion products (including protective oxide film that will result in localised attack at the areas at which the film is removed) and direct mechanical damage to the metal surface [53,54]. In situations where such mechanical damage is involved, the term 'erosion-corrosion' is often used. Erosion-corrosion can occur in high-velocity liquids ('liquid erosion-corrosion') and is accelerated in the presence of suspended solids ('solid/liquid erosion-corrosion'). Another form of damage associated with flowing liquids is 'cavitation' [54]. Damage to materials when solid particles are carried by a gas stream is called 'dry erosion' [55-60].

Dry erosion

Dry erosion, or in other words solid-particle erosion, implies the removal of material from component surfaces due to successive impact of hard particles entrained in a gaseous carrier fluid. Material removal due to solid-particle erosion is a consequence of a series of impacts, which results in a very intense contact between the hard particles and the component surface [55-60].

Factors that influence the dry erosion processes have been suggested by many researchers [48,61,62] and their combination suggests the following:

- Particle movement – impact velocity, impact angle, kinetic energy of the particles, interference between incoming and rebounding particles.
- Erosive particle – hardness, size, shape, concentration and density.
- Target material – hardness, tensile strength, ductility and metallurgical structure.

Erosion of metals usually involves plastic flow, whereas more brittle materials may wear predominantly by fracture [58,59]. The contrasting behaviour of ductile and brittle materials under dry erosion is described with respect to impact angle [56,58,60]. The relationship shown in Figure 2.3.1 has become widely recognised as a guide for the prediction of the behaviour of materials when the angle of impingement is defined.

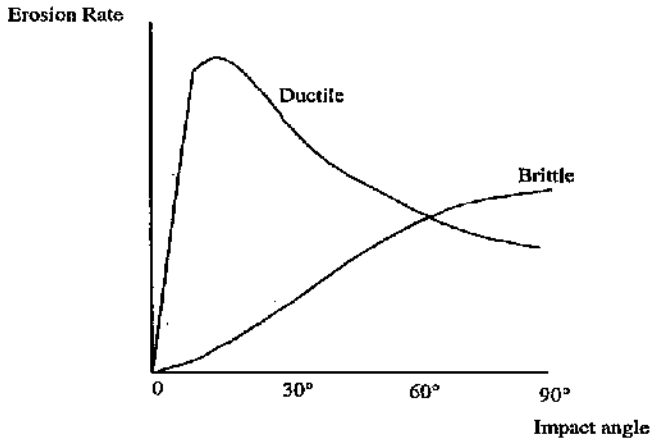

Figure 2.3.1. Dry solid particle impingement relationship with impact angle for ductile and brittle materials.

Liquid erosion-corrosion

Liquid erosion-corrosion (i.e. in the absence of solids) can occur in a number of aqueous flow regimes, e.g. pump impellers, steam-turbine blades, in pipes, especially in regions where local turbulence occurs such as in presence of deposits, entrance of a liquid into a tube, at valves, bends. Fluid dynamics is of major importance to the above problems as is also the corrosivity of the fluid in many fluid-material combinations [63-70].

A particularly severe situation is that arising from a liquid impinging at high velocity directly upon a component surface. This is the scenario which is studied in the present research; hence the hydrodynamics associated with a submerged impinging jet are summarised below.

A free turbulent jet usually possesses four flow regimes (see figure 2.3.2) [66]:

1. A regime of flow development, where the flow extends up to 6.4 nozzle diameter i.e. $0 < z < 6.4d$, where 'd' is the nozzle diameter. The constant velocity core or potential core within the flow development regime is the region of the impinging jet in which the velocity profile of the jet changes from pipe flow to a free jet flow. As the flow discharges from the submerged nozzle, the stream of the jet starts to mix with the surrounding fluid. The mixing zone grows in width along the downstream direction of the jet. This leaves a conical potential core wherein the fluid property and the velocity are relatively constant [66,67].
2. A transition region between 6.4d and 8d.
3. A region of developed flow, extending out to about 100d.
4. A terminal region where the centreline velocity decreases steeply towards zero.

In addition to the above, a free turbulent jet spreads out through a cone of half-angle about 10° [66], entraining a considerable amount of surrounding fluid in the outer part of the jet.

When a submerged jet collides perpendicularly with a flat plate in a stationary solution, there forms three distinct flow regimes along the surface of the plate. The extent of these can be discussed in terms of the radial distance 'r' from the stagnation point (the point of the flat plate directly under the jet) and the jet diameter, 'd' (see figure 2.3.2):

1. The stagnation (also called impingement and laminar) region: this is a layer of fluid on the flat plate in which the jet is deflected from the axial direction to a radial flow. The flow in this region is laminar [67,71-76]. According to [73], the radial velocity increases from zero at the stagnation point to a maximum at r/d~1 and then decreases.
2. The wall jet region: this is a region adjacent to the flat plate which commences at some distance from the stagnation point where the radial velocity starts to decay and the thickness of the boundary layer increases with extending radial positions [67]. Furthermore, in the wall jet region, where fully developed turbulent flow exists [74,77], the turbulent intensity starts to decay with increasing r [67,77,78].
3. The transition zone: this is a highly turbulent region [74,78] located between the stagnation and the wall jet regions. It is important to note that in the case when the submerged liquid jet strikes a flat metallic component, the maximum corrosion rate occurs at the transition phase of the two regions mentioned above [78].

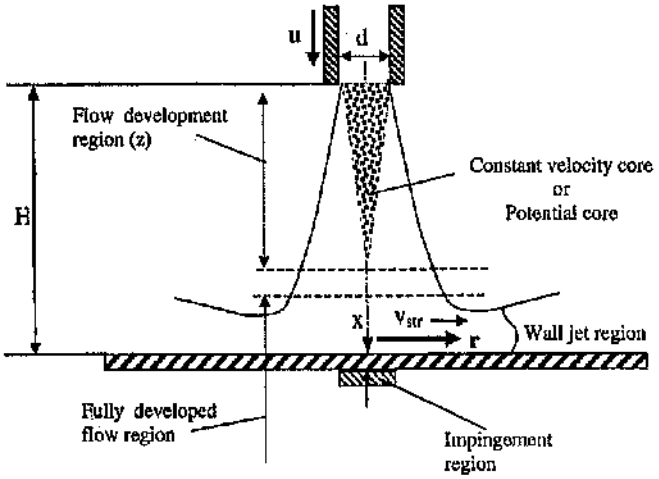

Figure 2.3.2 Submerged jet also called as free turbulent jet impinging onto a horizontal solid plate, showing typical velocity profiles in the main stream and the radial wall jet region [66,67,68].

Table 2.3.1 gives an indication of the radial extents of the stagnation and wall jet regions, suggested by various authors [67,69,71-78] (note that the size of the transition zone equals the difference between the stagnation and the wall jet regions). It is clear that there is no universal agreement in these respects; the varying zone sizes quoted in table 2.3.1 are very likely to be at least partly caused by the influence of the specific hydrodynamic conditions. For instance, it has been suggested [78] that the various regions increase in size as jet velocity increases.

Stagnation region	Wall jet region	Reference
r~1.0d		[71]
	r>2.0d	[72]
r ~0.5d		[73]
r ~1.1d		[74]
r =0.6-1.4d	r >4d	[67]
r =1.0d	r >2d	[75]
r =0.6-1.4d	r >3-5d	[76]
r =2.0d	r >4.0d	[78]
r =0.5d	r >1.25d	[77]
r =2.35d	r >3.0d	[69]

Table 2.3.1. Extents of the stagnation and wall jet regions, suggested by various authors [67,69,71-78].

Erosion-corrosion damage on a flat metallic component due to the action of a single-phase submerged impinging jet is associated with two possible mechanistic processes: Mass transfer [67,71,73,74,77-80] and/or shear stress [63,69,73,74,78-81].

Mass transfer

It is widely accepted [67,71,73,74,77-80] that the hydrodynamic parameter controlling erosion-corrosion for a number of systems is mass transfer. For instance it is quite clear that corrosion rates are influenced by mass transfer when this factor controls the corrosion rate (e.g. steel in seawater) on account of the role of the oxygen reduction cathodic reaction. In the stagnation zone, the mass transfer rate is most usually considered to be independent of radial positions, i.e. is uniform to the surface [73,77] and mass transfer is at its minimum in the stagnation region in relation to the

transition and wall jet regions [73,78]. Maximum mass transfer is said to occur in the transition region where the turbulent intensity increases rapidly and high local shear stress and velocity gradually develop [74,78]. A contrasting scenario has been presented by [67] according to which, maximum mass transfer develops at r<0.1d; between r=0.1d and 1.0d the local mass transfer rate is constant and beyond r=1.0d the mass transfer rate decreases with increasing radial distance.

It has been suggested by some [71,74], that maximum mass transfer is highly depended on the H/d parameter, and can have one or two peaks on the target surface. It has been described by [71] that for H/d=1.2, the maximum mass transfer has two peaks; one at r=0.6d and the other at r=1.95d. For H/d=8, mass transfer is maximum at stagnation point whereas in the more complicated case of H/d=5 there are several zones of different magnitude of mass transfer.

Shear stress

Shear stresses on a flat component under a submerged vertical impinging jet result from velocity gradients near the exposed surface [80]. The maximum velocity corresponds approximately to maximum shear stress [69], and as pointed by [74], the maximum shear stress coincides with position of maximum mass transfer. At the stagnation point, where the vertical and horizontal components are at their smallest [63], average shear stress is zero [69] and any significant erosion at it may be attributed to the surface roughness effects or to a non-shear dominant erosion mechanism, i.e. impact forces [69]. As the radial distance from the stagnation point increases, the water velocity and shear stress increase linearly up to a maximum value occurring at the edge of the stagnation zone [73] (which in the case of [73] is r=0.5d). On the other hand, R. C. Woolam et al [78] claims that the highest local shear stresses take place in the turbulent transition region (which according to [78] extends from r=2d to r=4d).

Silverman [64] has reviewed the impinging jet geometry. In cases where the corrosion is mass transfer limited, the corrosion rate is considered to be a function of the wall shear stress. Girald and Trass [63,69] have proposed that, at the wall jet region

(Figure 2.3.2) away from stagnation point, the shear stress 'τ_w' follows the equation for ratio r/d > 2-3 and Reynolds number 'Re' ranging from 2.5×10^4 to 1.25×10^5:

$$\tau_w = 0.0447 \rho u^2 \, Re^{-0.182} \, (r/d)^{-2}$$

where 'u' is the nozzle exit velocity (m/s); 'd' is nozzle diameter, 'r' is the distance from the stagnation point (m); 'ρ' is the liquid density (kg/m^3); τ_w is the shear stress (N/m^2).

Rajaratnam [68] has reported that the wall shear stress increases linearly with 'r' to a maximum value at $r/H \approx 0.14$ and then decreases as 'r' increases further. The maximum shear stress 'τ_m' is given by the expression below and is valid only for large impingement heights, i.e. H/d > 8.

$$\tau_m = 0.16 \, \rho \, u^2/(H/d)^2$$

where, τ_m – shear stress (N/m^2), ρ – liquid density (kg/m^3).

Some workers have claimed that shear stresses are important in developing erosion damage. As described in [69], in the wall-jet region pure erosion results from shear stresses only. It was also pointed out in [69] that if shear stress is not the only factor governing erosion in the wall-jet region, at least it is the dominant one.

In contrast, others, [79,81], suggest that shear stress is not a useful parameter to predict erosion-corrosion rate. Shear stresses in single-phase flow are in the order of ~0.05 MPa (as opposed to the tensile strength of metallic materials which are in the order of several hundreds MPa, e.g. 990 MPa for Ti-6Al-4V) [81,82] and as it was put in [81], it is hard to imagine that these can cause erosion damage to metallic surfaces. However, the relation between shear stress and flow rates is the matter of interest to the critical shear stress necessary for the breakdown of protective surface layers on metals [68], which can be the cause of the onset of erosion-corrosion.

Another possible mode of erosion damage under liquid impingement is the impact pressures that can result in plastic deformation of metallic targets, evident through slip and mechanical twinning [65,70]. Liquid impact produces a region where circumferential cracks can occur depending on the target material properties and the impact velocity. After impact, the flow moves radially and once it collides with a surface asperity, the force of impact can create a crack perpendicular to the surface. Subsequent impacts on existing cracks, pits or depressions can produce accelerated damage with large pieces of surface detached.

Cavitation

This phenomenon exists when pressure variations (resulting from large velocity changes, e.g. in pipe bends) cause the formation of vapour bubbles in regions of the liquid where the pressure is lower than the vapour pressure of the liquid. This is followed by collapse of these bubbles as the fluid encounters a higher pressure zone resulting in release of immense energy of the order of 1 – 2 GNm^2 [53] which subsequently leads to the damage of the surface e.g. mechanical 'cavitation' damage or to a combined 'cavitation corrosion' attack in corrosive environments. Bubble collapse in a cavitating system results in pressure transients at a surface and also micro-jets of liquid which impinge at velocities between 100 – 500 m/s [65,83]. The latter can, for instance, involve protective surface films being disrupted locally, exposing small anodic areas of bare metal surrounded by large surrounding undamaged cathodic areas [53]. The surface roughening provides better nucleation sites for new bubble formation and the corrosion process is intensified. Propellers, impellers and hydraulic turbine gear, bends and protrusions (flanges, tees and elbows) are the most common places to encounter corrosion by cavitation. Cavitation depends upon the fluid characteristic, material and fluid velocity. Vapour pressure, air content, surface tension, and fluid viscosity are parameters that influence cavitation wear [84].

Solid-liquid erosion-corrosion

Erosion of metals associated with impingement of solid particles entrained in a liquid stream is quite common in process industry, oil and gas refinery industry and many other multiphase flow industrial devices [61,85,86]. Other examples of erosive wear are in applications such as pipelines carrying sand/water slurries in mining operations and also in offshore oil extraction operations known as multiphase hydrocarbon transportation. Particles may also be contaminants such as fine airborne grit particles mixing into lubricating oil. Metal components in pipelines, in nozzles, valves, tees and bends are subjected to severe erosive wear resulting in premature failure of these components [87].

It seems very feasible that the hydrodynamic aspects described in the previous section are greatly overcome by the dominant effect of solid particles entrained in the impinging jet [69]. This emphasises the high contribution of mechanical erosion to the overall damage in solid/liquid erosion-corrosion conditions. However, there is clear evidence in literature of the role of corrosion and further modes of attack involving complex interactions between corrosion and erosion in contributing to the total material loss.

Aqueous erosion-corrosion has in the past been studied by weight or volume loss comparisons to provide a ranking of resistance to material loss through particle impact. Although this quantitative information is important from a practical viewpoint in determining the rate of material loss, it does not indicate how the individual processes of erosion and corrosion interact. Only recently [62,88-95] it has been recognised that, material loss by erosion-corrosion in aqueous systems is often governed by complex mechanisms, which include electrochemical corrosion and mechanical wear interactions. The actual material loss in a corrosive aqueous environment is often much higher than the sum of the losses attributed by pure corrosion and pure erosion mechanisms in isolation, and is recognised as the synergistic contribution.

One such approach used recently by some workers [90-93] defines synergy as the effect of corrosion in enhancing erosion damage:

$$TWL = E + C + S$$

TWL is the total loss (in weight or volume), E is loss due to pure erosion in the absence of corrosion, C is loss due to pure corrosion only under erosion-corrosion conditions, and S is the synergy which represents an indirect involvement of corrosion processes in enhancing erosive material loss.

In an alternative approach some workers [62,88,89,95] define the total loss as

$$TWL = E + C' + dC_e + dE_c$$

with the synergy effect as split into two separate components:

$$Synergy = dE_c + dC_e$$

where E = loss due to pure erosion

C' = corrosion rate under flow impingement but without solid particles

dC_e = additive effect of solid particles in enhancing corrosion

dE_c = effect of corrosion in enhancing erosion.

The increased corrosion rate due to particle erosion, dC_e, is defined as the difference between the measured corrosion rate under erosion, $C' + dC_e$, and the corrosion rate during flow without particles, C'. It is to be noticed that $C' + dC_e$ in the second approach is equivalent to C in the first approach and that $dE_c = S$.

In the case of ductile metals, impinging particles cause localised plastic deformation in the forms of craters with raised lips. Material removal is favoured at the plastically lifted lips by repeated bombardment. The material loss due to mechanical wear is

mainly associated with ploughing or cutting in the case of a ductile material and cracking in case of brittle material by an abrasive action of hard and sharp particles.

The general concept of erosion-corrosion involves two interdependent phenomena: the fluid mechanics of the solid-fluid flow (or momentum exchange between the solid particles and the liquid) and the wear of materials by collision of abrasive particles on the metallic surface [61]. The material loss of a surface material by solid particles in a fluid stream depends on the number of particles striking the surface, their velocity and their direction relative to the surface. Moreover, the erosion-corrosion rate in a slurry flow is recognised [86,87] to be dependent on several factors such as:

- The liquid (viscosity, density, pH, temperature)
- The target (ductility, metallographic structure, work hardening, residual stress levels)
- Particles (size distribution, density, shape, hardness)
- Flow-field (angle of impact, particle-particle interactions, squeeze film)

Finnie in 1960 [85] recognised that the erosion rate in slurry flow would be determined by the number of particles impacting a surface, the velocity and their direction. J. A. Humphrey [61] reviewed the fundamental knowledge of the fluid motion in erosion by liquid-solid particle impact. Importantly, he stressed that the velocity of the particles moving in a fluid towards a target is not equivalent to the free stream fluid velocity. The importance of the 'squeeze film' between the solid particles and the surface must first be realised in determining the final impact velocity of the particle. The cushioning effect of the squeeze film determines whether the particle will impact the surface or indeed be diverted by the streamlines as it approaches in the free stream [96]. Experimental investigations by Clark and Burmeister [86,96] have confirmed that the velocity of the particles on impact can be as low as 10% of the free stream velocity.

The corrosion component of the erosion-corrosion damage is likely to at least partly involve mass transfer phenomena of the types that are relevant to liquid erosion. Materials whose resistance depends upon a protective film are prone to erosion-

corrosion attack due to constant removal of the protective films (which may range from thick visible films of corrosion products to the thin invisible passivating films) from the metal surface [53]. In consequence, for both passive and active corrosion materials, corrosion rates are likely to increase by mass transfer effects.

Clearly, the mechanisms of the synergy interactions between corrosion and erosion are extremely system-specific but in general, some can involve corrosion processes of "loosening" the surface crystals so as to make their removal by erosion easier.

2.4. Titanium and titanium alloys

2.4.1. Relevance to marine industrial situation

Originally used primarily in the aerospace and chemical sectors, titanium use is now expanding rapidly into many other areas of successful applications, including offshore, power generation, oil and gas extraction, bio-medical, rail and road transportation, construction industry and sports and leisure. Titanium alloys bring the advantage of high strength, low weight and outstanding corrosion resistance at roughly 40% lower weight than steel, and at a cost, which is now said to be similar to many stainless steels [97,98].

Unalloyed titanium has provided more than twenty years of outstanding corrosion resistance and reliable service systems in sea-water environments in (a) power installations, (b) desalination plants and (c) oil refining and exploration installation. As a result of its immunity to ambient sea-water corrosion, titanium is considered to be technically the correct material for many critical applications including naval and offshore components.

In sea-water environment, titanium has been found to be superior in performance to the currently corrosion resistant materials based on copper alloys, cupro-nickels as

well as high Cr-Mo steel [99]. Nevertheless, corrosion problems caused by titanium are being experienced in industry, and are associated with galvanic corrosion, crevice corrosion and hydrogen absorption [99-111]. Detailed analysis of these problems will be given in section 2.4.2.1.

New alloys and simplified processing techniques have reduced costs so dramatically that even less demanding applications are now feasible. New alloys have been developed by Timet, Haynes International, Alcoa, McDonnell Douglas, and many others. Titanium powder metallurgy is being advanced at many companies, including Nuclear Metals, Ferralloy, and Pratt & Whitney. New forging, machining and casting techniques have improved efficiently and reduced costs at companies such as Howmet, Precision Castparts, and Ribtec. Automotive and aerospace applications have been developed since the 1980's at Honda, Ford, Rockwell, Rolls Royce and many other manufactures [112].

Titanium alloys will work continuously at temperatures up to 600°C, resisting creep and oxidation, and down to liquid nitrogen temperatures without loss of toughness. Titanium will survive indefinitely without corrosion in seawater and most chloride environments. The metallurgical characteristics which give titanium its favourable properties do not, however, help its wear resistance, and some form of treatment – surface engineering – is desirable if not essential when there is contact with other moving surfaces. In [113] A. Bloyce suggests that titanium's use is largely restricted to non-tribological applications, owing to their high friction and wear and a strong tendency to galling. According to NASURF [98] the metal's reputation for poor wear performance is routinely overcome by one or more of a range of surface engineering strategies. Such strategies include acid and alkaline anodising, heat treatment and work hardening, thermal spray coatings and thermal oxidation.

Titanium and titanium alloys in desalination

Titanium has proved itself as a solution to many problems relating to maintenance, corrosion and productivity of thermal desalination plants and is finding wider

application in the manufacturing of evaporator, condenser and brine heater tubes [114,115]. The first Multi-stage Flash Distillation (MSF) plant with titanium tubing was put in operation as early as 1965. Since then, many others have also been built for example in Japan, Peru and Indonesia. In 1984, the total weight of titanium used world wide was over 6,000 tons for desalination plants [99], while 14,000 kilometres of tubing is now in use in the Middle East [114]. The largest plant is in Saudi Arabia at Al-Jobail and contains over 2,500 tons of titanium [99]. At the same time, millions of kilometres of titanium tube, both seamless and welded, are being used for power plant condensers and associated auxiliary exchangers [114]. Figure 2.4.1.1, figure 2.4.1.2 and figure 2.4.1.3 demonstrate the use of titanium as heat exchanger in the desalination industry.

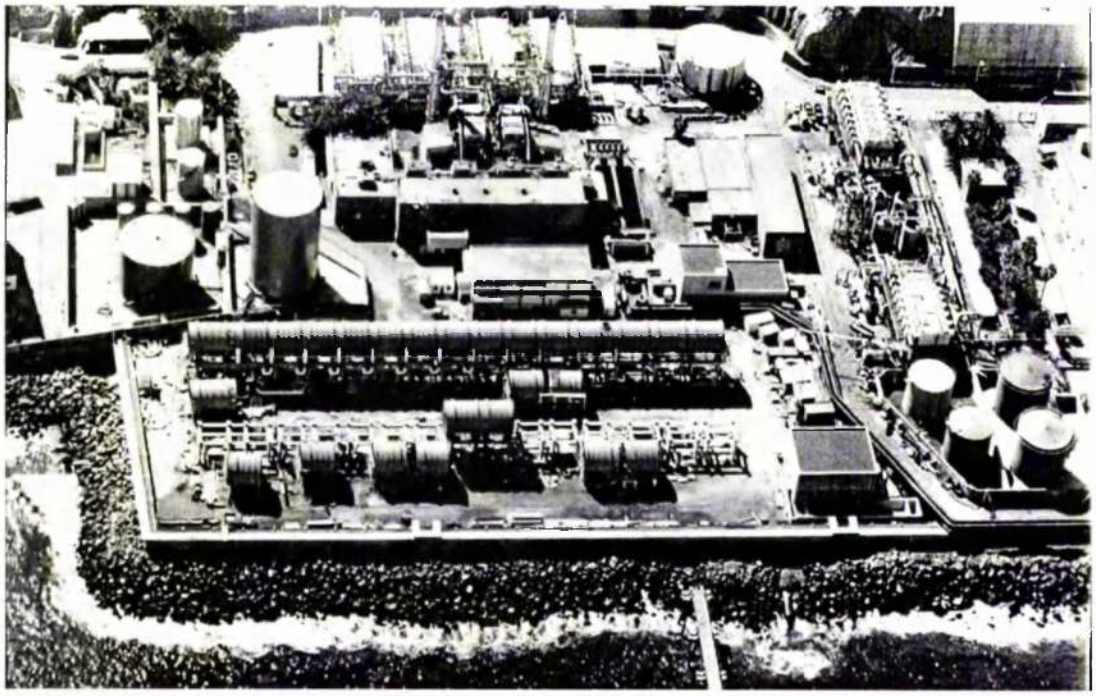

Figure 2.4.1.1. Las Palmas-Telde MED Desalination Plant (under construction).

Figure 2.4.1.2. Titanium grade 2 tubes ready to be installed in the Las Palmas-Telde MED Desalination Plant.

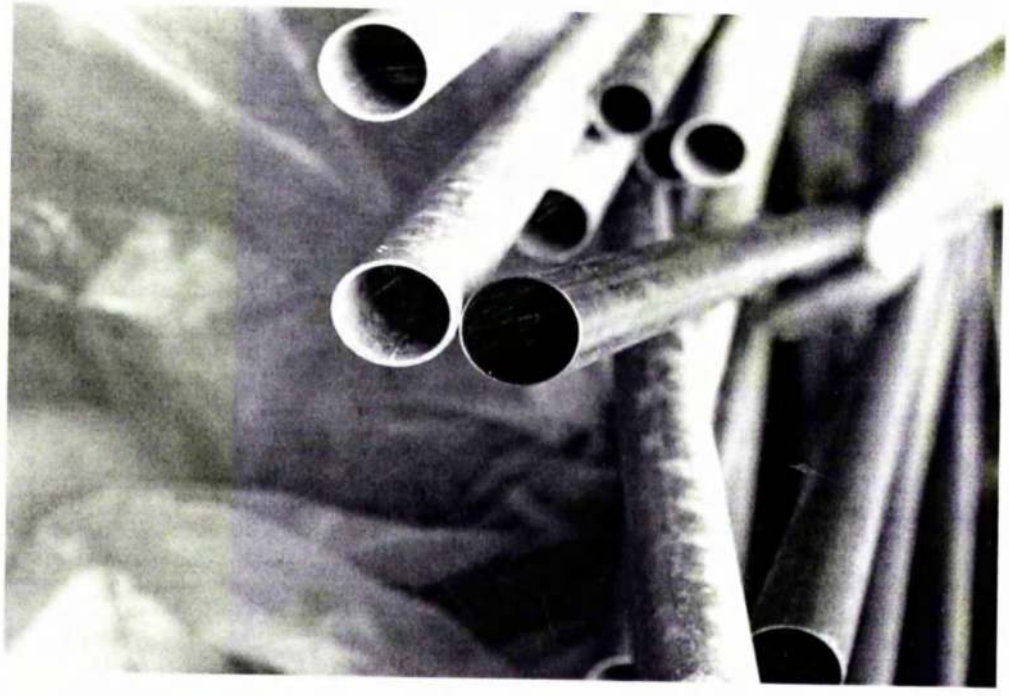

Figure 2.4.1.3. Titanium (Grade 2) tube shown to have much smaller wall thickness than that of aluminium alloy tube. Picture taken at the construction site of Las Palmas-Telde MED Desalination Plant.

The major issues dictating the use of titanium and alloys in desalination plant are corrosion resistance, thermal conductivity and cost. Factors relating to corrosion behaviour in desalination plant are included in the subsequent general section for corrosion of titanium but the other two issues are discussed at this point.

Heat transfer characteristics of titanium tubes

Although titanium has only 37% of the thermal conductivity of Cu-10%Ni, titanium alloys can easily provide equivalent or better overall heat transfer through reduced wall thicknesses and higher seawater velocities [15,107,114]. Copper alloy tubes of the heat exchanger for seawater desalination plants are usually specified to have a wall of standard thickness of 1.0 mm to 1.2 mm. On the other hand, because of the high corrosion resistance in seawater, titanium tubes require no corrosion allowance that copper alloy tubes require. This allows the design of tubes with reduced diameters for higher flow velocities and minimum wall thickness, which satisfies the required mechanical strength, thus increasing the tube heat transfer coefficients. At present 0.7 mm is the standard wall thickness of titanium tubes for seawater desalination plant use but with its zero erosion-corrosion allowance, titanium is successfully utilised in the 0.5 mm thickness in heat exchanger tubing [15,99, 100,114,116]. Many 0.5mm-thick titanium tubes have been used for over 20 years for condensers in nuclear power plants in France and Japan which require extremely high reliability, and operated in extremely good condition without trouble reported [100]. It is also noted in [99,116] that in new plants which have freedom of design, 0.3 and 0.4 mm thick tubes are projected for desalination plants.

In order to examine the possibility of reducing wall thickness [116], 4,080 titanium tubes of 22.2 OD × 0.4 mm wall thickness were installed in the surface condenser of a 50 MW fossil power plant newly built at Hikari Steel Works of Nippon Steel Corporation in 1989 as trial. After operation of five years and three months, two tubes were taken out from the area where the conditions are highly corrosive. The extracted tubes were examined and found to retain the quality of new tubes. Material quality

deterioration and corrosion were not noticed at all. Hydrogen absorption was not noticed either.

However, because of titanium's low elastic modulus and use in very thin walls, titanium tube bundles can be more susceptible to vibration and resultant fatigue damage in high or irregular shell side flow situations. This is easily corrected (but at a cost) by reducing (typically 10-30%) the tube support plate spacing relative to bundles designed for thick wall copper alloy tubing [15,99].

After six months operation of an actual condenser the decrease in the heat transfer rate of aluminium brass tubes, because of fouling, was greater than that of titanium tubes [100]. The flow of the coolant was kept at a low speed of 2.14 m/s or less. A similar result is also reviewed in [100] on the heat transfer rate comparison between titanium tubes and Cu-30%Ni tubes.

Increased tube seawater flow velocities do not only improve heat transfer in the clean condition but also maintain reasonable fouling factors with time. Maximum flow velocity recommended for Cu-10%Ni is approximately 2.6 m/sec. Titanium tubing, however, should be designed to velocities above 2.6 m/sec and, preferably, in the 3.5-5 m/sec range to minimise fouling from marine biofilms. Below the 2.6 m/sec velocity, the risk of progressive degradation in the heat transfer due to biofouling in seawater can be great [15]. However, even when a biofilm is formed on the surface of titanium tubes, it can be cleaned with sponge balls to keep the heat transfer characteristic at good level [100,107].

Tests on the heat transfer rate of a heat exchanger, that operated for 14 months as the condenser of a 30 MW turbine cooled by the seawater, showed a certain superiority of titanium tubes against Cu-30%Ni tubes even at a low flow velocity. When the flow velocity of the coolant was 2.14 m/sec or less, the heat transfer rate of the titanium tubes decreased about 5%, while in the case of the Cu-30%Ni tubes it decreased by as much as 12% [100].

Economic considerations

Many metal manufactures argue that titanium is a very expensive material compared to the conventional material for tubes i.e. copper alloy. If unit price per weight is compared, titanium is actually more expensive than the other materials. However, as the specific gravity of titanium is only 4.51 and, because of its excellent corrosion resistance, the wall thickness of its tubes is less than half of the wall thickness of copper alloy tubes (wall thickness for copper alloy tubes is typically 1.0 to 1.2 mm [15,99,100,114]), the unit price per length of titanium tubes becomes less [99, 100,114,117]. Previously the standard wall thickness of titanium tubes for desalination plants was 0.7 mm but the latest trend is for 0.5 mm thickness. It is claimed, as reviewed in [114], that titanium tubes as thin as 0.3 mm would have enough strength to be put in use over a long period of time in seawater desalination plants.

In addition to that, in those areas of a desalination plant, such as the vent condensers and heat rejection section, where no other material will last 30 years, the use of titanium provides an economical alternative. This is especially true if one considers the inevitable replacement of copper-alloy tubing (at least once and possibly twice in a 30 year lifetime) plus inflation and the resulting increase in copper-alloy costs in the future [117].

Despite the above facts, it has been noted [102] that the use of titanium tubing in the heat rejection condenser would add about 2.8% to the cost of the evaporator vessel/condenser components of the plant. Furthermore, the use of titanium tubing throughout would add over 21% to the cost of the same components.

It has been reported in [114] that Japan Titanium Society (JTS) has made an interesting price comparison for titanium and other conventional tubes made of copper-nickel, and aluminium brass, based on Al-Taweelah B Plant in Abu Dhabi (tube O.D. 34.0 mm; length 2200 km). From that comparison it was obvious that the price per kg of titanium tubes was higher than other conventional materials. However, the total cost would be less than Cu-30%Ni and nearly the same as Cu-10%Ni tubes.

Investigation results on the overall cost merit including the service life, operating ratio and maintenance cost have been reviewed by [114]. The investigation was made on model plants, in which tubes of aluminium brass, Cu-10%Ni and titanium were used. The plant using titanium had costs 46.3% higher in the initial investment but has service life two years longer than the plant using Cu-10%Ni tubes for the heat rejection section and brine heater, and aluminium brass tubes for heat recovery section. However, the water production costs for the titanium plant was lower than the other plants. It was concluded that the use of titanium would be economically feasible.

In that investigation 0.7 mm thick titanium tubes were used but according to JTS, the wall thickness could be reduced to 0.6 mm 0.5 mm or even to 0.4 mm making the titanium very economical. This comes into agreement with [99] where a similar comparison on the long term economic advantage of titanium is claimed – although this assertion is based on graphical data in [99] that clearly contains errors. Such reductions in wall thickness are said to be justifiable for titanium since zero leakage condenser efficiency can be achieved with titanium tubes. Moreover, the price data of early 1980's are not practical anymore because the prices of conventional copper alloy tubes have inflated much since then whereas no price inflation has been seen for titanium tubes [100,114,117].

2.4.2. Detailed durability aspects

2.4.2.1. General comments on the corrosion behaviour of Ti and Ti alloys in seawater

Technologies for application of titanium metal in a seawater environment have made remarkable progress in the last four decades [99]. This is due to intensive research and development work in the laboratory and field as well as to long term service trial, which have generated an exhaustive corrosion databank that has created enough confidence to permit users to switchover to a new construction material.

Titanium and its alloys are being increasingly used in power generation as well as a host of marine-based industries and operations due to their unique corrosion resistance in a chloride environment. They exhibit negligible corrosion rate in seawater and all neutral waters to a temperature as high as 260°C [99]. Contaminants such as iron and manganese oxides, sulphides, sulphates and carbonates present as contaminants do not affect passivity. The outstanding resistance of titanium to seawater, brines, brackish waters and chlorides (at least up to 60°C [118]) is of particular importance in marine service. The comparative behaviour of ferrous material as well as other corrosion resistant metal/alloys like copper, naval brass, aluminium and zinc in seawater both in temperate as well as tropical conditions show the superiority of titanium as a construction material for seawater applications [99,106].

Until the early 1980's no general corrosion, crevice corrosion or stress cracking had been noted with titanium in desalting environments up to 120°C, regardless of oxygen content, chlorination, and even in situations where seawater has been deliberately contaminated with H_2S or ammonia. Titanium maintains its excellent corrosion resistance in stagnant or slow-moving water, as well as in high-velocity flow [117]. In addition, titanium is at least twenty times more resistant to erosion than the best copper-base alloys [117]. According to experience in the operation of desalination distillation of Caspian seawater plant [119], titanium used in heat exchanger tubing displayed greater corrosion resistance than copper-nickel alloys, stainless steels and aluminium brass.

The titanium oxide film

The excellent corrosion resistance of titanium can be attributed to the formation of a highly stable, tenacious and permanent adherent passive oxide film [99,105,106,108-110,120,121]. The film may be only 0.2 nm thick, hence invisible to the eye, and it is primarily titanium dioxide (TiO_2) in a crystalline form or a somewhat amorphous form [110,121]. Because titanium metal itself is highly reactive with a high affinity

for oxygen, the passive oxide film forms spontaneously when fresh titanium metal is exposed to air, or traces of moisture.

The oxide film forms equally on welds as on parent metal, and on the industrial alloys as on commercially pure titanium. In situations where the oxide film is maintained or its formation supported – essentially in mildly reducing to strongly oxidising conditions over a wide range of pH and temperature – titanium will survive erosion, cavitation, pitting and crevice corrosion [106,109]. However, if the pH of the solution is lowered to a value less than one, which is never the case for seawater, the passive film can not be formed enough, and finally leads to active dissolution [105].

Fortunately the oxide film of titanium, which forms spontaneously and is always present in oxidising environments, is stable and self healing and in fact reforms almost instantaneously if mechanically damaged [108,120]. In practice air, moisture, moist gas, water, even heavily polluted brackish water and seawater will support the oxide film. Deaeration of an aqueous media does not affect the corrosion resistance of titanium, because water alone supports the oxide film. Only traces of moisture or oxygen are required to maintain passive behaviour in most environments. Notable exceptions are chlorine gas, red fuming nitric acid and methanol where specific concentrations of moisture from 1.5% up to 5% are required to support the oxide film on titanium alloys under the worst conditions of environment and temperature [108].

General corrosion

Titanium is immune to corrosion in all naturally occurring environments including seawater and most industrial waste water streams. It does not corrode in air, even if polluted or moist with ocean spray - two critical requirements from which the majority of corrosion resistant alloys based on copper or stainless steel suffer [99]. It does not corrode in soil and even in deep salt mine environments, where nuclear waste might be buried.

Titanium and its alloys are virtually immune to general corrosion in seawater, whether aerated, polluted, sulphide containing, or chlorinated, to temperatures as high as 315°C [15,107]. Exposure of titanium for years at various ocean depths has shown it is immune to corrosion in ambient temperature seawater [107]. However, when pH of the solution decreases remarkably to less than one, which is absolutely not applied to natural seawater, even titanium may suffer from general corrosion [105].

The immunity of titanium to general corrosion in seawater was also noted in [122]. Titanium samples were exposed to seawater in static conditions at Keahole Point, Hawaii. The results over an eight-month period indicated no effect due to corrosion on the titanium samples. No detectable change in the surface morphology of the samples was found.

Pitting attack

Unlike the stainless steels and copper alloys, pitting corrosion is not a concern for titanium, in chloride media, due to its tenacious (highly stable) oxide film [15,99,106,107,118]. In practice no evidence of such attack has ever been found either in laboratory or practical marine service exposure.

The breakdown potential of titanium is very high in most environments and pitting, which occurs when the potential of the metal exceeds the breakdown potential of its protective oxide film, is very rarely encountered and totally absent in ambient seawater. According to [99], titanium is resistant to seawater environment up to a temperature of 130°C. However, at high NaCl concentration and low pH brines, pitting can occur even at 80°C. The breakdown potential of titanium in phosphate and sulphate media is about 100V; in chlorides it is about 8-10V [106,107].

In a study carried out by T. Hodgkiess and A. Asimakopoulos [118], titanium exhibited total immunity to pitting corrosion. Along with titanium, 316L stainless steel, Incoloy 825 (a Cr- and Mo- containing alloy with high nickel content) and 304 austenitic stainless steel were also studied. After an uninterrupted exposure of four

and a half months to low-oxygen seawater at 25°C, no pits were visible on specimens of titanium. In 60°C aerated seawater, all the materials except titanium suffered extensive pitting attack. In particular, 316L stainless steel was observed to suffer extremely severe attack under aerated conditions at both 25°C and 60°C.

Crevice corrosion

Crevice corrosion is the only type of corrosion which is possible to occur on titanium in seawater [15,99,105-107,109,110,123]. The main environmental factors affecting the possibility of crevice corrosion are (a) concentration of chloride ion, (b) temperature, (c) pH and (d) shape of crevice. Crevice corrosion of titanium could occur only when the clearance of crevice is very tight and all of the above factors have become simultaneously critical [105].

Susceptible crevices can arise from adhering process stream deposits or scales, metal-metal joints, or gasket-metal flanges and other seal joints. Titanium crevice attack may be either uniform, and/or highly intergranular, and is usually associated with a layer of titanium hydride precipitates along the attacked surface (in α phase alloys) [110].

Although the behaviour of the crevice corrosion seems to vary dependent on the shape of crevice, it can be said that crevice corrosion is seldom observed at temperatures lower than 60°C and totally absent in ambient-temperature seawater [15,99,105-107,109,118,123]. When titanium tubes are used at a temperature on the metal surface of seawater side higher than 60°C, Pd coating should be considered in order to avoid the risk of crevice corrosion [105].

Immunity of pure titanium to crevice corrosion at temperatures ranging between 20°C and 30°C was supported in [124]. Test specimens of pure titanium and stainless steels 316L and 317L were exposed to the filtered seawater feed at the Desalination Research Plant (DRP) Doha, in Kuwait for 3,000 hours and at flow rate of 100 l/min. Severe attack was observed on stainless steel 316L, followed by that on stainless steel

317L. Titanium showed no sign of crevice attack during the exposure period, indicating the formation of an excellent protective layer on the surface of the specimens. It was noted in [118] that commercially pure titanium did not exhibit any crevice corrosion up to 60°C, whereas type 316L stainless steel was observed to be susceptible to crevice corrosion in low-oxygen seawater at 60°C and to suffer extremely severe crevice attack under aerated conditions at 25°C and 60°C.

However, severe crevice corrosion has been experienced in desalination units of Abu Dhabi National Oil Company's (ADNOC) where titanium is used at a maximum distillation temperature of 59°C [104]. Distillate cooler condensers, raw water heaters and ejector condensers use titanium tubes in combination with stainless steel alloy 904L (UNS N08904) tubesheets. Within one year of service, these exchangers suffered severe crevice corrosion, which included both materials, at tube-to-tubesheet joints (T/TS). In all cases, 904L tubesheets at the seawater inlet side suffered more severe crevice corrosion.

The attack initially appeared at the bottom of 904L tubesheet holes (through which the titanium tubes pass), spread along the periphery of the T/TS joints and extended through the thickness of the tubesheets. The depth of the crevice corrosion attack was typically 0.5 to 1.0 mm within one year of service. In the worst cases, crevice corrosion attack progressed up to two-thirds of the tubesheet thickness. After installation of aluminium alloy anodes and their subsequent replacement with iron anodes, propagation of crevice corrosion attack was controlled and units were successfully kept onstream.

Titanium also appears to suffer from crevice corrosion at tube joints in aerated or deaerated seawater at temperatures above 80°C and pH< 7 [99]. The greater the pH of brine, the higher becomes the critical temperature above which crevice corrosion of titanium tubes might occur. At temperatures close to the boiling point, seawater and neutral brines will develop reducing acidic conditions where crevice attack of titanium may occur. Opportunity of this kind of attack exists, for example in desalination brine heaters, where steam and water are at the highest temperature and

deposits of calcium carbonate may form on the inside of the tube and give conditions favourable to under deposit crevice attack [106,109].

It was reported in [105] that titanium tube was penetrated by crevice corrosion due to deposition of alcaline scale in tubes. This equipment was an oil product cooler and was operated at very low flow rate of seawater (no indication of temperature was given). It was reported that this kind of damage was solved when the minimum flow speed was kept at 0.2 m/sec.

Despite the above information based on industrial experience, it is recommended by Titanium Metals Corporation in Toronto-Ohio [107] that for utility operating ranges to approximately 80°C and for waters including seawater, cooling tower waters, waters contaminated with metal ions, sulphides, sulphates, carbonates and polluted waters Grade 1 and Grade 2 (commercially pure titanium) provide basic immunity to crevice corrosion. In the case of heat exchanger service above this temperature Grade 12 (additions of 0.2% to 0.4% Molybdenum and 0.6% to 0.9% Nickel define its chemical difference from that of Grade 2) would extend the immunity to approximately 260°C/315°C at a pH down to 3 while either Grades 7, 11, 16, or 17 (alloys containing palladium which contributes to an increase in crevice corrosion resistance) extend the immunity to a pH of 1 or less at 260°C and to an approximate pH of under 2 at 315°C [107].

Hydrogen absorption characteristics

Where titanium is incorporated into mixed metal plant or equipment, it will usually be the cathode if a galvanic couple exists or is created. Galvanic corrosion of less resistant metals may be harmful to titanium when used as the cathode, if conditions lead to hydrogen uptake and embrittlement. In seawater service, hydrogen absorption may be caused or aggravated [99,102,105,106,107,108,111] by:

1. Coupling of titanium to less corrosion resistant metal
2. Cathodic protection systems producing potentials lower than –0.9V (SCE)

3. Tensile load or residual stress if absorption is occurring
4. pH less than 3 or more than 12
5. High temperatures over 80°C, which cause an increase of corrosion at the anode and higher hydrogen activity at the cathode
6. Hydrogen sulphide, which will accelerate hydrogen uptake in the presence of a cathodic potential.

Since titanium has a strong affinity with hydrogen, it easily absorbs hydrogen and forms hydride (TiH_2). A lot of precipitation of hydride causes loss of ductility and the cracking of Ti components including tubes [105,111]. However, hydrogen absorbed by titanium in the seawater does not come directly from the environment. In many cases the hydrogen absorption was caused by excessive cathodic protection for tube sheets made of copper alloys [99,105,106,111]. It is suggested in [111] that at the negative potentials of cathodic protection, adsorbed H atoms are first produced:

$$H_2O + e^- = H_{ads} + OH^-$$

Part of H_{ads} combines to form hydrogen molecules which detach as gas:

$$2H_{ads} = H_2 \uparrow$$

The rest diffuses inside the metal and either remains as such (absorbed hydrogen) or combines with the metal in the form of TiH_2:

$$H_{ads} = H_{abs}$$

or

$$2H_{ads} + Ti = TiH_2.$$

No hydrogen absorption will occur as far as titanium is used alone in seawater. Even when titanium is used together with other metal, the hydrogen absorption can be avoided completely if proper cathodic protection is adopted.

In 6% NaCl titanium will not absorb hydrogen when immersed alone or coupled with naval brass in up to at least 100°C [100,102]. In the same solution titanium will still

not absorb hydrogen when coupled with copper alloys or stainless steels where temperature is up to 120°C. When titanium is immersed, however, in contact with mild steel in 6% NaCl, hydrogen absorption may occur. Titanium coupled with mild steel will absorb hydrogen at temperatures higher than 80°C [100,102].

Another point of concern, directly relevant to MSF plants, would be the possibility of hydrogen absorption in steam. Titanium coupled with mild steel will absorb hydrogen when it is exposed to steam of temperature 100°C or higher. Additionally titanium will not absorb hydrogen up to 120°C when it is exposed to steam alone or coupled with naval brass [100,102].

Influence of temperature

As the temperature goes up, both the amount of hydrogen absorption and the diffusion rate of hydrogen in titanium increase. When the temperature rises over 80°C, absorbed hydrogen diffuses actively from surface to inside of titanium [99,105-108]. This phenomenon is related to the distribution of hydride precipitation in the matrix. This suggests that the hydride is precipitated only at the surface at temperatures lower than 80°C. Therefore, even if titanium absorbs hydrogen in seawater at temperatures lower than 80°C, hydrogen absorption will never lead directly to the failure of titanium tubes [105].

Hydrogen embrittlement can be avoided by:

1. Electrical isolation of titanium in mixed metal structures by the use of insulating joints
2. Coating of titanium to reduce its effect as a cathode and/or restrict the area of titanium likely to be affected
3. Controlled cathodic protection and the choice of sacrificial anodes to limit the cathode potential: aluminium, aluminium-zinc alloy, zinc and magnesium anodes can not be recommended as their potentials are too negative [99,104,106].

It is noted in [107] that even at a negative potential level of –0.7V it would take 20 to 30 years to have hydriding of any significance occurred. It also reports an incidence where hydriding affected condenser tubing was shown to have had an out of control

cathodic protection system voltage at approximately -2.0V for several years. Even under this severe situation, with a corrected C.P. system, the affected tubes continued in service for over nine years.

Galvanic corrosion

Titanium is noble in most all chloride environments (sea, brackish and cooling tower systems). This necessitates protection of other metals when systems are not designed as all-titanium [15,107,108,110].

Galvanic corrosion of metals in contact with passive titanium usually results in corrosion of the less noble metal, such as copper alloys, aluminium alloys, carbon steels and magnesium alloys [15,106,108,110]. The extent and degree of galvanic attack will depend on the relative surface areas of the titanium and the other metal. Titanium should not be coupled directly to less noble metals such as copper, magnesium, zinc and aluminium. These are likely to experience accelerated corrosion and, in the process, titanium may pick up hydrogen, which is generated as the cathodic product of the cathodic reaction at sufficiently negative potentials [106,108]. A case reviewed in [110] reported that titanium tubes in a heat exchanger with a 316L stainless steel end plate, operating at high temperature, failed by hydrogen absorption. The type 316L corroded in a sour water environment and the galvanic couple set up caused titanium to act as the cathode. The hydrogen evolved at the cathode entered the titanium and caused embrittlement by TiH_2 formation.

Since all copper alloys have more negative corrosion potentials than titanium, their contact with titanium in seawater may cause galvanic corrosion on the side of copper alloys [101-104]. In actual condensers and MSF desalination plants where both titanium tubes and copper alloy tubesheets are used, galvanic corrosion may occur on the surface of tubesheets round titanium tubes [100,101]. Cathodic protection is applied to prevent this galvanic corrosion. Iron anodes can be used up to 70°C but above this temperature iron causes hydriding of the titanium and 9% Ni-Iron anodes are normally used [102].

Tests carried out in [101] showed that the extent of galvanic corrosion rates in desalination plants increases in relation to titanium in the following order: 30% cupro-nickel; 10% cupro-nickel; aluminium bronze (ABP5); aluminium bronze (ABP1) and naval brass. It was also noted in [103] that the value of the galvanic current between a titanium pipe and a less noble material is more depending on the presence or on the absence of biofilm on the titanium pipe walls than on the aeration or the seawater temperature. In the absence of biofilm on the titanium pipe walls, the protection current is dependent more on the seawater temperature and the potential imposed at the pipe mouth than on the oxygen concentration in solution. In all cases, for a first approach to the design of a cathodic protection system able to protect a copper alloy coupled with the titanium pipe and at the same time to avoid the titanium embittlement, a current value close to 1 mA/pipe can be assumed. In the presence of biofilm on the pipe walls, due for instance to insufficient chlorination, the protection current increases sharply and current values more than 5-6 mA/pipe can be necessary. This increase is due to the effect on the oxygen reduction induced by the bacterial growth on the titanium surfaces.

Two examples of troubles associated with galvanic corrosion in titanium tubed heat exchangers are reviewed in [105]. Both cases were found on the baffle plates made of copper alloy in a plant (details of the plant or the copper alloy not specified). These happened in overhead condensers in distillation unit, in which the seawater flows in the tube inside. The trouble occurred after eight years operation, and the same trouble has never been reported after the material of baffle plates was changed to titanium from copper alloy.

Studies [121] have also shown that there is no galvanic corrosion between the titanium alloys themselves.

Stress corrosion cracking (SCC)

Immunity of titanium to SCC in seawater can be expected [15,106,107,118,120]. (Only chemical process environments such as absolute methanol, red fuming nitric

acid, nitrogen tetroxide and cadmium induce SCC [107]). Ti-6Al-4V ELI (Extra Low Interstitial Alloy Content), a variant of the most widely available alloy, will not exhibit SCC in either smooth or notched components in seawater or brackish water, and is regularly selected for applications where high strength and corrosion resistance are required [106].

Titanium's high resistance to SCC was also noted in [120]. Titanium specimens under static loads of up to 80 per cent of their tensile strength were exposed for more than five years in a marine environment without any sign of failure.

Corrosive wear

In general, it is observed [125] that corrosion has an accelerating effect on the wear degradation of titanium and its alloys. Severe corrosive wear can take place during the breakdown of the protective film while in sliding contact [126]. However, titanium components can be anodised to ensure reproducible and constant surface properties. For example, anodised pure titanium and titanium alloys have been used for implant materials for years because of their high resistance to corrosion and biological tolerance [127].

Biofouling

Present in almost all environments, certain microbiological organisms naturally produce oxidising or reducing conditions which are highly localised and corrosive towards metal surfaces with which they are in contact. Operations affected by microbiologically influenced corrosion (MIC), or susceptible to it, include subsea and offshore activities. When water is stagnant or only limited or intermittent flow occurs, the problems are activated. Unlike copper and steel alloys, titanium and its alloys are believed to be immune to microbiologically induced corrosion [15,99,106]. In most fouling situations, the hard smooth titanium oxide film will resist deposit adhesion and facilitate cleaning. Typically titanium and its alloys resist corrosion attack under

marine deposits and biofilms below 90°C which is extended to temperatures as high as 260°C with grade 12 titanium (alpha alloy containing nickel and molybdenum) [15]. Titanium will also resist oxidising agents such as hydrogen peroxide, sodium hypochlorite etc, as well as the non-oxidising organic treatments used to remove fouling. To date, with the benefit of over thirty years experience of extensive exposure of titanium in conditions favourable to a wide spectrum of microbiological activity, not one single failure of titanium has occurred which can be ascribed to MIC [106].

Biofouling of titanium has been observed [120] after 800 hours immersion in seawater, indicating that little toxicity is displayed towards marine organisms. However, as reviewed in [99], titanium tubing exposed for 16 years to polluted and sulphide containing seawater in harbours and estuaries showed no evidence of corrosion caused by marine deposits and biofouling in general.

2.4.2.2. Ti and Ti alloys under erosion conditions

Introductory comments

Generally, in aqueous seawater environments, the hard tenacious TiO_2 surface film of titanium and its ability to repair itself instantly when damaged provide a high resistance barrier to erosion-corrosion [99,106,120,128,129]. It is suggested in [129] that according to service experience, in seawater and brines not containing significant solid content, flow rates as high as 20 and possibly 30 m/s are feasible with titanium. Inlet turbulence in tube exchangers, entrained gas bubble impingement, cavitation effects are generally not of concern in titanium tubing, piping and pump components [128]. Even in conditions where a high proportion of sharp, abrasive sand particles in seawater causes rapid erosion of copper-nickel alloys at flow rates of 2.5-3 m/s, titanium withstands flow rates in excess of 6 m/s [129]. The typically low concentrations of silt entrained in seawater are generally of little consequence, but

continuous exposure to high velocity slurries of hard particles can lead to finite metal removal [55,128].

Titanium alloys also exhibit relatively high resistance to non-aqueous fluids containing suspended solids. Critical conditions of excessive metal removal depend on the concentration , shape, size and hardness of the suspended particles, in addition to fluid velocity, impingement angle, local turbulence, and titanium alloy properties [56-60,130].

Erosion-corrosion in aqueous environments

Quantitative investigation of erosion-corrosion rates

All data and results available on the erosion-corrosion behaviour of Ti and Ti alloys in seawater are presented in Table 2.4.2.2.1, Table 2.4.2.2.2 and Table 2.4.2.2.3 and come originally from sources [129,131,132]. The data shown in Table 2.4.2.2.1 and Table 2.4.2.2.3 have also been quoted, as review information in [15,106,107,111,120,128,133,134].

Flow rate (m/s)	Type of test	Corrosion-erosion rate (mm/year)	Time of test
9.8	Model condenser	Less than 25×10^{-4}	12 months
1	Ducting	0.75×10^{-6}	4.5 years
8.5	Rotating disc	125×10^{-6}	60 days
9	Micarta wheel	275×10^{-6}	60 days
9	Micarta wheel	175×10^{-6}	60 days
0.6-1.3	Exposure	100×10^{-6}	6 months
7.2 plus air	Jet impingement	500×10^{-6}	30 days
7.2 plus air	Jet impingement	0.5 mg/day	15 days
7.2 plus air	Jet impingement	0.2 mg/day	15 days

Note: The last two data for jet impingement are of limited use since the area of the specimens is not given.

Table 2.4.2.2.1. Erosion-corrosion of commercially pure Ti in seawater [129].

Flow rate (m/s)	Test conditions	Corrosion-erosion rate (mm/year)	Time of test (days)	Ref.
45.7	Solid-free erosion-corrosion, 45 degrees impingement angle	0.025	30	[131]
2.4	Solid-free erosion-corrosion	0.0022	7	[132]
2.4	Slurry comprising 9 vol% in synthetic seawater, particle size: 105 – 425 μm	0.29	7	[132]

Table 2.4.2.2.2. Erosion-corrosion of Ti-6Al-4V in seawater [131,132].

Flow rate (m/s)	Suspended matter	Type of test	Corrosion-erosion rate (mm/year)	Time of test (hr)
2	40 g/l 60 mesh sand	Tube circulation	0.0025	2000
2	40 g/l 10 mesh emery	Rotating disc	0.0125	2000
3.5	1% 80 mesh emery	Rotating disc	0.0037	17.5
4.1	4% 80 mesh emery	Rotating disc	0.083	17.5
7.2	40% 80 mesh emery	Rotating disc	1.5	1

Table 2.4.2.2.3. Erosion of commercially pure Ti in seawater containing suspended solids [129].

T. Lindheim [135] studied the erosion performance of GRP (Glass Reinforced Plastics) under slurry erosion conditions and made comparisons with other common pipe materials such as commercially pure titanium and 6Mo Steel. Particle erosion tests that included the assessment of titanium and 6Mo Steel were conducted at water flow speed of 8 m/s and the angle between the impacting jet and sample surface was set at 45°. Quartz sand with an average particle size of 360μm and of semi-angular shape was used at a concentration of 40 - 45%. Results showed that titanium exhibited 40% higher volume loss rate than 6Mo Steel.

In another very recent study [95], the slurry erosion-corrosion behaviour of TiN coated α-Ti alloy (commercially pure titanium) was investigated. For matters of comparison, some results on pure titanium (Table 2.4.2.2.4) were also obtained under the same conditions. Erosion-corrosion tests were conducted at room temperature using an impinging jet with slurry impact velocity ranging from 4.8 to 12.8 m/s and at normal impact angle. The slurry consisted of 3.5 wt% NaCl aqueous solution and 10 wt% angular silica sand (109-177 μm). The area of the specimens was 3.1 cm^2.

Flow rate (m/s)	Corrosion-erosion rate (mm^3/min)
4.8	0.0025
6.4	0.0037
8	0.0055
9.6	0.014
11.2	0.023
12.8	0.034

Table 2.4.2.2.4. Erosion-corrosion rates of commercially pure Ti at various slurry impact velocities [95].

Damage on the surface of pure Ti specimens was associated with its corresponding plastic deformation and characterised by craters and flakes. The flake formation occurred when plastic deformation took place and the flakes tended to be easily removed by cracking after multiple particle impacts.

It is clear that there was some work on obtaining general assessment of erosion-corrosion rates of commercially pure titanium some 30 years ago. However, apart from some fairly recent work on Ti-6Al-4V and a very few quite recent tests on pure Ti in saline slurry, no further effort appears to have been undertaken on this topic. Also clear is the complete lack of any previous work on studying the mechanisms of erosion-corrosion of titanium and its alloys in aqueous environments.

Despite the dearth of experimental data, Tables 2.4.2.2.1, 2.4.2.2.2 and 2.4.2.2.3 do indicate that, in absence of solids, erosion-corrosion rates of commercially pure titanium in seawater are negligible up to 10 m/s. The data for Ti-6Al-4V provides some evidence of increased but still low erosion-corrosion rates at higher velocities. In heavily laden slurries, erosion-corrosion rates are low at low velocity (< 4 m/s) but appear to become appreciable at higher velocities for both Ti and Ti-6Al-4V.

It is apparent that no studies have been conducted in liquid-solid conditions at moderate solid loadings (say a few thousand ppm) which may be more relevant to movement and processing of many natural waters.

Reported practical experience

Ali El-Saie claims, [136], that titanium condenser tubes are proven twenty times more resistant to erosion than Cu-Ni-Fe-Mn (66-30-2-2) in the case of suspended sands and silt encountered within the tubes. However this statement is given without any references or data. Another similar statement without produced data or provided references is presented in [99] according to which, in a high velocity sand-laden seawater test (8.2 m/s), titanium performed a hundred times better than 18 Cr-8 Ni stainless steels, monel or 70%Cu-30%Ni.

Toshiba has supplied about 130 condensers for thermal and nuclear power plants in Japan. Titanium or Al-brass is applied for these condenser tubes. As reported in [137], it has been found that the tubes of some of those condensers after 40,000-50,000 hours of service are eroded at the steam side due to droplet impingement. This phenomenon is widely known as water droplet erosion and is caused by high velocity steam, containing small condensate droplets. With the titanium tubes, droplet erosion was detected after 51,000 hours of service, although no such erosion was detected after about 40,000 hours of service. From test results with droplet diameter: 300μm, droplet impact velocity: 200 m/s, and tube material: titanium, the erosion rate was 0.0014 mm/hr.

A similar case of water droplet erosion is reviewed in [138]. Briefly condenser tubes made of titanium have suffered external erosion in Finnish and Swedish nuclear power plants. This has been caused by high velocity steam, containing small condensate droplets, hitting the outer layers of titanium tubes with a speed of close to 200 m/s.

Non-aqueous erosion

Erosion is a serious problem in many critical components used in erosive environments. Examples of the components made out of Ti-6Al-4V alloy include the blades and discs of aircraft compressors, helicopter rotor blading, and valves, pipes and centrifugal pumps used in industrial waste water systems, municipal sewage

plants, seawater systems and for the transport of slurry in pulp and paper industry [55-57,59].

In general, erosion is affected by a number of factors which basically include: angle of impingement, eroded surface properties (microstructure, hardness and ductility), particle velocity and its size and hardness, and temperature effect [55-60]. The erosion behaviour of the Ti-6Al-4V in relation to the aspects just mentioned can be summed up as follows.

Angle of impingement

As clearly established in [56,60], Ti-6Al-4V exhibits maximum erosion rate at 30° impact angle, which is typical of its ductile nature. (Note that erosion rate is defined as the total mass loss divided by the total mass of erodent impacted). However, tests carried out in [58] showed semi-ductile behaviour of the alloy with the maximum erosion rate at an impingement angle of 45°, although the erosion rates were almost the same regardless of impingement angles.

Particle velocity and its size and hardness

Results in [55,56,59] very apparently indicate that Ti-6Al-4V, and titanium in general, is particle size dependent. In [56] the erosion rate of Ti-6Al-4V increased with the increase in particle size, but after a certain value of the particle size it remained constant. In this case silicon carbide particles varying in size from 12 to 150 μm were used, and the critical particle size, beyond which the erosion rate remained the same, was 77 μm. All experiments were run at 55 m/s velocity and 30° angle of impingement. Similar behaviour was also observed for the titanium alloy in [55] where the critical particle size was found to be about 50 μm. Again angle of impingement was 30° and impact velocity 50 m/s using silicon carbide particles.

The influence of grain size on the erosion rate of titanium was also observed in [59]. In this study experiments were carried out at a velocity of 40 m/s, impact angle of 90° degrees with 300 to 450 μm steel shot as erodent on pure titanium. In contrast to the two cases mentioned above, here the erosion rate was found to decrease with increasing grain size. Increase in grain size from 120 μm to 375 μm was found to lead

to a decrease in the erosion rate from 1.25×10^{-4} to 0.38×10^{-4}. According to the authors this is attributed to the increased interstitial content and resultant increased flow stress caused by stress hardening and strain rate hardening.

In [55], the variation of the erosion rate of Ti-6Al-4V with varying proportions of 600 grit particles mixed with 120, 240 and 320 grits was also studied when the mixture was accelerated by a high pressure gas. As the size of the particles changes, their mass also changes. Thus, when particles of varying sizes are accelerated in fluid stream at constant pressure, they travel at different velocities. It was found that in situations where particles of different sizes are accelerated under the same pressure differential, the larger size particles are less damaging in erosion and the velocity effect is larger in the case of fine particles. It was also noted that particle mixtures produce higher erosion of Ti-6Al-4V than that achieved by component particles. The authors felt that the explanation for the erosion behaviour of particle mixtures lies in the interaction between particles of different sizes as they are accelerated in the tube. Since smaller particles travel at higher speeds than larger particles, the particles of different sizes collide and thus larger particles get some boost in velocity at the expense of smaller particles (i.e. energy is transferred from smaller particles to larger particles). As larger particles become more erosive, they contribute more to erosion than the reduction in erosion rate caused by the slowing down of smaller particles.

It is stated, [55], that erosion is lower for softer particles, but for particles much harder than the target material, erosion is unaffected by particle hardness.

Temperature effect

As described in [60], the particle erosion rates of Ti_3Al-based, TiAl-based titanium aluminide intermetallic alloys and 304 stainless steel increase with increasing test temperature between 25°C and 500°C. Particle erosion tests were performed at 25°C, 300°C and 500°C using an air blast apparatus and 30° impingement angle.

It was noted, [60], that at 500°C the erosion rates for the titanium aluminides were significantly larger than those for 304 stainless steel. At 300°C, the erosion rates of Ti-52Al and Ti-48Al-3Mn-2Nb were again significantly larger than those of 304 stainless steel. This increase in the particle erosion rates of the titanium aluminide

alloys with increasing temperature between 25°C and 500°C is consistent with the increase in the particle erosion rate of Ti-6Al-4V between 25°C and 650°C as reviewed by the authors.

According to the authors a possible cause of this increase in erosion rate for the Ti_3Al-based alloy could be a change in the mechanism of material removal from one of flaking of work hardened material at low temperatures to ductile ploughing at elevated temperature. For the TiAl-based alloys, a decrease in ductility with increasing temperature could account for the increase in particle erosion rate with increasing test temperature.

Erosion mechanisms

It is stated, [56,57,59], that the dominant mode of material removal for Ti-6Al-4V is through lip formation along the perimeter of the crater formed by impact and their subsequent fragmentation and removal in the form of flakes or platelets.

Emiliani and Brown [57] observed that during incubation (early stage of erosion), a smooth protective glass layer was formed on the target surface of Ti-6Al-4V. It is believed by the authors that this layer was formed by thermal softening of the erodent on impact. The protective glass layer reduced and controlled the erosion rate by decreasing the incident of direct impacts upon the metallic surface.

A similar behaviour for the same titanium alloy was noted by Yerramareddy and Bahadur [56]. It was evident from their results that the erosion rate was decreasing from a high initial value to a lower steady state value. However there was no glassy layer observed on the surface of their specimens. According to them the likely cause of the increased erosion in the early stage in their case might have been the development of surface scale due to the capacity of titanium to absorb oxygen, hydrogen and nitrogen, all of which tend to induce embrittlement.

Cavitation attack

Information on the erosion of Ti-5Al-2.5Sn under cavitation attack is given by Buckley and Rao in [130,139]. In both cases all experiments were conducted in a viscous mineral oil with a 20 kHz ultrasonic oscillator vibrating at 50μm amplitude. The erosion rate of the Ti alloy was expressed as the mean depth of penetration rate (MDPR). MDPR is the average rate of erosion during a given interval and is computed from the mass loss measurements of the test specimens according to the equation:

$$\text{MDPR} = \text{Mass loss per unit area} / (\text{Density} \times \text{Time interval})$$

According to their results, Ti-5Al-2.5Sn had an MDPR of 0.5 μm/hr while on copper, another material tested under the same conditions, it was 542.3 μm/hr.

It was also found that the surface roughness and the ratio of pit depth to pit width increased with the duration of cavitation attack on Ti-5Al-2.5Sn.

3. EXPERIMENTAL PROCEDURES

3.1. Test materials

Two copper-nickel alloys, Cu-30%Ni and Cu-10%Ni, were used to study the effects of corrosion products on corrosion kinetics. Cu-30%Ni was supplied in the form of unused tubes manufactured for use in the heat recovery section of a MSF plant. It was cut into cross-section rings and the cross-section area was tested. Cu-10%Ni was supplied in the form of flat plate from which square specimens were cut. Round specimens of pure titanium, two titanium alloys and two stainless steels were also examined. The chemical analysis of all alloys investigated are shown in table 3.1.1, some of their mechanical properties in table 3.1.2 and the area of specimens in table 3.1.3.

Alloy	Composition
Cu-10%Ni	85Cu-12Ni-2Fe-1Mn
Cu-30%Ni	65Cu-31Ni-2Fe-2Mn
Ti:G2	Alpha alloy - commercially pure titanium
Ti-6Al-4V	Alpha-beta alloy with 6Al and 4V
Ti-5111	Near alpha alloy with 5Al-1Zr-1Sn-1V-0.8Mo-0.1Si
316L (UNS S31603)	Austenitic stainless steel with 16.31Cr-2.1Mo-10.14Ni-0.019C-1.71Mn-0.24Cu-0.028P
Z100 (UNS S32760)	Superduplex stainless steel with 24.6Cr-4.0Mo-8.4Ni-0.025C-0.86Mn-0.61Si

Table 3.1.1. The composition of the alloys investigated.

Alloy	0.2% Proof Stress (MPa)	UTS (MPa)	Hardness (HV)
Cu-10%Ni	140	310	
Cu-30%Ni	190	380	
Ti:G2	345-480	480-620	160-220
Ti-6Al-4V	830-1000	970-1100	300-400
Ti-5111	680-800	750-900	
316L	205	515	
Z100	550	750	

Table 3.1.2. Mechanical properties of the alloys investigated.

Alloy	Specimen area (cm^2)
Cu-10%Ni	1.0
Cu-30%Ni	0.93
Ti:G2	8, 5, 0.28
Ti-6Al-4V	5
Ti-5111	5
316L	5
Z100	8, 5, 3.8

Table 3.1.3. Areas of test specimens used.

The composition of Ti-6Al-4V and Ti:5111 alloys was also analysed in Sheffield Testing Laboratories LTD by ICP AES techniques. The results of the chemical analysis of the two Ti alloys are shown in table 3.1.4 and agree with the standard specification given in table 3.1.1.

	Ti-6Al-4V	Ti:5111
Aluminium	5.70	4.71
Vanadium	3.82	1.10
Iron	0.17	0.12
Zirconium	<0.02	1.14
Tin	<0.02	1.10
Silicon	<0.02	0.04
Molybdenum	<0.02	0.87

Table 3.1.4. The composition of Ti-6Al-4V and Ti:5111 alloys as analysed in Sheffield Testing Laboratories LTD by ICP AES techniques.

3.2. Static tests

All the materials listed in table 3.1.1, with the exclusion of the superduplex stainless steel, were included in the tests under static conditions. In this type of experimental work the area of Ti:G2 specimens used was 8 cm^2. The samples were first mounted in resin. This was followed by surface grinding through 240, 400, 800 and 1200 grit and

finally diamond polishing with a diamond paste of 1 micron. The specimens were then degreased thoroughly in an ultrasonic bath using methanol, and rinsed with distilled water and dried.

Test conditions

For initial comparison purposes, a few experiments were conducted in artificial seawater (52-54 mS/cm). Artificial seawater was prepared with "Instant Ocean" salt (which contains all the main inorganic constituents present in natural seawater) mixed in distilled water. The samples were pre-conditioned, after polishing had taken place, for 1 hour in air prior to the experiments. The investigation was focused on the corrosion behaviour in quiescent-open to the atmosphere distilled water (1.5 – 7 μS/cm) at 20°C and 50°C. In some experiments carbon dioxide was bubbled into the distilled water from a CO_2 cylinder.

Testing equipment and procedure

Electrochemical corrosion measurements were undertaken for all the previously mentioned conditions, using a computer-controlled Potentiostat. In the case of distilled water a modified electrochemical corrosion testing cell was used in order to obtain reproducible results without interference from electrical resistance effects between the auxiliary electrode and the working electrode in the low-conductivity water. In this cell, which had been developed and tested in earlier work [86], a piece of titanium mounted in resin played the role of the auxiliary electrode which was placed very close to the working electrode at a standard distance of 2.5 mm by the help of elastic bands, while the reference electrode was measuring the potential through a salt bridge (see Figure 3.2.1). It was felt that this provided a reasonable measurement of average electrode potential along the working electrode surface as opposed to the somewhat more accurate but highly localised electrode potential which would have been measured by the case of Luggin Capillary. All polarisation tests were started after the free corrosion potential, E_{corr}, of the sample had settled. The

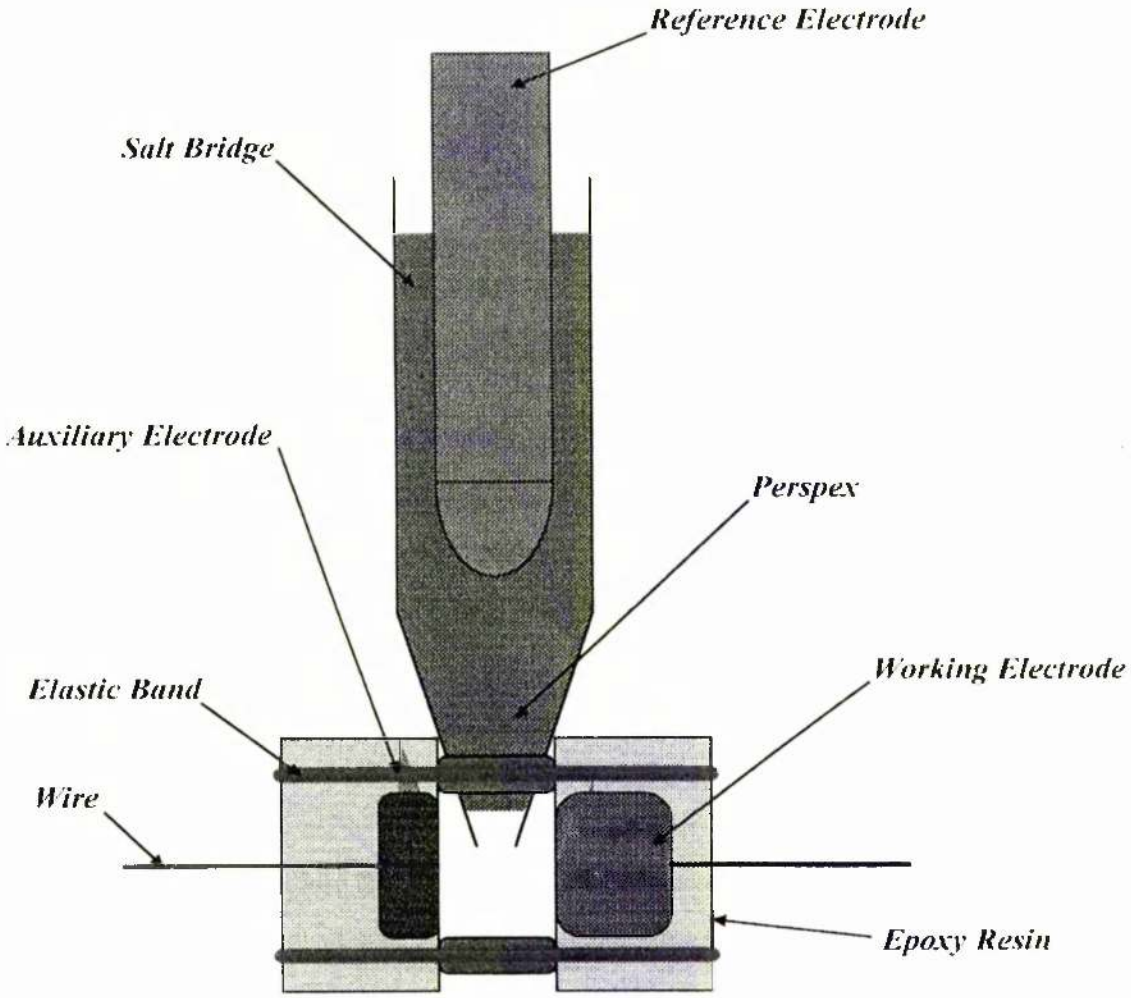

Figure 3.2.1. The experimental set-up for polarisations in static conditions. (Not to scale. Distance between working electrode and auxiliary electrode = 2.5 mm.)

3.3. Erosion – corrosion tests

Five metals, comprising Ti:G2, Ti-6Al-4V, Ti:5111, austenitic stainless steel and superduplex stainless steel were studied in this part of the experimental work (the composition of the five alloys is already given in table 3.1.1). The two stainless steel alloys were selected as standard materials to be compared to titanium and titanium alloys. As an attempt to investigate the behaviour of the materials in relation to the

size of the exposed surface, various specimen areas were used for pure Ti and Z100 (see table 3.1.3).

Mounting and polishing

Specimens were mounted in a non-conducting epoxy resin made by mixing Buehler No. 20-3572 ultra-mount powder with Buehler No. 20-3574 hardener liquid. An electrical-connecting wire was soldered to the rear side of the specimen in order to enable electrochemical polarisation experiments to be undertaken. In the case of experiments where only total weight loss was required to be obtained, the specimen was not mounted but fitted in a holder made of epoxy resin, so it could be removed and weighted after the experiment.

A small group of experiments in erosion-corrosion conditions comprised the study of concentric pure Ti specimens as shown in Figure 3.3.1. The central cylindrical specimen of diameter 6 mm was mounted concentrically with an outer ring shaped specimen of area 7.5 cm^2. Electrical connecting wires were attached to the rear side of the separate specimens so that there was no electrical contact between the two specimens. The specimens were mounted in a non-conductive epoxy resin as stated earlier.

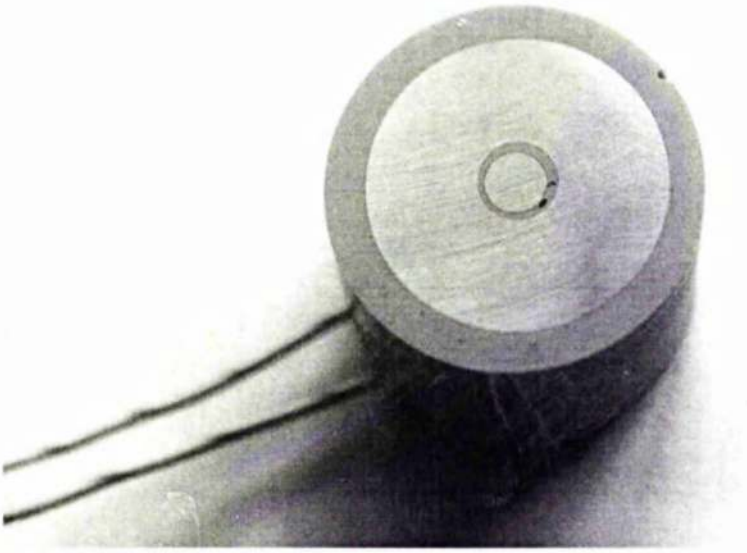

Figure 3.3.1. Assembly of concentric specimen mounted in non-conductive epoxy resin.

All specimens were investigated in the as-polished condition. The polishing process comprised successive grinding on 240, 400, 800, 1200 SiC grit papers and finally 1-micron diamond polishing. The equipment used was a polishing disc type Metaserv Universal Polisher and the specimen was polished on a polishing cloth (Microcloth®) using a diamond abrasive type Meta-D from Buehler Ltd. The polished surface was first washed thoroughly with distilled water and then air-dried.

Liquid erosion-corrosion measurement

Figure 3.3.2 shows the liquid jet impingement rig of closed circulating loop comprising a low-pressure centrifugal pump, which feeds saline water from a 40-litre reservoir to a higher-pressure pump. The circulating water was constantly filtered to provide a liquid-jet free from suspended solids. The system comprised stainless steel pipes with the exit nozzle diameter of 1 mm.

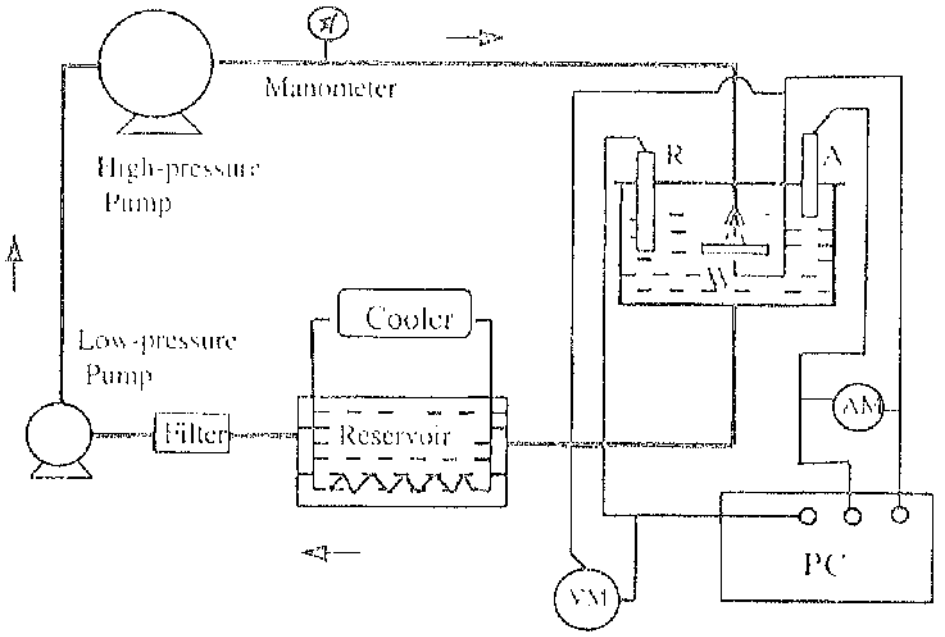

Figure 3.3.2. Schematic diagram of the liquid jet impingement rig comprising a three-electrode cell: where, R - reference electrode; A - auxiliary electrode; W - working electrode; VM – voltmeter; AM – ammeter; PC – computer controlled potentiostat.

Experiments were carried out at 19° ± 1°C and 50° ± 2°C in a 3.5% NaCl solution (made with distilled water). The saline water was directed at 90°C to the specimens surface as a submerged jet at a velocity of 71.1 m/sec and the distance between the nozzle and the specimen was kept constant at all impingement tests at 5 mm.

The temperature of the system was maintained constant by using a custom-made thermostat-controlled heating device for experiments performed at higher temperature (50°C). For experiments at ambient temperature (19°C), a water-cooling coil of stainless steel was used through which fresh tap water was circulating.

Both straight total weight loss tests and electrochemical polarisation tests (anodic scans) were carried out under liquid impingement. In the case of anodic scan tests, electrochemical monitoring was achieved by using the traditional three-electrode (working electrode, reference electrode SCE and auxiliary electrode) cell arrangement

attached to the impinging test rig through a computer controlled potentiostat (model Multistat 2 by Sycopel Scientific Ltd). The scan rate was set at 15 mV/min.

All impingement tests were carried out for 12 hours. After each experiment, specimens were washed with distilled water and ultrasonically bathed to remove all possible remaining corrosion products from the surface before air drying and weighing.

Solid-liquid erosion-corrosion measurement

The solid-liquid erosion-corrosion experiments utilised a separate rig as shown in figure 3.3.3, which also comprised a closed loop in which tests were conducted either for 4, 8, 16 or 72 hours. The nozzle diameter of the solid-liquid rig was 4 mm and the solid-liquid slurry jet was subjected to 90° impingement. The jet velocity was calculated by measuring the volume flow rate and thus using $V = C \times A$ where:

V = volume flow rate of water, m^3/s,
A = cross-sectional area of nozzle = $\pi \times 4 \times 10^{-6}$ m^2,
C = jet velocity, m/s.

In the first phase of the experimental programme, the jet velocity was measured as 12.4 m/s. In later phases, after a pump had been changed, the velocity was 12.8 m/s. These different velocities are identified in the 'Results chapter'. A few tests were carried out at 30° and 60°. The stand off distance was always kept at 5 mm.

The solid-liquid slurry was made of 3.5% NaCl solution plus an initial concentration of 1800 ppm of silica sand type Congleton HST60, as erodent. The size distribution of the type of sand particles used as erodent is shown in table 3.3.1. Two samples of solution were taken over each experiment (the first one after 5 minutes from the start of the experiment and the second one towards the end of the experiment) in order to work out the actual concentration of sand in the solution for each test.

Size μm	1000	710	500	355	250	180	125	90	63
Wt, %	trace	0.1	1.0	5.6	29.6	41.6	21.0	1.0	0.1

Table 3.3.1. Particle size distribution of silica sand type Congleton HST60.

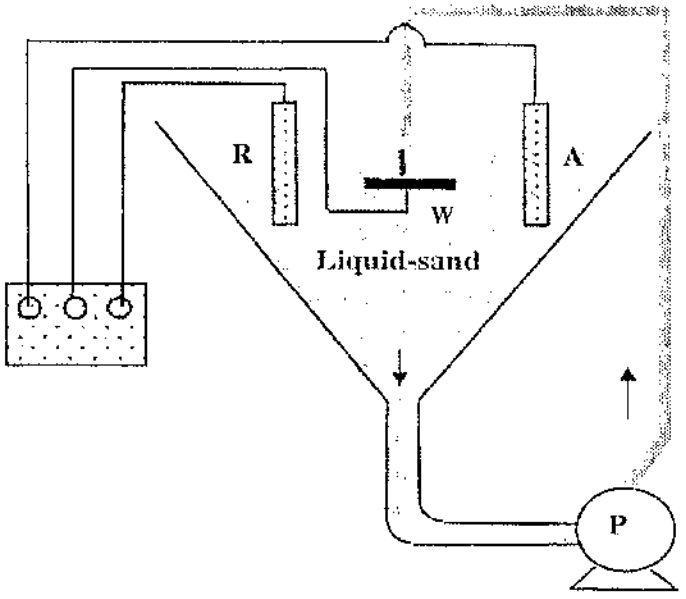

Figure 3.3.3. Schematic diagram of solid-liquid impingement rig, where R - reference electrode; A - auxiliary electrode; W - working electrode.

All solid-liquid impingement tests were carried out at temperature 18° – 20°C. Similarly to liquid erosion-corrosion tests, the temperature of the solution was kept constant by the help of a water-cooling coil of stainless steel through which fresh tap water was circulating. In the case of electrochemical polarisation the same three-electrode arrangement mentioned earlier was used. Tests were also carried out under cathodic protection (CP) at electrode potential being held at –0.8V. The choice of –0.8V CP potential is based on the back extrapolation of the anodic polarisation curve of titanium (see figure 6.3.36) obtained in solid/liquid erosion-corrosion. Back extrapolation shows that at –0.8V the current density exhibited by titanium is very small ~ 0.01 $\mu A/cm^2$. Normally, full cathodic protection requires the use of potential equal to Eo for the metal in question. For titanium, Eo ~ -2.0 V (SCE). However at –

2.0 V titanium could possibly be affected by hydrogen embritlement which would be likely to complicate the assessment of the erosion damage.

Examination techniques

Different modes of attack and damage mechanisms were assessed using mainly a light optical microscope. Surface profiles were also undertaken using Taylor Hobson Pneumo Talysurf (Form TalySurf Series 2 model). Some specimens were also examined using a scanning electron microscope (SEM) type Leica Cambridge Stereoscan 360.

4. RESULTS OF CORROSION STUDIES ON COPPER-NICKEL ALLOYS UNDER STATIC CONDITIONS

Both copper-nickel alloys were tested in artificial seawater and distilled water at ambient temperature (20°C), in distilled water at 50°C, again at 50°C in distilled water combining CO_2 bubbling and in distilled water at ambient temperature with CO_2 bubbling.

4.1. Cu-10%Ni

4.1.1. Tests in seawater at 20°C

Figures 4.1.1a and 4.1.1b show the anodic polarisation curves generated from tests in artificial seawater at 20°C. It is quite clear that Cu-10%Ni is very active upon initial immersion in seawater (immediate tests). The current passing through the specimens reached high values while the shift in the potential from E_{corr} was still considerably low. It was also noted that, in the case when specimens were exposed to seawater for some days before being polarised, the polarisation curves were steeper (indicating lower corrosion rates) in comparison to the immediate tests. Thus after 2 days in seawater the corrosion behaviour of the sample exhibited what could be interpreted as a slight passivity which was even greater after 7 days. This suggests that, under extended periods in seawater and in static conditions, a protective film builds up on the surface of Cu-10%Ni. The values of E_{corr} were all in the range –220 mV to -233 mV. No change in the pH of the solution was observed throughout all experiments.

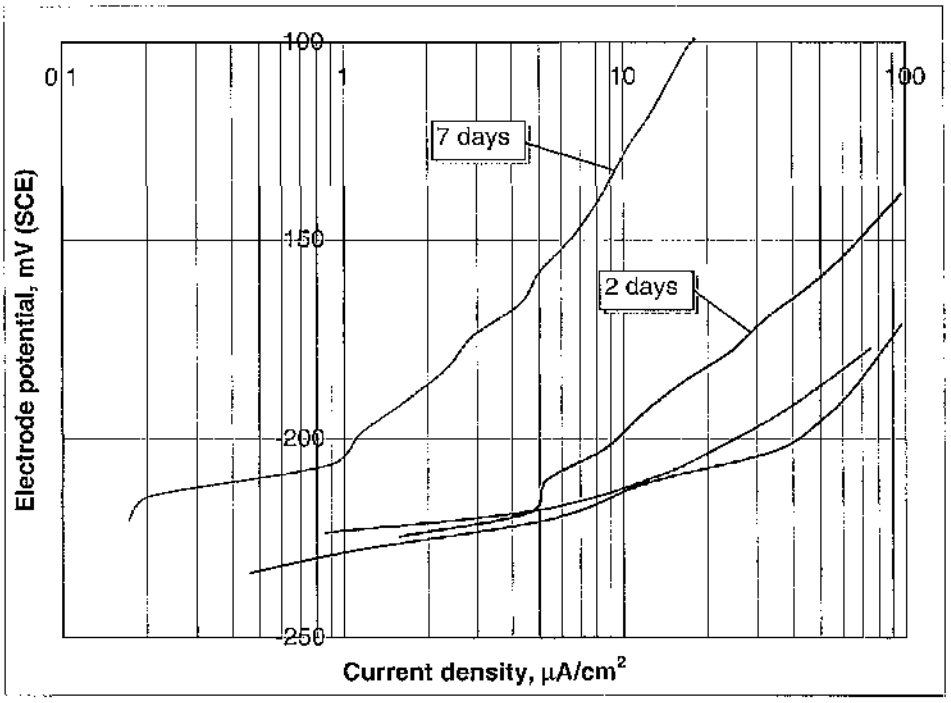

Figure 4.1.1a. Anodic polarisation tests of Cu-10%Ni in artificial seawater at 20°C after 1 hour immersion except where stated.

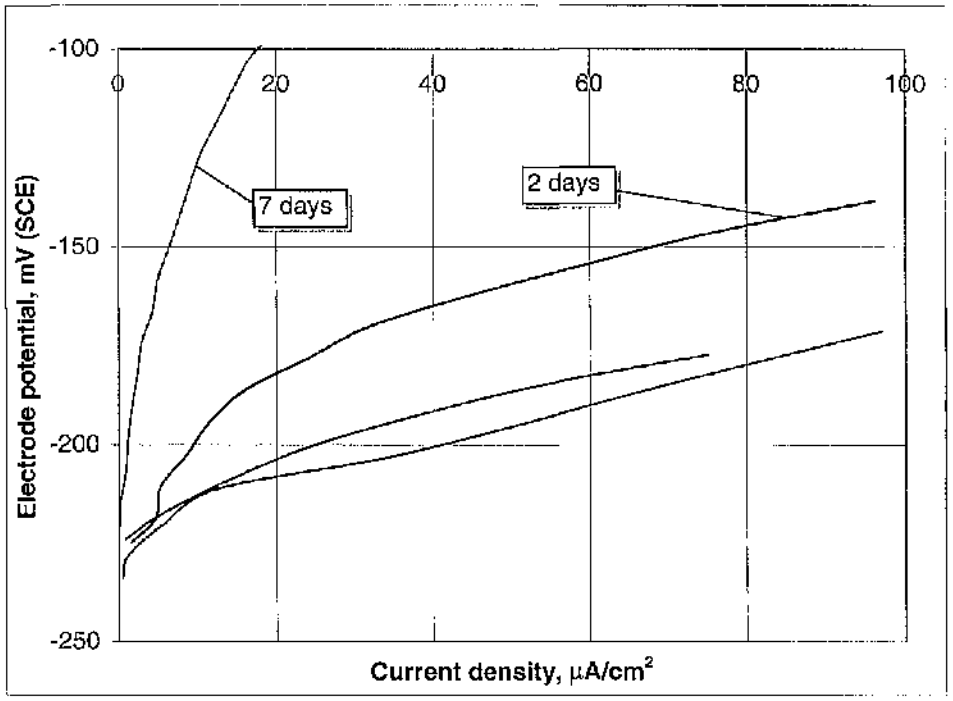

Figure 4.1.1b. Anodic polarisation tests of Cu-10%Ni in artificial seawater at 20°C after 1 hour immersion except where stated.

4.1.2. Tests in distilled water at 20°C

Figures 4.1.2a and 4.1.2b show the anodic polarisation curves generated in distilled water at 20°C, in comparison with those in seawater at 20°C. There was a large difference in the values of E_{corr} between the two environments; between -32 mV to -85 mV for distilled water and in the range -220 mV to -233 mV for seawater. Evidently the corrosion rate of Cu-10%Ni is lower in distilled water than in seawater. No sign of passivity was shown from the specimen exposed for 2 days in distilled water, prior to the anodic polarisation, in relation to the immediate tests. The corrosion resistance was much higher after 7 days exposure but a continued improvement was not apparent in the test period of 60 days. In all tests the conductivity of the solution appeared to be relatively higher after the specimen had been anodically polarised and presumably that was caused by metal dissolution. The pH of the solution was also increased possibly due to the cathodic reaction of hydrogen evolution, $2H^+ + 2e^- \longrightarrow H_2$, on the auxiliary electrode surface. This increase in pH and conductivity was not only observed over anodic polarisations. In the case of the 60 day period of exposure the solution was inspected and replaced by fresh distilled water every 5 days. Both conductivity and pH was increased after those 5 days seemingly for the same reasons mentioned above. Table 4.1.1. and Table 4.1.2. show the conductivity and pH values respectively before and after polarisation tests. The pH values of around 5.3-5.4 measured before the tests represent the expected acidic conditions of distilled water as after it has come to equilibrium with the CO_2 in the air atmosphere.

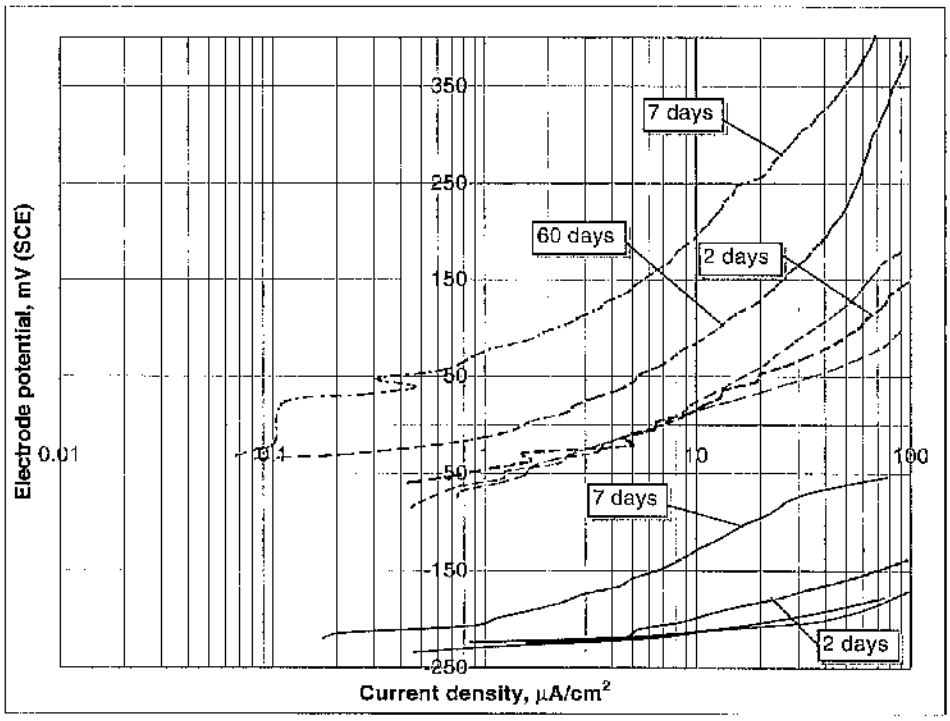

Figure 4.1.2a. Anodic polarisation curves of Cu-10%Ni in distilled water at 20°C in comparison to artificial seawater at 20°C after 1 hour of immersion except where stated. Dotted lines = distilled water, full lines = seawater.

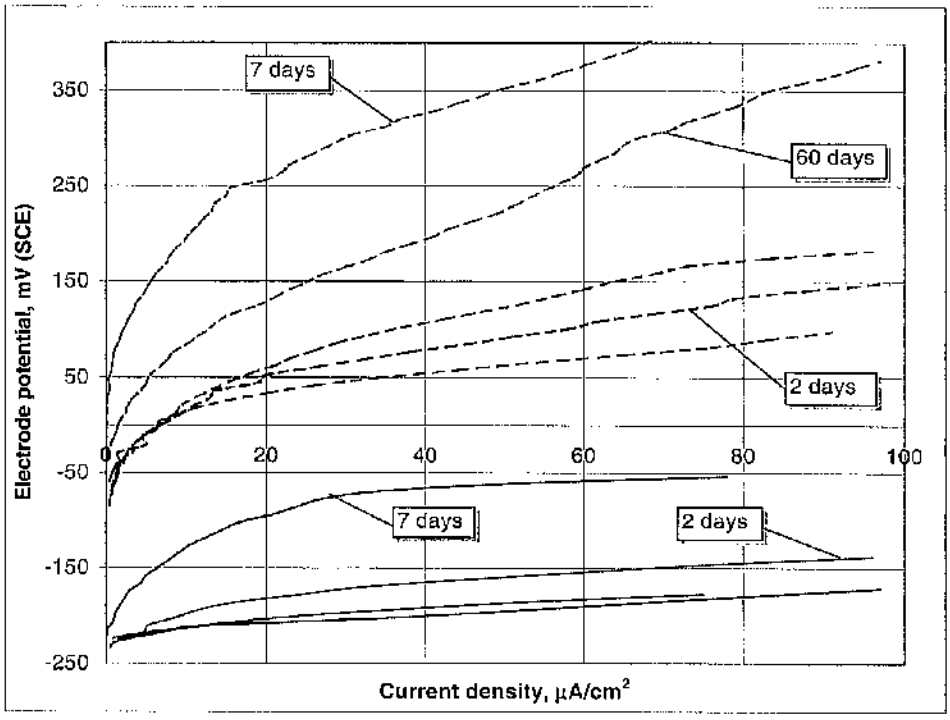

Figure 4.1.2b. Anodic polarisation curves of Cu-10%Ni in distilled water at 20°C in comparison to artificial seawater at 20°C after 1 hour of immersion except where stated. Dotted lines = distilled water, full lines = seawater.

	Before polarisation	After polarisation
Immediate test	5.1	38.5
Immediate test	3.5	65.2
Immediate test	5.2	52.7
Polarisation after 2 days of exposure	12	57
Polarisation after 7 days of exposure	14.8	42.8
Polarisation after 60 days of exposure	18.7	60.7

Table 4.1.1. Conductivity values before and after polarisation tests of Cu-10%Ni in distilled water at 20°C (μS/cm).

	Before polarisation	After polarisation
Immediate test	5.42	6.45
Immediate test	5.4	5.76
Immediate test	5.3	6.05
Polarisation after 2 days of exposure	5.75	6.15
Polarisation after 7 days of exposure	5.7	6.56
Polarisation after 60 days of exposure	5.47	6.3

Table 4.1.2. pH values before and after polarisation tests of Cu-10%Ni in distilled water at 20°C.

4.1.3. Tests in distilled water at 50°C

Figures 4.1.3a and 4.1.3b show the anodic polarisation curves generated after 1 hour of immersion in distilled water at 50°C in comparison to those in distilled water at 20°C. The higher temperature did not seem to have a dramatic effect on the corrosion behaviour of the alloy. For instance, the values of E_{corr} were in the range -60 mV to -85 mV for both conditions. However, as the curves indicate, the samples tested at 50°C exhibited a slight passivity in relevance to the ones tested in distilled water at 20°C. Again both pH and conductivity of the solution were found to be significantly increased after the specimens had been polarised. Table 4.1.3. and Table 4.1.4. show the conductivity and pH values respectively before and after polarisation tests.

Before polarisation	After polarisation
2.2	44.4
1.9	47.1
1.7	49

Table 4.1.3. Conductivity values before and after polarisation tests of Cu-10%Ni after 1 hour of immersion in distilled water at 50^0C (μS/cm).

Before polarisation	After polarisation
5.38	6.6
5.3	6.8
5.33	6.42

Table 4.1.4. pH values before and after polarisation tests of Cu-10%Ni after 1 hour of immersion in distilled water at 50^0C.

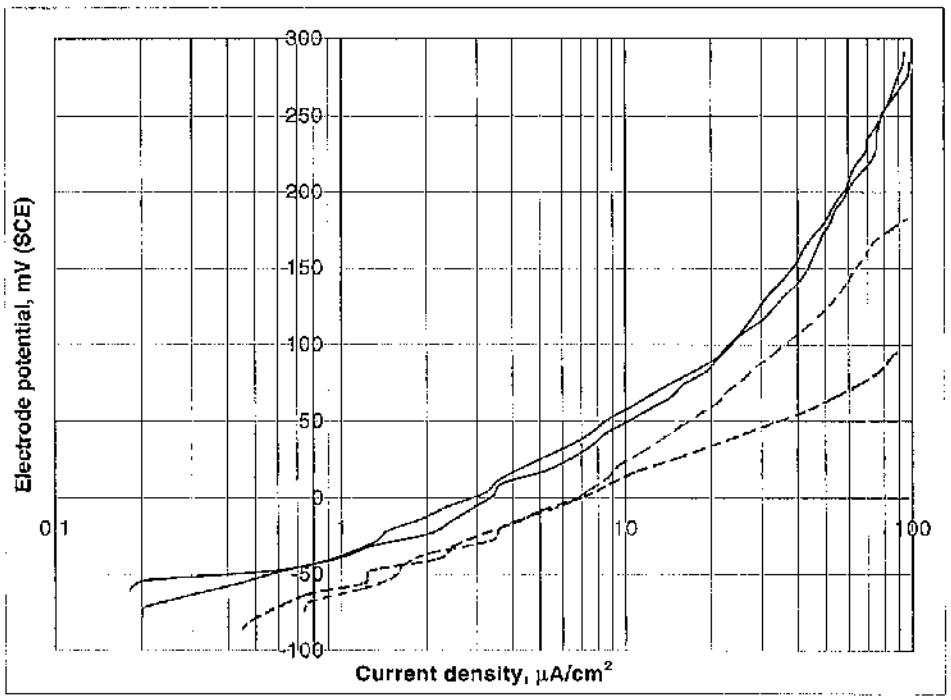

Figure 4.1.3a. Anodic polarisation curves of Cu-10%Ni after 1 hour of immersion in distilled water at 50°C in comparison to distilled water at 20°C. Dotted lines = 20°C, full lines = 50°C.

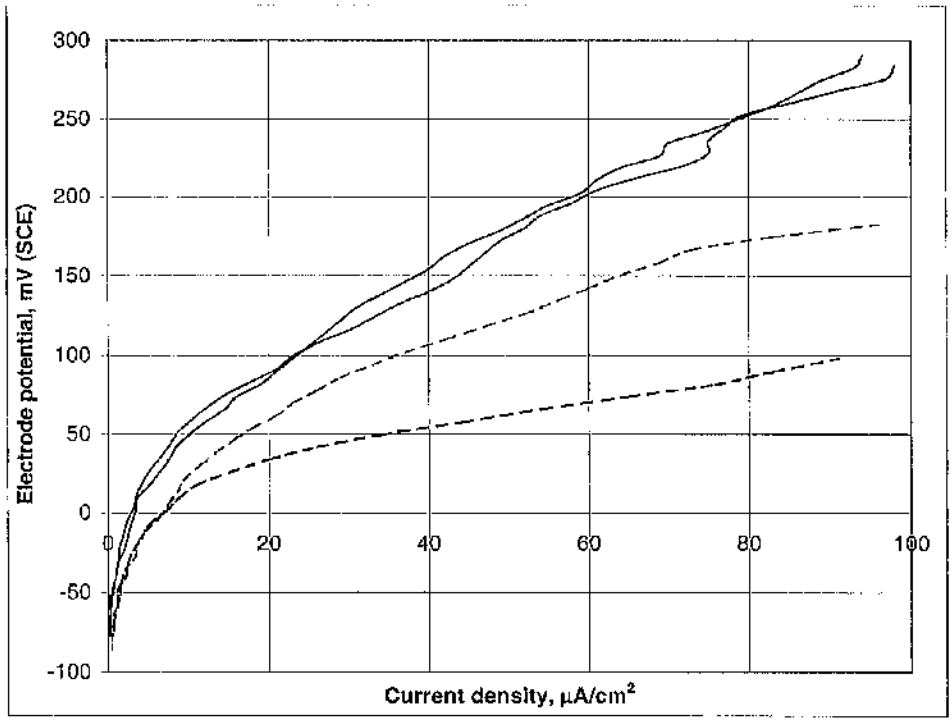

Figure 4.1.3b. Anodic polarisation curves of Cu-10%Ni after 1 hour of immersion in distilled water at 50°C in comparison to distilled water at 20°C. Dotted lines = 20°C, full lines = 50°C.

4.1.4. Tests in distilled water at 20°C with CO_2

Figures 4.1.4a and 4.1.4b show the anodic polarisation curves generated after 1 hour of immersion in distilled water at 20°C with the injection of CO_2, in comparison with those in distilled water at 20°C. There was a small difference in the values of E_{corr} between the two environments; between -74 mV to -85 mV for distilled water at 20°C and in the range -104 mV to -106 mV for distilled water at 20°C with CO_2. Despite divergence at potentials remote from E_{corr}, in the more relevant potential range immediately positive to E_{corr}, the injection of CO_2 into the distilled water did not seem to have a clear effect on the corrosion resistance of Cu-10%Ni.

The pH was noticeably reduced when CO_2 was introduced into the solution (table 4.1.5). This can be attributed to the formation of carbonic acid,

$$CO_2 + H_2O \longrightarrow H_2CO_3$$

which was followed by hydrogen ion evolution,

$$H_2CO_3 \longrightarrow H^+ + (HCO3)^- \quad \text{and}$$
$$(HCO_3)^- \longrightarrow H^+ + (CO_3)^{2-}$$

It was also observed that the conductivity of the solution was increased in a short period of few minutes after the cylinder had started bubbling CO_2 prior to polarisation. After the anodic polarisation had taken place the conductivity had further increased slightly (Table 4.1.6). The conductivity increases imply some dissolution of the metal although a significant contributor to these conductivity changes would be the $(HCO_3)^-$ and $(CO_3)^{2-}$ ion productions resulting from injections of CO_2 as described above.

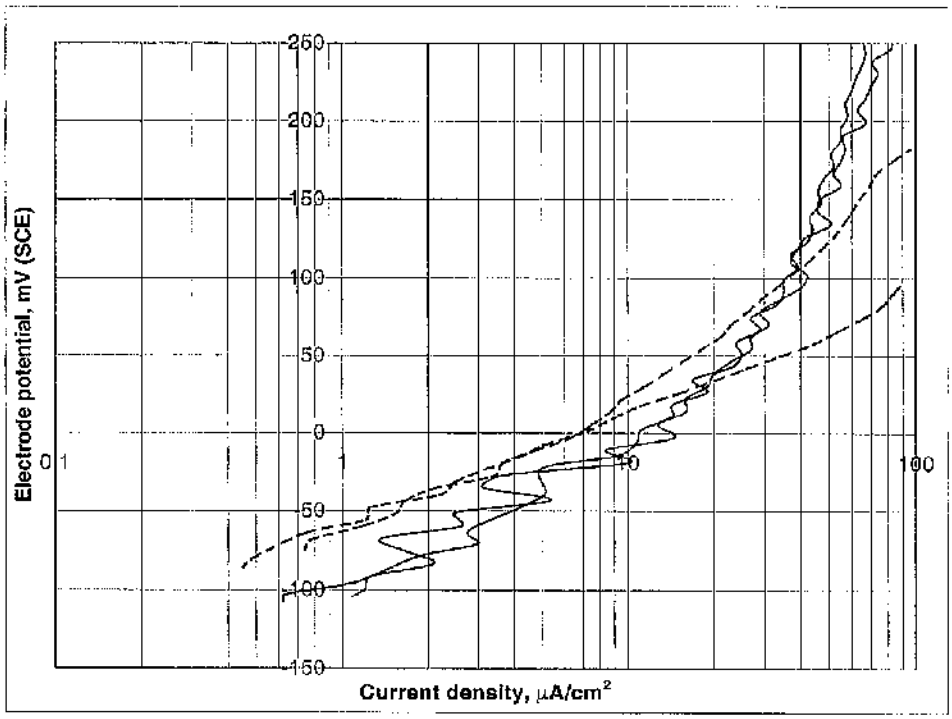

Figure 4.1.4a. Anodic polarisation curves of Cu-10%Ni after 1 hour of immersion in distilled water at 20°C with injected CO_2, in comparison to distilled water at 20°C. Dotted lines = 20°C, full lines = 20°C + CO_2.

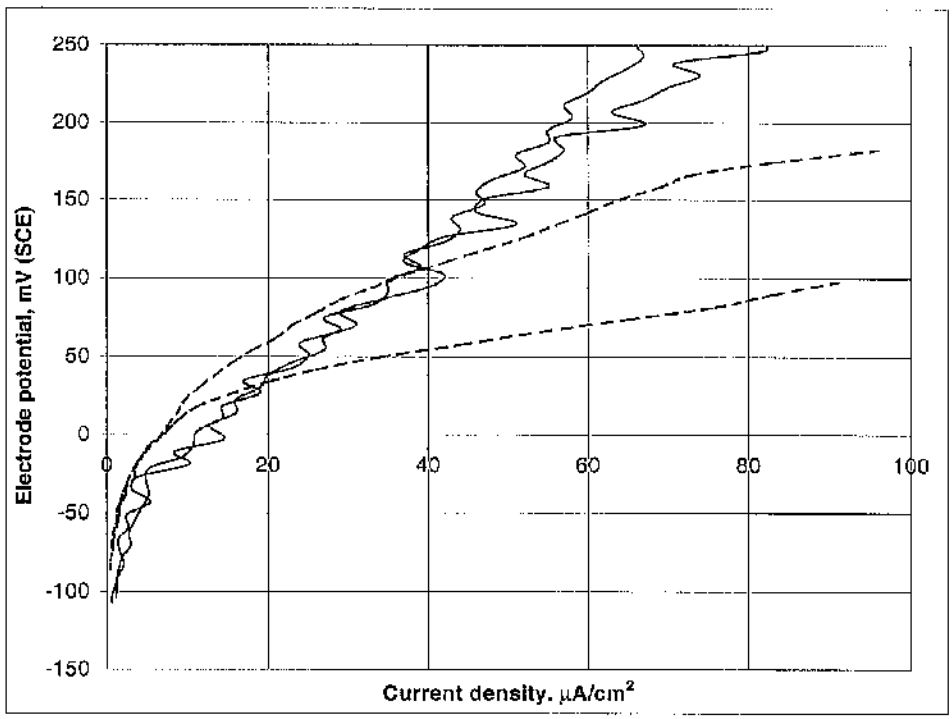

Figure 4.1.4b. Anodic polarisation curves of Cu-10%Ni after 1 hour of immersion in distilled water at 20°C with injected CO_2, in comparison to distilled water at 20°C. Dotted lines = 20°C, full lines = 20°C + CO_2.

Before the addition of CO_2	After the addition of CO_2	After polarisation
4.95	4.14	4.05
4.96	4.1	4.06
4.96	4.08	4.02

Table 4.1.5. pH values before and after the addition of CO_2, and after polarisation of Cu-10%Ni after 1 hour of immersion in distilled water at 20°C.

Before the addition of CO_2	After the addition of CO_2	After polarisation
3	32.3	51.15
3.9	41	58.7
6.4	32	48.5

Table 4.1.6. Conductivity values before and after the addition of CO_2, and after polarisation of Cu-10%Ni after 1 hour of immersion in distilled water at 20°C.

4.1.5. Tests in distilled water at 50°C with CO_2

Figures 4.1.5a and 4.1.5b show the anodic polarisation curves generated in distilled water at 50°C with the injection of CO_2, in comparison to those in distilled water at 50°C. There was a slight difference in values of E_{corr} between the two environments; between -79 mV to -94 mV for distilled water at 50°C with CO_2 and in the range -60 mV to -74 mV for distilled water at 50°C without CO_2. The injection of CO_2 in distilled water at 50°C did not seem to have any deleterious effect on the corrosion behaviour of the alloy in relevance to its behaviour at 50°C without CO_2. The pH was noticeably reduced when CO_2 was introduced into the solution (table 4.1.7) while the conductivity was increased (table 4.1.8) presumably for the same reasons already described in section 4.1.4.

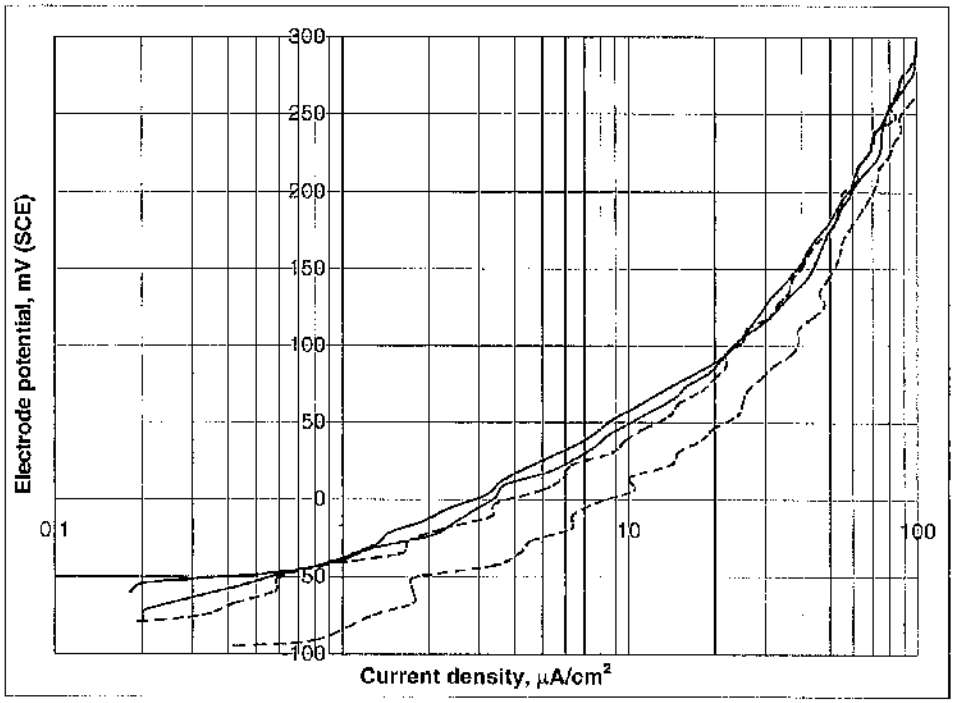

Figure 4.1.5a. Anodic polarisation curves of Cu-10%Ni after 1 hour of immersion in distilled water at 50°C with injected CO_2, in comparison to distilled water at 50°C. Dotted lines = 50°C + CO_2, full lines = 50°C.

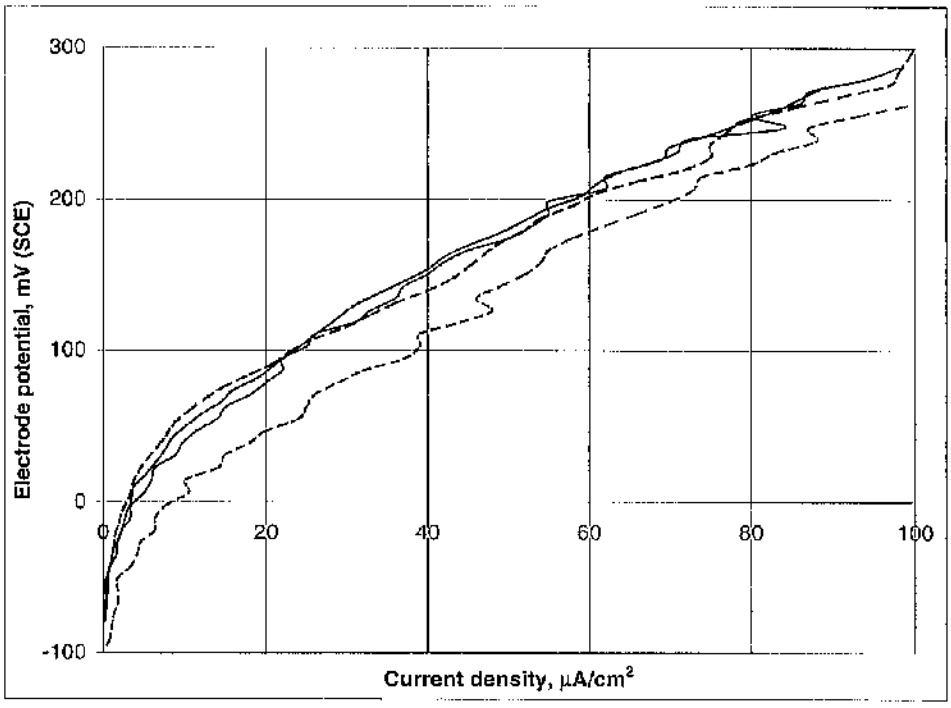

Figure 4.1.5b. Anodic polarisation curves of Cu-10%Ni after 1 hour of immersion in distilled water at 50°C with injected CO_2, in comparison to distilled water at 50°C. Dotted lines = 50°C + CO_2, full lines = 50°C.

Before the addition of CO_2	After the addition of CO_2	After polarisation
4.95	4.14	4.05
4.96	4.1	4.06
4.96	4.08	4.02

Table 4.1.7. pH values before and after the addition of CO_2, and after polarisation of Cu-10%Ni after 1 hour of immersion in distilled water at 50°C.

Before the addition of CO_2	After the addition of CO_2	After polarisation
3	32.3	51.15
3.9	41	58.7
6.4	32	48.5

Table 4.1.8. Conductivity values before and after the addition of CO_2, and after polarisation of Cu-10%Ni after 1 hour of immersion in distilled water at 50°C.

4.1.6. Microscopy

Tests in seawater at 20 ℃

After anodic polarisation immediately upon exposure to seawater, the surface of the specimen had an 'etched' appearance, i.e. revealing the grain structure (figure 4.1.6). This implies general corrosion with some selective attack at the grain boundaries. In the case when Cu-10%Ni was left exposed to seawater for 2 days without subsequent anodic polarisation, thick general corrosion covered most of the sample's surface. At several points where the general corrosion was not that thick, the grain structure was revealed (figures 4.1.7a and 4.1.7b). It appears as if the attack was firstly on the grain lattice and then progressively a thick layer of general corrosion covered most of the surface. When the specimen was anodically polarised after 2 days in seawater, the corrosion features remained the same apart from the fact that the 'etching effect' appeared to be slightly more severe than the one before polarisation (figures 4.1.8a and 4.1.8b). A similar behaviour was observed when samples of Cu-10%Ni were left in seawater for 7 days and then anodically polarised.

Again after 7 days in seawater most of the surface was covered by a uniform layer of general corrosion with only patches of etched surface apparent (figures 4.1.9a and 4.1.9b). After polarisation took place, signs of pitting corrosion appeared on the surface, apparently resulting from localised breakdown of the alloy's protective film (figures 4.1.10a and 4.1.10b). This relatively thick layer of general corrosion as mentioned earlier, fairly implies that the protective film forming on Cu-10%Ni's surface consists of corrosion products resulting from the early attack on the metal. When samples of Cu-10%Ni were anodically polarised after 2 day and 7 day exposure in seawater, the corrosion rates obtained were lower than immediate tests (see figures 4.1.1a and 4.1.1b).

Tests in distilled water at 20 ℃

Similarly to seawater at 20°C, Cu-10%Ni showed an etched appearance when anodically polarised immediately after initial exposure to distilled water (figures 4.1.11a and 4.1.11b). This attack covered evenly almost the entire surface of the samples in a light to dark brown colour but at some points black regions of corrosion products were also present. When samples of Cu-10%Ni were left in distilled water for 2 days without polarisation, uniform corrosion products covered almost the entire surface leaving only patches of clean metal (figure 4.1.12a). At high magnification the clean patches appeared to be full of numerous particles which probably were discontinuous corrosion products (figure 4.1.12b). After anodic polarisation took place, the surface exhibited regions showing the grain structure but also showed regions of thicker corrosion products plus shallow pits. Possibly, as the attack progresses, shallow pits grow bigger and eventually join together to form dark regions of general corrosion (figure 4.1.13a). At high magnification the dark regions appear to be uniform and even, giving possible evidence of a protective film being developed (figure 4.1.13b).

When samples of bright Cu-10%Ni were left in distilled water for 7 days, large parts of the surface appeared bright at low magnification and the rest was covered by regions of thicker corrosion products (figure 4.1.14a). At high magnification the bright surface appears to consist of numerous tiny particles which might be the beginning of a protective corrosion product layer (figure 4.1.14b). This is consistent with the low corrosion rate, in comparison to immediate tests, obtained when sample of Cu-10%Ni was anodically polarised after 7 day exposure in distilled water (see figures 4.1.2a and 4.1.2b). However, as shown in figure 4.1.15a, a sample exposed for 7 days suffered severe pitting attack after anodic polarisation as numerous circular pits and similar circular regions consisting of individual particles appeared over the entire surface. The rest of the metal matrix remained bright or slightly discoloured and contained lots of single particles and tiny pits. It was also observed that most pits had a centred depth (figure 4.1.15b).

In the case when Cu-10%Ni was left exposed to distilled water for 60 days without polarisation, general corrosion products covered almost the entire surface of the

specimen leaving only patches of slightly discoloured metal. Pitting corrosion was also present over the whole surface and consisted of large but rather shallow pits. Figures 4.1.16a and 4.1.16b show the above features. When polarisation took place after 60 days, the extent of the damage remained relatively the same with the only difference being the appearance of additional small shallow pits (presumably produced during the anodic polarisation scan) especially at points where general corrosion product was not as thick (figures 4.1.17a and 4.1.17b). It was also noted that pits were surrounded by a rather clean metal matrix. Presumably pits were acting as anodic sites driving in this way the surface closely around them to act as cathodic site.

Tests in distilled water in other conditions

Less detailed studies were conducted in distilled water at 20°C with CO_2 injection and at 50°C with and without CO_2 injection. These experiments comprised anodic polarisations upon immediate exposure together with microscopical examination of the anodically polarised specimens.

Tests in distilled water at 50^0C

The higher temperature did not seem to have a severe effect on the surface of Cu-10%Ni specimens after anodic polarisation upon initial exposure. Most of the surface appeared to be covered by a thin film together with isolated 'etched' regions and a few dark patches of general corrosion (figure 4.1.18a). Crevice attack was also present round the edge of the surface in the form of surface etching (figure 4.1.18b).

Tests in distilled water at 20^0C with CO_2

The entire surface of Cu-10%Ni when anodically polarised upon initial exposure in distilled water with CO_2 injection, appeared etched (figure 4.1.19a). However, at high magnification the presence of particles within the grains was quite clear indicating initiation of further corrosion (figure 4.1.19b).

Test in distilled water at 50^0C with CO_2

In the case when Cu-10%Ni was anodically polarised at 50°C in distilled water with CO_2 injection, dark general corrosion covered unevenly large parts of the surface (figure 4.1.20a). Small patches showing the grain structure plus minor pitting were also present on parts of the surface where the metal was just slightly discoloured (figure 4.1.20b).

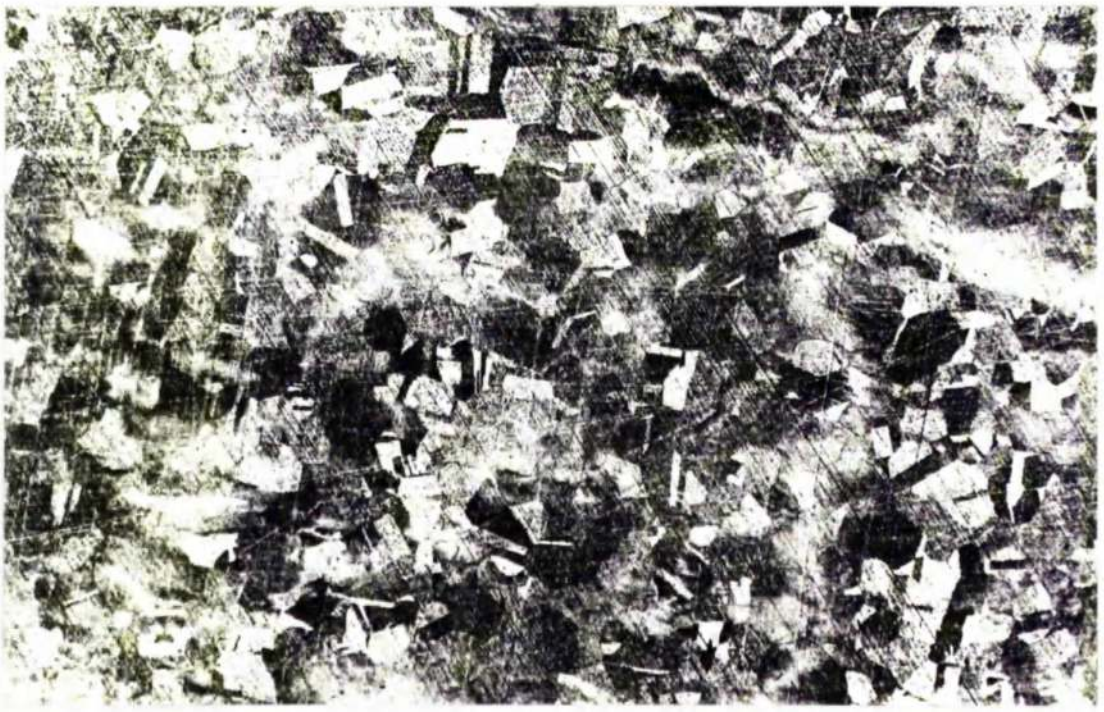

Figure 4.1.6. "Etched" appearance on Cu-10%Ni after anodic polarisation upon initial exposure to seawater at 20°C.

Figure 4.1.7a. Uniform layer of general corrosion on Cu-10%Ni after 2 day exposure in seawater at 20°C.

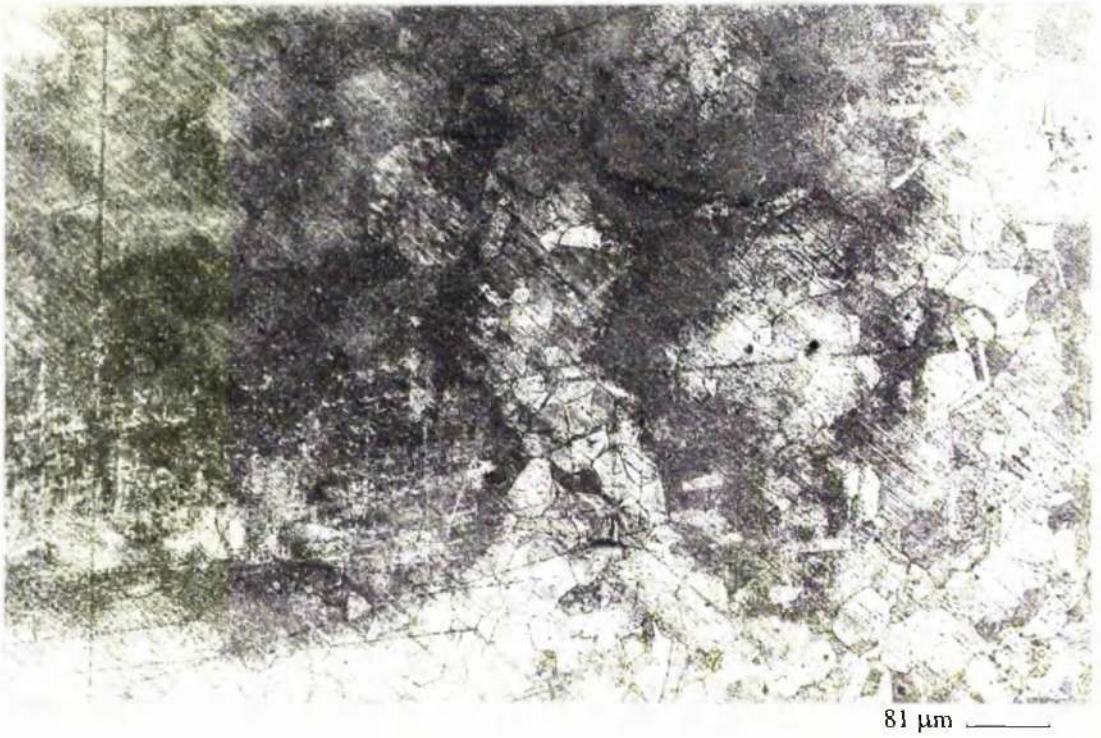

Figure 4.1.7b. General corrosion and intergranular attack on Cu-10%Ni after 2 day exposure in seawater at 20°C.

Figure 4.1.8a. Uniform layer of general corrosion on Cu-10%Ni when anodically polarised after 2 day exposure in seawater at 20°C.

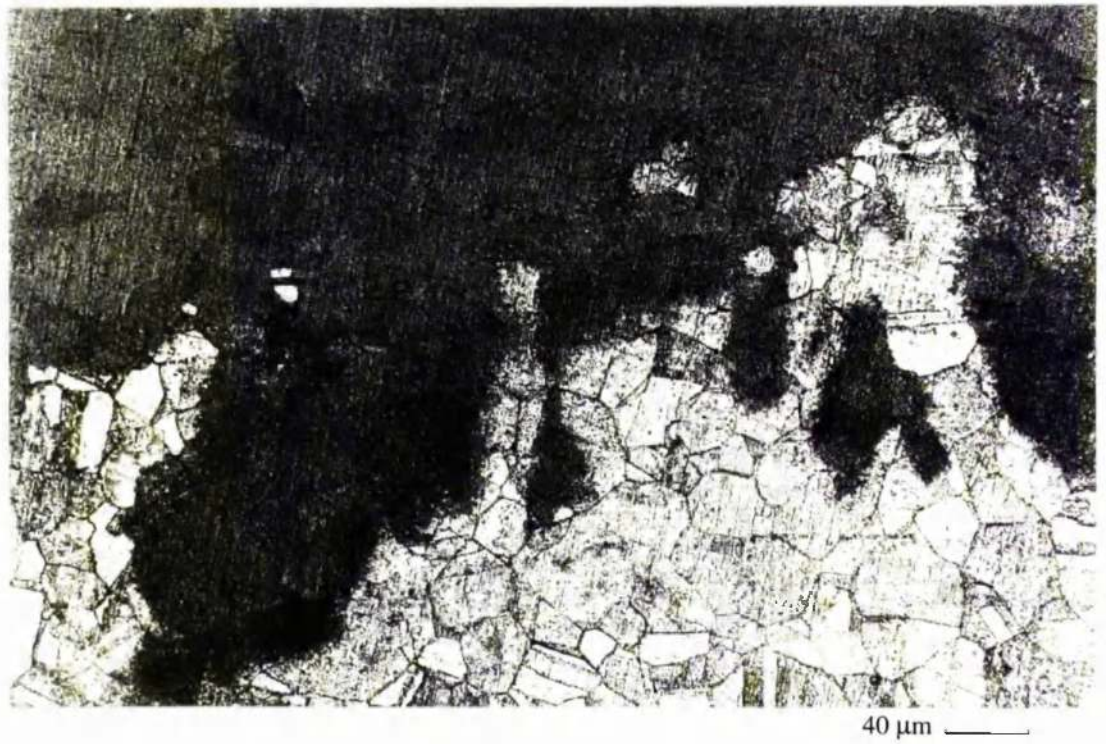

Figure 4.1.8b. General corrosion and intergranular attack on Cu-10%Ni when anodically polarised after 2 day exposure in seawater at 20°C.

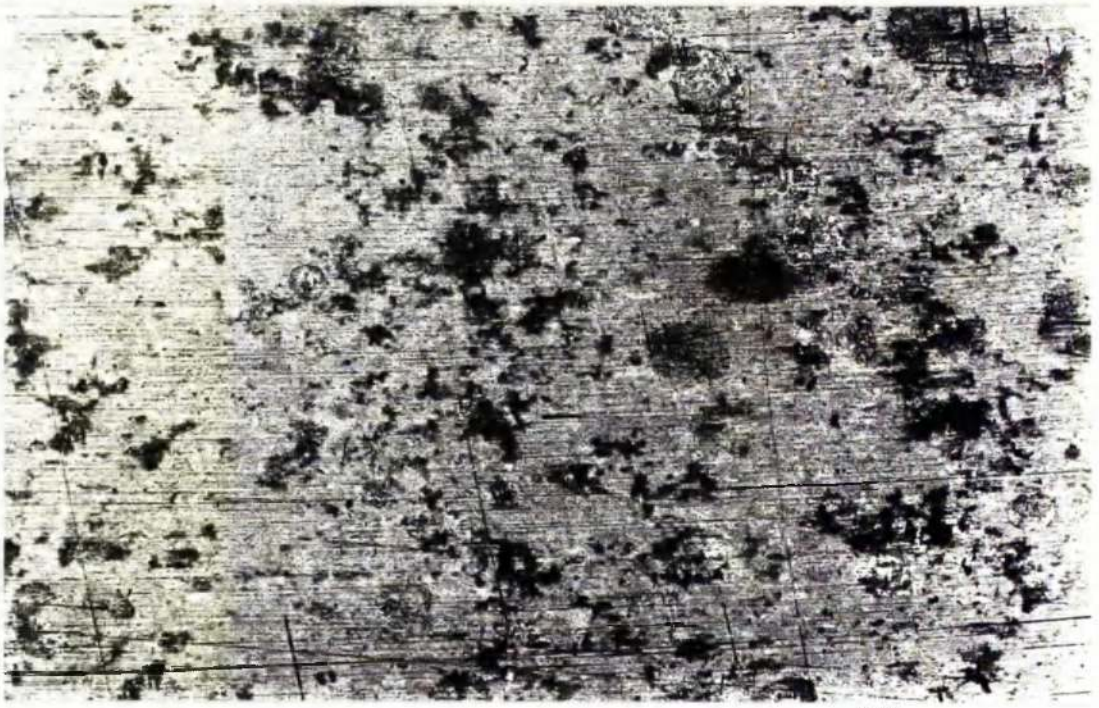

Figure 4.1.9a. Uniform layer of general corrosion on Cu-10%Ni after 7 day exposure in seawater at 20°C.

Figure 4.1.9b. General corrosion and "etched" surface on Cu-10%Ni after 7 day exposure in seawater at 20°C.

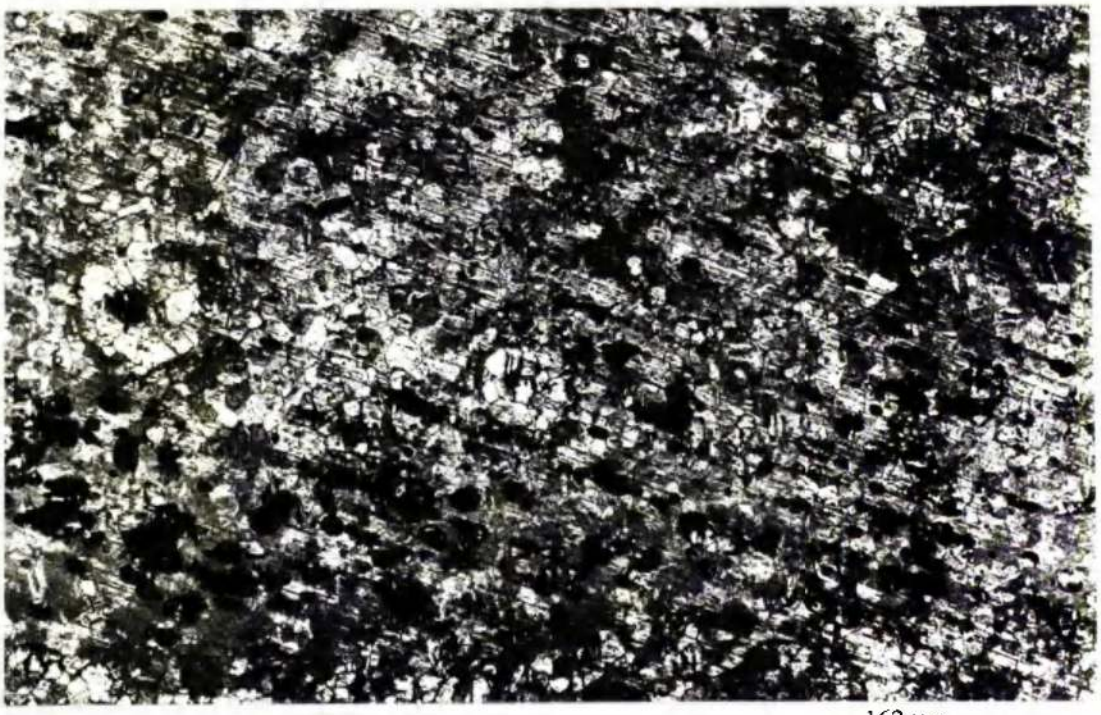

Figure 4.1.10a. Pitting attack on the surface of Cu-10%Ni when anodically polarised after 7 day exposure in seawater at 20°C.

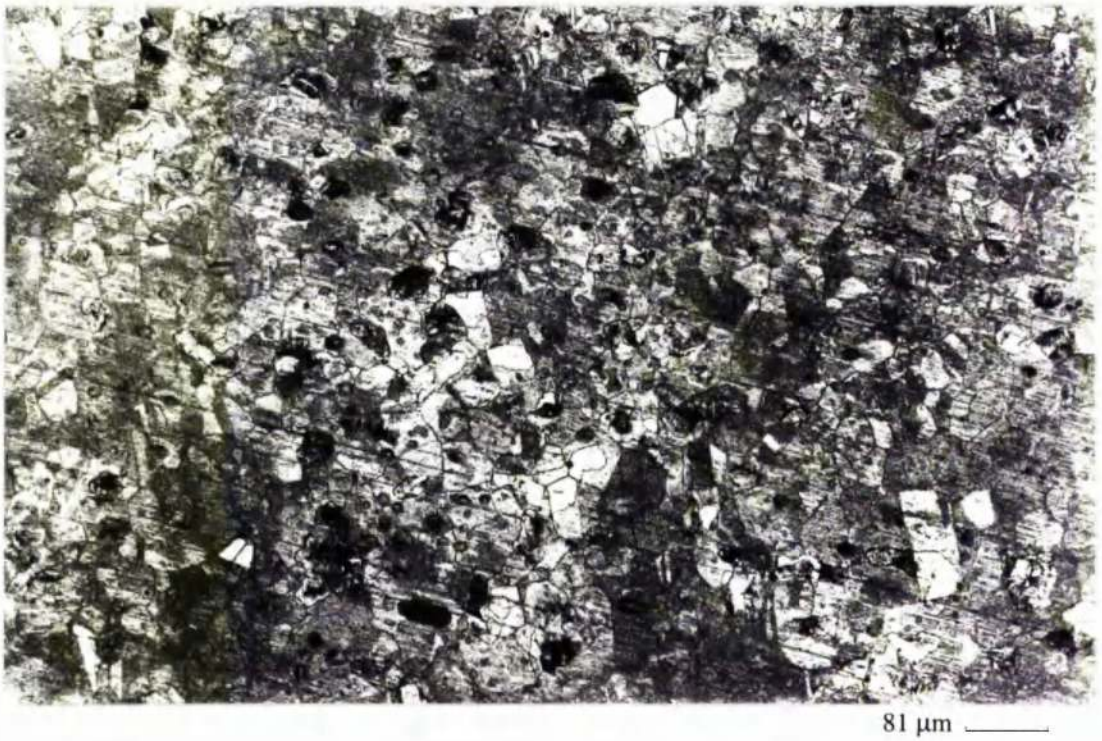

Figure 4.1.10b. Sings of pitting and intergranular corrosion on Cu-10%Ni when anodically polarised after 7 day exposure in seawater.

Figure 4.1.11a. Etched appearance on Cu-10%Ni after anodic polarisation upon initial exposure to distilled water at 20°C.

Figure 4.1.11b. Close-up view of the above features.

Figure 4.1.12a. General corrosion and clean patches on Cu-10%Ni after 2 day exposure in distilled water at 20°C.

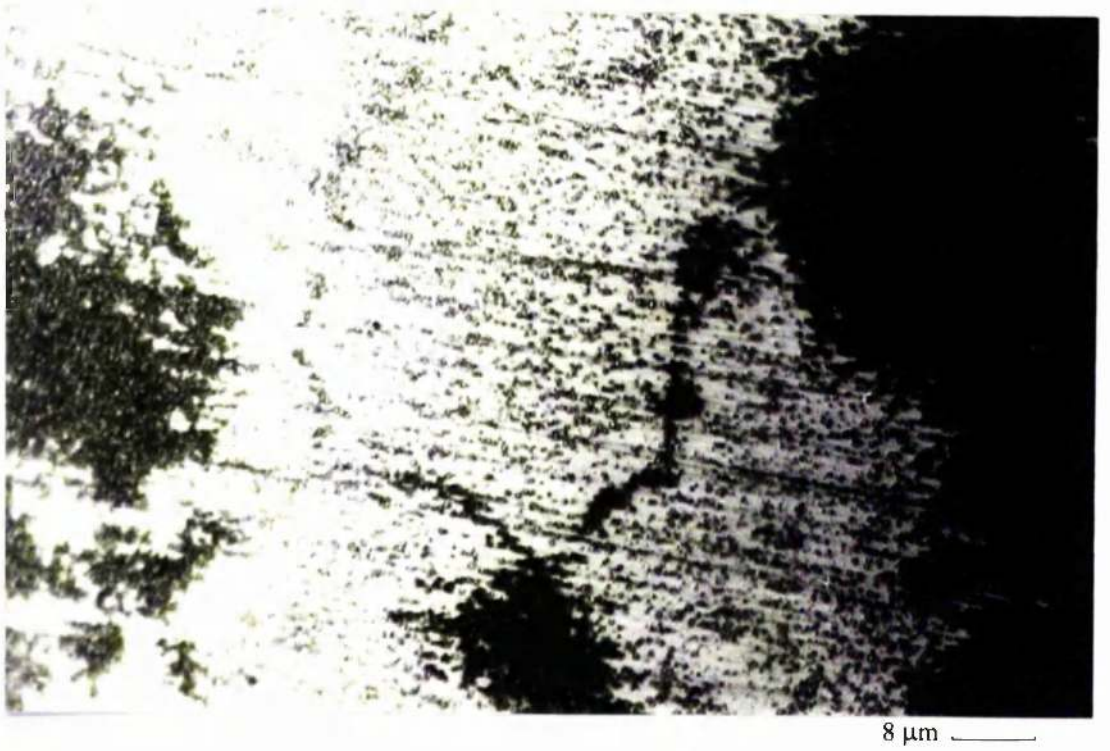

Figure 4.1.12b. At high magnification the clean patches appear to be full of numerous particles.

Figure 4.1.13a. Etched appearance and general attack with shallow pitting on Cu-10%Ni when anodically polarised after 2 day exposure in distilled water at 20°C.

Figure 4.1.13b. At high magnification the dark regions on the above picture appear to be uniform.

Figure 4.1.14a. Bright surface with regions of thicker corrosion products on Cu-10%Ni after 7 day exposure in distilled water at 20°C.

Figure 4.1.14b. High magnification reveals numerous particles on the bright surface.

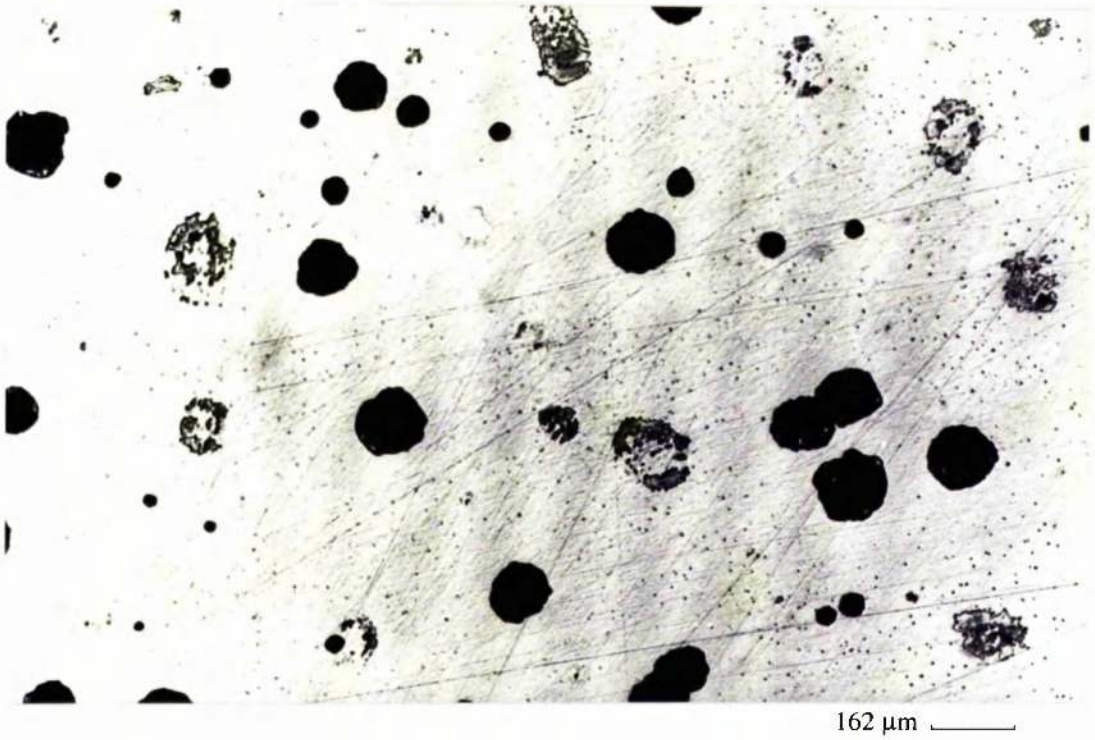

Figure 4.1.15a. Pitting attack and circular regions consisting of individual particles on Cu-10%Ni when anodically polarised after 7 day exposure in distilled water at 20°C.

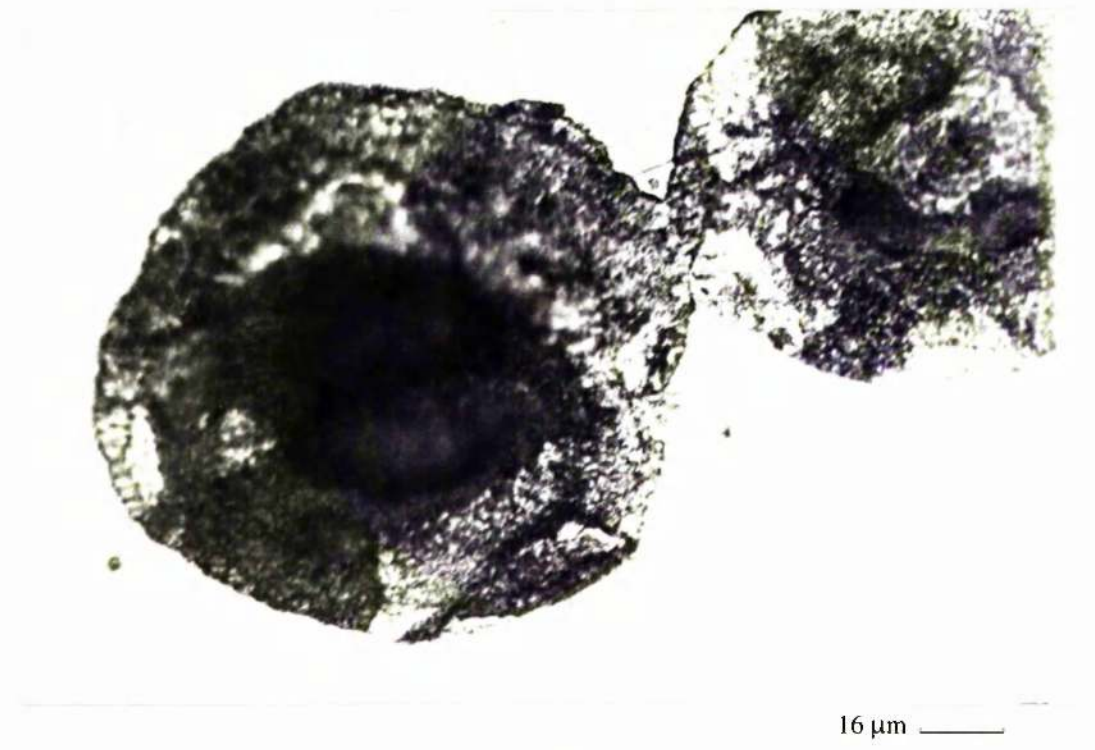

Figure 4.1.15b. Pits were noted to have a centred depth.

Figure 4.1.16a. General corrosion and pitting attack on Cu-10%Ni after 60 day exposure in distilled water at 20°C.

Figure 4.1.16b. At high magnification pits are shown to be shallow.

Figure 4.1.17a. Pitting and general attack on Cu-10%Ni when anodically polarised after 60 day exposure in distilled water at 20°C.

Figure 4.1.17b. Small shallow pits were also present on Cu-10%Ni when anodically polarised after 60 day exposure in distilled water at 20°C.

Figure 4.1.18a. Regions of intergranular corrosion and few dark patches on Cu-10%Ni when anodically polarised in distilled water at 50^0C.

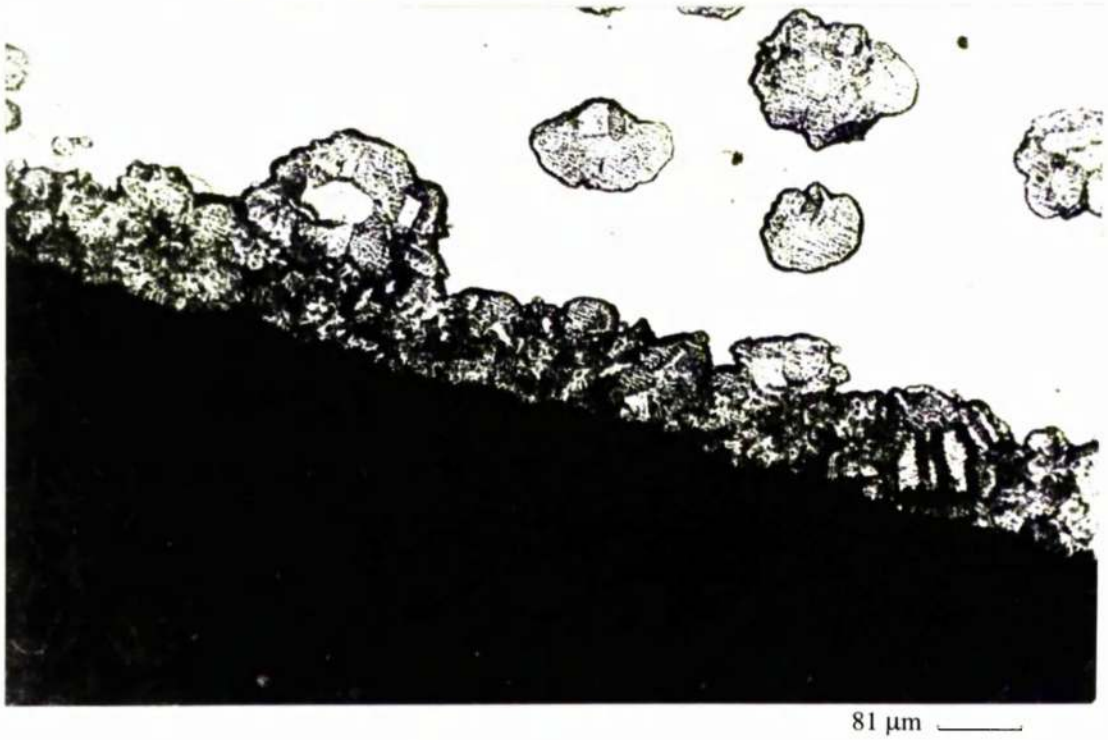

Figure 4.1.18b. Crevice corrosion on Cu-10%Ni when anodically polarised in distilled water at 50^0C.

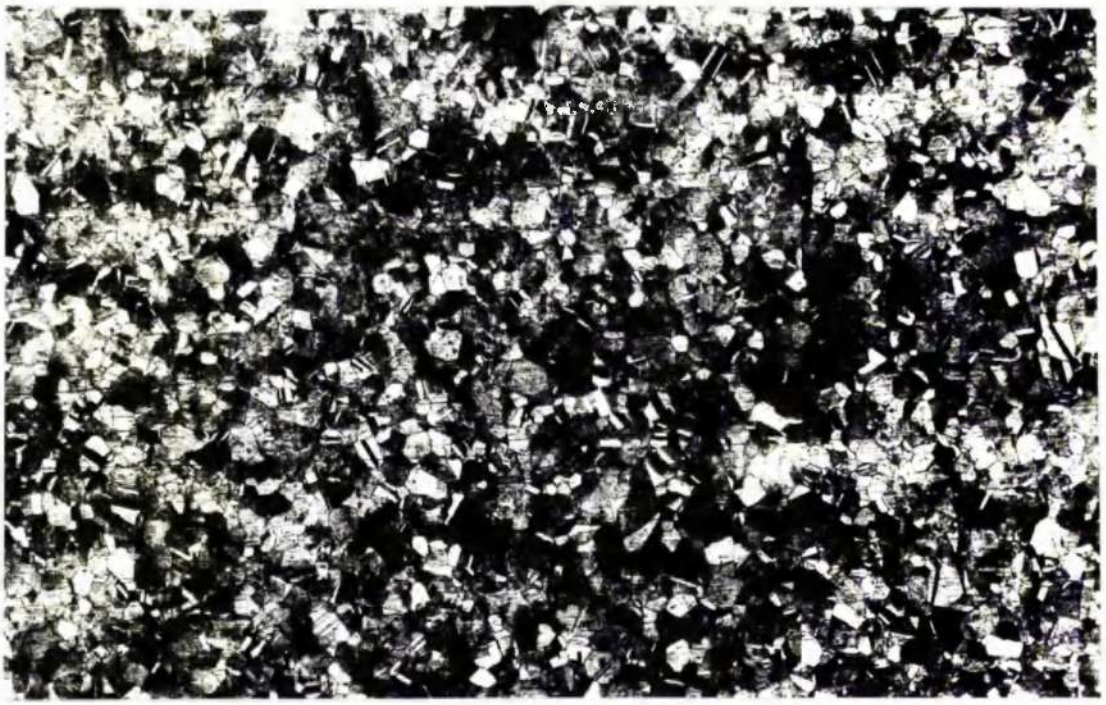

Figure 4.1.19a. Etched appearance of Cu-10%Ni when anodically polarised in distilled water at 20°C with CO_2 injection.

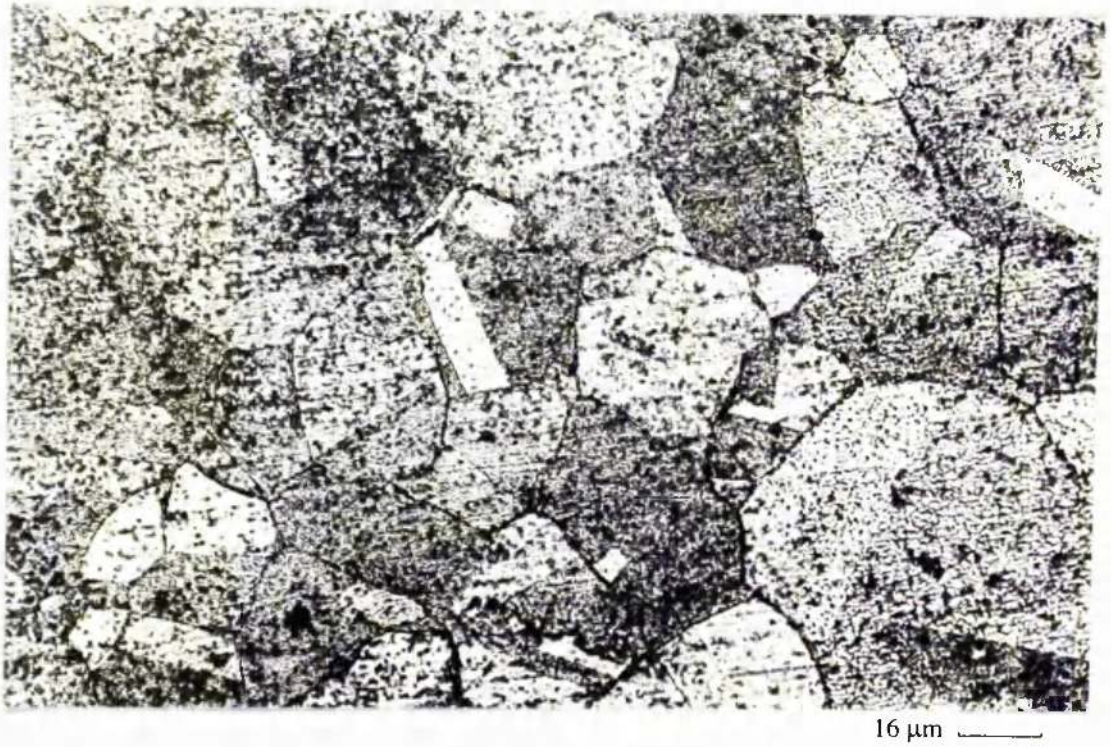

Figure 4.1.19b. At high magnification the surface shown in the previous photograph is full of tiny particles.

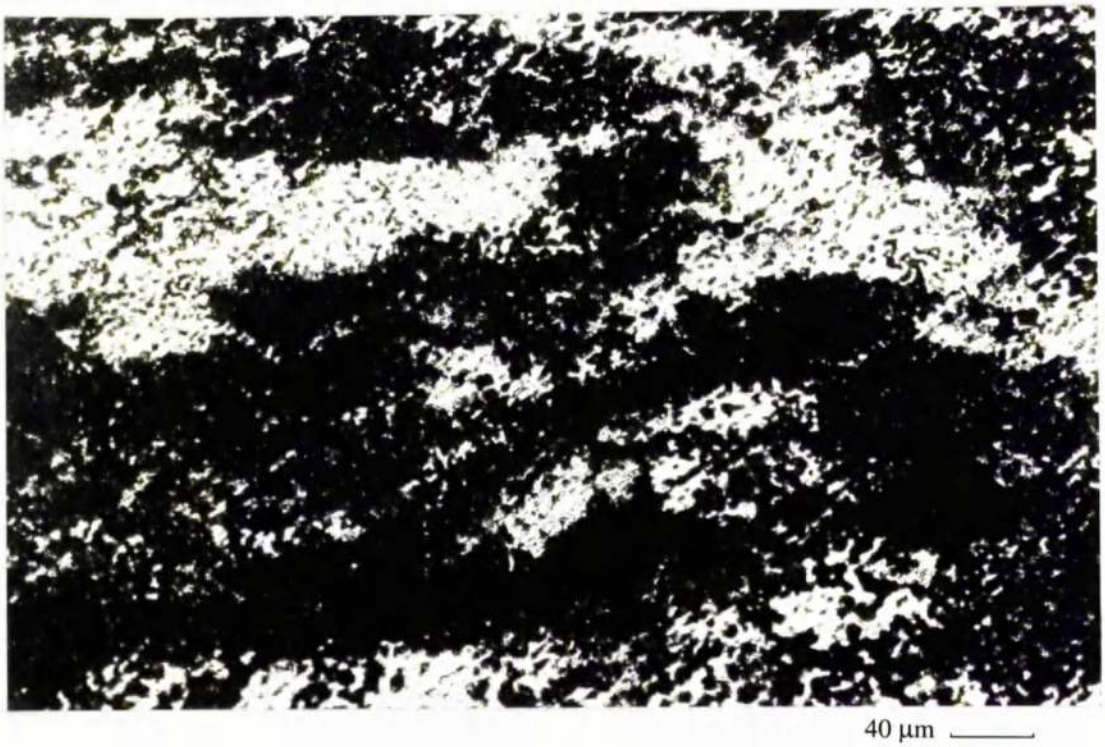

Figure 4.1.20a. General corrosion on Cu-10%Ni when anodically polarised in distilled water at 50^0C with CO_2 injection.

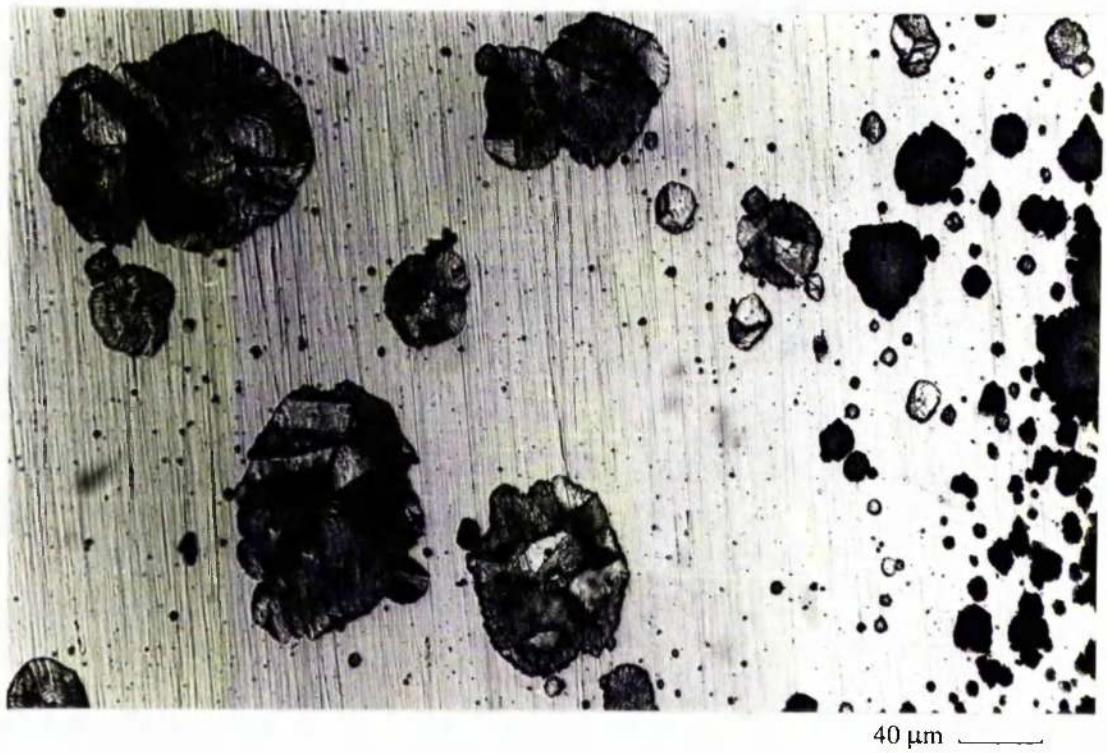

Figure 4.1.20b. Regions of revealed metal grain structure with minor pitting on Cu-10%Ni when anodically polarised in distilled water at 50^0C with CO_2 injection.

4.2. Cu-30%Ni

4.2.1. Tests in seawater at 20°C

Figures 4.2.1a and 4.2.1b show the anodic polarisation curves generated from tests in artificial seawater at 20°C. The values of E_{corr} were all in the range -217 mV to -230 mV. It is possible that some of the variations in the anodic polarisation curves around E_{corr} were associated with differences in the residual cathodic reaction as a result of small variations in the dissolved oxygen content. However, the main feature of these curves is that Cu-30%Ni is active in seawater. It was also noted that in the case when specimens were exposed to seawater for 2 days before being polarised, the polarisation curve was slightly steeper over the initial 100 mV of potential shift in comparison to the immediate tests. However, after 7 days in seawater the polarisation curve was less steep. These trends provide an indication that the tendency to the formation of a protective film is not systematic in the early days of exposure. No change in the pH of the solution was observed after the anodic polarisations had taken place.

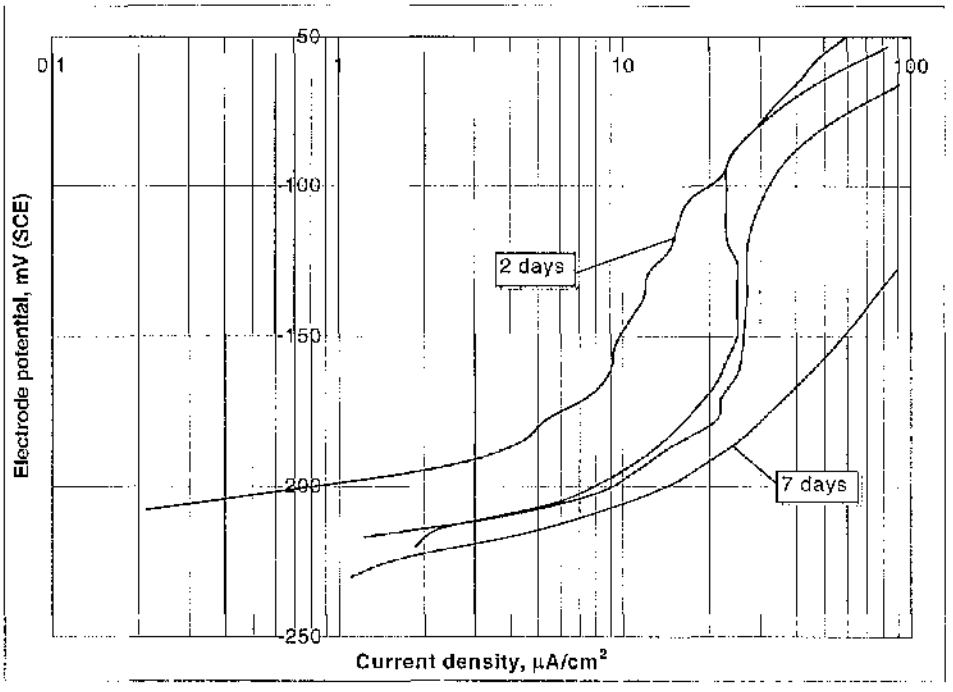

Figure 4.2.1a. Anodic polarisation tests of Cu-30%Ni in artificial seawater at 20°C after 1 hour immersion except where stated.

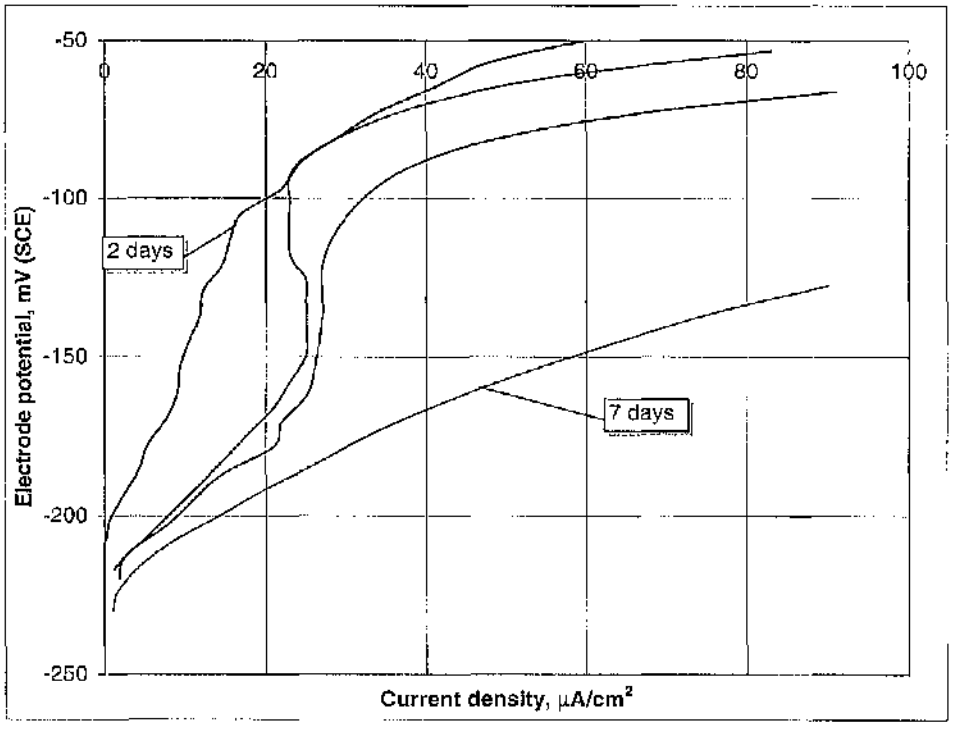

Figure 4.2.1b. Anodic polarisation tests of Cu-30%Ni in artificial seawater at 20°C after 1 hour immersion except where stated.

4.2.2. Tests in distilled water at 20°C

Figure 4.2.2a shows the anodic polarisation curves generated in distilled water at 20°C in comparison with those in seawater at 20°C. There was a large difference in the values of E_{corr} between the two environments; between -45 mV to -126 mV for distilled water and in the range -217 mV to -230 mV for seawater. Clearly the corrosion rate of Cu-30%Ni in relevance to the current density of the polarisation is much lower in distilled water than in seawater. There appeared to be no substantial changes in corrosion resistance in distilled water as a function of time. In all tests the conductivity of the solution was noticed to be relatively higher after the specimen had been anodically polarised and presumably that was caused by metal dissolution. The pH of the solution was also increased apparently due to the cathodic reaction of hydrogen evolution, $2H^+ + 2e^- \longrightarrow H_2$, during the polarisation experiment. This increase in pH and conductivity was not only observed over anodic polarisations. In the case of the 60 day period of exposure the solution was inspected and replaced by

fresh distilled water every 5 days. Both conductivity and pH were slightly increased after those 5 days seemingly for the same reasons mentioned above. Tables 4.2.1 and 4.2.2 show the conductivity and pH values respectively before and after polarisation tests.

The findings for Cu-30%Ni in distilled water at 20°C so far presented were conducted on cross sections of tube material (see section 3.1). To check that these findings were not unrepresentative of corrosion behaviour of the outside surface the tube, a few anodic polarisation experiments upon initial and 60-day exposure to distilled water at 20°C comprised small flattened segments (of 1 cm^2 area) of the tube. These tests yielded quite similar results (figure 4.2.2b) to the main series of anodic polarisation tests.

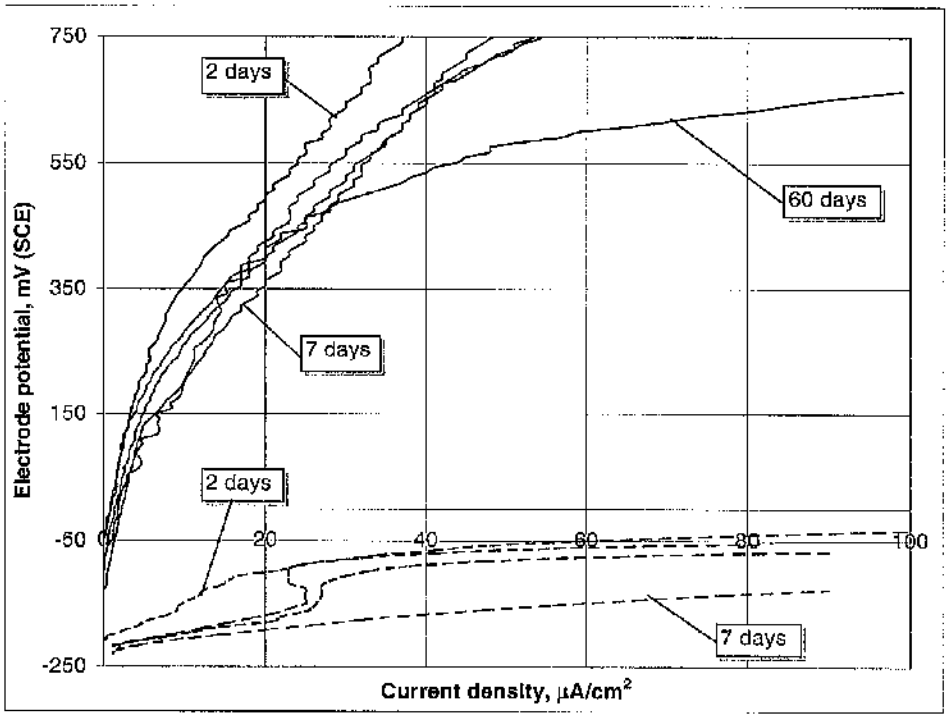

Figure 4.2.2a. Anodic polarisation curves of Cu-30%Ni in distilled water at 20°C in comparison to artificial seawater at 20°C after 1 hour of immersion except where stated. Dotted lines = seawater, full lines = distilled water.

	Before polarisation	After polarisation
Immediate test	5.3	16.3
Immediate test	6.1	18
Immediate test	2.6	10.4
Polarisation after 2 days of exposure	18.5	37.7
Polarisation after 7 days of exposure	13.7	26.1
Polarisation after 60 days of exposure	16.85	35.6

Table 4.2.1. Conductivity values before and after polarisation tests of Cu-30%Ni in distilled water at 20°C (μS/cm).

	Before polarisation	After polarisation
Immediate test	5.34	6.12
Immediate test	5.17	5.95
Immediate test	5.28	6.15
Polarisation after 2 days of exposure	5.83	6.24
Polarisation after 7 days of exposure	6.24	6.74
Polarisation after 60 days of exposure	5.3	6.03

Table 4.2.2. pH values before and after polarisation tests of Cu-30%Ni in distilled water at 20°C (μS/cm).

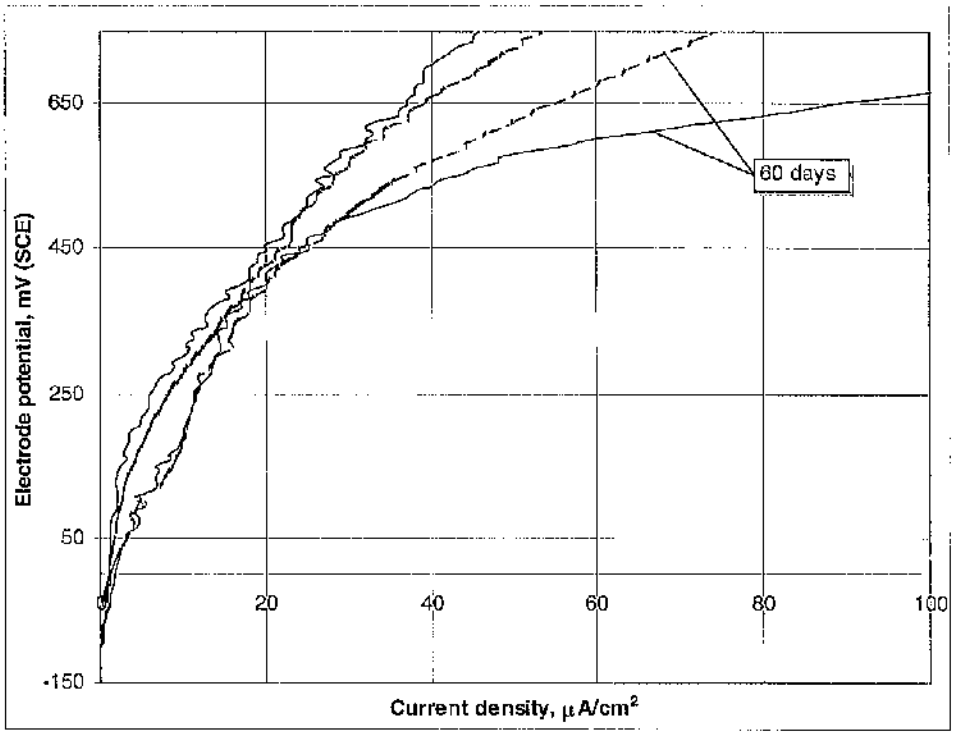

Figure 4.2.2b. Anodic polarisation curves of cross-section Cu-30%Ni specimens and outer surface Cu-30%Ni specimens in distilled water at 20°C after 1 hour of immersion except where stated. Dotted lines = outer surface specimens, full lines = cross-section specimens.

4.2.3. Tests in distilled water at 50°C

Figures 4.2.3a and 4.2.3b show the anodic polarisation curves generated upon initial exposure to distilled water at 50°C in comparison with those in distilled water at 20°C. The values of E_{corr} were all in the range -45 mV to -80 mV for both conditions. Evidently, the high temperature had a great effect on the corrosion behaviour of the alloy. As the curves indicate, the samples tested at 50°C exhibited much flatter polarisation curves implying higher corrosion rates than the ones tested in plain distilled water. Apparently the high temperature retarded the establishment of a protective film on the surface of the metal. Again both pH and conductivity of the solution were found to be significantly increased after the specimens had been polarised. Table 4.2.3. and Table 4.2.4. show the pH and conductivity values respectively before and after polarisation tests.

Before polarisation	After polarisation
2.96	43.6
1.75	31.7
1.52	35.5

Table 4.2.3. Conductivity values before and after polarisation tests of Cu-30%Ni after 1 hour of immersion in distilled water at 50°C (μS/cm).

Before polarisation	After polarisation
5.43	5.8
5.4	5.95
5.36	6.03

Table 4.2.4. pH values before and after polarisation tests of Cu-30%Ni after 1 hour of immersion in distilled water at 50°C.

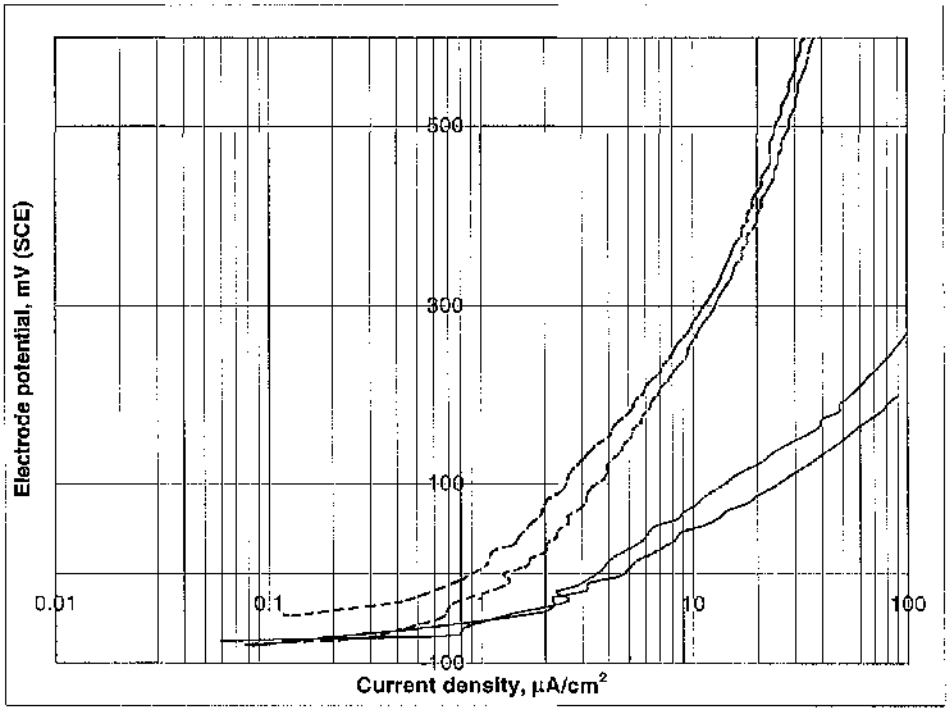

Figure 4.2.3a. Anodic polarisation curves of Cu-30%Ni after 1 hour of immersion in distilled water at 50°C in comparison to distilled water at 20°C. Dotted lines = 20°C, full lines = 50°C.

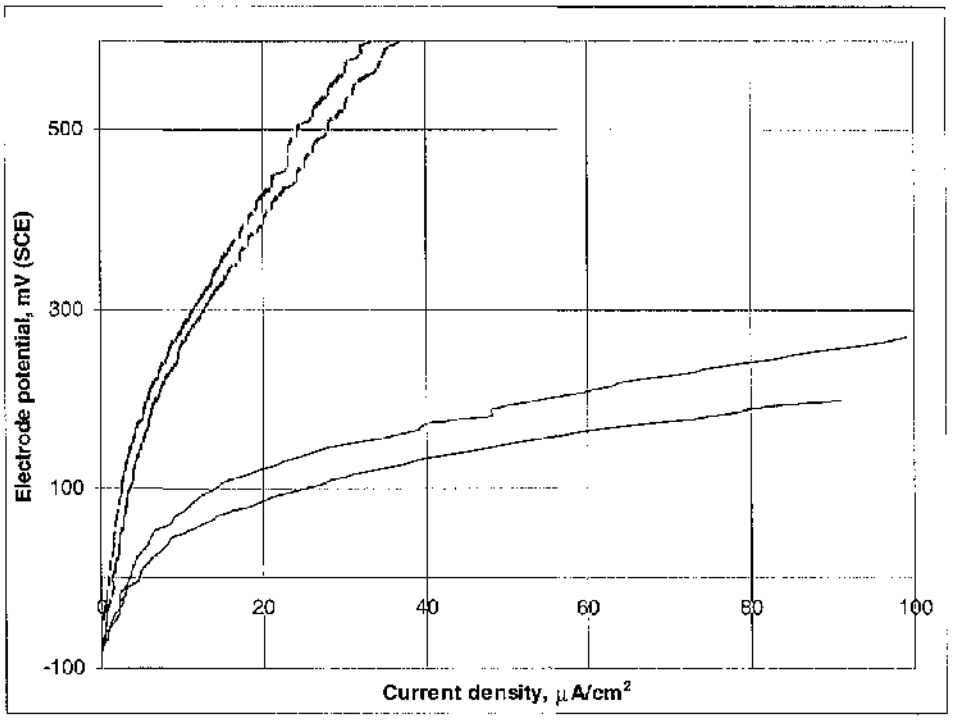

Figure 4.2.3b. Anodic polarisation curves of Cu-30%Ni after 1 hour of immersion in distilled water at 50°C in comparison to distilled water at 20°C. Dotted lines = 20°C, full lines = 50°C.

4.2.4. Tests in distilled water at 20°C with CO_2

Figures 4.2.4a and 4.2.4b show the anodic polarisation curves generated upon initial exposure to distilled water at 20°C with the injection of CO_2, in comparison to those in distilled water at 20°C. The values of E_{corr} were all in the range -45 mV to -79 mV for both conditions. Clearly, Cu-30%Ni exhibits very active behaviour when CO_2 is introduced in distilled water implying difficulties in establishing a protective film. As shown in tables 4.2.5 and 4.2.6, similar changes in conductivity and pH were noted as have been described earlier (see section 4.1.4) for Cu-10%Ni.

Before the addition of CO_2	After the addition of CO_2	After polarisation
2.91	32.5	50
2.8	31.5	47.7
3	31	49.7

Table 4.2.5. Conductivity values before and after the addition of CO_2, and after polarisation of Cu-30%Ni after 1 hour of immersion in distilled water at 20°C.

Before the addition of CO_2	After the addition of CO_2	After polarisation
5	4.02	3.98
4.98	4.03	3.98
4.98	4.02	3.98

Table 4.2.6. pH values before and after the addition of CO_2, and after polarisation of Cu-30%Ni after 1 hour of immersion in distilled water at 20°C.

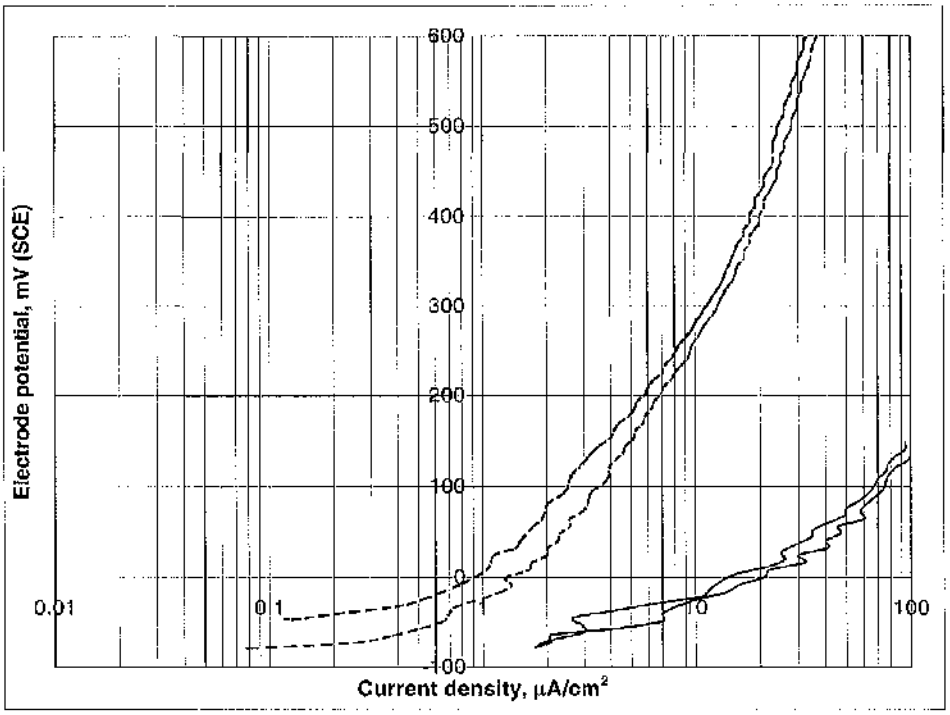

Figure 4.2.4a. Anodic polarisation curves of Cu-30%Ni after 1 hour of immersion in distilled water at 20°C with injected CO_2, in comparison to distilled water at 20°C. Dotted lines = 20°C, full lines = 20°C + CO_2.

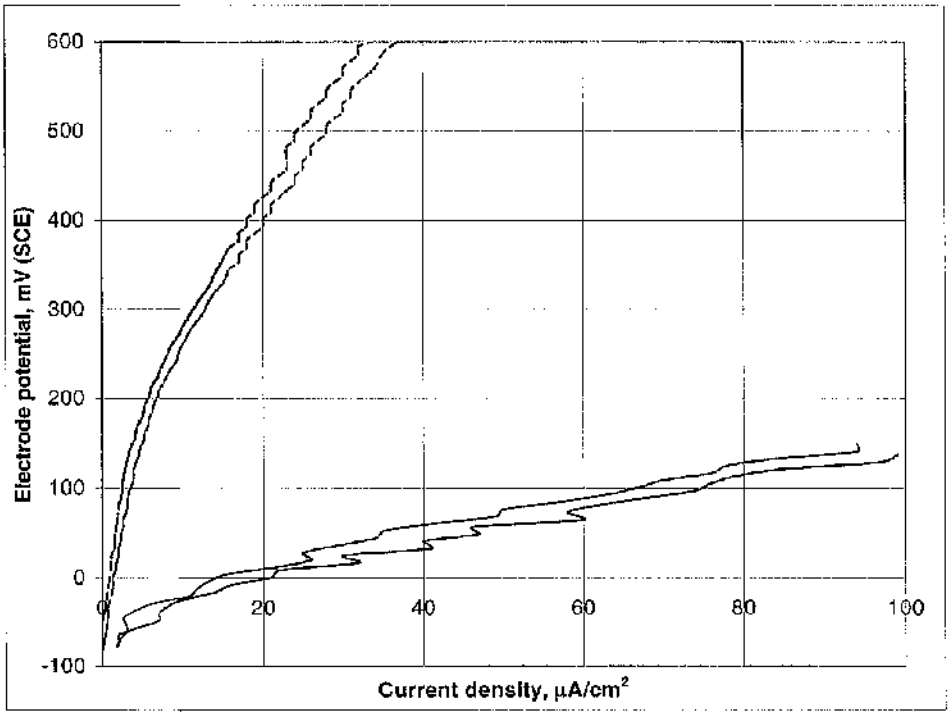

Figure 4.2.4b. Anodic polarisation curves of Cu-30%Ni after 1 hour of immersion in distilled water at 20°C with injected CO_2, in comparison to distilled water at 20°C. Dotted lines = 20°C, full lines = 20°C + CO_2.

4.2.5. Tests in distilled water at 50°C with CO_2

Figures 4.2.5a and 4.2.5b show the anodic polarisation curves generated in distilled water at 50°C with the injection of CO_2, in comparison to those in distilled water at 50°C. The values of E_{corr} were all in the range -74 mV to -83 mV for both conditions. Evidently, the injection of CO_2 in distilled water at 50°C reduced the corrosion resistance of Cu-30%Ni. The corrosion rate of the alloy is higher in distilled water at 50°C with CO_2 than without CO_2 which indicates that the implication of CO_2 at 50°C has an increased deleterious effect on the protective film of Cu-30%Ni since 50°C is already shown to reduce the corrosion resistance of the alloy (see section 4.2.3). Both conductivity and pH behaved the same way as reported in section 4.2.4. Table 4.2.7. shows the conductivity values of the distilled water at 50°C before and after the addition of CO_2, and after polarisation and Table 4.2.8. shows the pH values of the same states.

Before the addition of CO_2	After the addition of CO_2	After polarisation
3.1	33.4	40.5
2.8	32	38
2.3	31.4	44.7

Table 4.2.7. Conductivity values before and after the addition of CO_2, and after polarisation of Cu-30%Ni after 1 hour of immersion in distilled water at 50°C.

Before the addition of CO_2	After the addition of CO_2	After polarisation
4.9	4.07	3.9
5	4	3.95
5	3.95	3.85

Table 4.2.8. pH values before and after the addition of CO_2, and after polarisation of Cu-30%Ni after 1 hour of immersion in distilled water at 50°C.

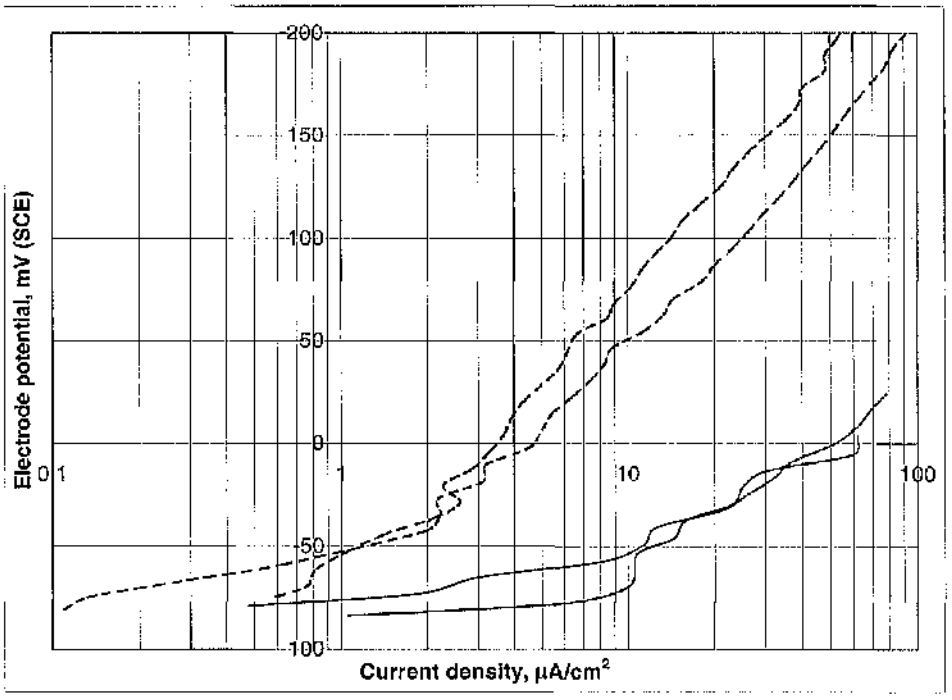

Figure 4.2.5a. Anodic polarisation curves of Cu-30%Ni after 1 hour of immersion in distilled water at 50°C with injected CO_2, in comparison to distilled water at 50°C. Dotted lines = 50°C, full lines = 50°C + CO_2.

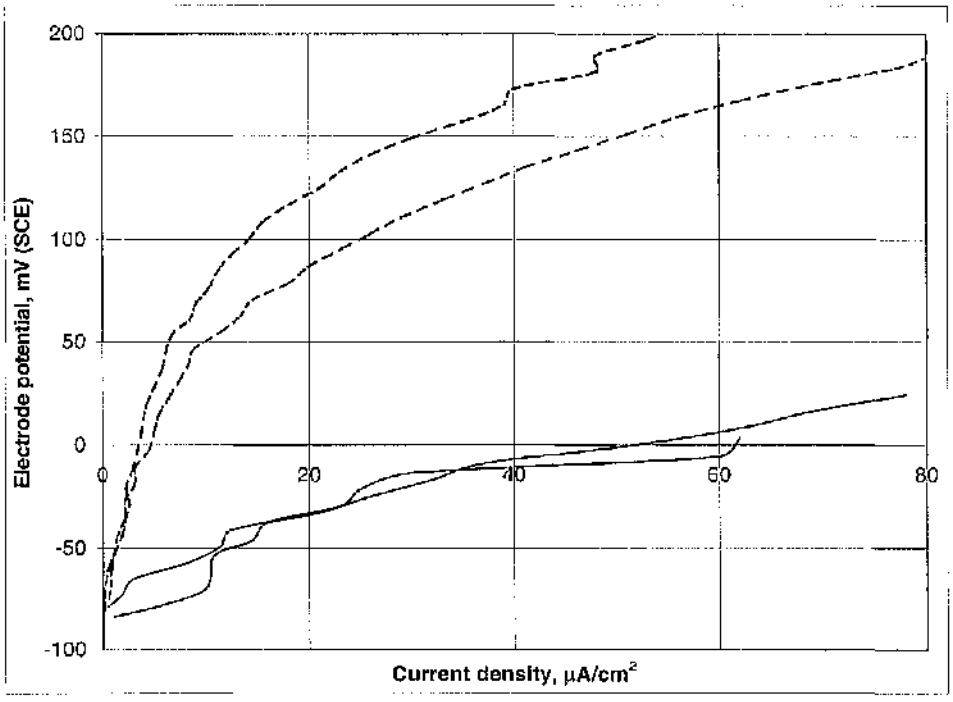

Figure 4.2.5b. Anodic polarisation curves of Cu-30%Ni after 1 hour of immersion in distilled water at 50°C with injected CO_2, in comparison to distilled water at 50°C. Dotted lines = 50°C, full lines = 50°C + CO_2.

4.2.6. Microscopy

Tests in seawater at 20°C

A generally thinly-filmed surface also containing patches of thicker corrosion products and pitting attack were the main features for Cu-30%Ni when anodically polarised immediately after initial exposure to seawater at 20°C. As figure 4.2.6a shows, numerous small shallow pits were over the whole metal matrix and were even more evident at high magnification (figure 4.2.6b). In the case when Cu-30%Ni was left exposed to seawater for 2 days without polarisation, light general corrosion in a light brown colour covered almost 100% of the specimen's surface (figure 4.2.7a). At high magnification (figure 4.2.7b) general corrosion seems to be uniform on the metal matrix implying a corrosion product layer being formed over the 2-day period. As shown in figure 4.2.8a, the specimen after polarisation suffered general corrosion in the same way but slightly more severe in relation to the one before polarisation. Again it was noted that the surface was covered uniformly by the corrosion products (figure 4.2.8b).

When samples of Cu-30%Ni were left in seawater for 7 days, general corrosion including dark regions covered the entire surface. Crevice corrosion was also noted round the inside edge of the specimen (figure 4.2.9a). At high magnification (figure 4.2.9b) the presence of numerous small shallow pits was quite clear. It appears that small pits progressively join together to form dark regions of general corrosion especially at the crevice. When polarisation took place after 7 days the main features of damage remained the same (figure 4.2.10). The corrosion damage on the surface of Cu-30%Ni when anodically polarised after 7 days immersion in seawater at 20°C is clearly greater than in the case when the alloy was anodically polarised after 2 days immersion and also polarised upon initial exposure. This is consistent with the higher corrosion rate that the alloy exhibited when it was anodically polarised after 7 day exposure in seawater in comparison to immediate and after 2 days polarisations (see figures 4.2.1a and 4.2.1b).

Tests in distilled water at 20°C

As shown in figures 4.2.11a and 4.2.11b, a thin surface film together with thicker patches of corrosion products and shallow pits were the main features for Cu-30%Ni when anodically polarised immediately after initial exposure to distilled water at 20°C. In the case when Cu-30%Ni was left exposed to distilled water for 2 days without polarisation, slight general corrosion was the only sign of damage observed on the surface (figure 4.2.12a). The corrosion was noted to be more intense on the inside edge of the specimen and as shown in figure 4.2.12b it consisted of particles all lined-up in a wavy arrangement. This kind of behaviour could be attributed to the metallurgy and manufacturing procedures of the tube. However when the specimen was anodically polarised, the surface suffered intense pitting attack. As shown in figure 4.2.13a, numerous small pits were over most of the surface leaving the rest of the metal matrix slightly discoloured by a thin layer of general corrosion. Larger pits were also present at several points on the surface (figure 4.2.13b).

When samples of Cu-30%Ni were exposed to distilled water for 7 days, general corrosion appeared to be significantly darker in comparison to the one after 2 days in distilled water. Small shallow pits at a few points were also included on the metal matrix implying initiation of pitting attack (figures 4.2.14a and 4.2.14b). As shown in figure 4.2.15a, the damage became much worse after the specimen had been polarised. Black general corrosion covered most of the surface and pitting attack became quite severe. At points where the surface was not covered by black general corrosion, numerous pits were evident and the metal matrix was full of tiny particles (figure 4.2.15b).

In the case when Cu-30%Ni was left exposed to distilled water for 60 days without polarisation, pitting was extended over the whole surface and the main surface was covered by uniform general corrosion in a dark brown colour (figures 4.2.16a and 4.2.16b). After polarisation pitting progressed to a much greater extent causing severe damage to the surface (figures 4.2.17a and 4.2.17b).

As already mentioned in section 4.2.2, anodic polarisation tests upon initial exposure to distilled water at 20°C were also carried out on the outer surface of Cu-30%Ni tube. Rectangular samples of $1cm^2$ were cut off the tube and then flattened by cold working. General corrosion and pitting were the main features for a specimen of outer surface when anodically polarised immediately after initial exposure to distilled water at 20°C. General corrosion consisted of black regions surrounded by numerous pits of various sizes. The rest of the metal matrix remained clean and bright (figure 4.2.18a). At a few points where general corrosion was not so intense, the grain structure was clear indicating selective attack at the grain boundaries (figure 4.2.18b). As previously described in this section, similar features were exhibited by cross section specimens tested under the same conditions (see figures 4.2.11a and 4.2.11b). In the case when specimen of outer surface was exposed to distilled water for 60 days, a thin layer of general corrosion covered evenly the entire surface (figure 4.2.19). No pitting corrosion was developed in contrast to the cross section specimen immersed in distilled water for 60 days (see figures 4.2.16a and 4.2.16b). When the specimen was anodically polarised pitting corrosion appeared over the entire surface (figure 4.2.20a). Under the same conditions, a cross section specimen exhibited the same corrosion damage but to a much greater extent (see figures 4.2.17a and 4.2.17b). As shown in figure 4.2.20b, pits were noted to be noticeably deep. However the existence of particles like the ones before polarisation was not evident any more presumably because general corrosion was now slightly thicker.

Tests in distilled water in other conditions

Tests in distilled water at 50^0C

The corrosion damage on Cu-30%Ni specimens that had been anodically polarised in this environment consisted of large regions of general corrosion with selective attack at the grain boundaries ("etched" surface) and minor pitting attack which consisted of tiny shallow pits scattered over the entire surface. Figure 4.2.21a shows region of general corrosion with "etched" surface surrounded by minor pitting and figure 4.2.21b shows at high magnification a region of "etched" surface including numerous small pits

Tests in distilled water at 20^0C with CO_2

A light general corrosion product film and shallow pitting were the main features for Cu-30%Ni when anodically polarised in distilled water at 50^0C with CO_2 (figure 4.2.22a). High magnification revealed the metal grain structure beneath the thin film (figure 4.2.22b).

Tests in distilled water at 50^0C with CO_2

In the case when Cu-30%Ni was anodically polarised at 50^0C in distilled water with CO_2 injection, a uniform thin layer of corrosion covered all of the surface in a light to dark brown colour (figure 4.2.23a) but the active anodic polarisation behaviour (figures 4.2.5a and 4.2.5b) demonstrates that this corrosion product was not providing a high degree of protection. High magnification (figure 4.2.23b) did not show evidence of any other kind of damage (e.g. pitting).

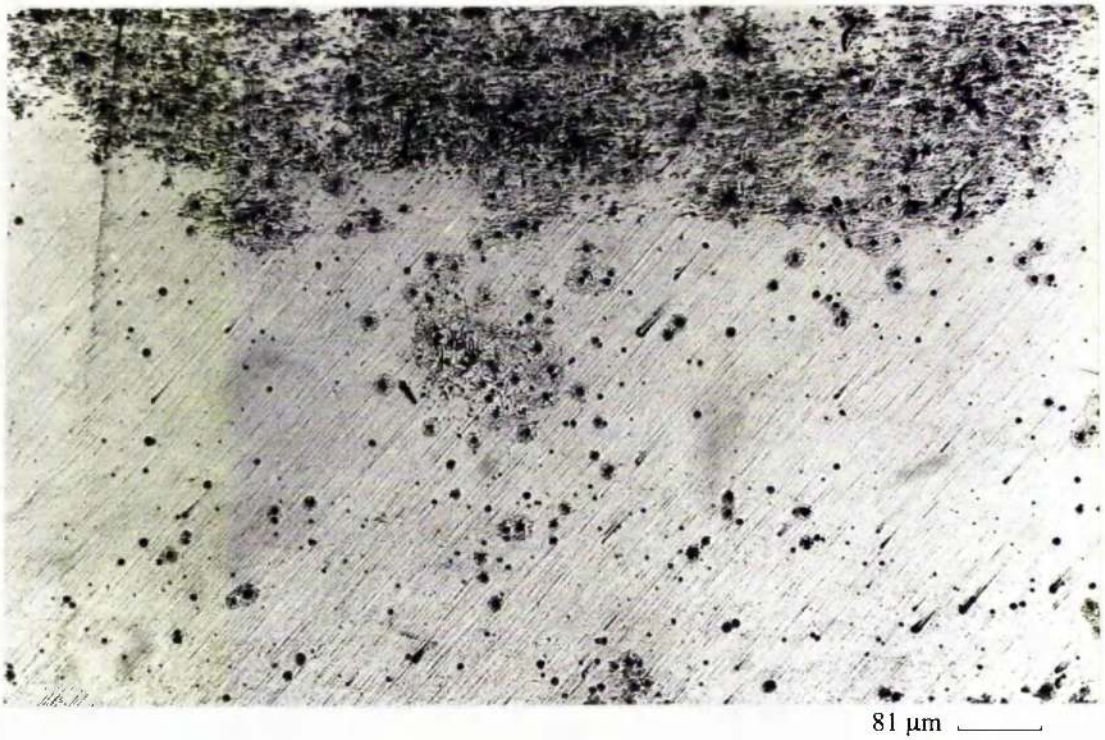

Figure 4.2.6a. Thin film and patches of thicker corrosion products and pitting attack on Cu-30%Ni when anodically polarised after initial exposure to seawater at 20°C.

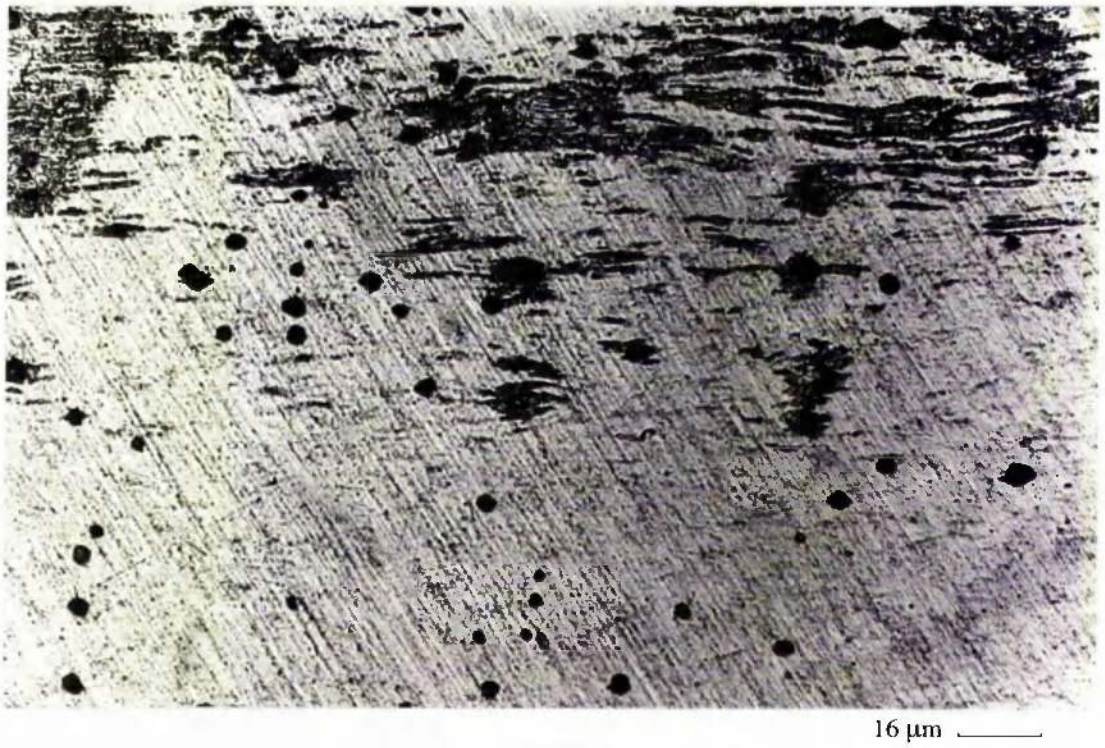

Figure 4.2.6b. High magnification reveals tiny particles over the entire surface of Cu-30%Ni when anodically polarised after initial exposure to seawater at 20°C.

Figure 4.2.7a. General corrosion on Cu-30%Ni after 2 day exposure in seawater at 20°C.

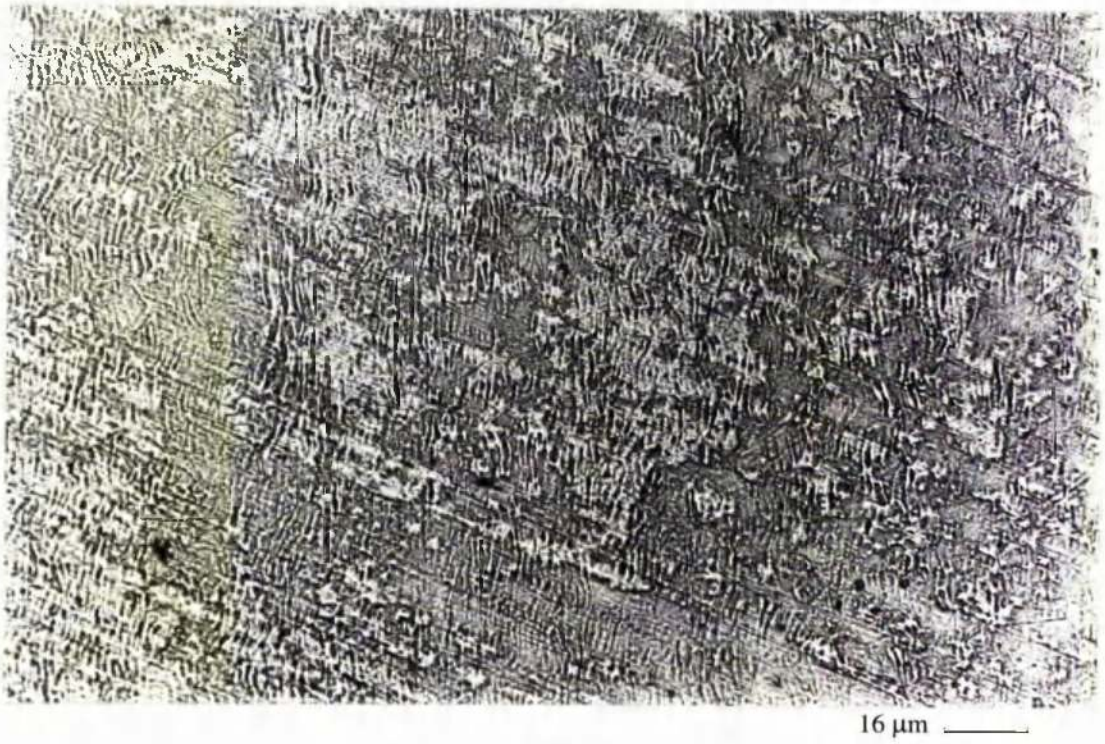

Figure 4.2.7b. At high magnification general corrosion is noted to be uniform on Cu-30%Ni after 2 day exposure in seawater at 20°C.

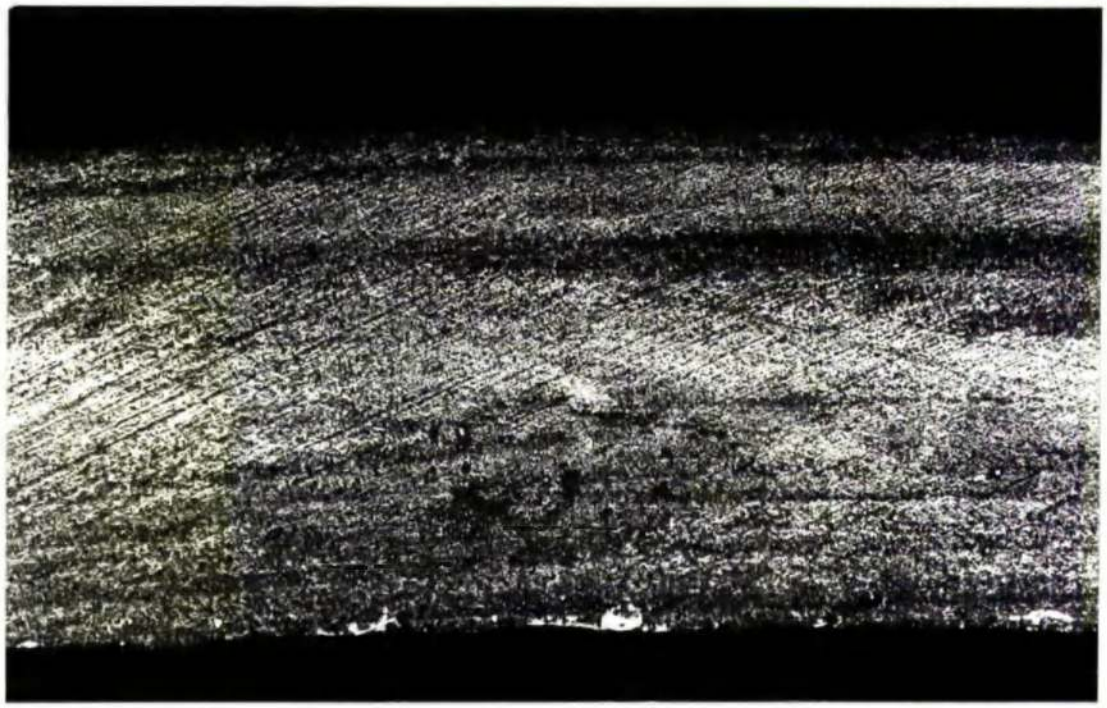

Figure 4.2.8a. General corrosion on Cu-30%Ni when anodically polarised after 2 day exposure in seawater at 20°C.

Figure 4.2.8b. High magnification shows general corrosion to be uniform on Cu-30%Ni when anodically polarised after 2 day exposure in seawater at 20°C.

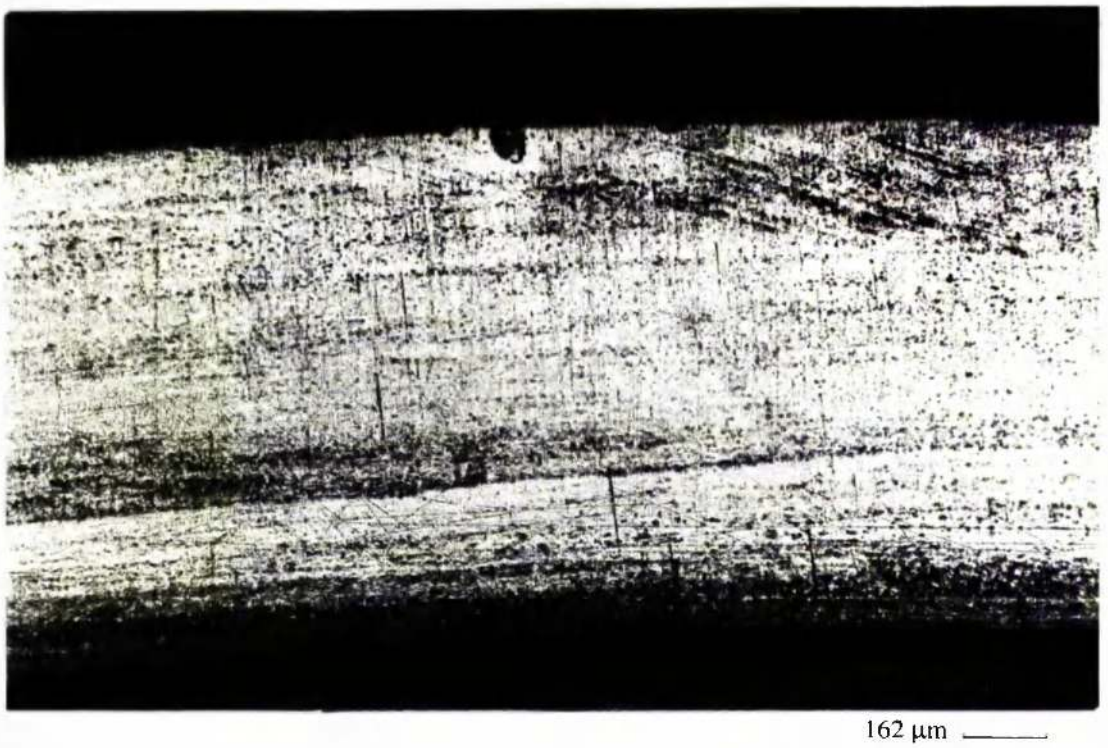

Figure 4.2.9a. General attack and crevice corrosion on Cu-30%Ni after 7 day exposure in seawater at 20°C.

Figure 4.2.9b. Pitting attack on Cu-30%Ni after 7 day exposure in seawater at 20°C.

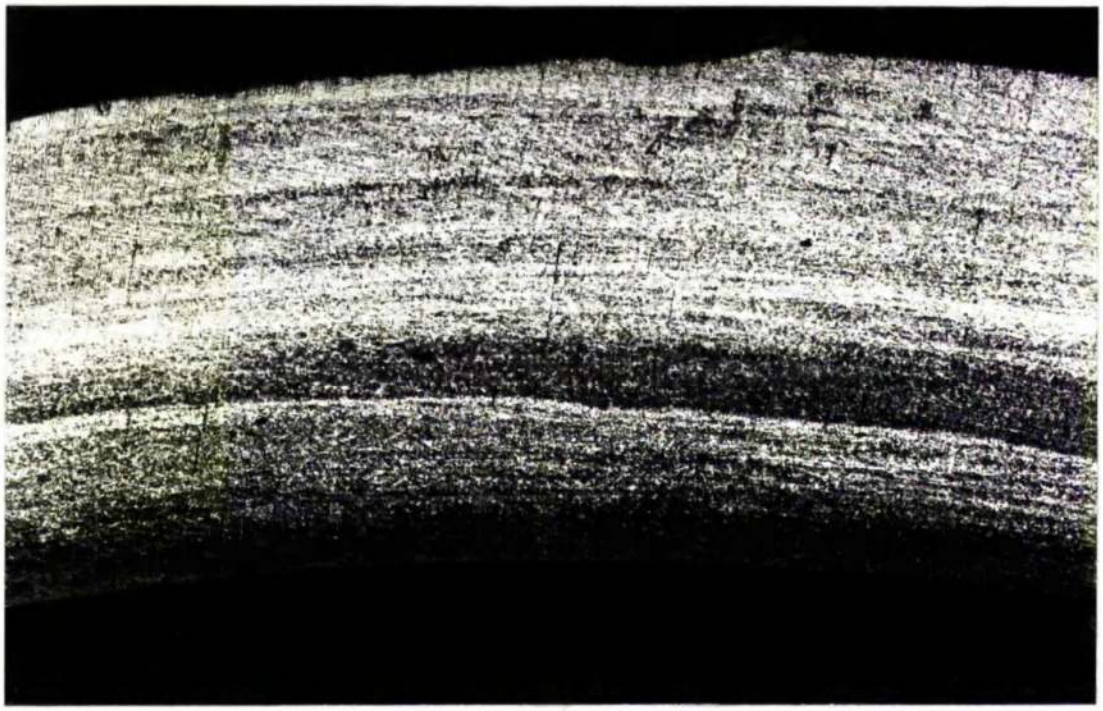

Figure 4.2.10. General attack and crevice corrosion on Cu-30%Ni when anodically polarised after 7 day exposure in seawater at 20°C.

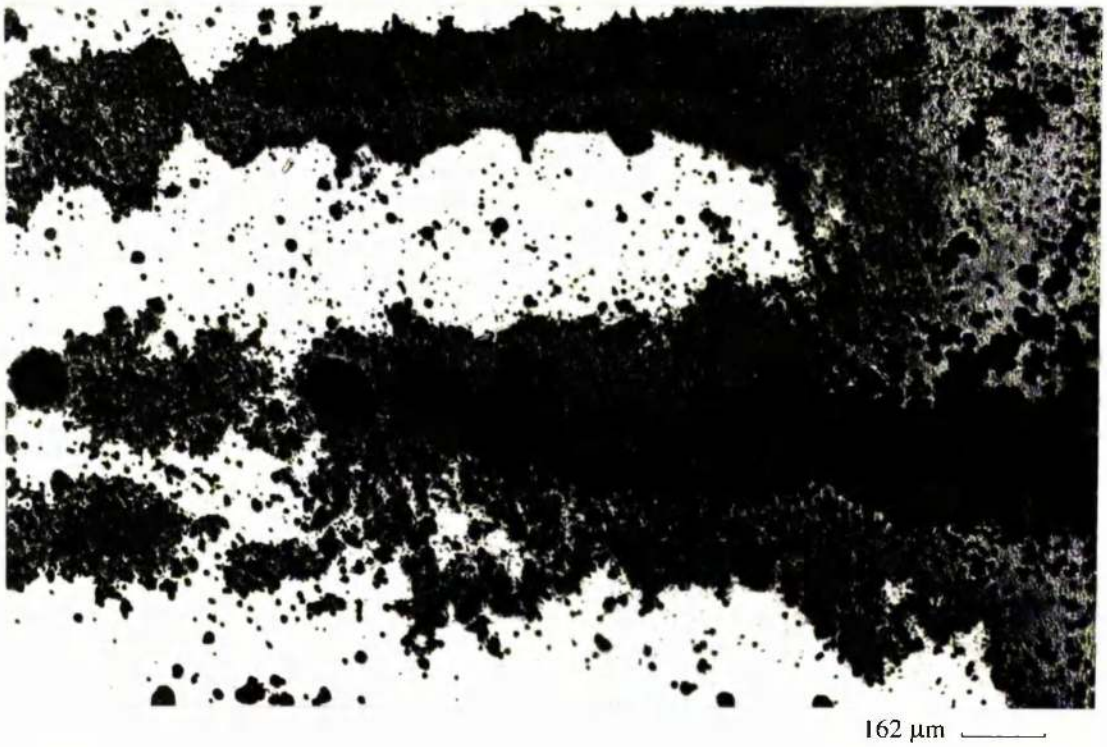

Figure 4.2.11a. Cu-30%Ni after anodic polarisation upon initial exposure to distilled water at 20°C.

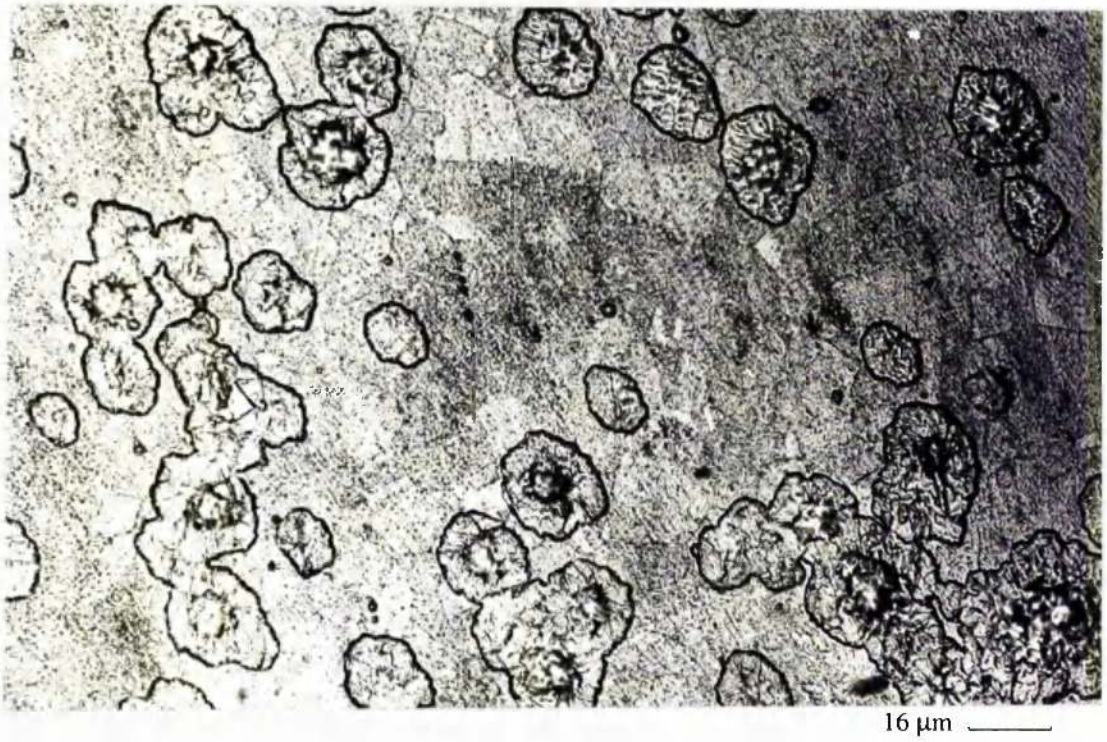

Figure 4.2.11b. High magnification reveals shallow pitting on Cu-30%Ni when anodically polarised after initial exposure to distilled water at 20°C.

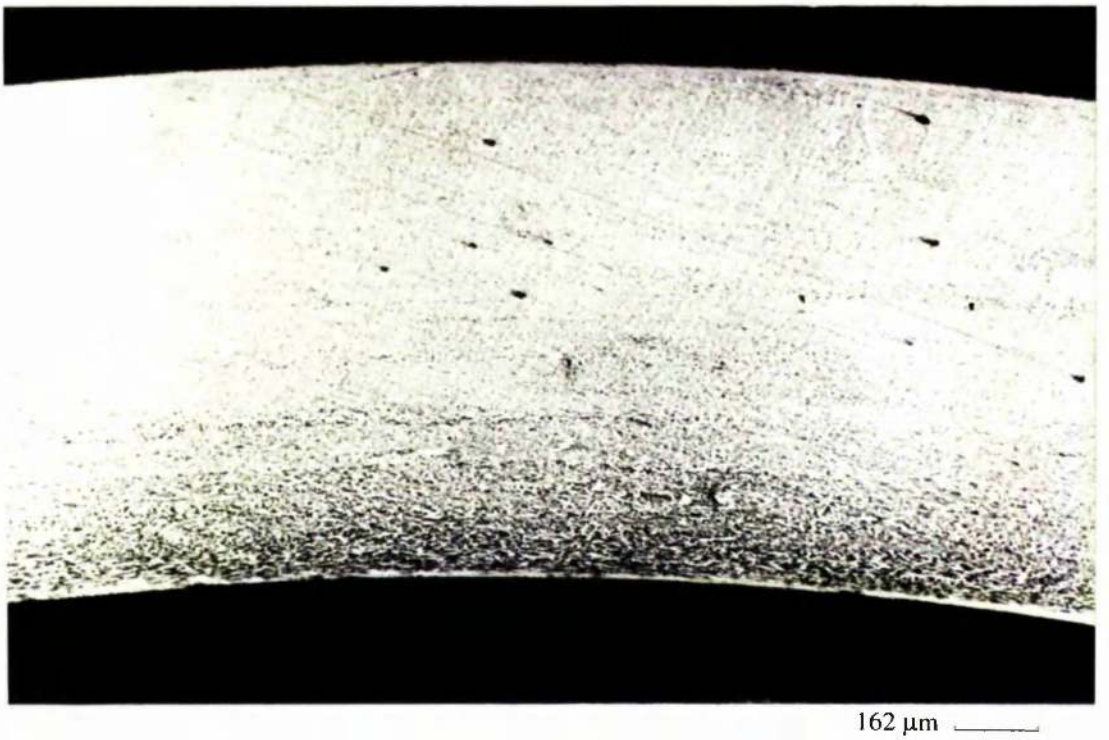

Figure 4.2.12a. Light general corrosion on Cu-30%Ni after 2 day exposure in distilled water at 20°C.

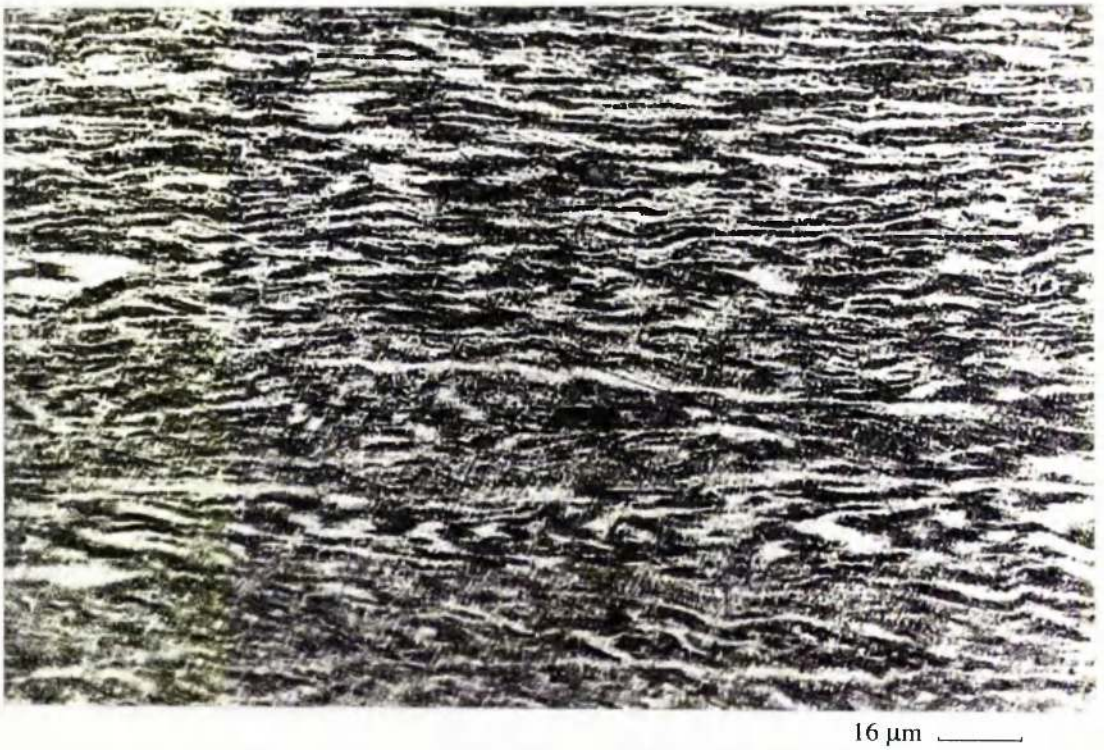

Figure 4.2.12b. Formation of particles noted on the inside edge of Cu-30%Ni after 2 day exposure in distilled water at 20°C.

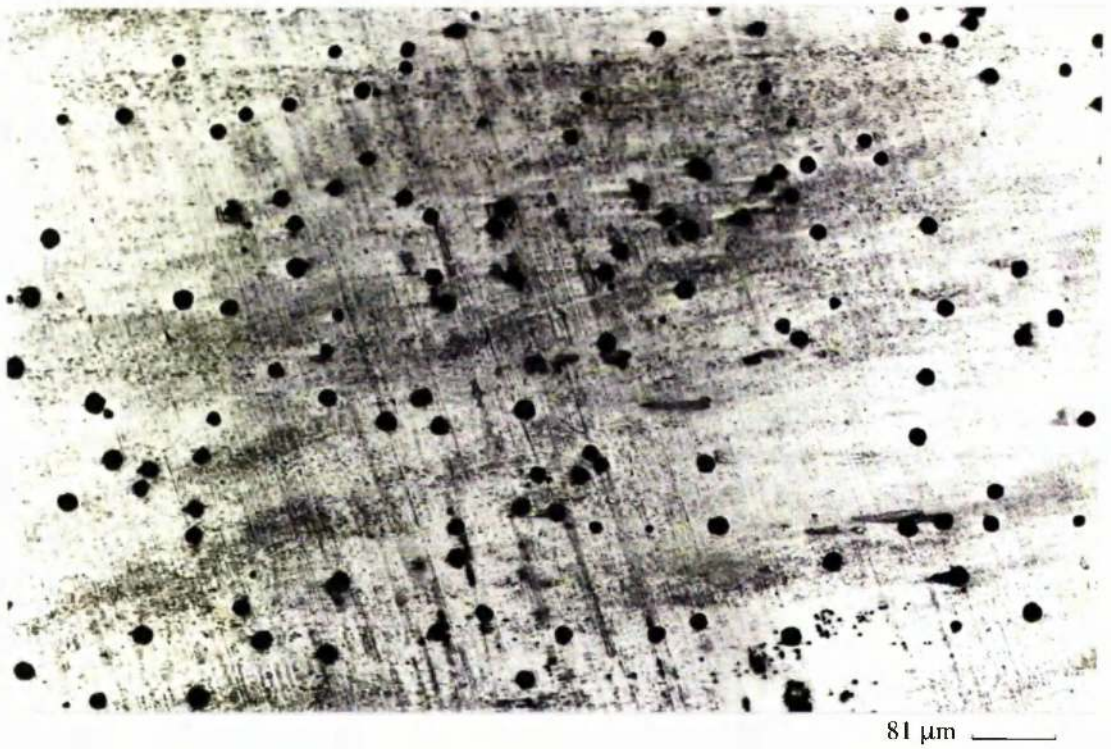

Figure 4.2.13a. Pitting corrosion on Cu-30%Ni when anodically polarised after 2 day exposure in distilled water at 20°C.

Figure 4.2.13b. Large pits were also present on Cu-30%Ni when anodically polarised after 2 day exposure in distilled water at 20°C.

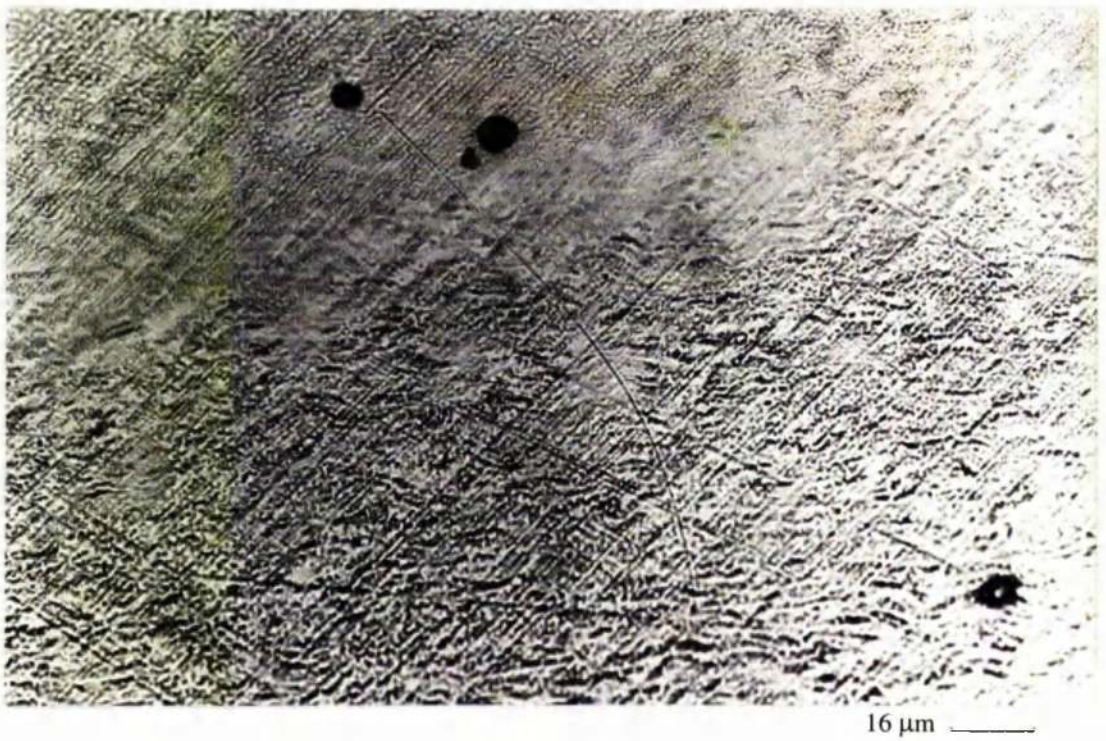

Figure 4.2.14a. General corrosion and few small pits on Cu-30%Ni after 7 day exposure in distilled water at 20°C.

Figure 4.2.14b. Group of numerous shallow pits attack on Cu-30%Ni after 7 day exposure in distilled water at 20°C.

Figure 4.2.15a. Severe pitting attack and dark general corrosion on Cu-30%Ni when anodically polarised after 7 day exposure in distilled water at 20°C.

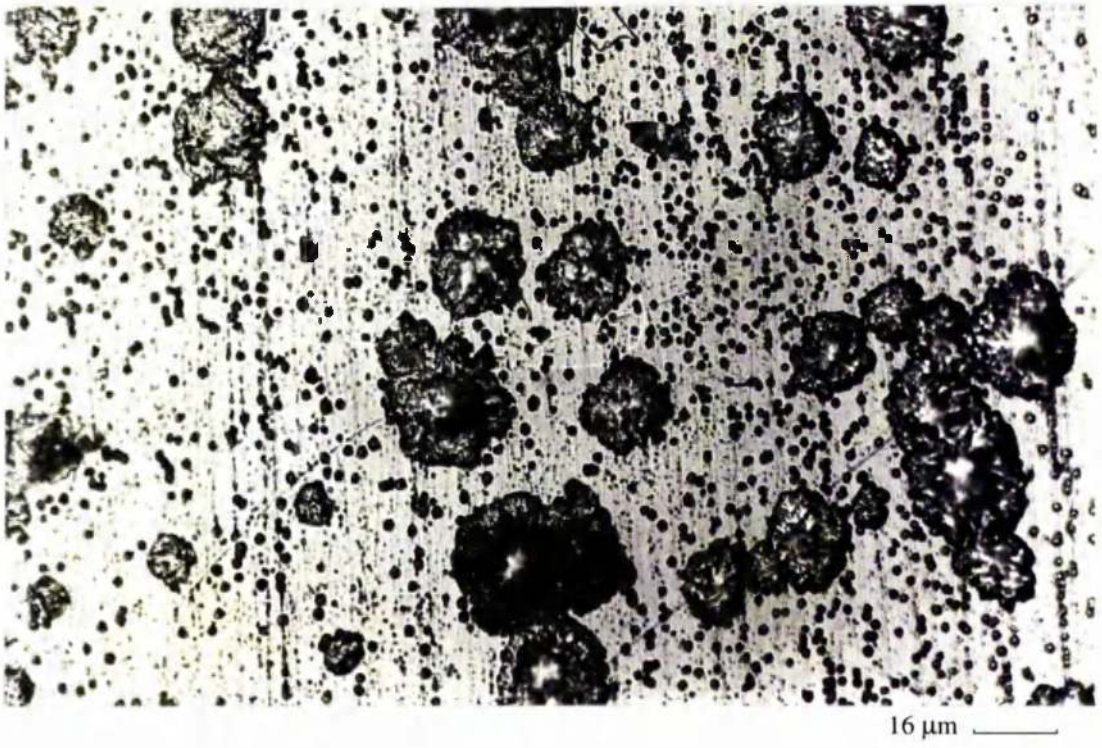

Figure 4.2.15b. Pitting corrosion and numerous tiny particles on Cu-30%Ni when anodically polarised after 7 day exposure in distilled water at 20°C.

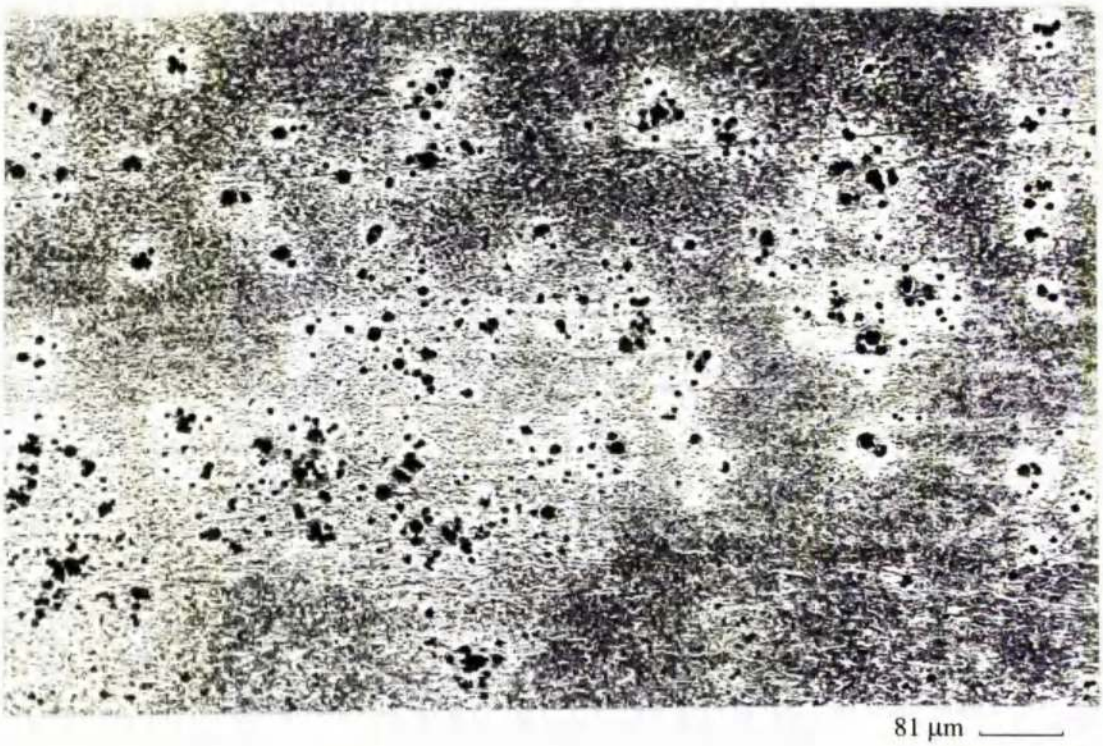

Figure 4.2.16a. Uniform general corrosion and pitting attack on Cu-30%Ni after 60 day exposure in distilled water at 20°C.

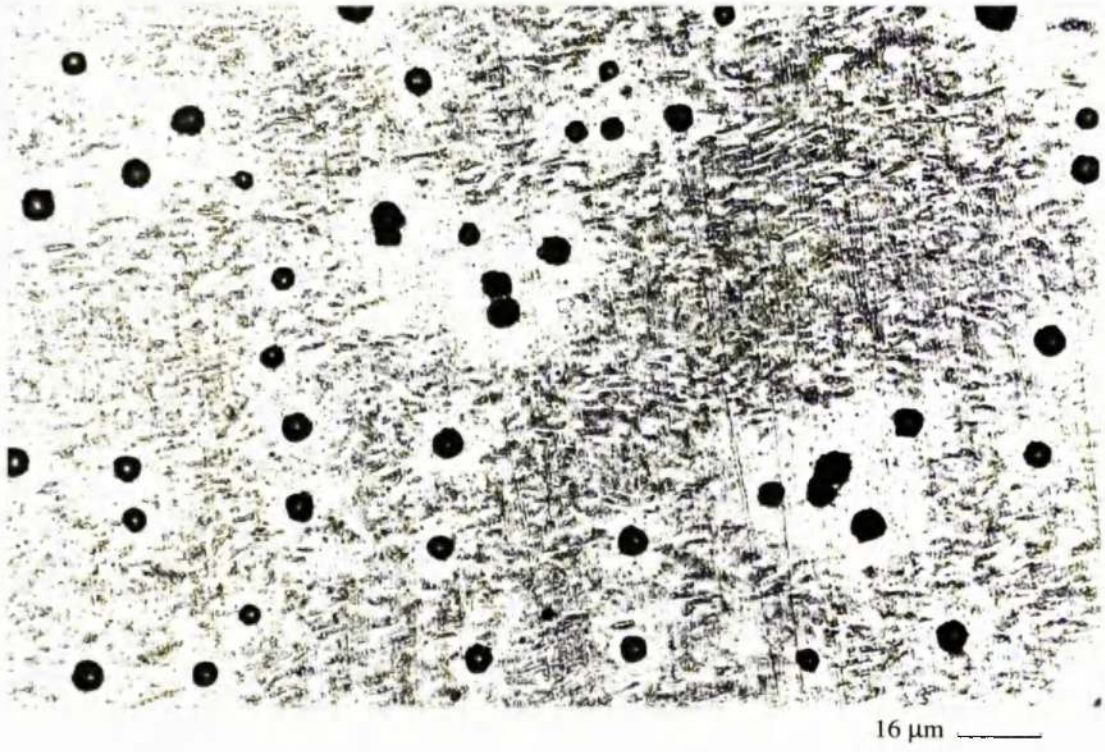

Figure 4.2.16b. Pits were noted to be rather deep on Cu-30%Ni after 60 day exposure in distilled water at 20°C.

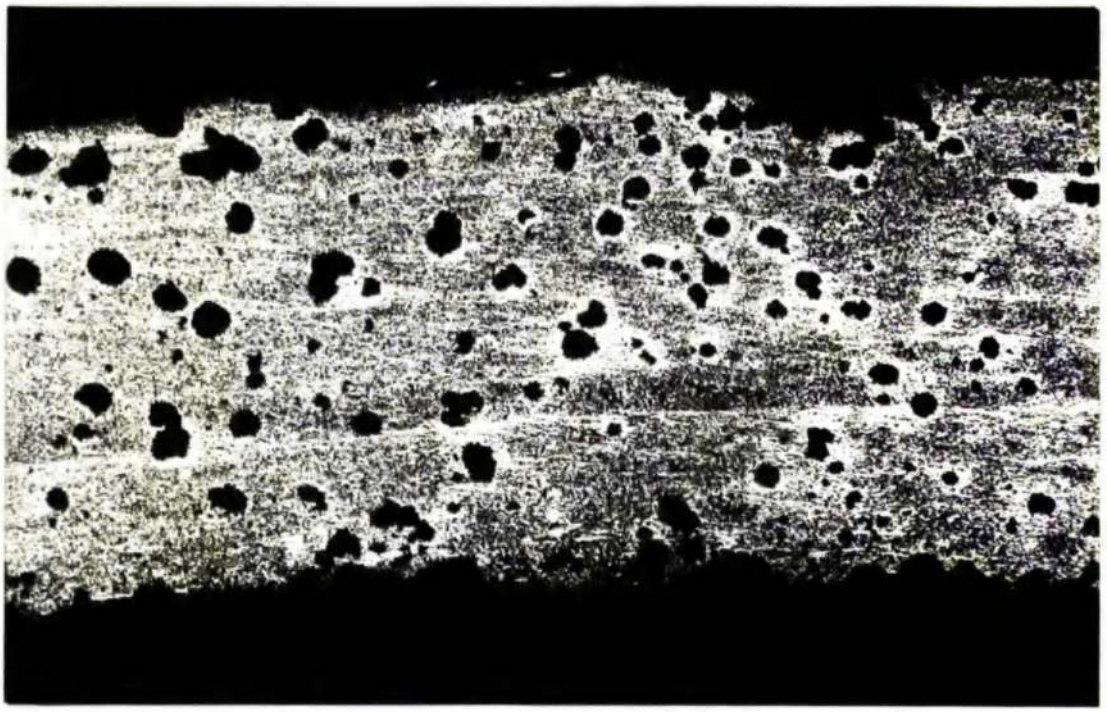

Figure 4.2.17a. Severe pitting attack and uniform general corrosion on Cu-30%Ni when anodically polarised after 60 day exposure in distilled water at 20°C.

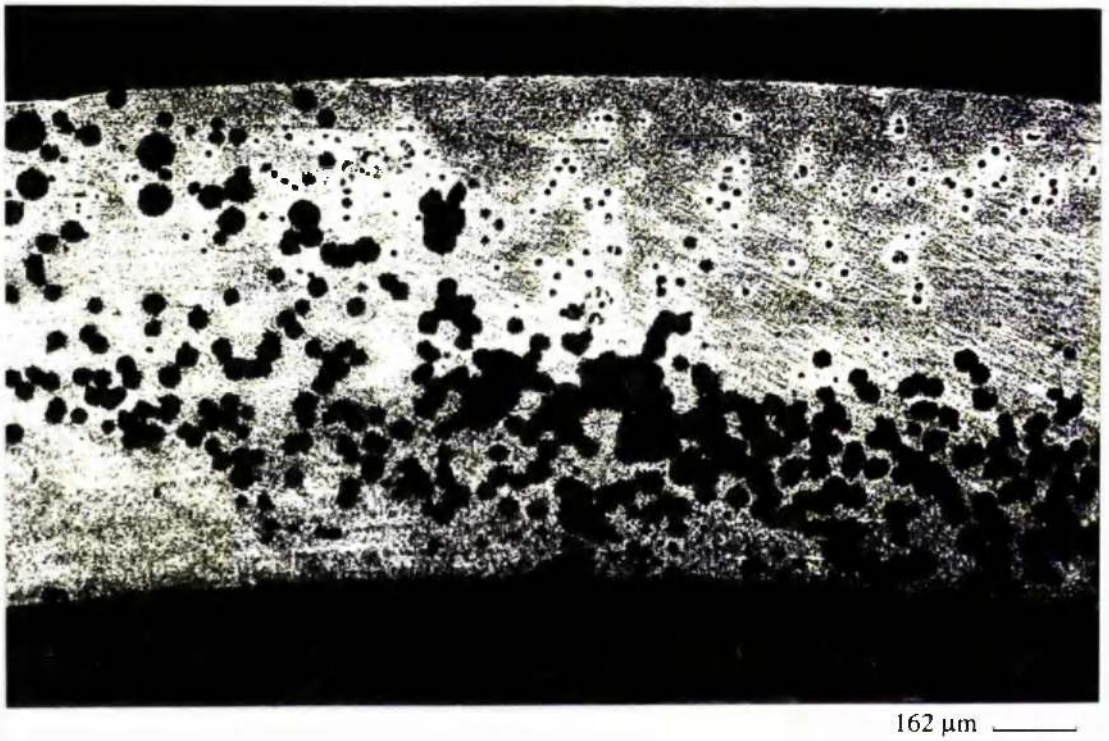

Figure 4.2.17b. Quite severe and extensive pitting attack on another part of the specimen shown in the previous figure.

Figure 4.2.18a. General corrosion and pitting on the outer surface of Cu-30%Ni when anodically polarised after initial exposure to distilled water at 20°C.

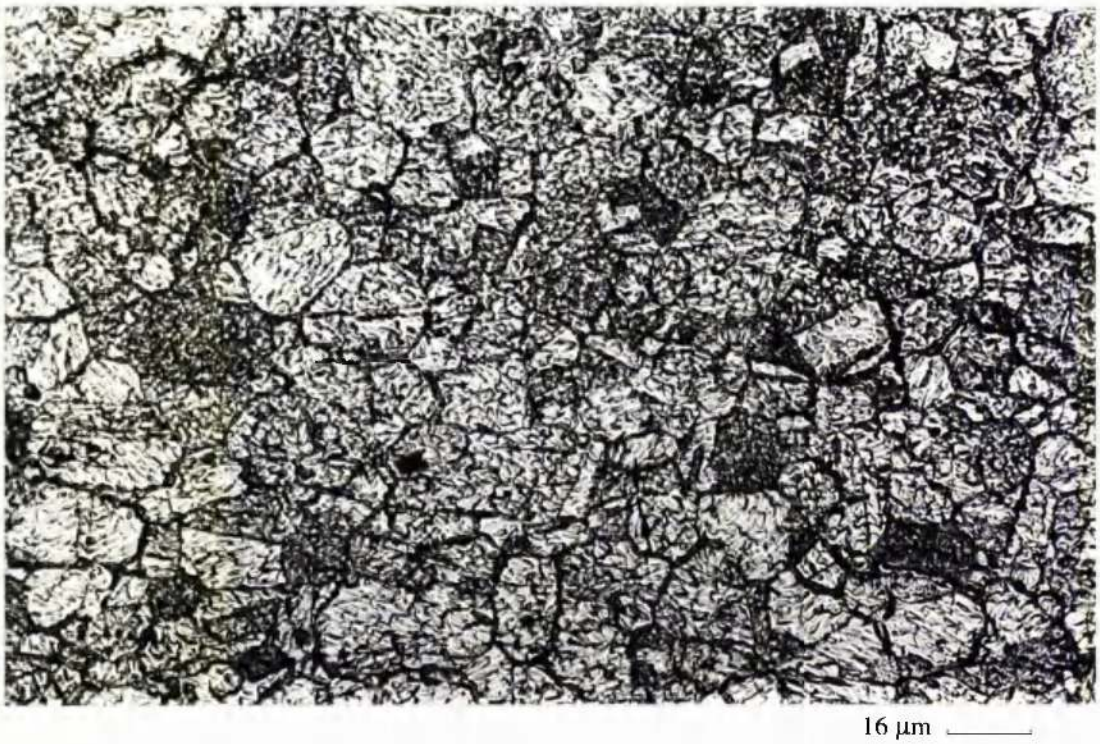

Figure 4.2.18b. Region of general corrosion with "etched" appearance on the outer surface of Cu-30%Ni when anodic polarised after initial exposure to distilled water at 20°C.

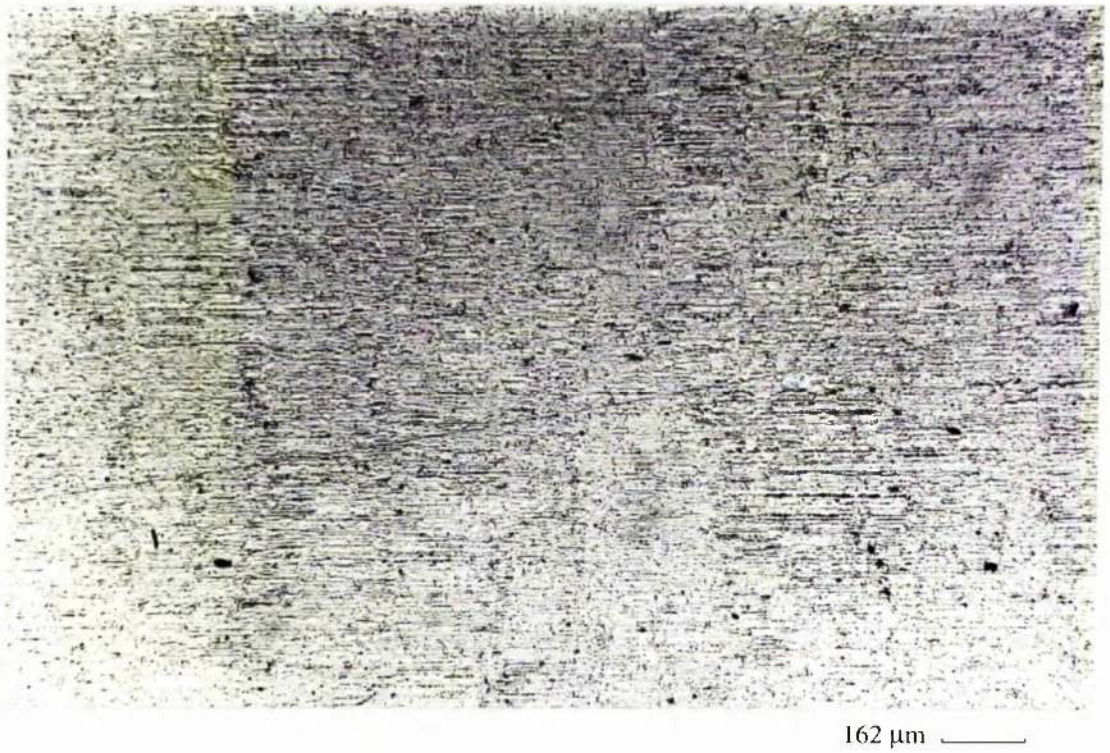

Figure 4.2.19. Thin layer of general corrosion on the outer surface of Cu-30%Ni after 60 day exposure to distilled water at 20°C.

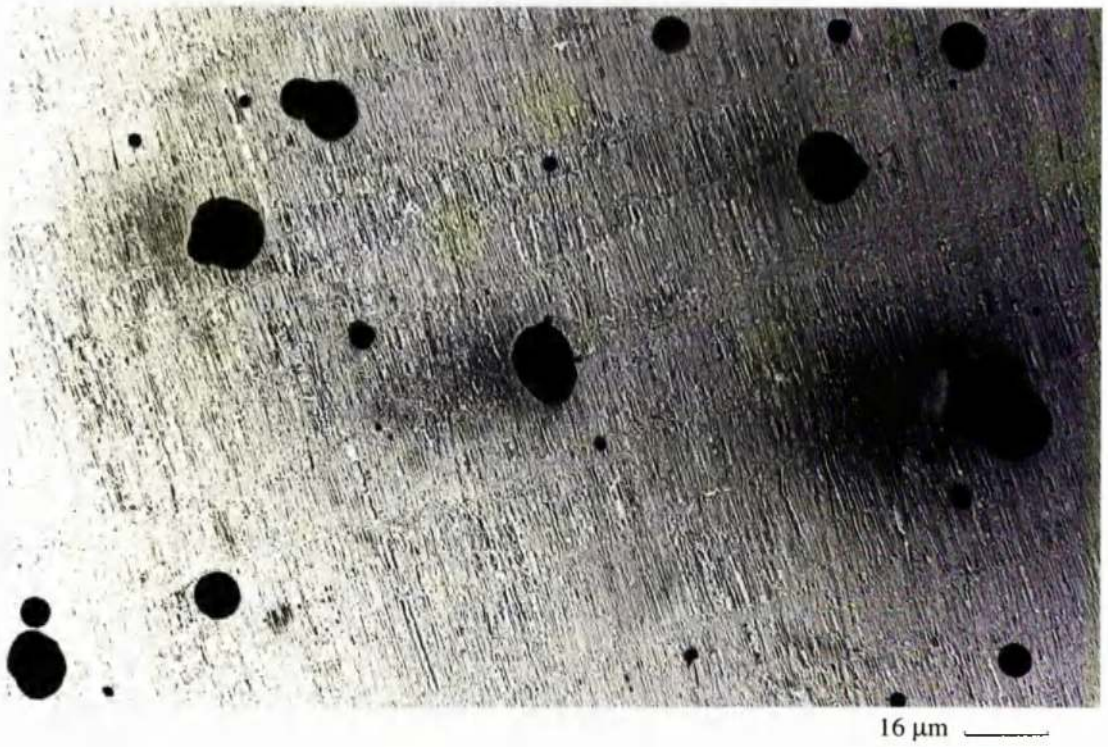

Figure 4.2.20a. Pitting attack on the outer surface of Cu-30%Ni when anodically polarised after 60 day exposure in distilled water at 20°C.

Figure 4.2.20b. Pits were noted to be rather deep on the outer surface of Cu-30%Ni when anodically polarised after 60 day exposure in distilled water at 20°C.

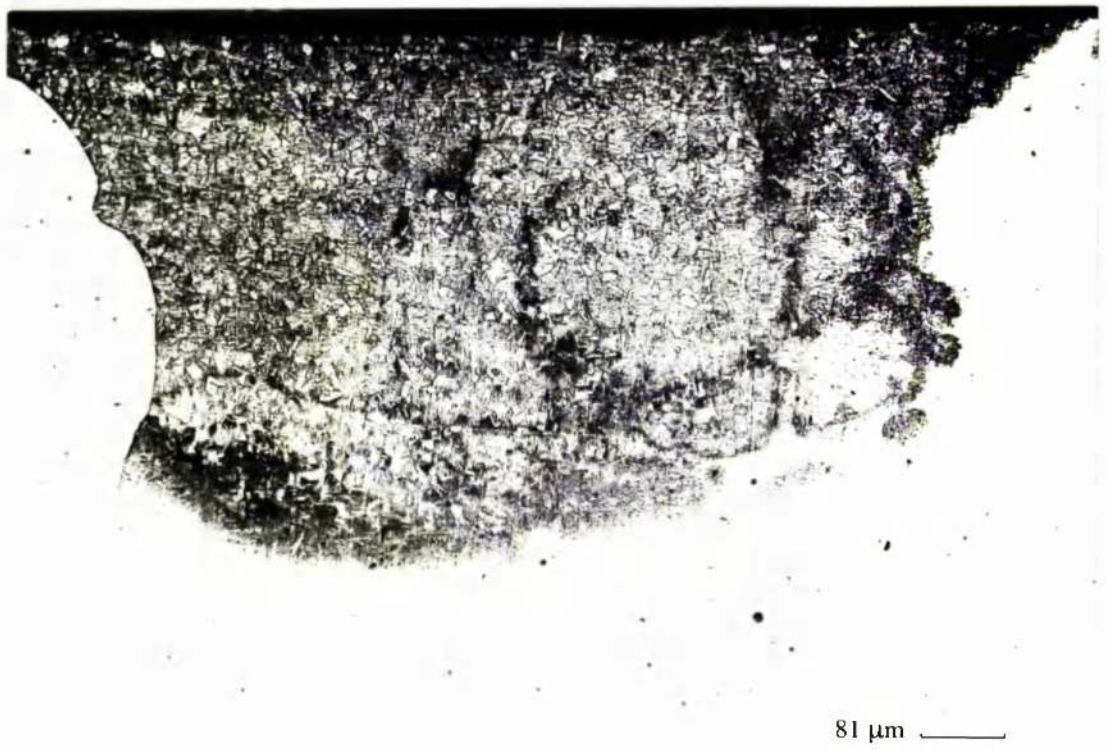

Figure 4.2.21a. Region of general corrosion and minor pitting on Cu-30%Ni when anodically polarised upon initial exposure to distilled water at 50^0C.

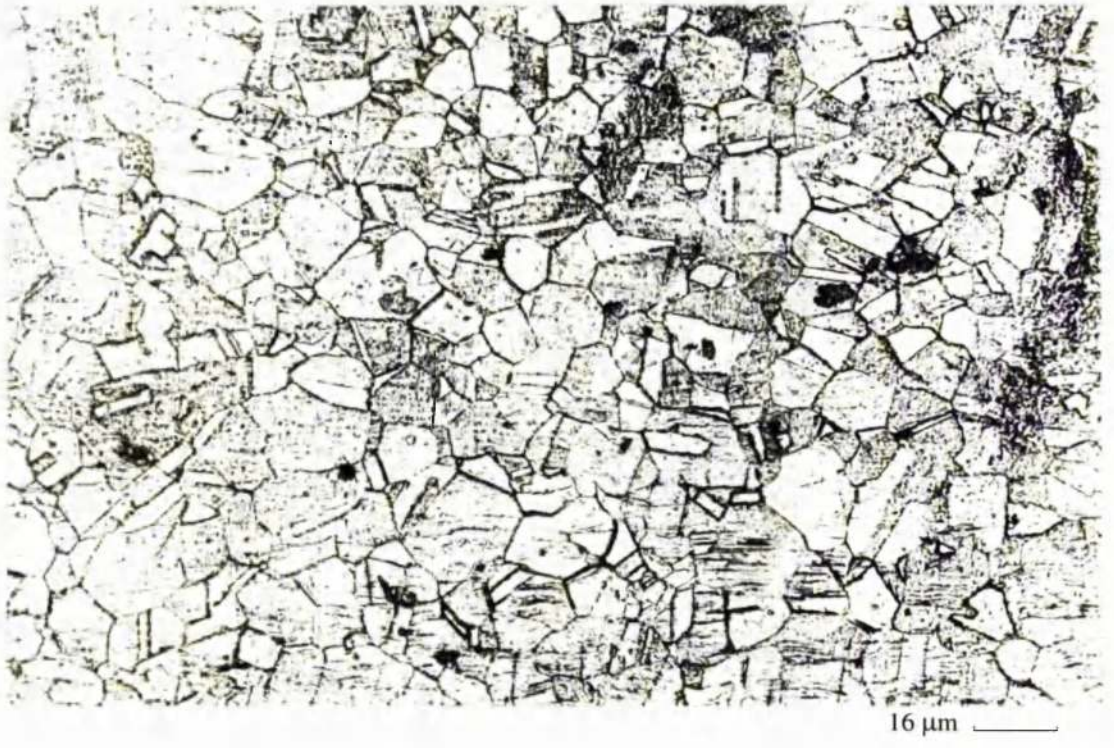

Figure 4.2.21b. Etched appearance on Cu-30%Ni when anodically polarised upon initial exposure to distilled water at 50^0C (high magnification).

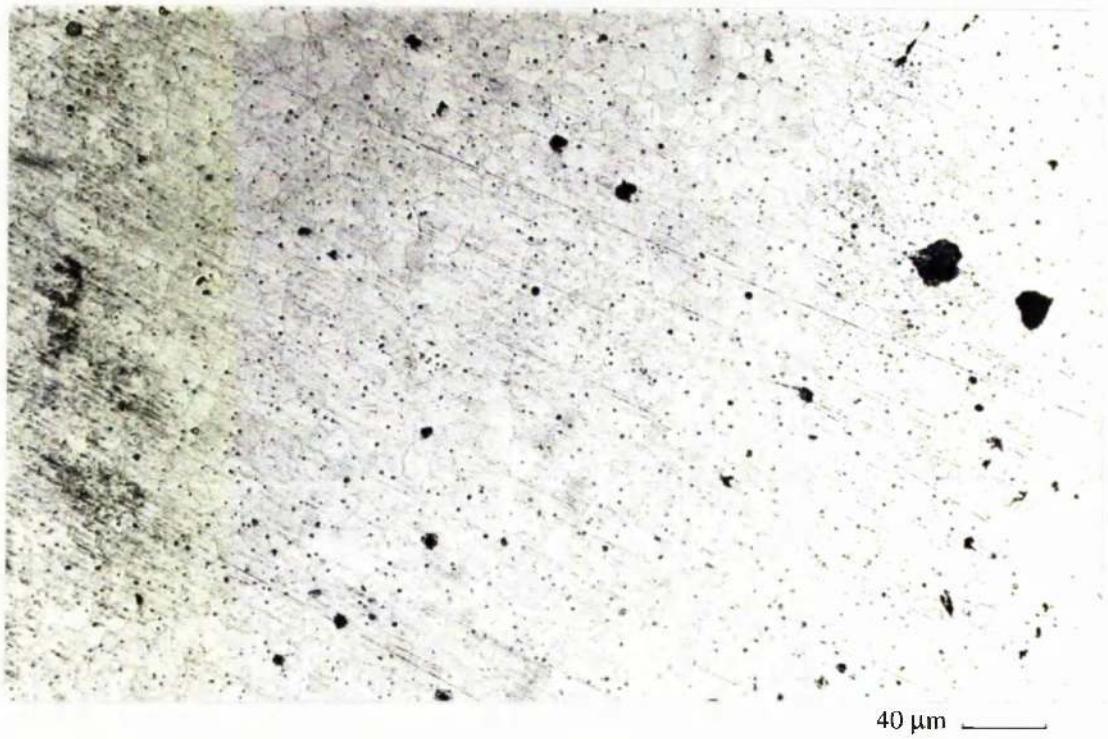

Figure 4.2.22a. Light general corrosion product film and pitting attack on Cu-30%Ni when anodically polarised upon initial exposure to distilled water at 20°C with CO_2 injection.

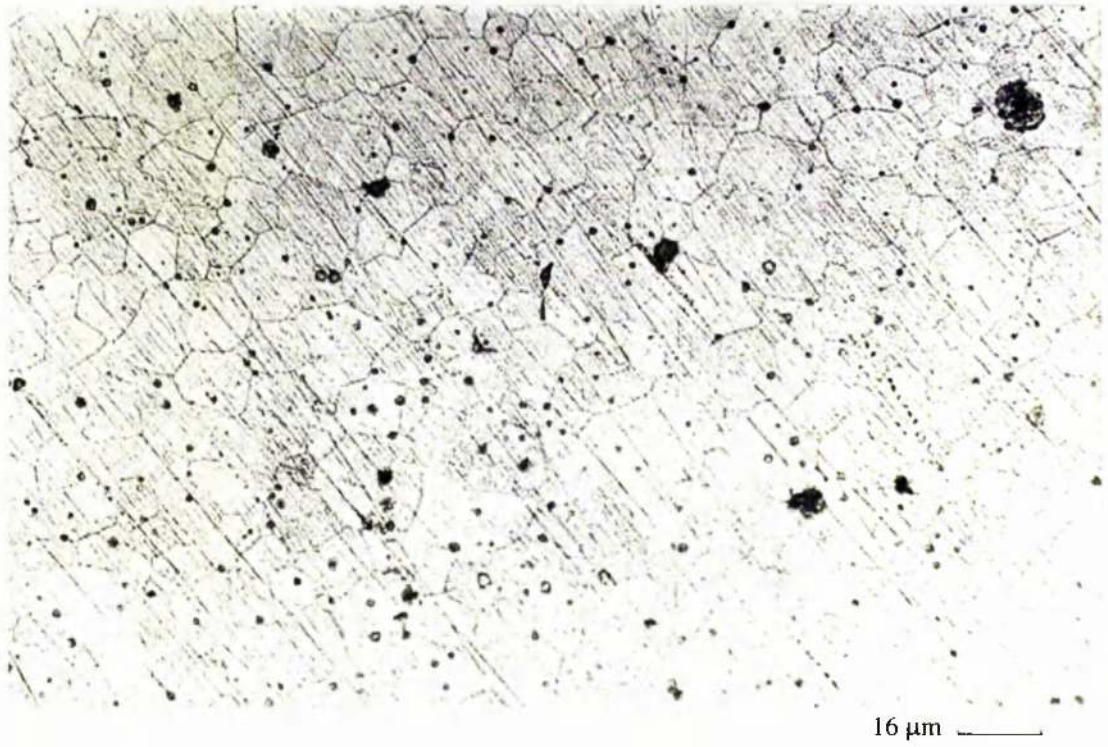

Figure 4.2.22b. High magnification reveals grain structure on Cu-30%Ni when anodically polarised upon initial exposure to distilled water at 20°C with CO_2 injection.

Figure 4.2.23a. Uniform layer of general corrosion on Cu-30%Ni when anodically polarised upon initial exposure to distilled water at 50^0C with CO_2 injection.

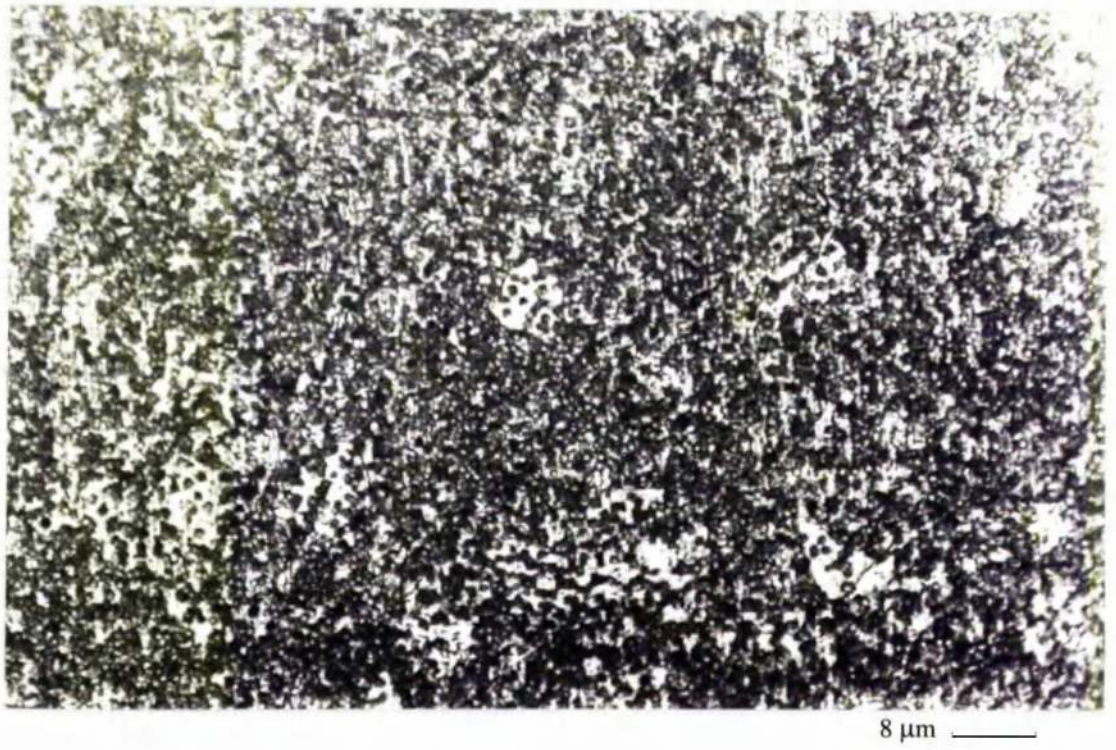

Figure 4.2.23b. Close-up view of the picture in figure 4.2.23a.

Durability Studies Relevant to Marine Equipment

By

Dimitris Mantzavinos

Vol. II

A thesis submitted to

The Department of Mechanical Engineering

University of Glasgow

UNIVERSITY
of
GLASGOW

in fulfilment of the requirement for

The Degree of Doctor of Philosophy

5. DISCUSSION OF RESULTS ON COPPER-NICKEL ALLOYS UNDER STATIC CONDITIONS

5.1. Summarising results

Both copper-nickel alloys were tested in artificial seawater and distilled water at 20°C, in distilled water at 50°C, again at 50°C in distilled water combining CO_2 injection, and in distilled water at 20°C with CO_2 injection. Briefly, Cu-10%Ni displayed much lower corrosion rates in all various distilled water environments than in seawater. The alloy suffered mainly general corrosion with selective attack at the grain boundaries but pitting corrosion was also noted especially when samples were anodically polarised after extended periods of exposure in distilled water (7 and 60 days). Cu-30%Ni displayed lower corrosion rates in distilled water at 20°C than all the other various environments when anodically polarised. It was clearly observed that high temperature (50°C) and the injection of CO_2 in the solution stimulated the corrosion of this alloy to higher rates than in seawater and distilled water at 20°C. In seawater at 20°C and distilled water at 20°C with and without the injection of CO_2, the alloy suffered general corrosion and showed a great tendency to pitting attack (greater than the one Cu-10%Ni exhibited under the same conditions). Signs of selective attack at the grain boundaries were also evident in the case when samples were anodically polarised in distilled water at 50°C.

In connection with interpretation of the anodic polarisation results in order to yield information on relative corrosion rates, it has been necessary to draw conclusions from a qualitative comparison of the general rate of increase of corrosion with polarisation. Unfortunately the anodic polarisation data were not amenable to manipulation to yield accurate estimates of corrosion rates because appropriate linear regions of potential/log current density plots were not obtained. This was probably due to the occurrence of complex corrosion processes involving a tendency to form protective layers.

5.2. Comparison between Cu-10%Ni and Cu-30%Ni

Tests in seawater at 20°C

Figure 5.1 shows the anodic polarisation curves generated from tests in artificial seawater at 20°C on both alloys. It is quite clear that Cu-30%Ni was more corrosion resistant than Cu-10%Ni when anodically polarised immediately after initial exposure to seawater at 20°C. At longer exposures both alloys displayed anodic polarisation behaviour typical of the gradual establishment of a protective corrosion-product layer. Since the observed trends in this respect were non-systematic between 2-day and 7-day exposures, detailed comparison of the two alloys from the electrochemical tests is not possible except to make the tentative postulation that the eventual establishment of a protective layer (see next paragraph) will probably reduce any differences in corrosion behaviour between the two materials.

Microscopic examination showed that for specimens that were anodically polarised upon initial exposure to seawater at 20°C, Cu-10%Ni exhibited uniform general corrosion with selective attack at the grain boundaries (figure 4.1.6) whereas Cu-30%Ni suffered some pitting attack (figures 4.2.6a and 4.2.6b). The most prominent feature resulting from the 2-day and 7-day exposures for both alloys was the apparent gradual development of a thin, patchy, discontinuous surface corrosion-product film (see figures 4.1.7a, 4.1.7b, 4.1.9a and 4.1.9b for Cu-10%Ni and figures 4.2.7a, 4.2.7b, 4.2.8a and 4.2.8b for Cu-30%Ni). This was presumably responsible for the general trends towards a relatively better corrosion resistance indicated in figure 5.1 for anodically polarised specimens after the same exposure times. This is consistent with the assumption that this uniform layer of corrosion products found on the same samples acts as a protective film and comes into agreement with information in the literature that copper-nickel alloys display significantly lower corrosion rates after initial protective film formation is complete [3,34,38,39]. The appearance of numerous shallow pits on the surface of the Cu-10%Ni alloy after anodic polarisation of a 7-day exposure (figures 4.1.10a and 4.1.10b), is a possible indicator of a vulnerability towards breakdown of the developing protective film in extreme conditions. Pitting and crevice corrosion was also observed on the Cu-30%Ni alloy

even without polarisation after 7 days' exposure to seawater at 20°C (figures 4.2.9a and 4.2.9b). This provides more evidence that this higher-Ni alloy may be inherently somewhat more vulnerable to this type of attack.

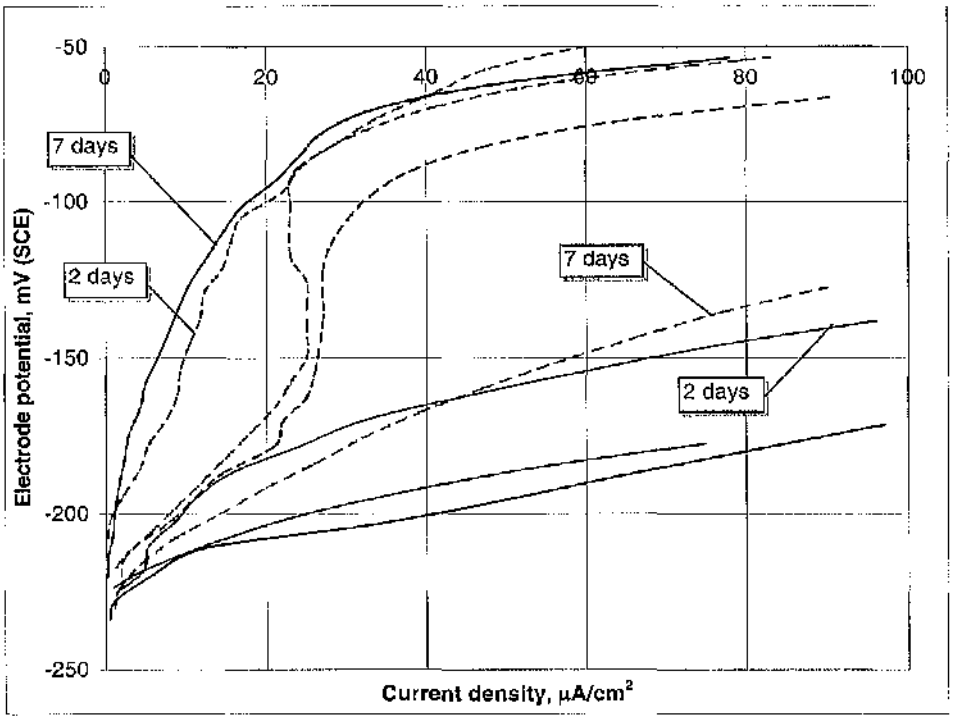

Figure 5.1. Anodic polarisation tests of Cu-10%Ni and Cu-30%Ni in artificial seawater at 20°C after 1 hour immersion except where stated. Dotted lines = Cu-30%Ni, full lines = Cu-10%Ni.

Tests in distilled water at 20°C

As figure 5.2 shows, Cu-30%Ni displayed lower corrosion rate than Cu-10%Ni in distilled water at 20°C when anodically polarised upon initial exposure or after long periods of time (2 days, 7 days, 60 days). Similarly to seawater, Cu-10%Ni exhibited a general but irregular trend towards higher corrosion resistance, in relevance to immediate tests, after 2-60 days' immersion in distilled water at 20°C whereas similar trends were not noticeable for Cu-30%Ni presumably because of the more passive behaviour of this alloy upon initial immersion. Even after 60 days of immersion in distilled water at 20°C, Cu-30%Ni was still noticeably more corrosion resistant than Cu-10%Ni.

Microscopical examination provided supporting evidence for the general interpretation of the electrochemical monitoring described in the previous paragraph. Thus, microscopic examination of Cu-10%Ni specimens, after the one-hour exposure followed by anodic polarisation, confirmed the active corrosion behaviour indicated by figure 5.2 by revealing a general surface etching which signifies general attack (figures 4.1.11a and 4.1.11b). In contrast, more evidence of a partly-protective corrosion product was provided for Cu-30%Ni after anodic polarisation of a 1-hour specimen (figures 4.2.6a and 4.2.6b) and particularly after 2-days exposure without anodic polarisation (figures 4.2.7a and 4.2.7b). Thus, the overall evidence in this investigation is indicative that in distilled water at 20°C a protective film does not form as readily for Cu-10%Ni as for Cu-30%Ni.

Moreover, indications of the trend towards the gradual build-up of a protective corrosion product on Cu-10%Ni were provided by samples removed without final anodic polarisation after a 7-day immersion which revealed a thin, patchy, discontinuous surface corrosion-product film (figure 4.1.14a) which was presumably responsible for the relatively better corrosion resistance indicated in figure 5.2 for anodically polarised specimens after the same exposure time. Evidence of the vulnerability of localised breakdown of the protective corrosion product even in distilled water at 20°C was present for both alloys. For example, microscopical examination of 7-day exposed Cu-10%Ni specimens after anodic polarisation, revealed a quite different mode of attack, namely pitting (figures 4.1.15a and 4.1.15b), than the general surface etching characteristic of one-hour samples of the same alloy. Moreover, the microscopical evidence indicated a somewhat greater tendency towards pitting attack for the higher-Ni alloy. For instance, Cu-30%Ni displayed numerous shallow pits when anodically polarised upon initial exposure to distilled water at 20°C (figure 4.2.11b), but that was not the case for the lower-Ni alloy subjected under the same conditions. Also a few very shallow pits were clearly present on the surface of Cu-30%Ni after 7 days immersion (figures 4.2.14a and 4.2.14b), and specimens of the same alloy subjected to final anodic polarisation were found to be extensively pitted (figures 4.2.13a, 4.2.13b, 4.2.15a and 4.2.15b).

This evidence of the susceptibility of these Cu-Ni alloys to corrosion attack by pitting in distilled water at 20°C even when covered by surface films was strengthened by the

findings from much longer exposures of 60 days both from the less steep anodic polarisation curves (figure 5.2) and, more visibly, from microscopic examination of unpolarised specimens which revealed for both alloys a more-apparent less-patchy corrosion product coating but with the additional presence of pits (figures 4.1.16a, 4.1.16b, 4.2.16a and 4.2.16b). When anodic polarisation took place at the end of the 60-day period pitting was more severe on the surface of the two alloys (figures 4.1.17a, 4.1.17b, 4.2.17a and 4.2.17b).

Further evidence of continuing corrosion damage during longer-term experiments was obtained from electrical conductivity measurements. Continued increases in conductivity in 7-day and 60-day experiments (see table 4.1.1 for Cu-10%Ni and table 4.2.1 for Cu-30%Ni) are also indicative of some continuing corrosion, mainly pitting as shown by the microscopic examination, for both alloys despite the gradual formation of protective corrosion layer.

In order to verify that the main series of tests on tube cross-sections of the Cu-30%Ni alloy were reasonably representative of attack on the outer surface (as clearly is the case in the operation in an MSF plant), as indicated in section 4.2.2, additional anodic polarisation tests on segments of the outer surface of the Cu-30%Ni tube material were carried out. These yielded quite similar results to the main series of tests on cross-section specimens. Microscopic examination on outer surface anodically polarised specimens upon initial exposure and after 60 days immersion in distilled water at 20°C, revealed comparable features to cross-section specimens tested under the same conditions, i.e. pitting attack and regions of general corrosion (see figures 4.2.11a, 4.2.11b, 4.2.16a, 4.2.16b, 4.2.17a and 4.2.17b for cross section surface and figures 4.2.18a, 4.2.18b, 4.2.19, 4.2.20a and 4.2.20b for outer surface). There was some slight indication that the pitting was more intense on the cross-section samples and there was the additional possible complication that the samples taken from the side of the Cu-30%Ni tube were flattened by cold working. Nevertheless, the overall conclusion from the results is that the cross-section specimens were representative of the behaviour of the outer surface.

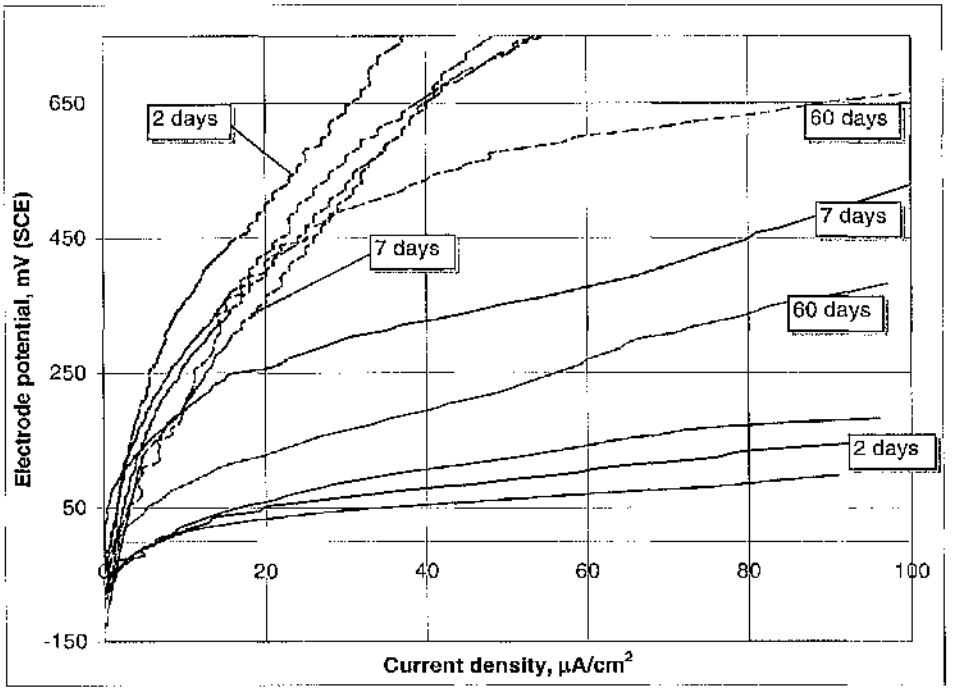

Figure 5.2. Anodic polarisation tests of Cu-10%Ni and Cu-30%Ni in distilled water at 20°C after 1 hour immersion except where stated. Dotted lines = Cu-30%Ni, full lines = Cu-10%Ni.

Tests in distilled water at 50^{0}C

Figures 5.3a and 5.3b show the anodic polarisation curves generated upon initial exposure to distilled water at 50°C on both alloys. It is evident that the behaviour of the two alloys is much more similar than in the same tests at 20°C (see figure 5.2). As already described in sections 4.1.3 and 4.2.3, the Cu-10%Ni alloy is not much different at 50°C than at 20°C (figure 4.1.3) but the 30%Ni alloy exhibits much more active corrosion at 50°C than at 20°C (figure 4.2.3) and this is why the two alloys exhibit rather similar behaviour at the higher temperature. It is thus apparent, and perhaps not surprising, that the ability of the Cu-30%Ni alloy to produce a protective film upon immediate exposure at 20°C is not the case at the higher temperature.

This similar behaviour of the two alloys when anodically polarised in distilled water at 50°C is confirmed visually by microscopic examination. Most of the surface of both alloys appeared to be covered by a thin film together with isolated "etched" regions of

general corrosion (figures 4.1.18a and 4.2.21a). In contrast to Cu-30%Ni, the lower-nickel alloy also featured clear evidence of attack at the crevice (figure 4.1.18b).

These studies of the effect of increasing the temperature to 50°C have been extended to 80°C [140], by experimental work carried out in the same laboratory that this present work took place, and the same comparative behaviour has been observed. That is, both copper-nickel alloys exhibited similar behaviour of a rapidly increasing current when anodically polarised in distilled water at 80°C which implies non-protective corrosion behaviour. Indications of a tendency towards the establishment of a more protective corrosion product at 80°C on both copper-nickel alloys were provided by some anodic polarisation tests undertaken on specimens after immersion for 7 and 15 days in distilled water at 80°C but microscopical examination of copper-nickel samples, removed from the distilled water after immersion for 30 days at 80°C without any electrochemical testing, revealed some differences between the two alloys. Thus, Cu-10%Ni specimens had a more-general disposition of corrosion product on their surfaces whereas on Cu-30%Ni the corrosion product was more discrete and there were numerous shallow pits which were not evident on the lower-nickel alloy.

The overall picture from these findings at the elevated temperatures is that the corrosion behaviour of the two copper-nickel alloys upon early exposure to distilled water at 50°C and 80°C is much more similar than at 20°C. Moreover, some differences may emerge with longer exposure times in which the higher-Ni alloy may have a greater tendency to form a protective corrosion product but nevertheless be rather prone to pitting attack (as at 20°C).

Tests in distilled water at 20^0C with CO_2

Figure 5.4 shows the anodic polarisation curves generated upon initial exposure to distilled water at 20°C with CO_2 injection on both alloys. Although the anodic plots diverge at potentials remote from E_{corr}, they are all in the same "band" at points up to about 100 mV displaced from E_{corr}. This is indicative of similar corrosion resistance

between the two alloys and again demonstrates the lesser ability of the Cu-30%Ni alloy to form a protective corrosion product upon immediate exposure to more severe conditions than are provided by plain distilled water at 20°C. The additional severity for Cu-30%Ni in these particular tests is obviously caused by the lower pH associated with CO_2 injection (see table 4.2.6).

Microscopic examination revealed light etching plus shallow pitting on Cu-30%Ni when anodically polarised in distilled water at 20°C with CO_2 injection (figures 4.2.22a and 4.2.22b), whereas in the same conditions Cu-10%Ni displayed only a general surface etching which signifies general attack (figures 4.1.19a and 4.1.19b). This again indicates a more-pronounced susceptibility to pitting attack of the higher-nickel alloy and might also explain the diverging anodic polarisation plots displayed by this alloy at relatively positive potentials (figure 5.4).

Tests in distilled water at 50°C with CO_2

Figure 5.5 shows the anodic polarisation curves generated upon initial exposure to distilled water at 50°C with CO_2 injection on both alloys. It is evident that, in these conditions, the Cu-30%Ni alloy is more corrosion active than the lower-nickel material. Thus, although the comparison has been made only on one-hour exposure tests, the anodic polarisation results provide an indication that Cu-30%Ni possesses inferior corrosion resistance than the 10%Ni alloy when carbon dioxide is present at 50°C. Microscopic examination on anodically polarised specimens in distilled water at 50°C with CO_2 injection revealed a thin dark discontinuous surface corrosion-product film with regions of "etched" surface and possibly minor pitting for Cu-10%Ni (figures 4.1.20a and 4.1.20b). Microscopical examination did not reveal the actual mode of attack on the Cu-30%Ni alloy. As argued later (section 5.3), it may be that some kind of selective attack on the Ni alloy constituent was involved.

The results of the electrochemical tests described in this section come into agreement with [46] where it is pointed out that the presence of carbon dioxide in distilled water at 50°C results in apparently lower corrosion resistance of the Cu-30%Ni alloy in

comparison with the Cu-10%Ni material. It is relevant to note at this point that in recent work [140] produced in the same laboratory as this present work there has been no obvious evidence (in relation to both alloys) of an additional severity introduced by injection of CO_2 into distilled water at 80°C in comparison to distilled water at 80°C without CO_2. It was considered that that feature was associated with the fact that increasing the temperature from 50°C to 80°C in the absence of injected CO_2 introduces an extra degree of severity in itself; such that the presence of CO_2 does not represent any significant additional corrosivity.

Hence, and as also postulated in [46], there is quite a reasonable amount of evidence indicating that improvements in corrosion resistance may not be obtained by the use of Cu-30%Ni alloy rather than Cu-10%Ni in distilled water environments containing high levels of carbon dioxide especially at high temperature. On the other hand, Cu-30%Ni possesses better corrosion resistance than the lower-Ni alloy in seawater flowing conditions. According to general experience [19,34,36], Cu-30%Ni is used successfully in condensers and heat exchangers with water velocities up to 5.5 m/s (when surface is smooth), whereas Cu-10%Ni under such conditions is limited to a maximum flow velocity of 3.0 m/s. This superiority of Cu-30%Ni to Cu-10%Ni in seawater flowing conditions is directly linked to the vast use of Cu-30%Ni tubes, as condensers and heat exchangers, in MSF desalination plants.

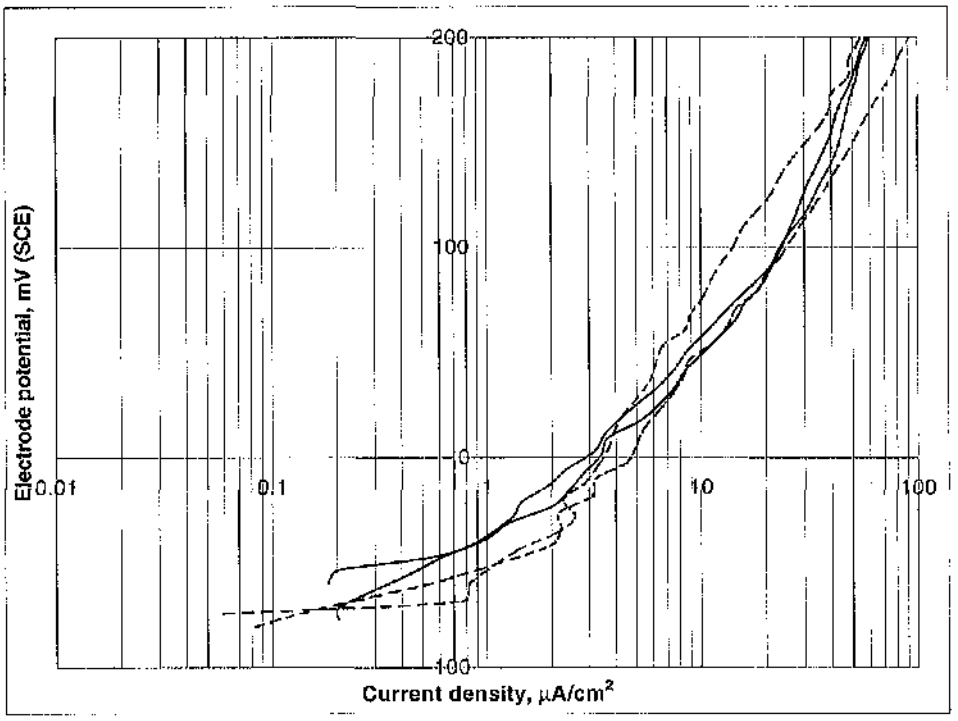

Figure 5.3a. Anodic polarisation tests of Cu-10%Ni and Cu-30%Ni in distilled water at 50°C after 1 hour immersion. Dotted lines = Cu-30%Ni, full lines = Cu-10%Ni.

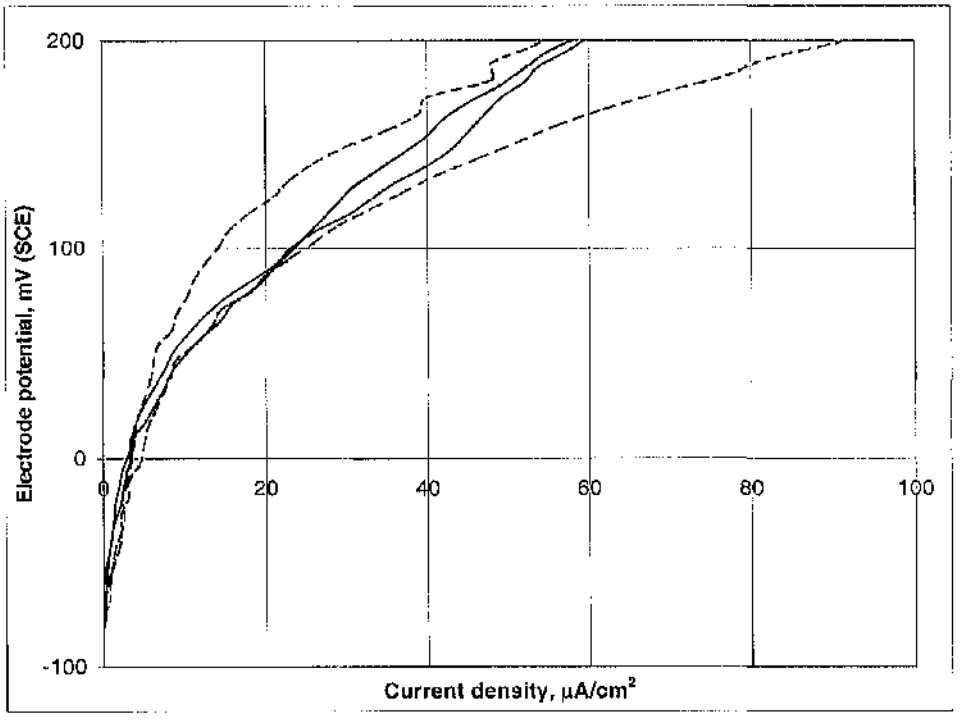

Figure 5.3b. Anodic polarisation tests of Cu-10%Ni and Cu-30%Ni in distilled water at 50°C after 1 hour immersion. Dotted lines = Cu-30%Ni, full lines = Cu-10%Ni.

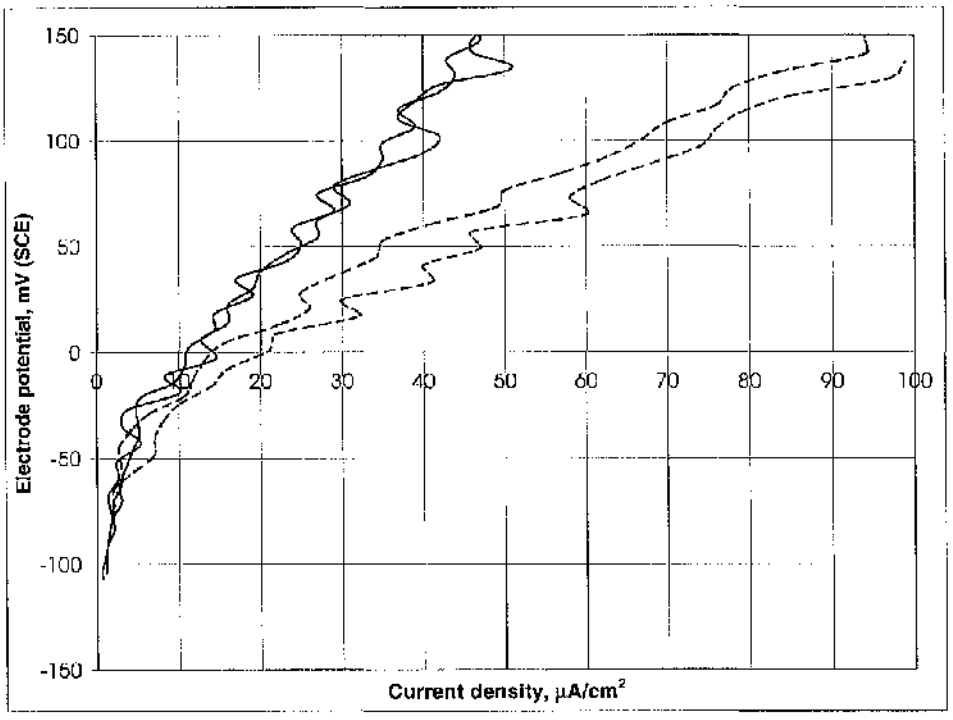

Figure 5.4. Anodic polarisation curves of Cu-10%Ni and Cu-30%Ni after 1 hour of immersion in distilled water at 20°C with injected CO_2. Dotted lines = Cu-30%Ni, full lines = Cu-10%Ni.

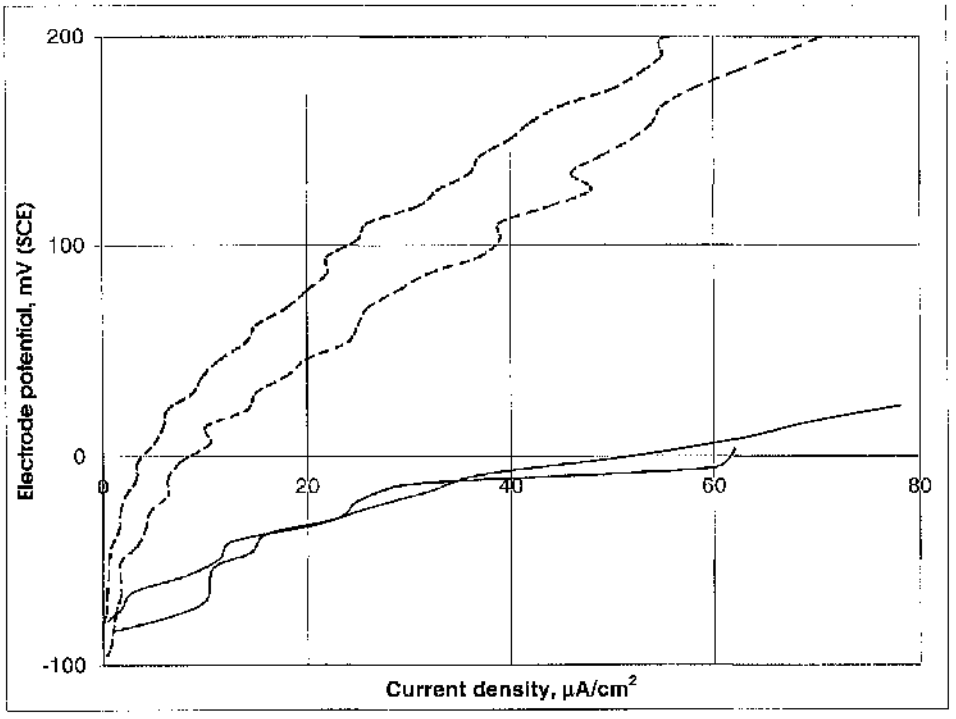

Figure 5.5. Anodic polarisation curves of Cu-10%Ni and Cu-30%Ni after 1 hour of immersion in distilled water at 50°C with injected CO_2. Dotted lines = Cu-10%Ni, full lines = Cu-30%Ni.

5.3. Relevance to industrial situation

In relation to the vapour-side corrosion of copper-nickel alloys in multistage flash desalination plants, this research has demonstrated the deleterious effects, on both alloys, of increased temperature and this is in accord with the observations of serious vapour-side corrosion in the elevated temperature regions of plants. With regard to the influence of CO_2, the argument is that CO_2 can cause tube damage in MSF desalination plants if present in the vapour in the high temperature stages [11-13]. Carbon dioxide evolved reacts with water and carbonic acid is formed: $CO_2 + H_2O \leftrightarrow H_2CO_3$ [13]. If the steam and evolved gases are trapped in the evaporator (say by inefficient venting) then the condensation of the trapped vapours in the form of stagnant pockets is quite possible [11-13]. In consequence, acidic vapour-side condensate will cause corrosion in the presence of an oxidant, like oxygen which is conveniently available [11]. In this respect it has been argued [14] that CO_2 dissolved in saturated vapour can reduce the corrosion resistance of Cu-30%Ni alloy only with the inclusion of air (oxygen) and that, on account on the electropositive nature of copper, Cu-30%Ni can not be affected by CO_2-loaded steam alone.

However, experimental results shown earlier in this thesis (see figures 5.2, 5.4 and 5.5) have demonstrated quite clearly that, even in de-aerated water (caused by sweeping O_2 out of the water by the CO_2 injection), CO_2 can have a significant effect on the corrosivity of Cu-30%Ni especially at high temperature.

This effect is plausible when it is considered that 30% Ni is present in the alloy and the $Ni^{2+} + 2e^- = Ni$ standard electrode potential (-0.25 V on the SHE scale) is considerably more negative than for $2H^+ + 2e^- = H_2$ (zero on SHE scale). Thus the lower pH associated with CO_2 presence could cause increased corrosive attack. This might involve an actual nickel de-alloying mechanism – although no convincing evidence of this phenomenon has been found in this project. Based on this respect, it is reasonable to assume that improvements in corrosion resistance are unlikely to be obtained by the use of Cu-30%Ni alloy rather than the lower-Ni alloy in environments containing high levels of carbon dioxide.

Whilst the current project has demonstrated the influence of CO_2 in reducing the corrosion resistance of Cu-30%Ni upon immediate exposure to distilled water containing CO_2 at 20°C and 50°C, no experiments have been conducted for long exposures in these conditions. Moreover, other work [140] has not provided clear evidence of an introduced severity associated with CO_2 at the higher temperature of 80°C – which is nearer to temperatures in which the vapour-side corrosion is experienced in MSF plants. Thus a role of CO_2 alone in the problem has not been unambiguously demonstrated. In this respect, A. M. Shams El Din and R. A. Mohammed [14] have recently demonstrated that Cu-30%Ni subjected to the action of falling distilled water droplets in an O_2/CO_2 atmosphere exhibits a corrosion rate five times higher than that measured in the absence of droplet bombardment. This drop in corrosion resistance is evidently attributed to the conjoint mechanical/erosive action of the droplets and provides evidence for a possible (maybe additional) role of erosion-corrosion, induced by impinging water droplets, in the operational problem of MSF distillers.

6. CORROSION AND EROSION-CORROSION STUDIES ON Ti AND Ti ALLOYS

6.1. Static conditions

The experimental techniques and procedures followed to conduct static experiments in this section have already been described in Chapter 3.

Static tests in distilled water

Figure 6.1.1 shows the anodic polarisation curves generated from two tests on commercially pure titanium after one hour exposure in quiescent distilled water. It is quite clear that Ti:G2 exhibits passivity over an extremely wide range of potential in distilled water at ambient temperature.

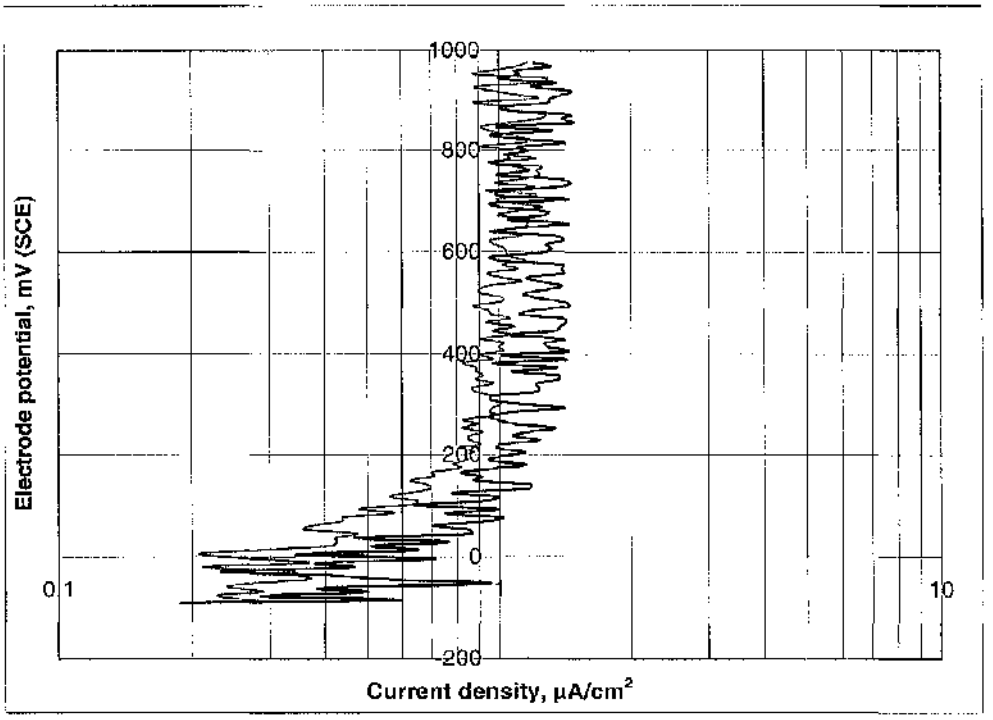

Figure 6.1.1. Anodic polarisation curves of Ti:G2 in distilled water at ambient temperature.

In both tests the conductivity of the solution appeared to be somewhat higher after the specimens had been anodically polarised possibly indicating a very small metal dissolution. The pH of the distilled water was also slightly increased apparently due to the cathodic reaction of hydrogen evolution, $2H^+ + 2e^- \rightarrow H_2$, during the test. Table 6.1.1 and Table 6.1.2 show the conductivity and pH values respectively before and after polarisation.

	Before polarisation	**After polarisation**
Test 1	2.5	11
Test 2	3.1	13.4

Table 6.1.1. Conductivity values (in μS/cm) before and after anodic polarisation tests of Ti:G2 in distilled water at ambient temperature.

	Before polarisation	**After polarisation**
Test 1	5	5.5
Test 2	5.1	5.5

Table 6.1.2. pH values before and after anodic polarisation tests of Ti:G2 in plain distilled water at ambient temperature.

Anodic polarisation at 80°C yielded essentially the same result as at ambient temperature (figure 6.1.1) except for a slightly higher passive current density at the elevated temperature (Figure 6.1.2).

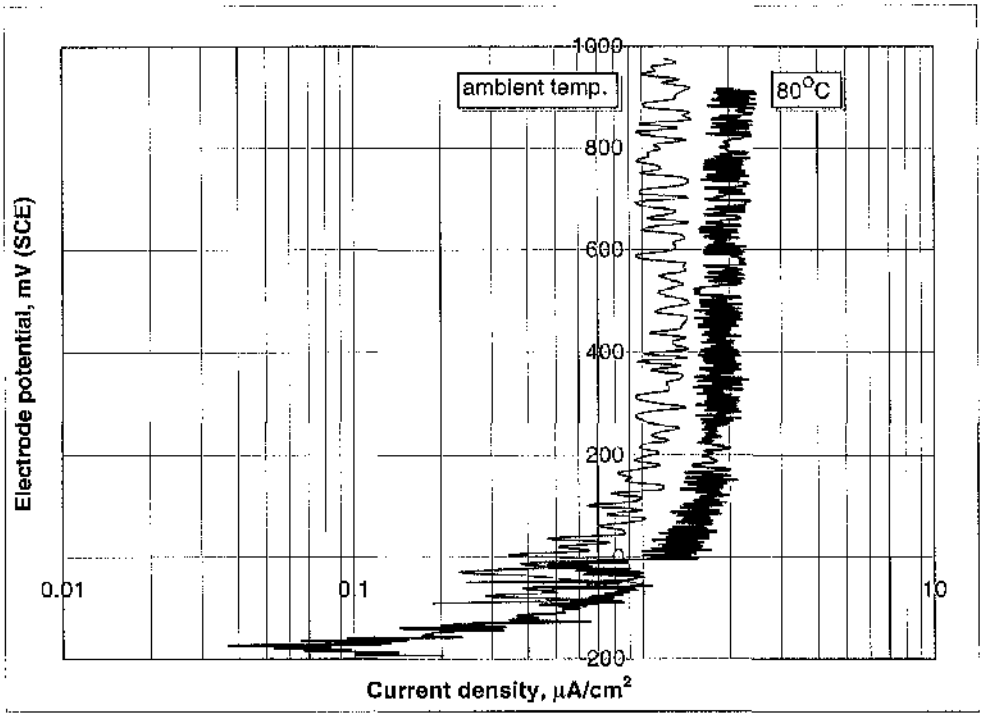

Figure 6.1.2. Anodic polarisation of Ti:G2 in distilled water at 80° in comparison to ambient temperature.

Static tests in distilled water with CO_2

As shown in figure 6.1.3, the injection of CO_2 to the distilled water at ambient temperature did not have any serious effect on the passive behaviour of Ti:G2. Although the current fluctuations appear rather extensive in figure 6.1.3, they only extend to a few $\mu A/cm^2$. It is thought that contributing factors in this behaviour are CO_2 bubbles intermittently interfering with the electrode reactions on the surface of the sample, or to some turbulence in the solution caused by the CO_2 bubbles although the possibility of easier breakdown, and instant reforming, of the protective film by the addition of CO_2 should not be disregarded.

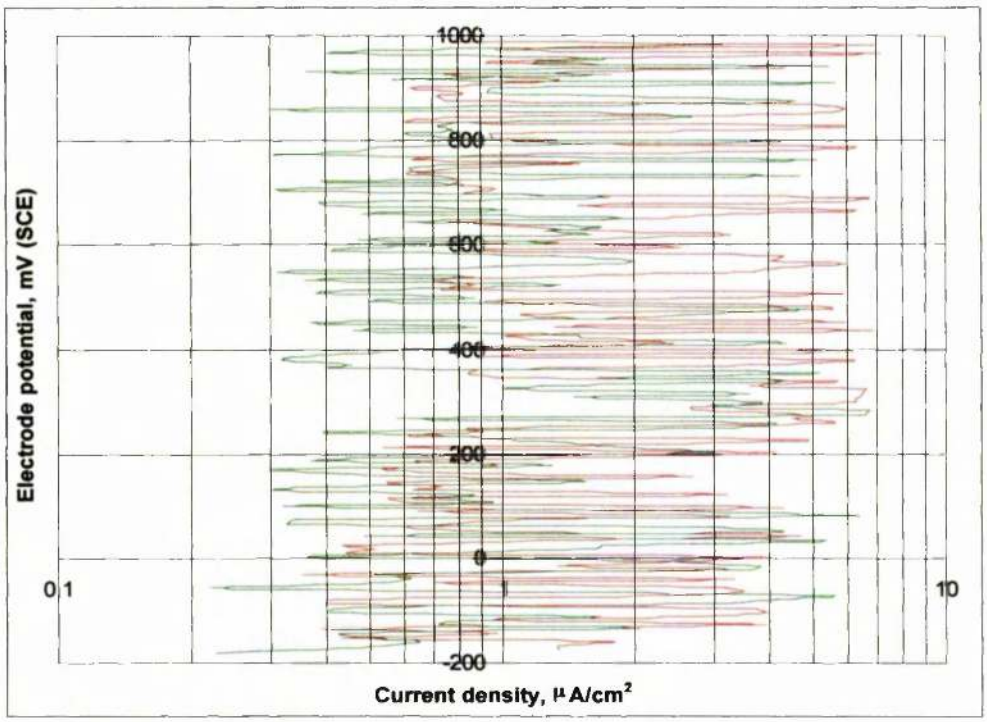

Figure 6.1.3. Anodic polarisation curves of Ti:G2 in distilled water at ambient temperature containing CO_2.

The pH was noticeably reduced when CO_2 was introduced into the solution (Table 6.1.3). This can be attributed to the formation of carbonic acid,

$$CO_2 + H_2O \rightarrow H_2CO_3$$

which was followed by hydrogen ion evolution,

$$H_2CO_3 \rightarrow H^+ + (HCO_3)^- \quad \text{and}$$

$$(HCO_3)^- \rightarrow H^+ + (CO_3)^{2-}$$

Before the addition of CO_2	After the addition of CO_2	After polarisation
5.1	4.2	4
5	4	4

Table 6.1.3. pH of distilled water before and after the addition of CO_2, and after polarisation of Ti:G2.

It was also observed that the conductivity of the solution was increased in a short period of few minutes after the cylinder had started bubbling CO_2 prior to polarisation. After the anodic polarisation had taken place the conductivity had further increased slightly (Table 6.1.4). The conductivity increases might imply some dissolution of the metal but the polarisation curves (figure 6.1.3) do not support this interpretation. Moreover, as will be mentioned later in another section, no corrosion damage of any sort was evident on the surface of the specimens. Consequently a significant contributor to these conductivity changes would be the $(HCO_3)^-$ and $(CO_3)^{2-}$ ion productions resulting from injections of CO_2 as described above.

Before the addition of CO_2	After the addition of CO_2	After polarisation
3	35	43
2.3	35	46.7

Table 6.1.4. Conductivity of distilled water before and after the addition of CO_2, and after polarisation of Ti:G2 (μS/cm).

The raise of temperature to 50°C combined with the addition of CO_2 in the solution did not reduce the corrosion resistance of Ti:G2 (figure 6.1.4). Once again Ti:G2 exhibited high corrosion resistance, in fact the current densities just above Ecorr were even lower at 50°C with CO_2 than at ambient temperature with and without CO_2 (see also figures 6.1.1 and 6.1.3).

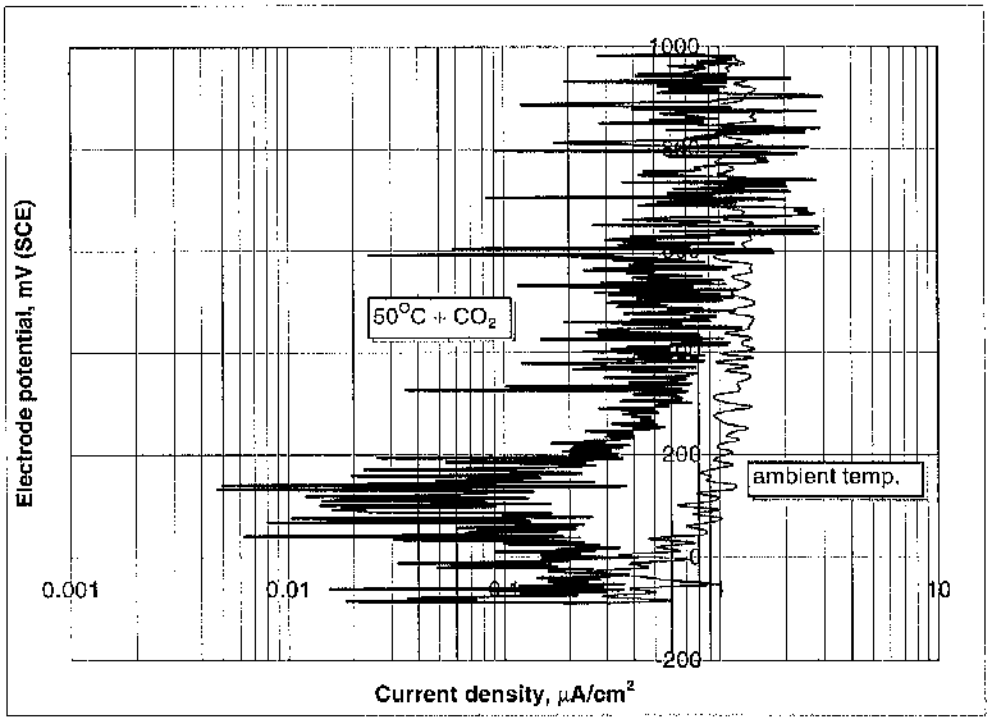

Figure 6.1.4. Anodic polarisation of Ti:G2 in distilled water at 50° containing CO_2 in comparison to ambient temperature.

Figure 6.1.5 shows the anodic polarisation curves generated from tests on Ti:G2 in all static environments already mentioned, and compared to 80°C distilled water with CO_2. Despite some differences in the various anodic polarisation curves, it is clear that in all the conditions studied, including the most severe of 80°C + CO_2, Ti maintains a passive behaviour. Figure 6.1.5 also provides clear evidence that 316L stainless steel possesses somewhat similar corrosion resistance to Ti in distilled water but for a possible greater tendency for passive film breakdown as indicated by the shift to higher currents for 316L at potentials above about +400 mV (SCE) relatively in the severe conditions represented by 80°C + CO_2. In large contrast, Cu-30%Ni

exhibits highly active corrosion behaviour upon initial exposure to the same environment.

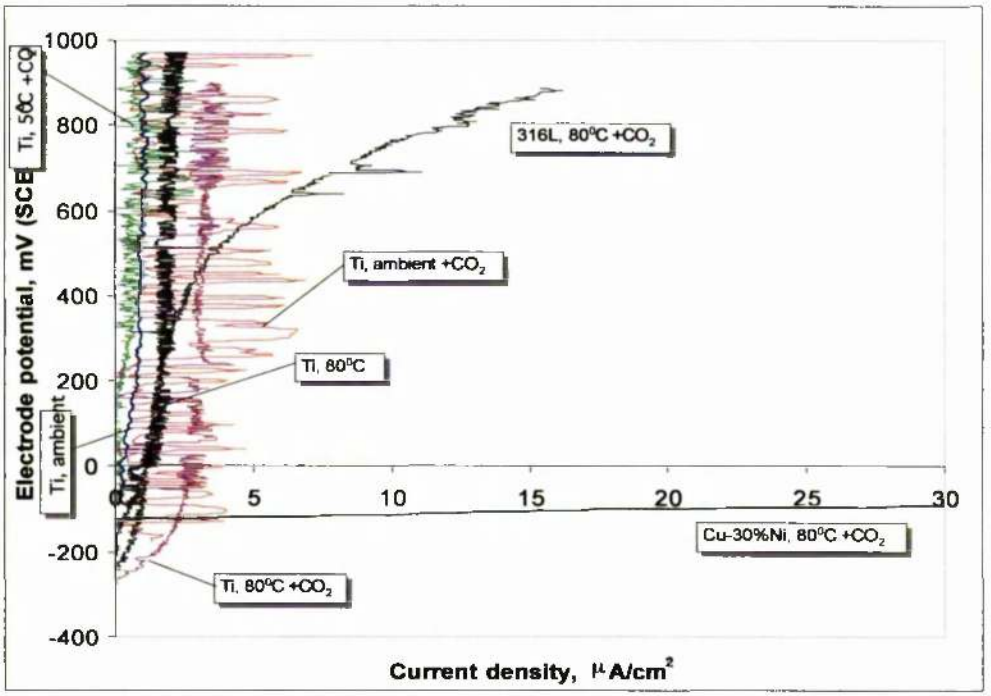

Figure 6.1.5. Anodic polarisation curves of Ti:G2 over a range of distilled water conditions from 20°C to 80°C, with and without injection of CO_2 in comparison to 316L and Cu-30%Ni at 80°C with CO_2.

Static tests in seawater at ambient temperature and 50°C

Figure 6.1.6 and figure 6.1.7 show the anodic polarisation curves generated from tests on Ti:G2, Ti-6Al-4V and Ti:5111 in seawater at ambient temperature and 50°C respectively. Quite clearly, pure titanium and the two alloys display excellent corrosion resistance at both temperatures, although pure titanium seems to be somewhat superior to both alloys in that it exhibits a lower passive current density and the passive current density is highest for the Ti:5111 alloy. Figure 6.1.8 reveals that there is only a small shift to higher passive current densities in the polarisation curves which implies that seawater at this higher temperature has an insignificant effect on the corrosion resistance of the three materials.

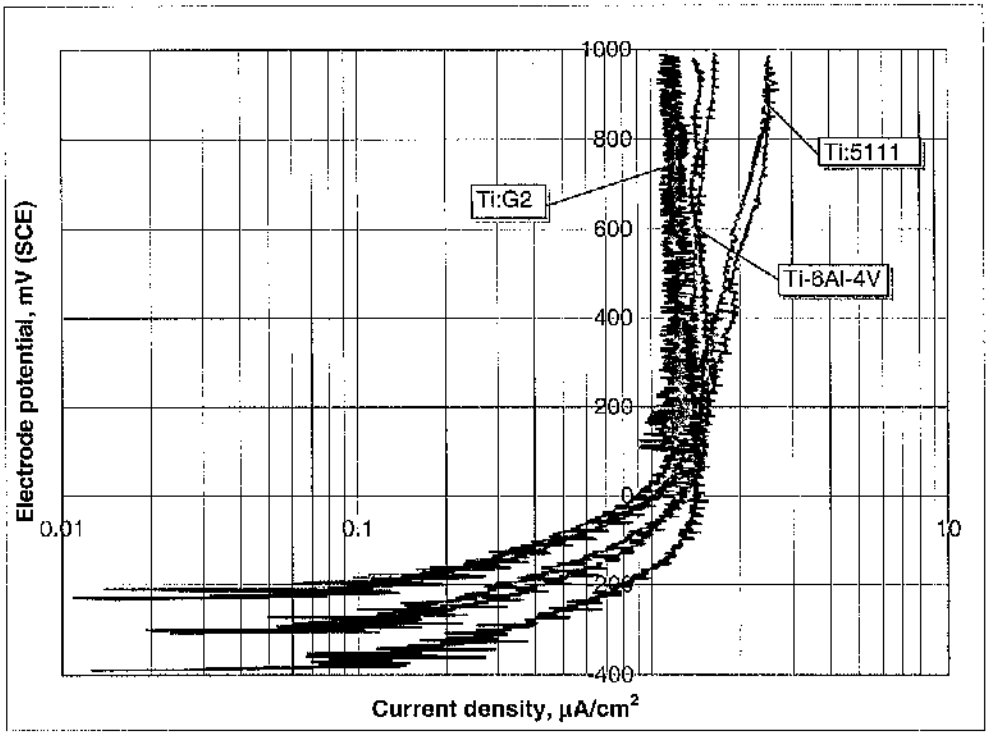

Figure 6.1.6. Anodic polarisation of Ti:G2, Ti-6Al-4V and Ti:5111 in seawater at ambient temperature (duplicate experiments).

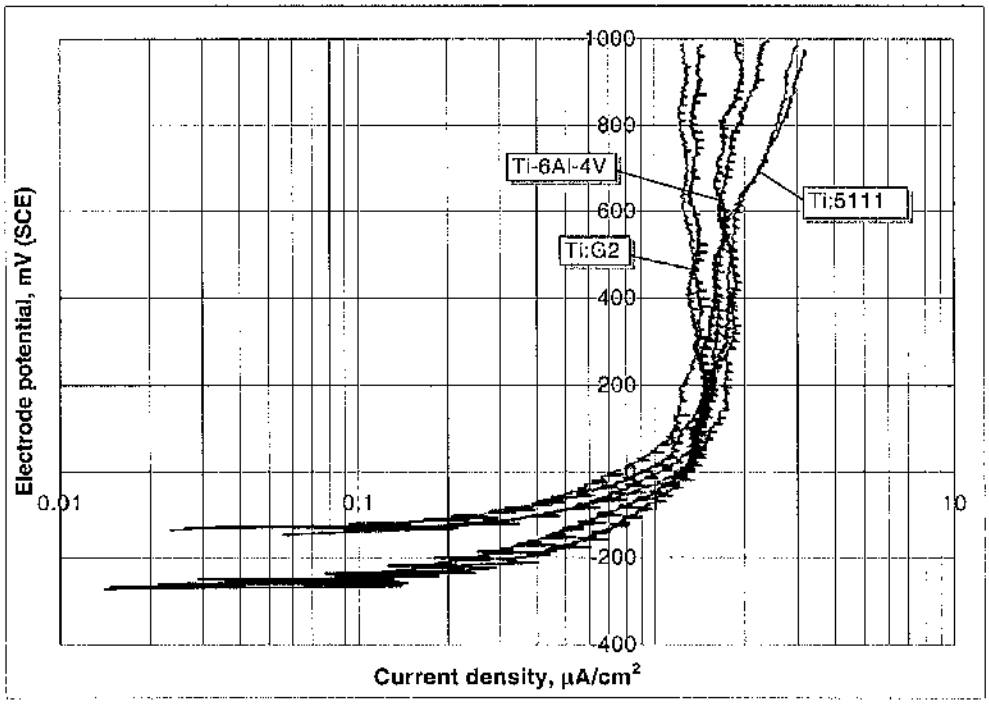

Figure 6.1.7. Anodic polarisation of Ti:G2, Ti-6Al-4V and Ti:5111 in seawater at 50°C (duplicate experiments).

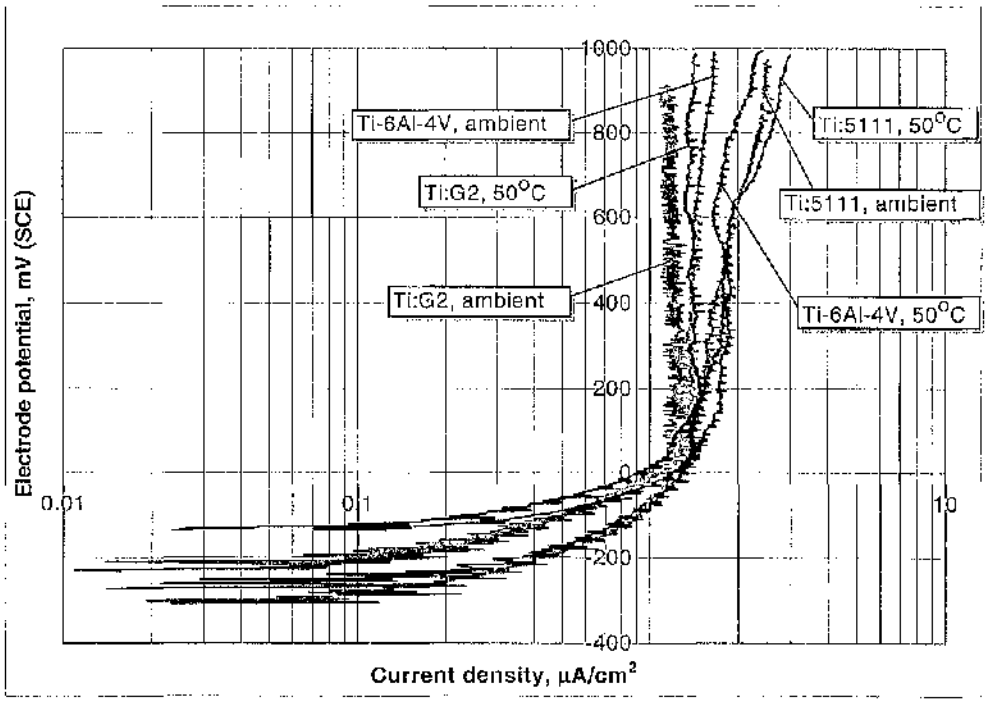

Figure 6.1.8. Anodic polarisation of Ti:G2, Ti-6Al-4V and Ti:5111 in seawater at ambient temperature in comparison to 50°C.

Microscopy

After the anodic polarisation tests in all static conditions described in this section, no sign of any corrosion damage was evident on the surface of Ti:G2, Ti-6Al-4V and Ti:5111. After testing, the samples of pure titanium and the two alloys were examined under the microscope and their surface looked just as bright as before they were tested and there was no evidence of pitting or crevice corrosion at the metal/resin interference.

6.2. Liquid erosion-corrosion conditions

All liquid erosion-corrosion tests, as stated earlier in the experimental techniques for erosion-corrosion tests section, were carried out for 12 hours in 3.5% NaCl; at an impinging velocity of 71.1 m/s. Apart from ambient water temperature, 50°C was also applied and in both cases total weight losses, over the 12 hour period, and anodic scans, at the end of the 12 hours, were obtained. For comparison reasons stainless steel 316L was also tested under all same conditions.

Liquid erosion-corrosion tests at ambient temperature and 50°C

Figure 6.2.1 shows the anodic polarisation curves of Ti:G2, Ti-6Al-4V, Ti:5111 and 316L generated from liquid erosion-corrosion tests at ambient temperature. A curve of Ti:G2 in static conditions is also included in the graph. Quite clearly, and as would normally be expected, Ti and Ti alloys are more corrosion resistant under static conditions although under liquid erosion-corrosion they still exhibit very passive behaviour. Furthermore, as shown in the graph, the rest potential in static tests was much more negative than the one in liquid erosion-corrosion, presumably due to concentration polarisation of the O_2-reduction cathodic reaction in static conditions. The anodic polarisation results demonstrate that over the 12 hour period of impingement a protective layer was formed on the surface of Ti and the two alloys. It is also evident that at early stages of the anodic scans both Ti and the alloys displayed a region of current fluctuation. This region is shown magnified in figure 6.2.2. Finally, it is quite obvious that under liquid impingement conditions 316L is more vulnerable and less corrosion resistant than Ti and Ti alloys since 316L clearly exhibits a breakdown to rapidly rising current at a potential of about +250 mV.

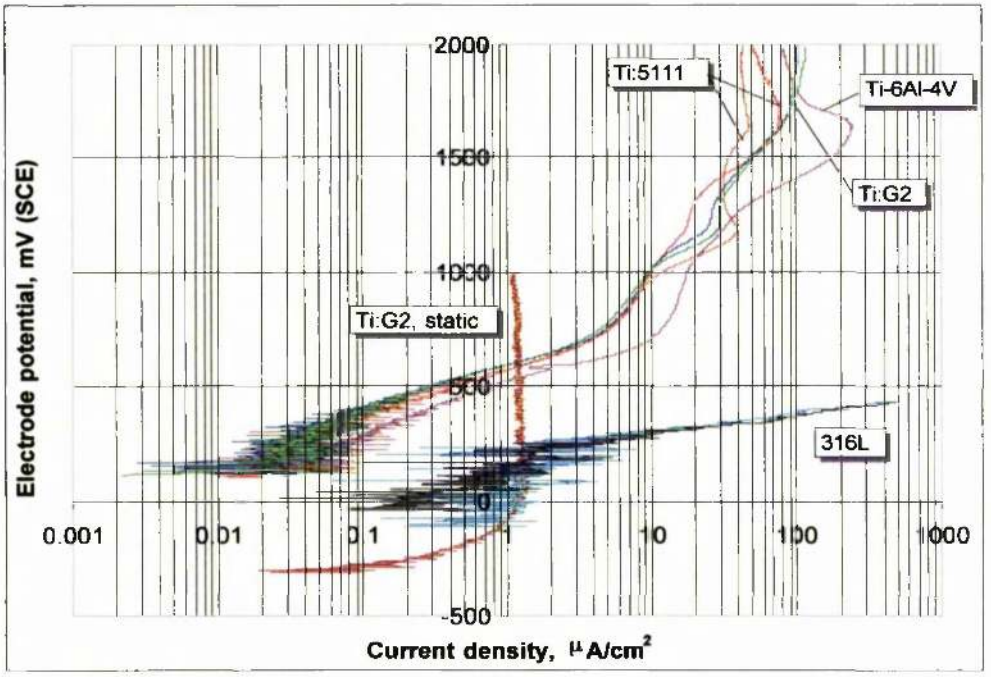

Figure 6.2.1. Anodic polarisation of Ti:G2, Ti-6Al-4V, Ti:5111 and 316L after 12 hours of liquid erosion-corrosion at ambient temperature. Ti:G2 under static conditions also shown.

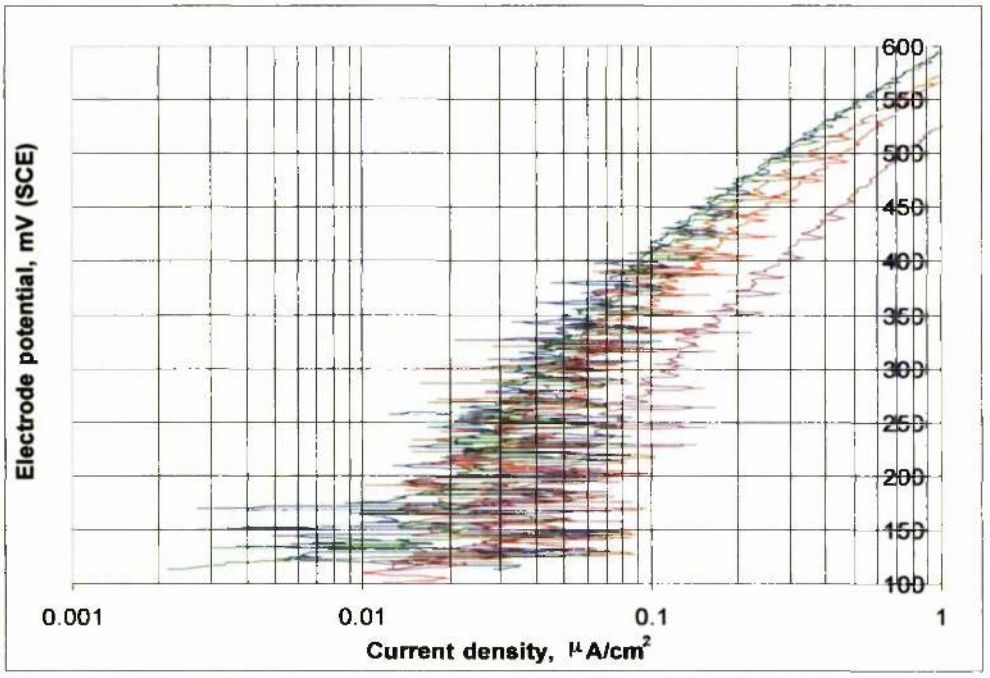

Figure 6.2.2. Magnification of Ti:G2, Ti-6Al-4V and Ti:5111 curves shown in figure 6.2.1, at the region of scattering.

Figure 6.2.3 shows the anodic polarisation curves of Ti:G2, Ti-6Al-4V, Ti:5111 and 316L generated from liquid erosion-corrosion tests at 50°C. A curve of Ti:G2 at ambient temperature is also shown. Similarly to static conditions, the increase of temperature to 50°C in liquid erosion-corrosion doesn't have any serious effect on the corrosion resistance of Ti:G2 and Ti:5111. However, at 50°C the scattering effect is much more intense and that indicates some possible instability in the performance of the passive film on the surface of the samples. On the other hand, Ti-6Al-4V looks more vulnerable than Ti:G2 and Ti:5111 and not as passive as at ambient temperature. Evidently, 316L exhibits much more active behaviour than both pure Ti and the two alloys at 50°C. In addition to that it is quite clear that under liquid erosion-corrosion conditions, the raise of temperature results in a significant drop in the corrosion resistance of 316L.

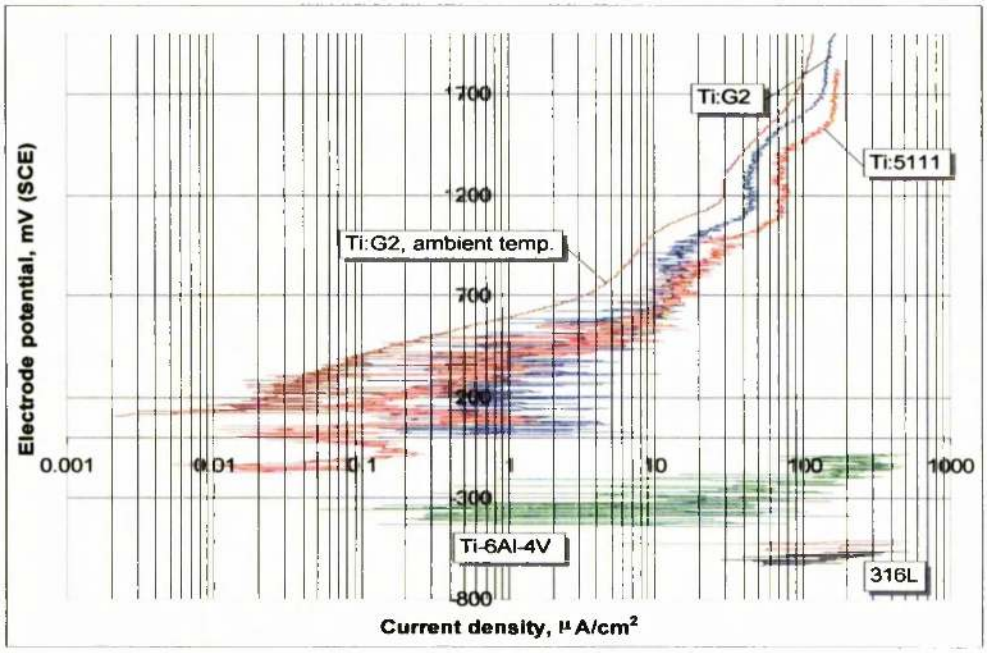

Figure 6.2.3. Anodic polarisation of Ti:G2, Ti-6Al-4V, Ti:5111 and 316L after 12 hours of liquid erosion-corrosion at 50°C. Ti:G2 at ambient temperature also shown.

Total weight loss tests

As mentioned earlier, liquid erosion-corrosion tests were also carried out to obtain total weight losses. Again, tests were conducted in 3.5% NaCl at an impinging velocity of 71.1 m/s. At both ambient temperature and 50°C, and over the usual 12 hour period, Ti:G2, Ti:5111 and Ti-6Al-4V did not exhibit any evidence of measurable weight loss. Under the same conditions, 316L also exhibited zero weight loss at ambient temperature. However at 50°C 316L gave a weight loss of 0.2 mg in each of two tests. Clearly, high temperature has a deleterious effect on the erosion-corrosion resistance of this stainless steel and this is in agreement with the relevant anodic polarisation results (figure 6.2.3) for 316L presented in the previous section.

Microscopy

Liquid erosion-corrosion tests at ambient temperature

Samples of Ti:G2, Ti-6Al-4V and Ti:5111 did not exhibit any detectable effect on their surface either visually or under the light microscope when subjected to ambient temperature liquid erosion-corrosion tests for 12 hours at 71.1 m/s without electrochemical intervention. However, anodic polarisation at the end of the 12 hours led to the formation of clearly visible fully developed films producing interference colours on the surface of both pure Ti and the two alloys. These interference colours clearly represented the presence of films thicker than the normal (invisible to the eye) passive film on titanium.

Figure 6.2.4 shows the surface of Ti:G2 as a whole after anodically polarised after 12 hours of liquid erosion-corrosion at ambient temperature and 71.1 m/s. No evidence of any corrosion or erosion damage was present except for the development of a visible film which covered the entire surface. Apparently the hydrodynamic conditions led to the formation of layers of different thicknesses in a circular arrangement starting from the centre of the specimen as demonstrated by the different interference colours. Figure 6.2.5 shows at higher magnification part of the surface outside the central region. Scratches reveal bare metal underneath the film at locations where damage during handling after the experiment had occurred. It should be emphasised by reference back to the anodic polarisation curves (figure 6.2.1) that

these films formed after polarisation of the specimen to the very positive potentials (+ 2000 mV) and high current densities (50 – 100 $\mu A/cm^2$).

Figure 6.2.6 shows the surface of a Ti-6Al-4V sample as a whole when anodically polarised after 12 hours of liquid erosion-corrosion at 71.1 m/s. Again no signs of any corrosion or erosion damage were observed but a clearly visible film of various thicknesses covered the entire surface. However at a circular region around the centre of the specimen the film appeared to be not as intense as on the rest of the matrix area. This is also shown at higher magnification in figure 6.2.7.

Similarly to Ti:G2 and Ti-6Al-4V, and under the same conditions, Ti:5111 developed no corrosion or erosion damage and demonstrated more or less the same features after anodic polarisation (figure 6.2.8). The rather faint half circular region around the centre of the specimen is also shown at higher magnification in figure 6.2.9 where it becomes quite evident that its film is not as intense and uniform as the one covering the centre of the specimen.

Figure 6.2.10 shows the surface of 316L as a whole after 12 hours of liquid erosion-corrosion at 71.1 m/s without anodic polarisation. An interesting feature that was observed was a rather faint dark ring around the centre of the specimen. This ring is shown at higher magnification in figure 6.2.11 where it becomes quite evident that it consists of a non-uniform surface in contrast to the centre and the rest of the metal matrix. There was hardly any damage in the centre of the specimen (figure 6.2.12) apart from some possible pitting initiation.

Figure 6.2.13 shows some definite damage in the centre of a 316L stainless steel sample when anodically polarised after 12 hours of liquid erosion-corrosion at 71.1 m/s. Clearly the anodic polarisation had a deleterious effect on 316L. At higher magnification, the area around the centre (figure 6.2.14) appeared to be largely nonuniform. Further out, where the surface was back to a more or less uniform state, a few comets were present. Figure 6.2.15 shows at very high magnification a small comet with a pit at its head. It also shows a scratch and a small bright patch of bare

metal which indicate the formation of a surface film, although undoubtedly it was of different thickness and also less protective as those on pure Ti and the two alloys.

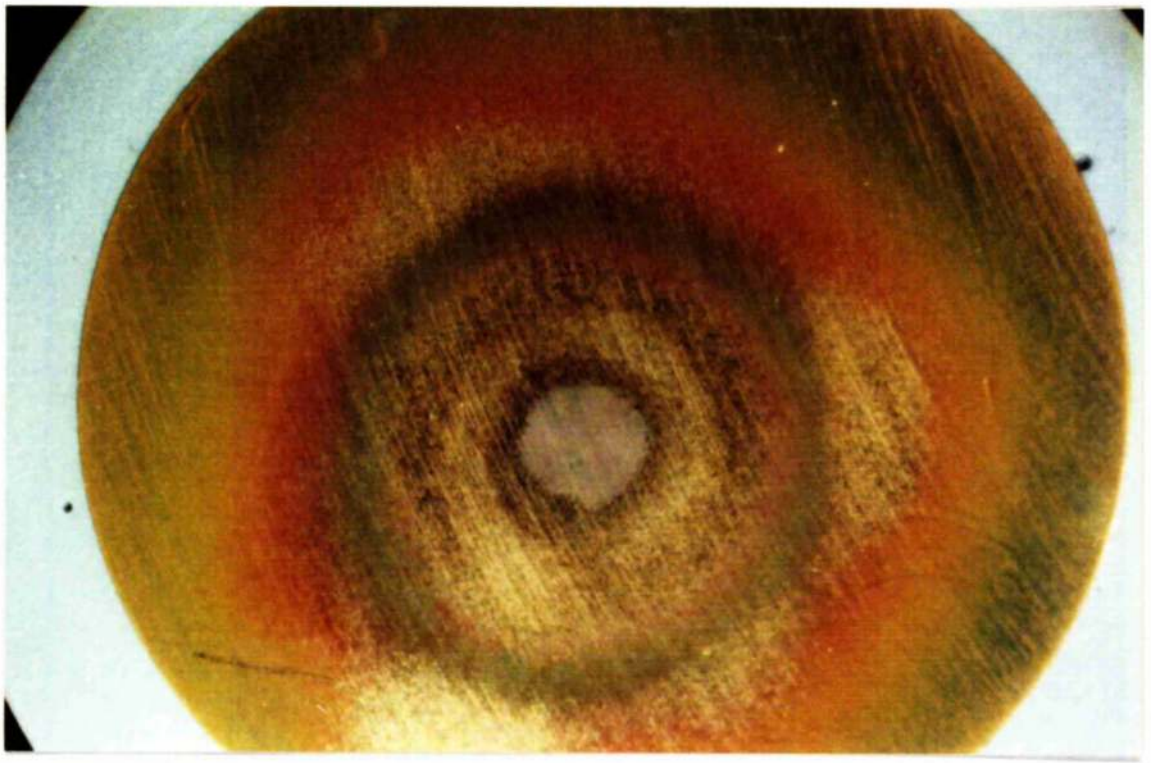

Figure 6.2.4. Ti:G2 when anodically polarised after 12 hours of liquid erosion-corrosion at ambient temperature and 71.1 m/s impinging jet velocity (diameter of specimen 32 mm).

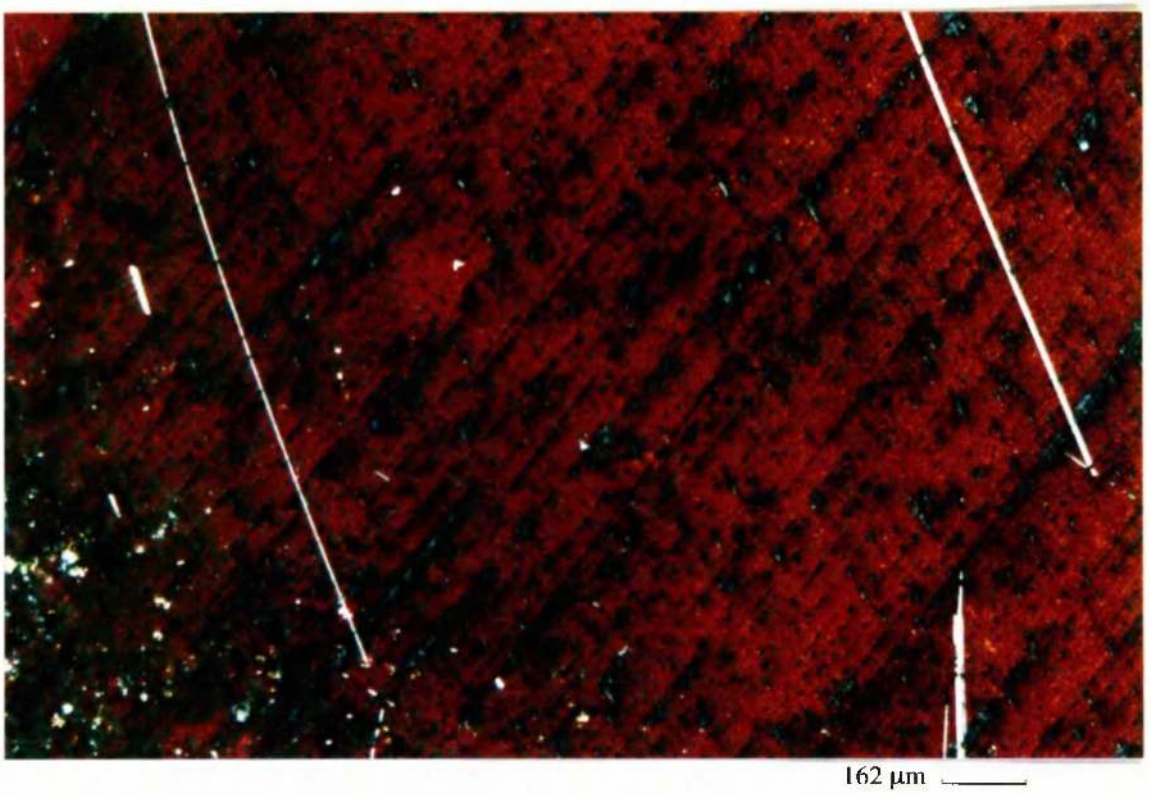

Figure 6.2.5. Part of the surface outside the central region of the Ti:G2 specimen shown in figure 6.2.4. Scratches reveal bear metal underneath.

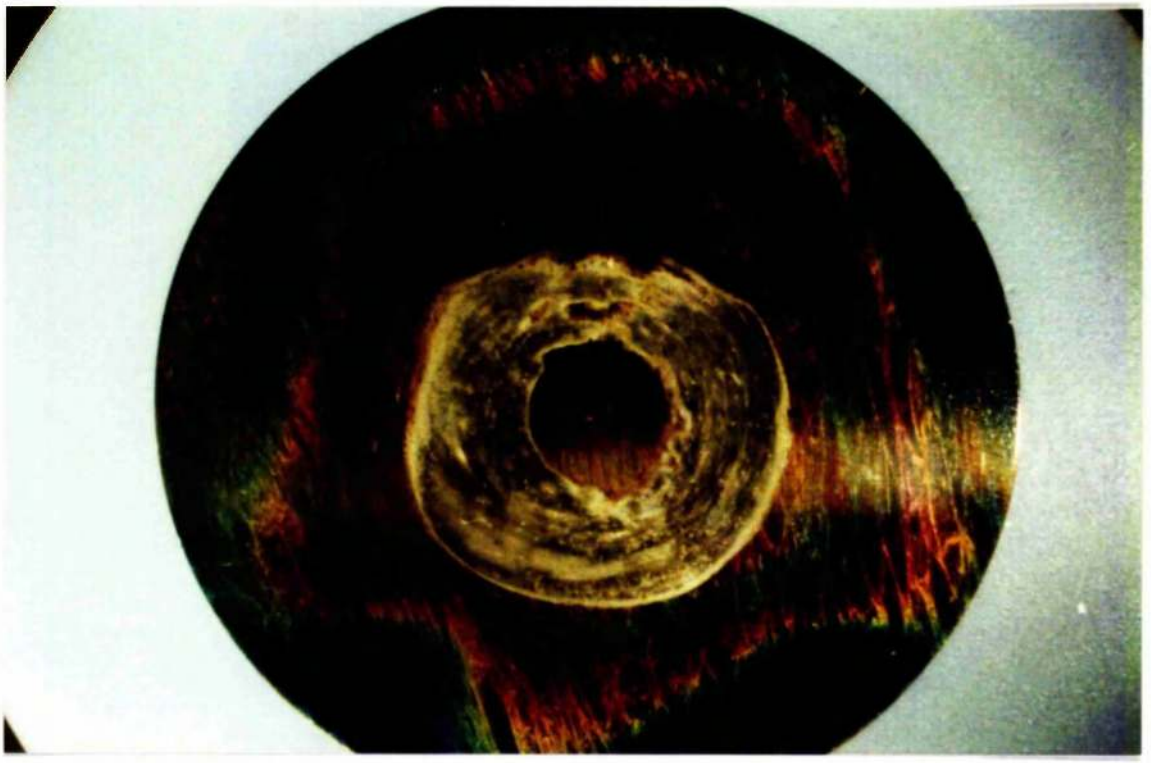

Figure 6.2.6. Ti-6Al-4V when anodically polarised after 12 hours of liquid erosion-corrosion at ambient temperature and 71.1 m/s impinging jet velocity (diameter of specimen 26 mm).

Figure 6.2.7. At higher magnification, film at white circular region round the centre of the Ti-6Al-4V specimen shown in figure 6.2.6 appears to be not as intense as on the rest of the matrix area.

Figure 6.2.8. Ti-5111 when anodically polarised after 12 hours of liquid erosion-corrosion at ambient temperature and 71.1 m/s impinging jet velocity (diameter of specimen 26 mm).

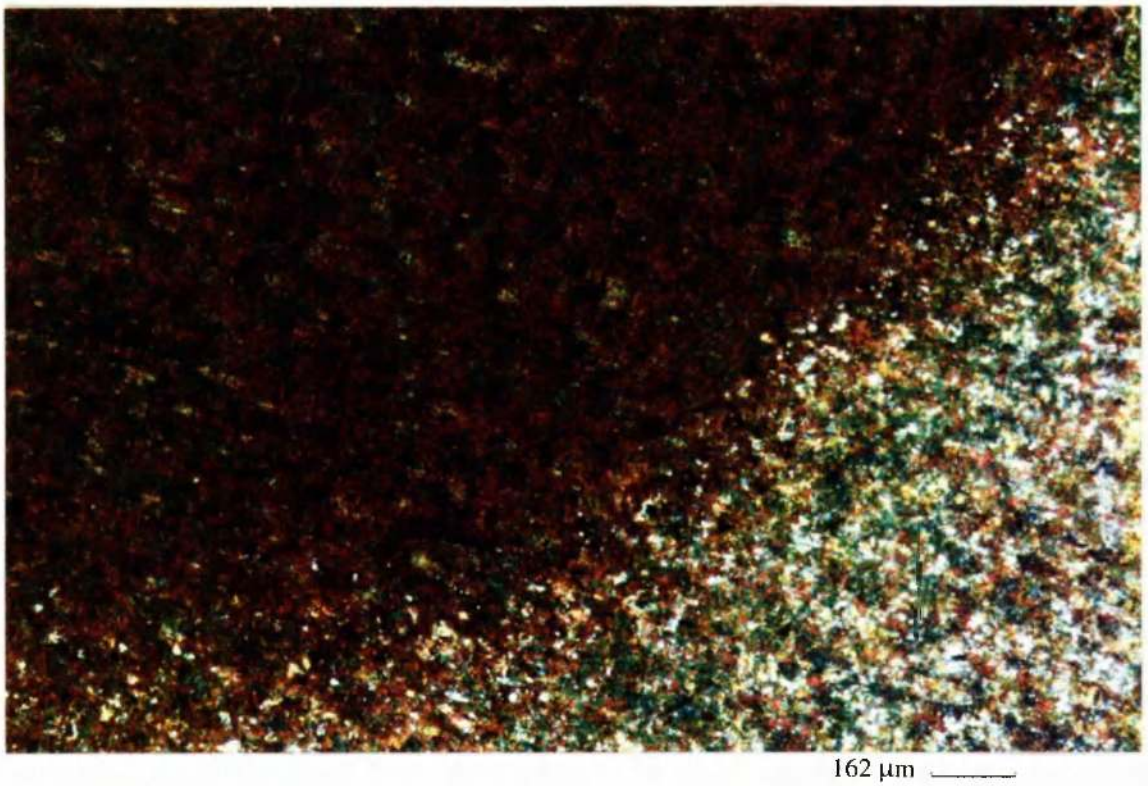

Figure 6.2.9. At higher magnification, film at faint half circular region round the centre of the Ti-5111 specimen shown in figure 6.2.8 appears to be weak and not as intense and uniform as at the centre.

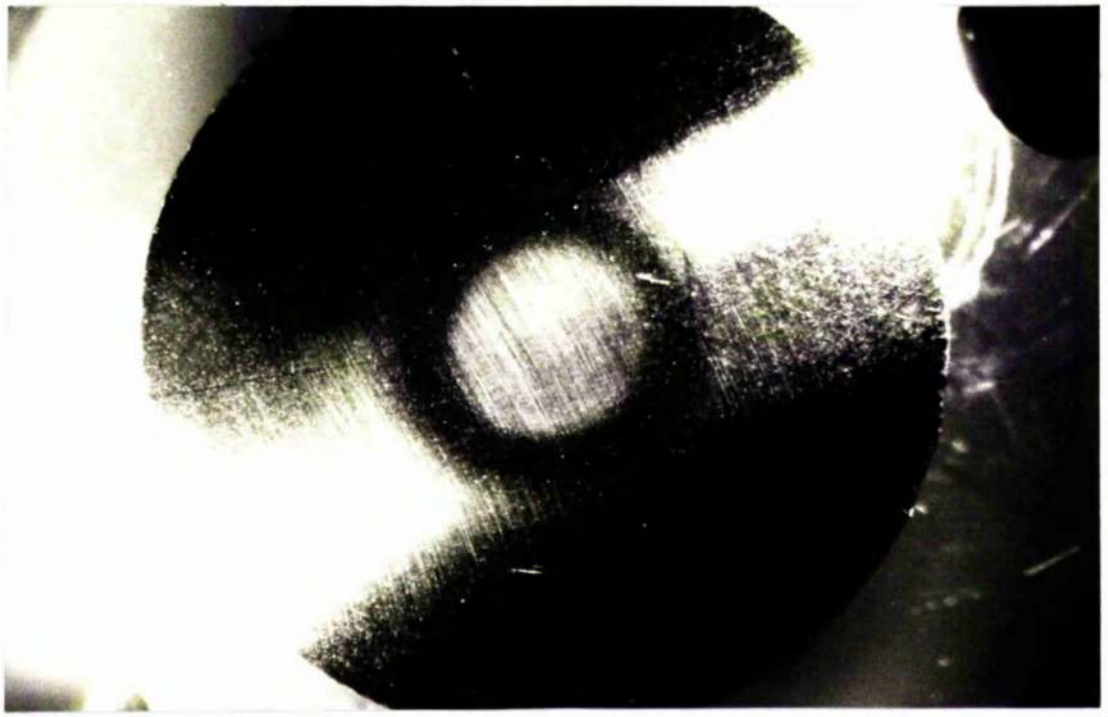

Figure 6.2.10. 316L as a whole after 12 hours of liquid erosion-corrosion at ambient temperature and 71.1 m/s impinging jet velocity (diameter of specimen 26 mm).

Figure 6.2.11. At higher magnification, ring round the centre of the 316L specimen shown in figure 6.2.10 consists of disuniformed surface.

Figure 6.2.12. Clean surface with some possible pitting initiation in the centre of the 316L specimen shown in figure 6.2.10.

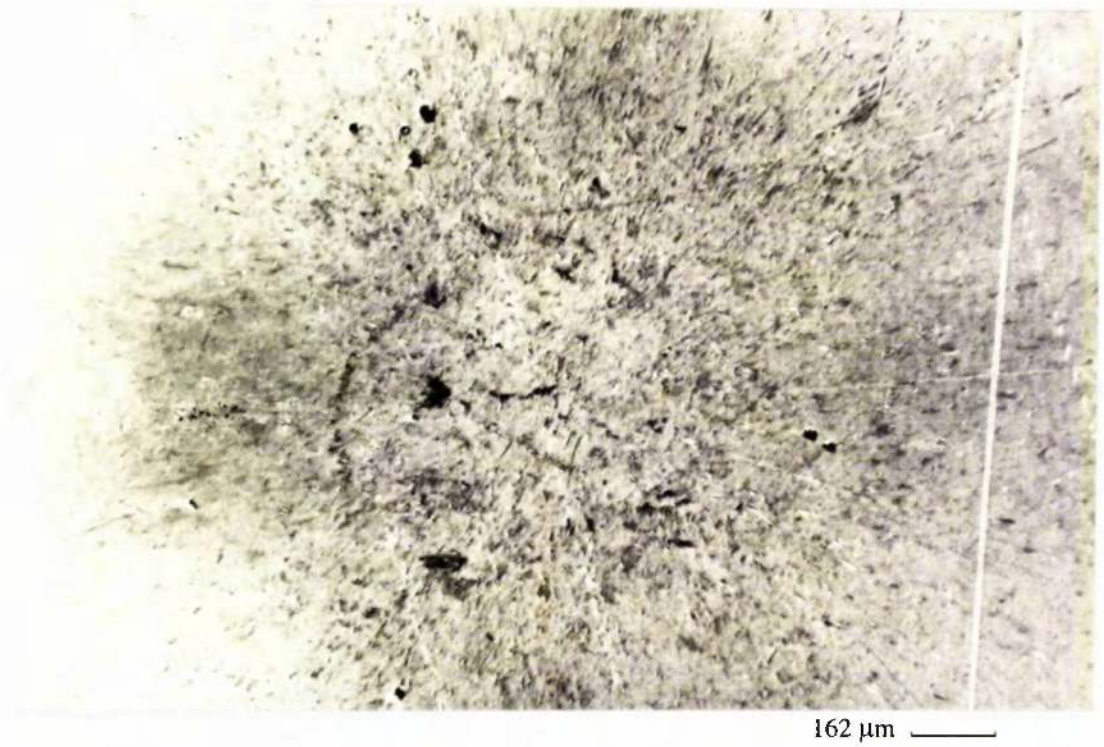

Figure 6.2.13. Damage in the centre of 316L specimen when anodically polarised after 12 hours of liquid erosion-corrosion at ambient temperature and 71.1 m/s impinging jet velocity.

Figure 6.2.14. At higher magnification, the area round the centre of the 316L specimen in figure 6.2.13 appeared to quite disuniformed.

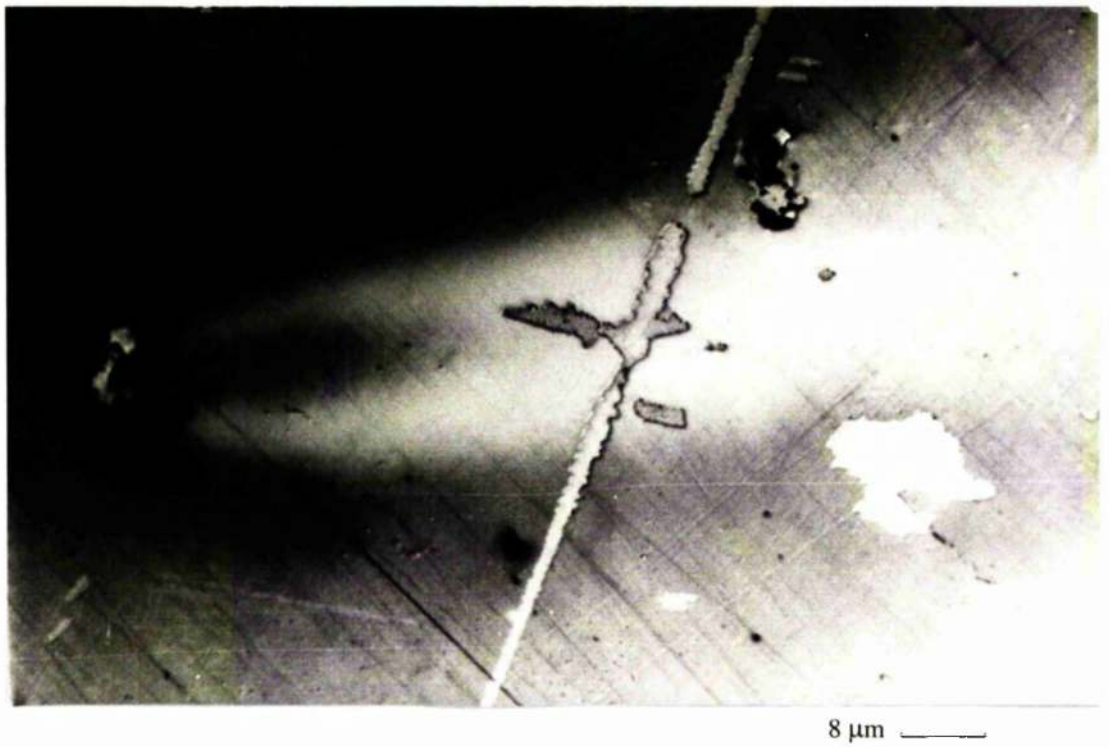

Figure 6.2.15. Comet with pit at its head on the 316L specimen also shown in the previous two figures. Scratch and bright patch of bare metal indicate the presence of passive film.

Liquid erosion-corrosion tests at 50°C

Figures 6.2.16 to 6.2.24 show surface features of specimens after 12 hours of liquid erosion-corrosion at 50°C and 71.1 m/s impinging jet velocity **without any electrochemical intervention**. Figure 6.2.16 shows the surface of Ti:G2 as a whole. The formation of rings around the centre of impingement, apparently under the influence of the hydrodynamic conditions, is quite obvious while the rest of the metal matrix remained clean and bright. Figure 6.2.17 shows at higher magnification the centre of impingement (right part of the photograph) with the first dark ring around the centre and the next brighter region. Evidently, pitting developed both in the centre region and around the centre of the specimen in contrast to 12 hours liquid erosion-corrosion at ambient temperature where pitting did not occur at all. A second specimen of Ti:G2 exposed to the same experimental conditions showed similar features to the above, i.e. pits in the centre and also discontinuous patches of blue film in the bright ring between the two darker rings (figure 6.2.18).

Figure 6.2.19 shows the surface of Ti-6Al-4V as a whole after 12 hours of liquid erosion-corrosion at 50°C and 71.1 m/s impinging jet velocity. Similarly to Ti:G2, the presence of coloured rings and pits in the centre (impinging target) (figure 6.2.20) of the specimen were quite evident. Again, this is in contrast with the relative 12-hour liquid erosion-corrosion tests on Ti-6Al-4V at ambient temperature where coloured rings and pits in the centre were totally absent.

Similar to Ti:G2 and Ti-6Al-4V, and under the same experimental conditions, Ti:5111 also developed coloured rings around the centre while the rest of the metal matrix remained clean and bright (figure 6.2.21). However, unlike Ti:G2 and Ti-6Al-4V, pitting was not observed on the surface of Ti:5111.

Twelve hour liquid erosion-corrosion tests at 50°C and 71.1 m/s impinging velocity were also carried out on 316L stainless steel. Figure 6.2.22 shows similar rings on 316L as on Ti and the alloys., although the films consisting the rings were not as coloured. Figures 6.2.23 and 6.2.24 show pits and other general surface attack in the centre and further out respectively. Clearly enough, under liquid erosion-corrosion at 50°C pitting on 316L appears to be more intense than on Ti:G2 and Ti-6Al-4V.

Figures 6.2.25 – 6.2.27 show the surface of Ti:G2, Ti-6Al-4V and Ti:5111 respectively as a whole when anodically polarised after 12 hours of liquid erosion-corrosion at 50°C and 71.1 m/s impinging velocity. It is noticeable that the films formed on Ti and the alloys after anodic polarisation at 50°C are more extensive than in the case of free liquid erosion-corrosion at 50°C.

Figures 6.2.28 and 6.2.29 show respectively at higher magnification a scratch along the outer region of Ti:G2 and bare patches in the impinging region of Ti:G2 (specimen shown in figure 6.2.25) where the film was damaged. Since in free liquid erosion-corrosion conditions at 50°C Ti:G2 suffered some obvious pitting (see figure 6.2.17), it is fair to presume that after anodic polarisation the film apparently obliterated any possible damage due to pitting.

Figure 6.2.30 shows rings of film on a 316L specimen that was anodically polarised after 12 hours of liquid erosion-corrosion at 50°C and 71.1 m/s impinging velocity. The surface around the rings consists of 'bare metal' which implies the presence of a very thin film. Under these experimental conditions, severe pitting in the impinging region (figure 6.2.31) is the main feature of 316L.

In an attempt to determine the chemical composition of the films developed on the Ti-base materials after 12 hours of liquid erosion-corrosion at 50°C and 71.1 m/s, anodically polarised specimens Ti:G2 and Ti:5111 (shown in figures 6.2.25 and 6.2.27 respectively) were subjected under S.E.M. examination. Unfortunately, the films proved to be too thin to be detected and therefore chemically analysed.

However, at high magnification the various zones of film on the Ti:5111 specimen appeared to possess different roughness. The region of the Ti:5111 specimen directly under the impinging jet was clearly non-uniform (figure 6.2.32) while the surface covered by the first dark ring (dark-blue in colour as shown in figure 6.2.27) around the impinging target remained smooth (figure 6.2.33). However, the part of the film on the outer edge of the first dark ring appeared to be highly affected and quite rough (figure 6.2.34). That was followed by the light coloured ring shown in figure 6.2.27, which was noted to be as uniform as the first dark ring described just earlier. Another region on the Ti:5111 specimen that featured film of rather high roughness was the

outer edge (figure 6.2.35) of the light coloured ring and beyond that the rest of the surface was quite smooth and featureless.

Rings of different roughness on the Ti:G2 specimen were not as well defined as on the Ti:5111 specimen since the film on Ti:G2 covered rather evenly the entire surface. Quite interestingly, directly under the impinging jet, Ti:G2 (figure 7.2.36) developed much thicker film than Ti:5111 (figure 7.2.37).

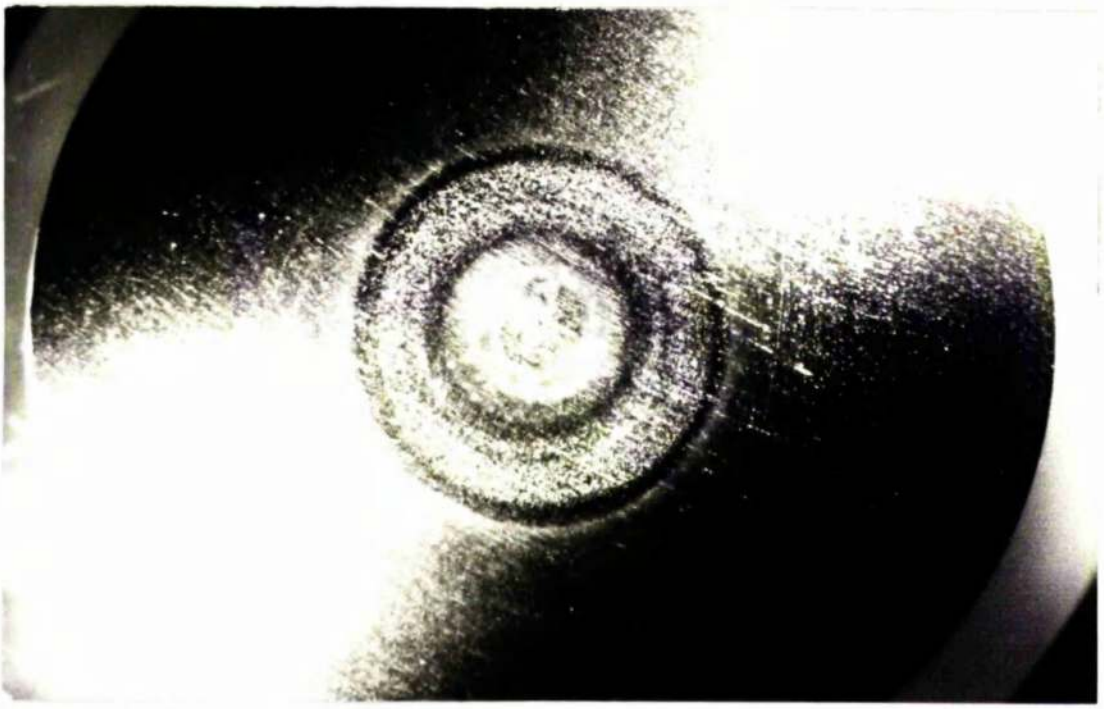

Figure 6.2.16. Ti:G2 after 12 hours of liquid erosion-corrosion at 50°C and 71.1 m/s impinging jet velocity **without electrochemical intervention** (diameter of specimen 32 mm).

Figure 6.2.17. Centre of impingement (right side), first dark ring and next brighter region with pits on the Ti:G2 specimen shown in figure 6.2.16.

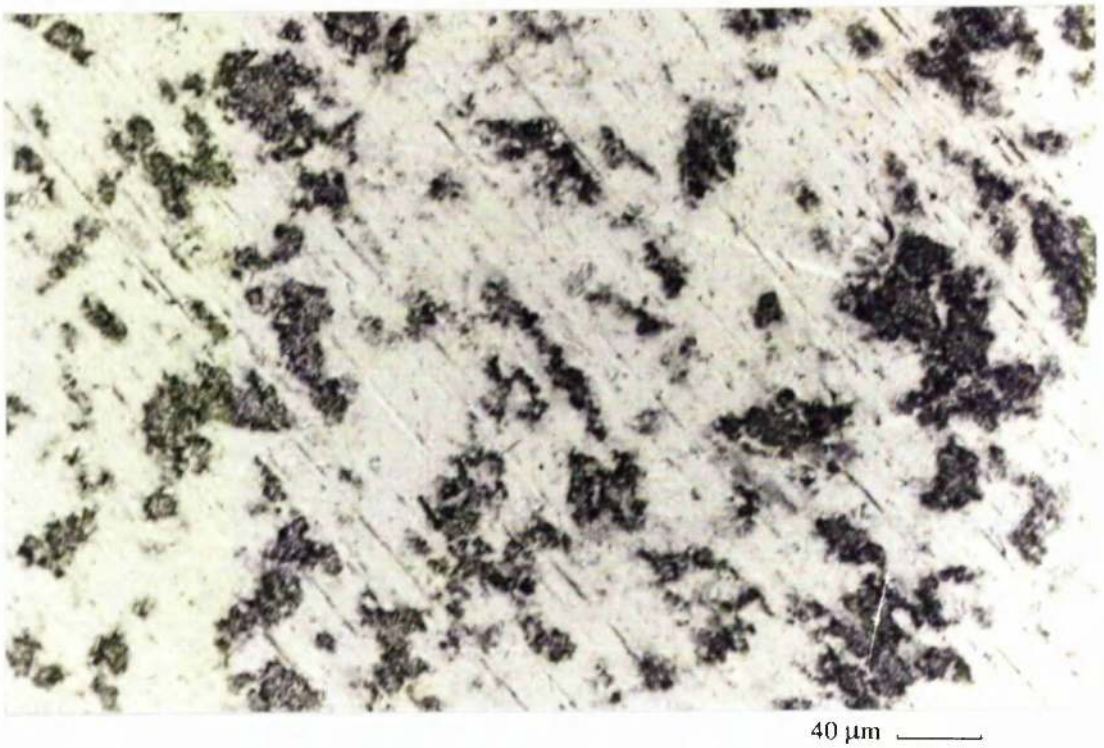

Figure 6.2.18. Discontinuing patches of blue film on Ti:G2 in the bright ring between the two darker rings shown in figure 6.2.16.

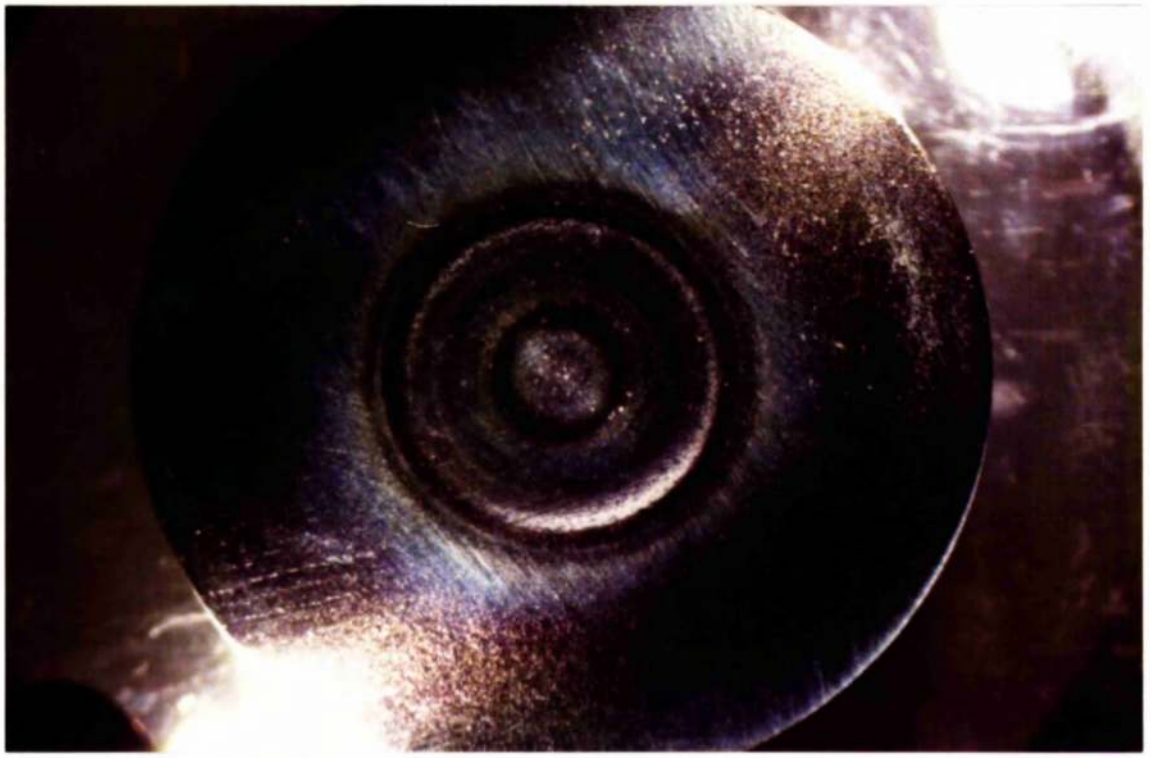

Figure 6.2.19. Ti-6Al-4V after 12 hours of liquid erosion-corrosion at 50°C and 71.1 m/s impinging jet velocity **without electrochemical intervention** (diameter of specimen 26 mm).

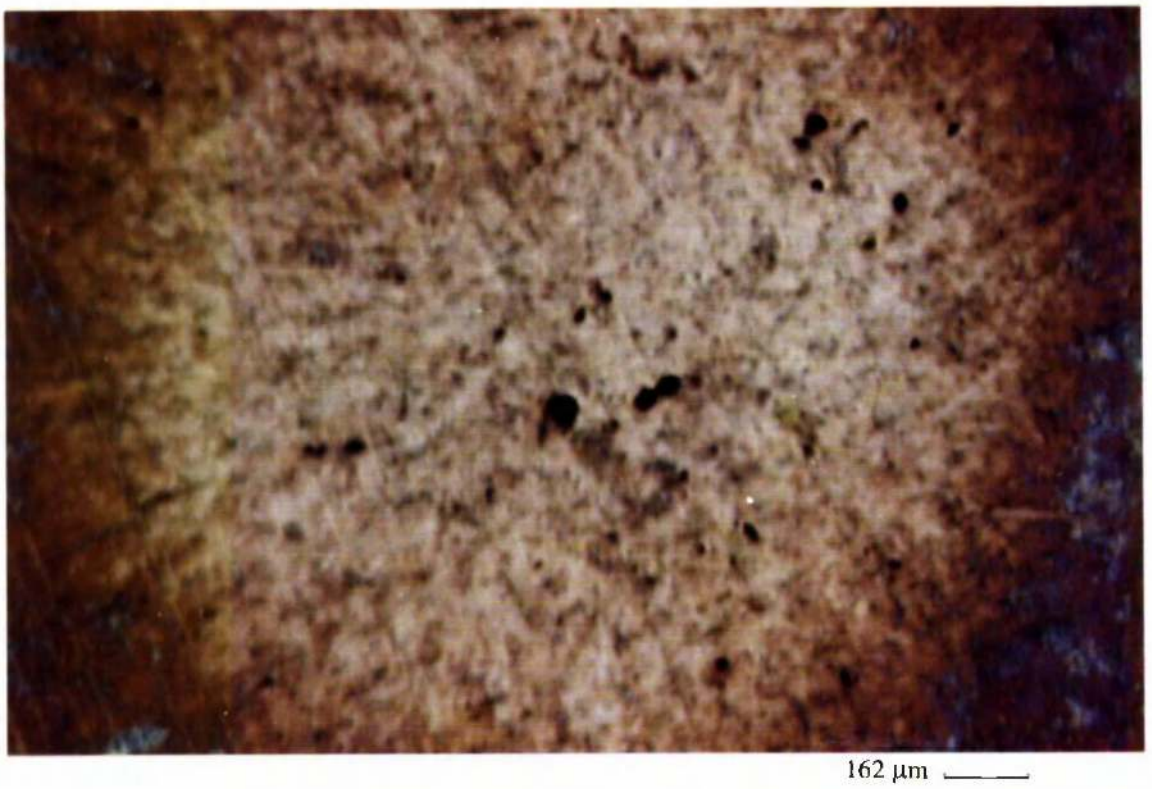

Figure 6.2.20. Pits in the centre (impinging region) of the Ti-6Al-4V specimen shown in figure 6.2.19.

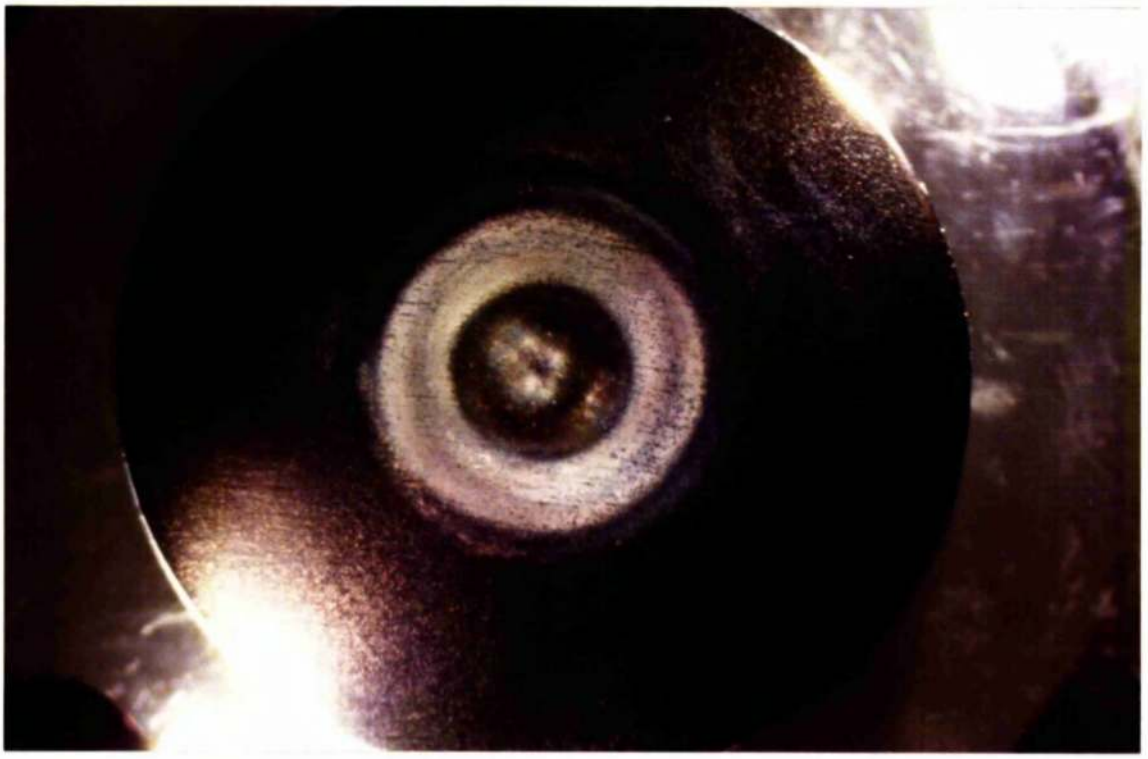

Figure 6.2.21. Ti:5111 after 12 hours of liquid erosion-corrosion at 50°C and 71.1 m/s impinging jet velocity **without electrochemical intervention** (diameter of specimen 26 mm).

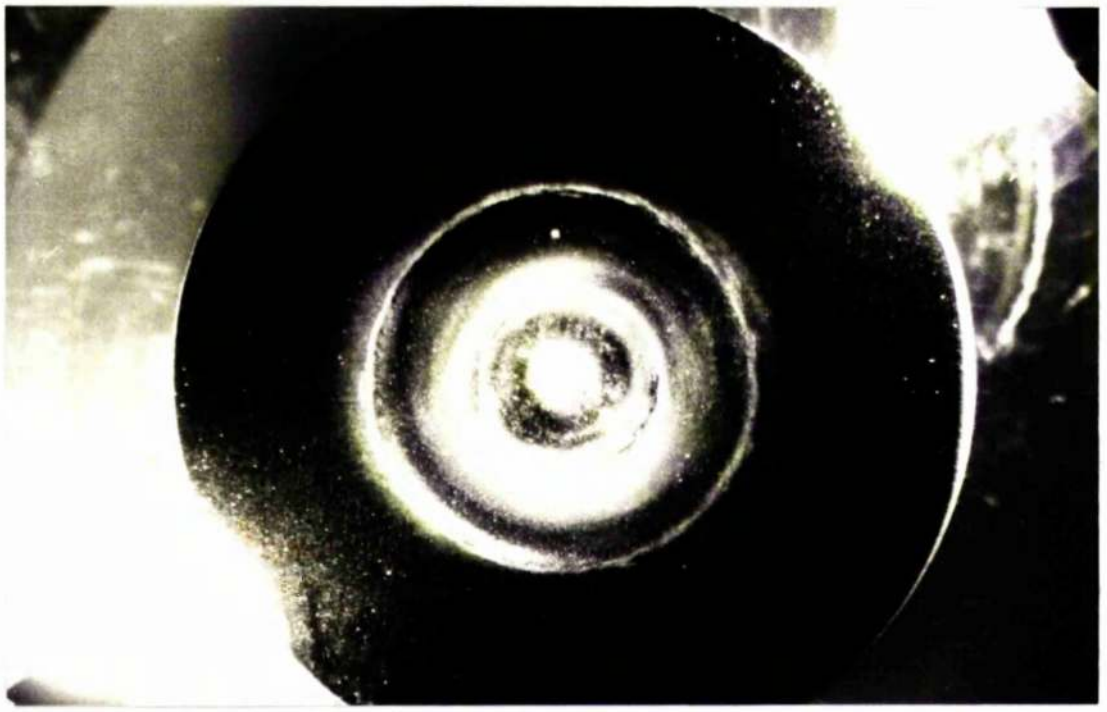

Figure 6.2.22. 316L after 12 hours of liquid erosion-corrosion at 50°C and 71.1 m/s impinging jet velocity **without electrochemical intervention** (diameter of specimen 26 mm).

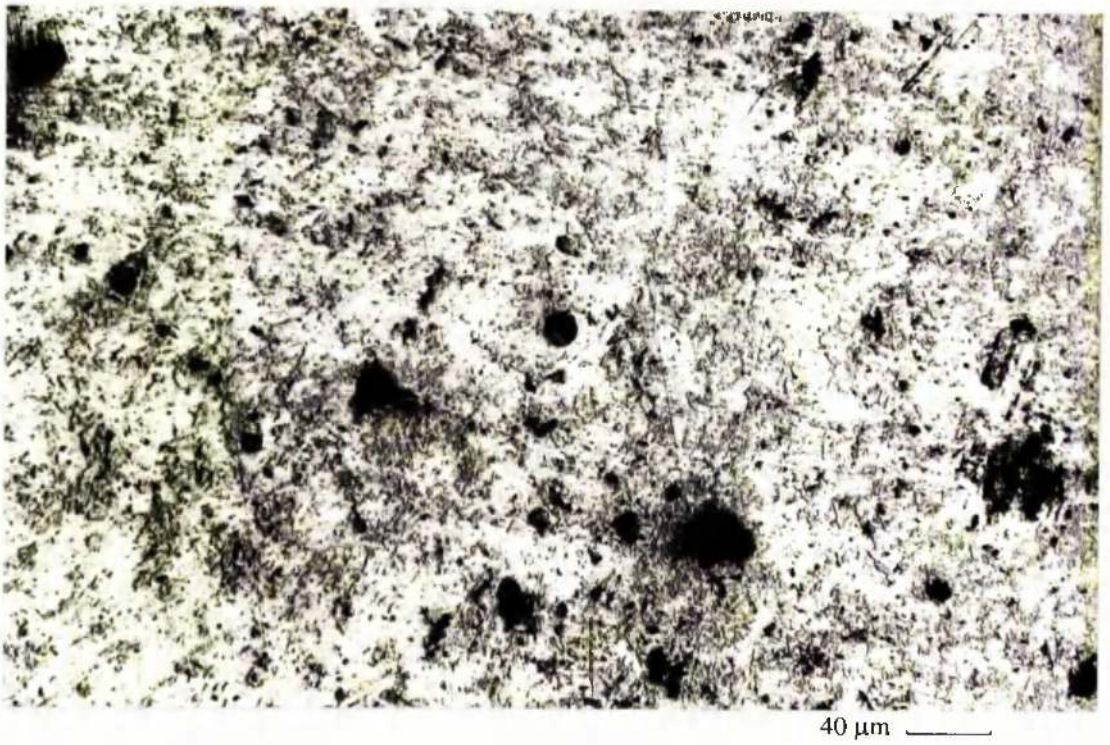

Figure 6.2.23. Pits in the centre (impinging region) of the 316L specimen shown in figure 6.2.22.

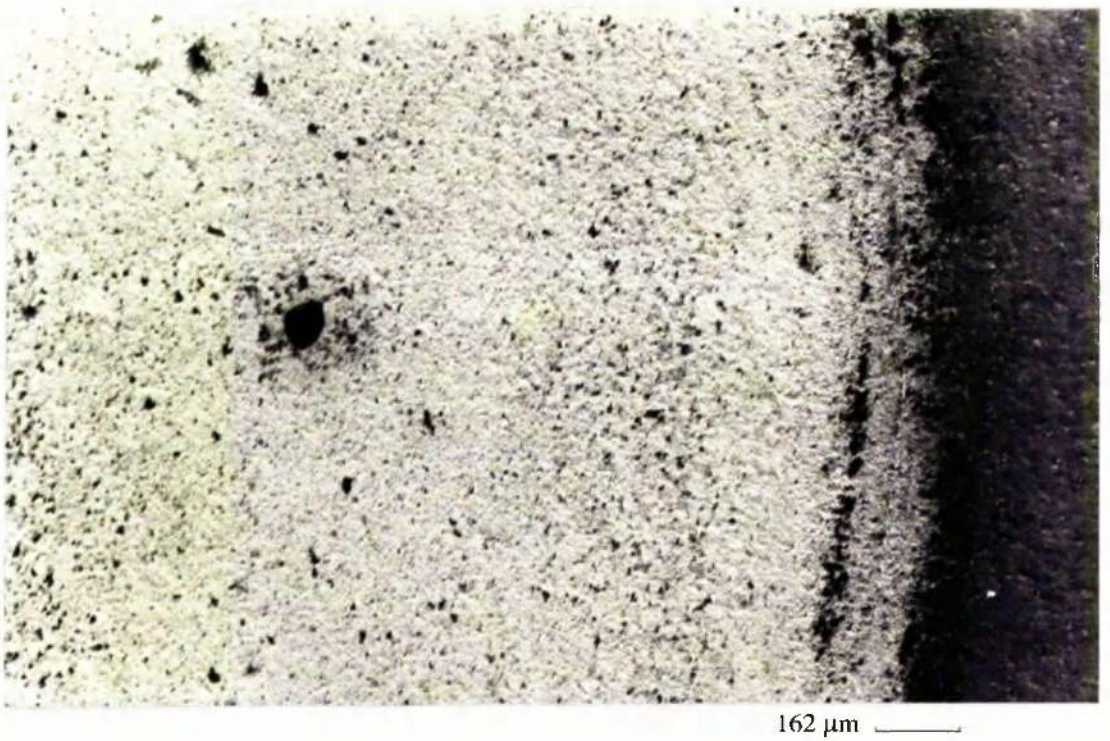

Figure 6.2.24. Pits outside the centre of the 316L specimen shown in figure 6.2.22. Last dark ring towards the outer surface also shown on the right of the photo.

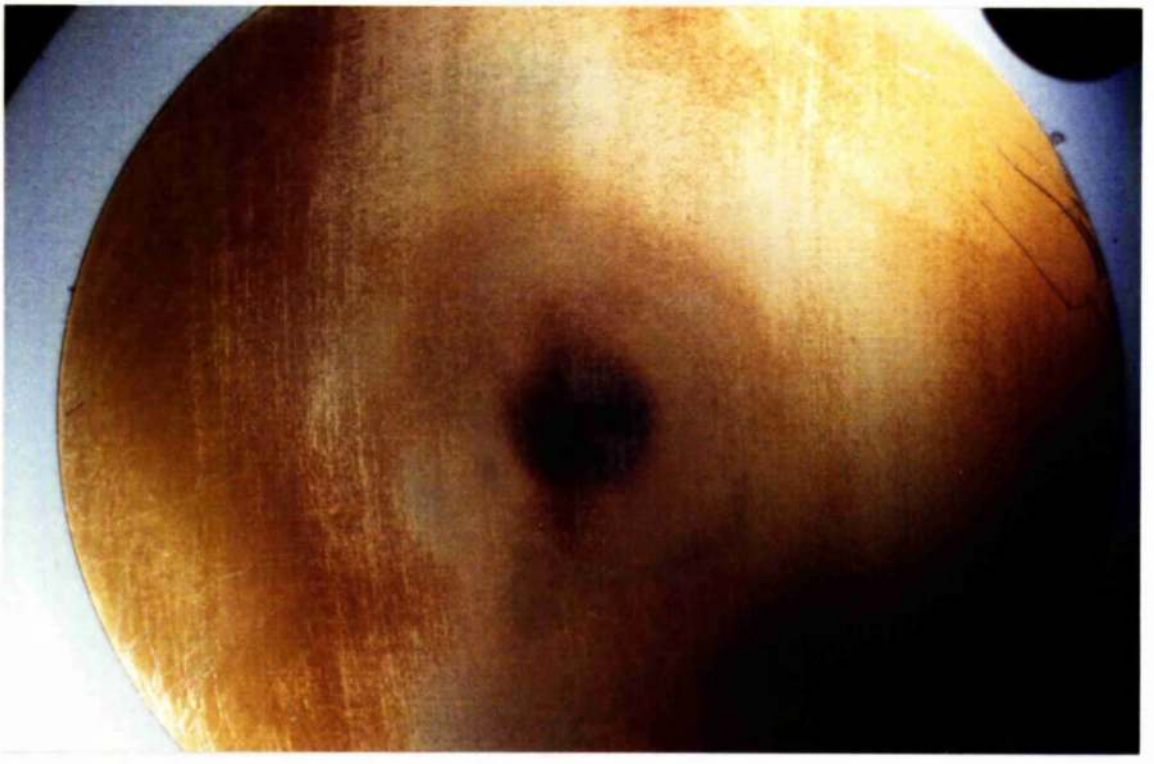

Figure 6.2.25. Ti:G2 when anodically polarised after 12 hours of liquid erosion-corrosion at 50°C and 71.1 m/s impinging jet velocity (diameter of specimen 32 mm).

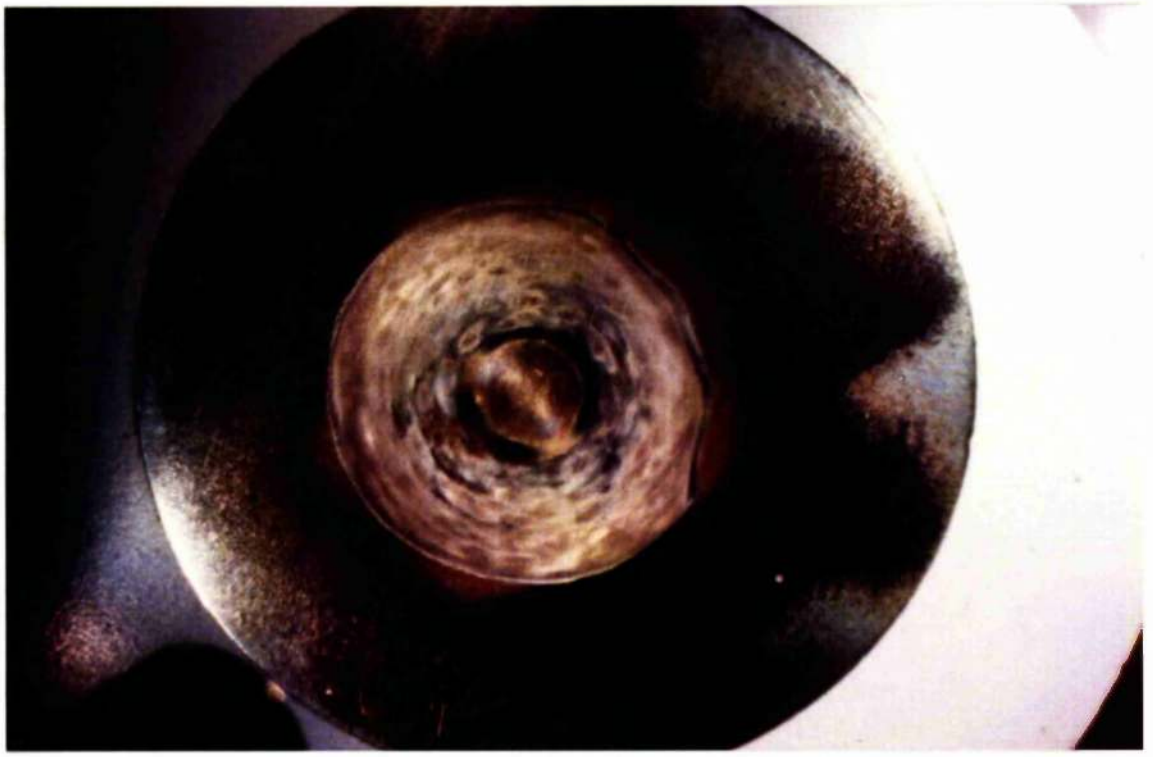

Figure 6.2.26. Ti-6Al-4V when anodically polarised after 12 hours of liquid erosion-corrosion at 50°C and 71.1 m/s impinging jet velocity (diameter of specimen 26 mm).

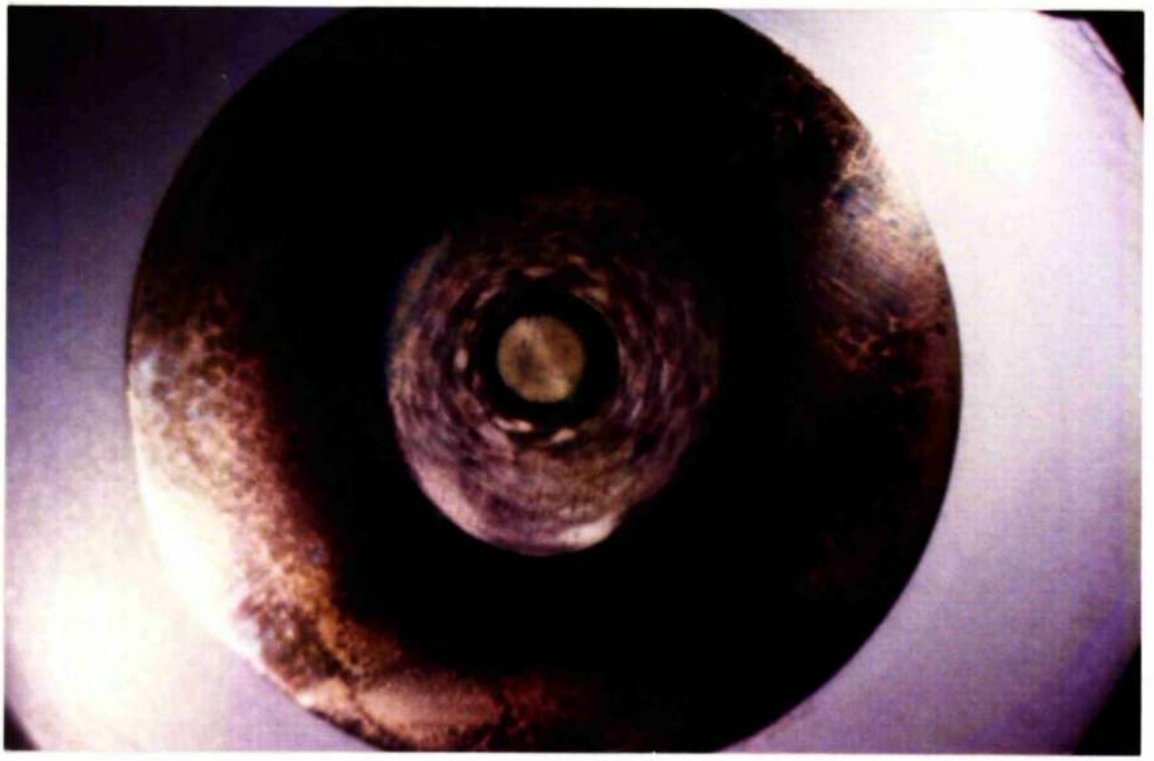

Figure 6.2.27. Ti:5111 when anodically polarised after 12 hours of liquid erosion-corrosion at 50°C and 71.1 m/s impinging jet velocity (diameter of specimen 26 mm).

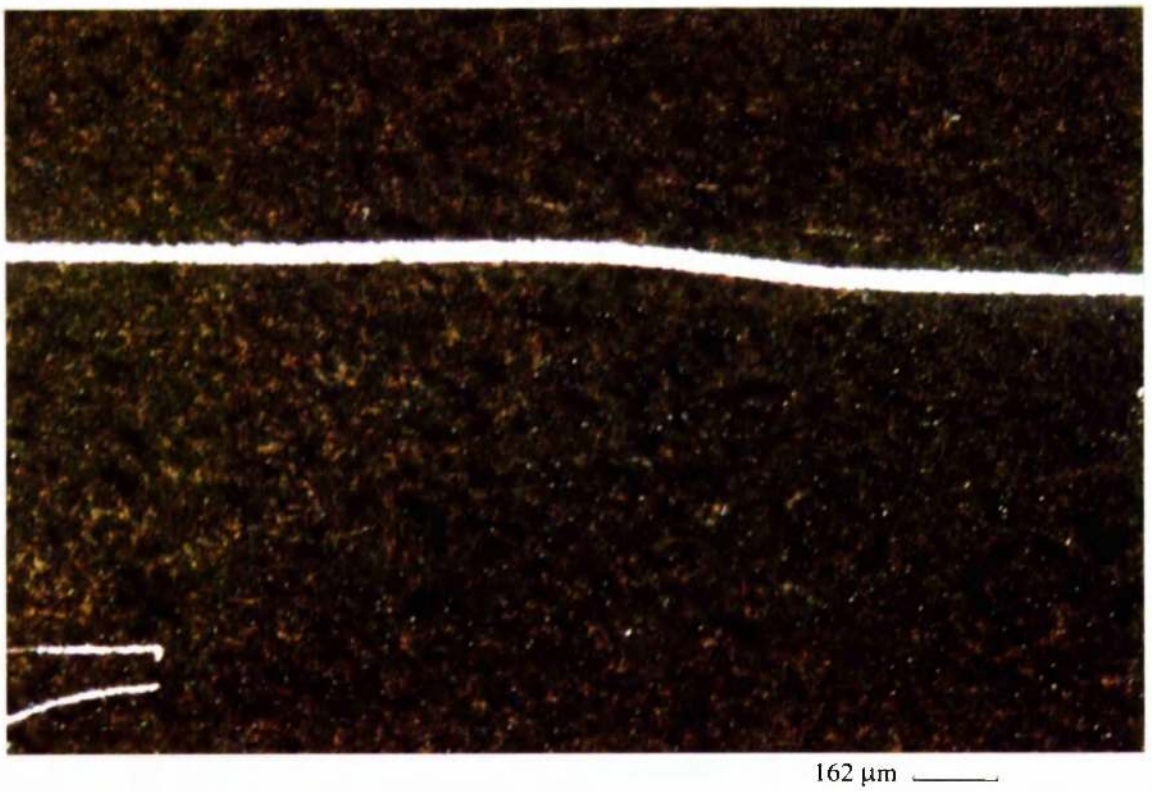

Figure 6.2.28. Part of the surface outside the central region of the Ti:G2 specimen shown in figure 6.2.25. Scratches reveal bare metal underneath.

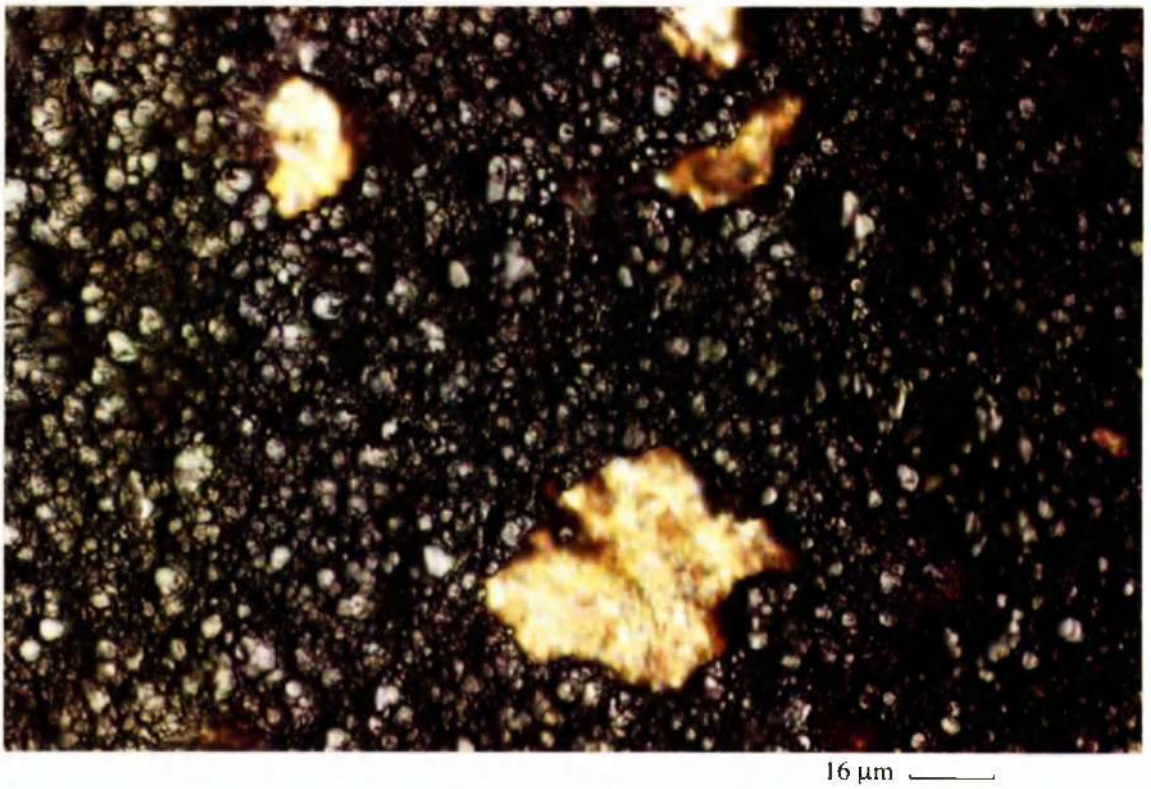

Figure 6.2.29. Bare patches ,where the film was damaged, in the impinging region of the Ti:G2 specimen shown in figure 6.2.25.

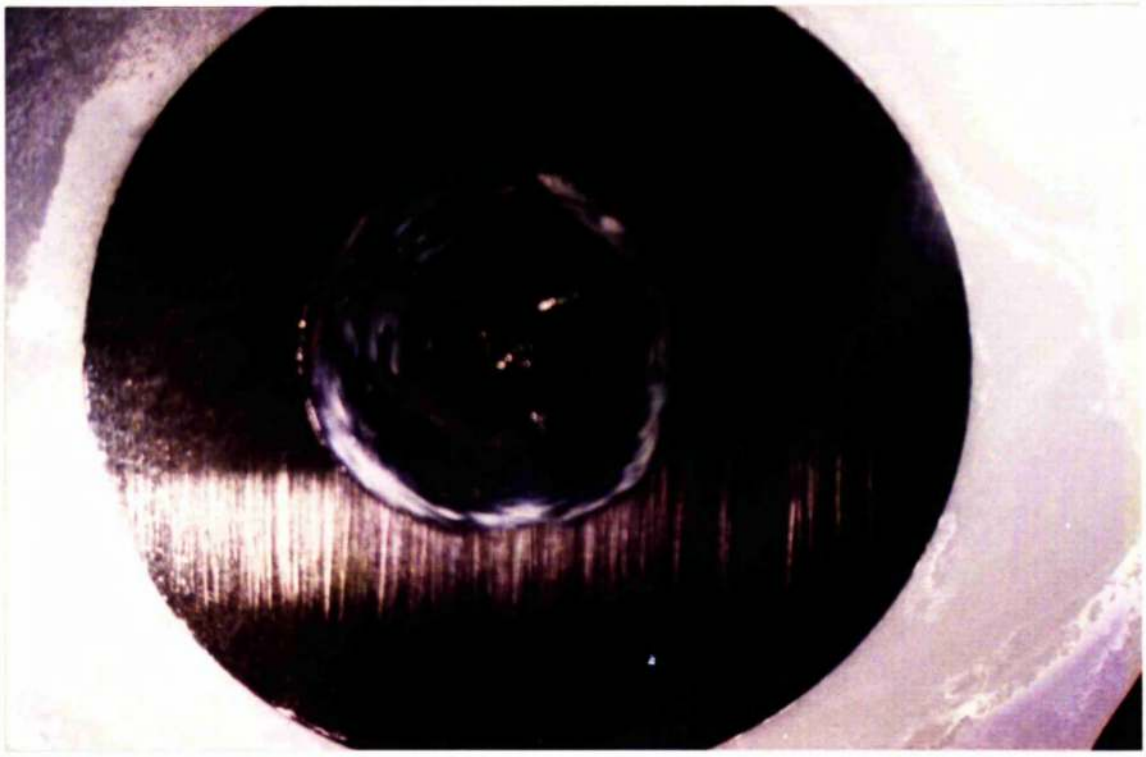

Figure 6.2.30. 316L when anodically polarised after 12 hours of liquid erosion-corrosion at 50°C and 71.1 m/s impinging jet velocity (diameter of specimen 26 mm).

Figure 6.2.31. Severe pitting in the centre of the 316L specimen shown in figure 6.2.30.

Figure 6.2.32. Non-uniform surface on the region directly under the jet of a Ti:5111 specimen when anodically polarised after 12 hours of liquid erosion-corrosion at 50°C and 71.1 m/s (S.E.M. image).

Figure 6.2.33. Uniform surface just outside the impinging target (i.e. on first dark ring in dark-blue colour also shown in figure 6.2.27) of a Ti:5111 specimen when anodically polarised after 12 hours of liquid erosion-corrosion at 50°C and 71.1 m/s (S.E.M. image).

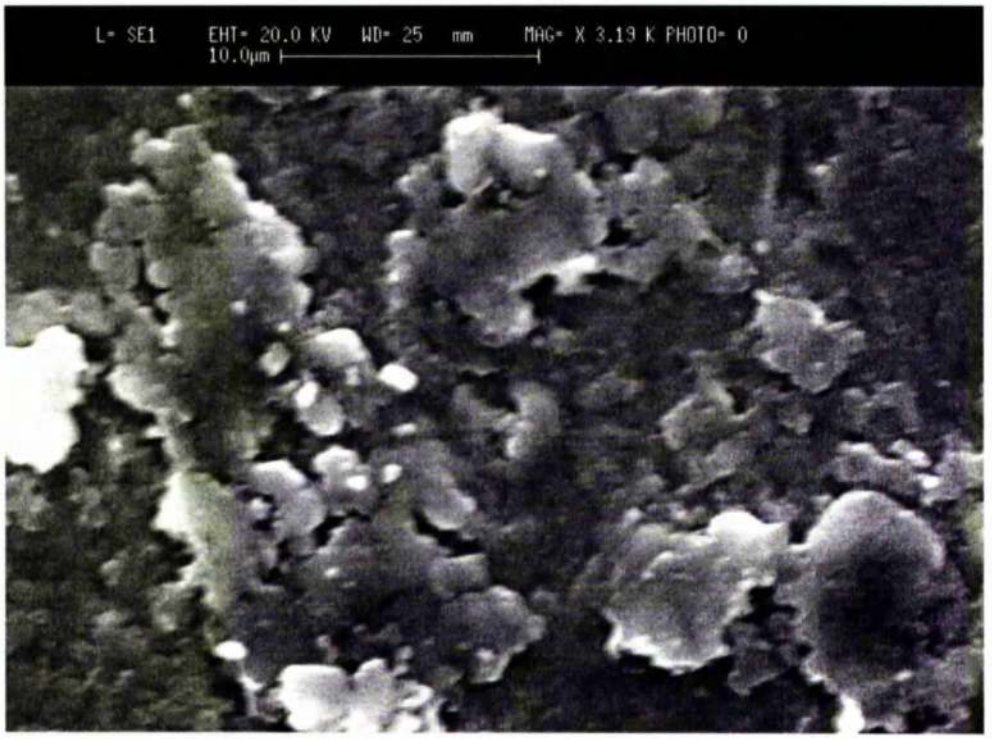

Figure 6.2.34. Surface of high roughness on the outer edge of the first dark ring around the impinging target of a Ti:5111 specimen when anodically polarised after 12 hours of liquid erosion-corrosion at 50°C and 71.1 m/s (S.E.M. image).

Figure 6.2.35. Non-uniform surface on the outer edge of the light-coloured ring (also shown in figure 6.2.27) of a Ti:5111 specimen when anodically polarised after 12 hours of liquid erosion-corrosion at 50°C and 71.1 m/s (S.E.M. image).

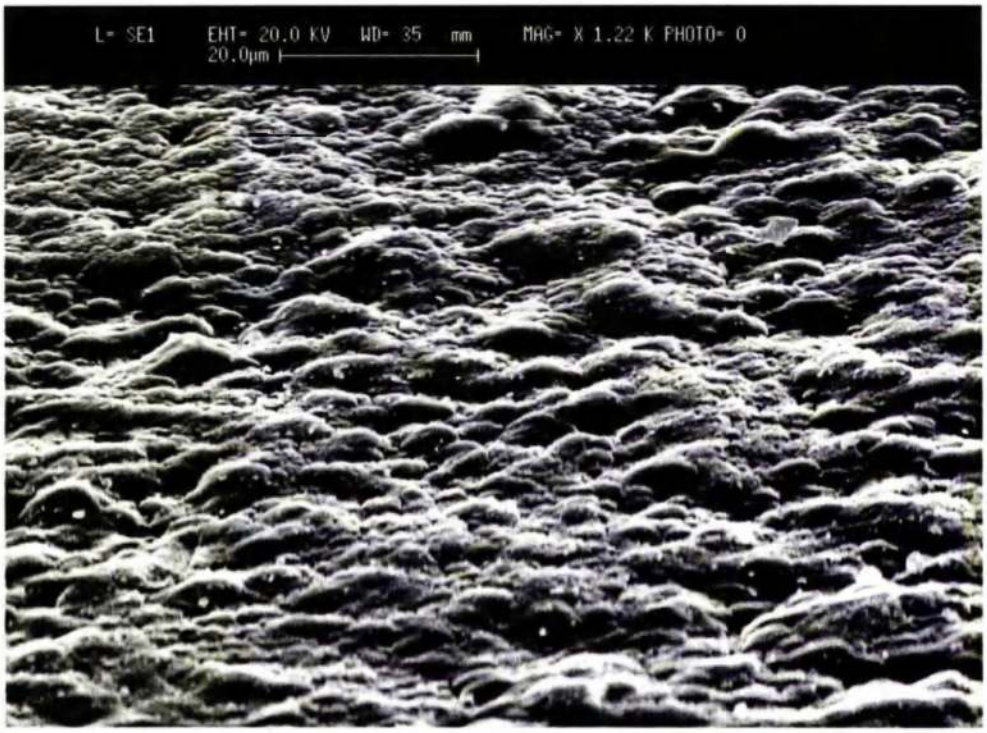

Figure 6.2.36. Film on the region directly under the jet (shown in a tilted position) of a Ti:G2 specimen when anodically polarised after 12 hours of liquid erosion-corrosion at 50°C and 71.1 m/s (S.E.M. image).

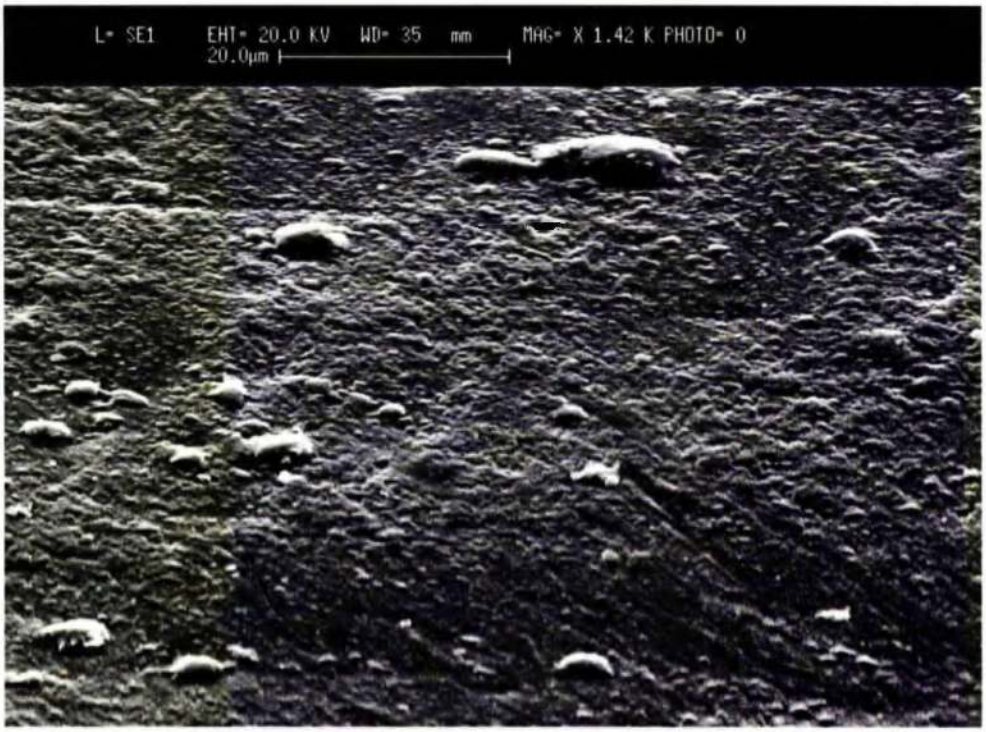

Figure 6.2.37. Film on the region directly under the jet (shown in a tilted position) of a Ti:5111 specimen when anodically polarised after 12 hours of liquid erosion-corrosion at 50°C and 71.1 m/s (S.E.M. image).

6.3. Solid/liquid erosion-corrosion conditions

Tests in respect to time effect

In the initial phase of the examination of the behaviour of pure Ti and the two alloys under solid/liquid erosion corrosion, experiments were conducted over different time periods with the velocity of the jet and the sand concentration in the solution kept constant at 12.4 m/s and 1500-1600 ppm respectively. For comparison reasons 316L stainless steel was also tested under the same conditions, although only at 16 hour time period. The specimen area was 8 cm^2 for Ti:G2 and 5 cm^2 for Ti-6Al-4V, Ti:5111 and 316L. After testing, total weight losses and surface profiles were obtained from each specimen.

Tables 6.3.1 to 6.3.4 show all results (weight losses and wear scar depths) for each material.

Exposure time	Weight loss (mg)	Average weight loss (mg)	Scar depth (μm)	Average scar depth (μm)
4 hours	0.8	0.8	7.0	7.0
8 hours	1.5, 1.1	1.3	22.0, 12.0	17.0
16 hours	2.4, 1.7	2.05	40.0, 28.0	34.0
72 hours	7.6, 10.0, 9.8	9.13	91.0, 130.0, 124.0	115.0

Table 6.3.1. Weight losses and wear scar depths for Ti:G2 under solid/liquid erosion-corrosion at different exposure periods.

Exposure time	Weight loss (mg)	Average weight loss (mg)	Scar depth (μm)	Average scar depth (μm)
4 hours	0.9	0.9	9.0	9.0
8 hours	1.3, 1.2	1.25	21.0, 15.0	18.0
16 hours	2.7, 2.8	2.75	27.0, 35.0	31.0
72 hours	7.1, 7.8, 8.7	7.86	76.0, 88.0, 103.0	89.0

Table 6.3.2. Weight losses and wear scar depths for Ti:5111 under solid/liquid erosion-corrosion at different exposure periods.

Exposure time	Weight loss (mg)	Average weight loss (mg)	Scar depth (μm)	Average scar depth (μm)
4 hours	1.0	1.0	7.0	7.0
8 hours	1.4, 1.1	1.25	19.0, 15.0	17.0
16 hours	2.1, 2.2	2.15	22.0, 24.0	23.0
72 hours	6.6, 9.0, 8.1	7.9	72.0, 114.0, 99.0	95.0

Table 6.3.3. Weight losses and wear scar depths for Ti-6Al-4V under solid/liquid erosion-corrosion at different exposure periods.

Exposure time	Weight loss (mg)	Average weight loss (mg)	Scar depth (μm)	Average scar depth (μm)
16 hours	4.6, 4.3, 5.1	4.7	37.0, 32.0, 42.0	37.0

Table 6.3.4. Weight losses and wear scar depths for 316L under solid/liquid erosion-corrosion at 16 hours exposure period.

As tables 6.3.1 to 6.3.3 and figures 6.3.1 – 6.3.2 indicate, at short time periods (4 and 8 hours) it is difficult to differentiate between the three Ti-base materials in terms of total weight loss or scar depth. However, after 16 hours and more clearly after 72 hours it appears as though both alloys are somewhat superior to pure Ti in terms of both weight loss and wear scar depth. Additionally as both graphs indicate, pure Ti and the alloys exhibit rather linear behaviour in weight loss and scar depth with time. In terms of weight loss (figure 6.3.1) 316L appears to possess much poorer erosion-corrosion resistance than pure Ti and the alloys. However in terms of scar depth (figure 6.3.2) there does not appear to be much difference between 316L and all the other materials.

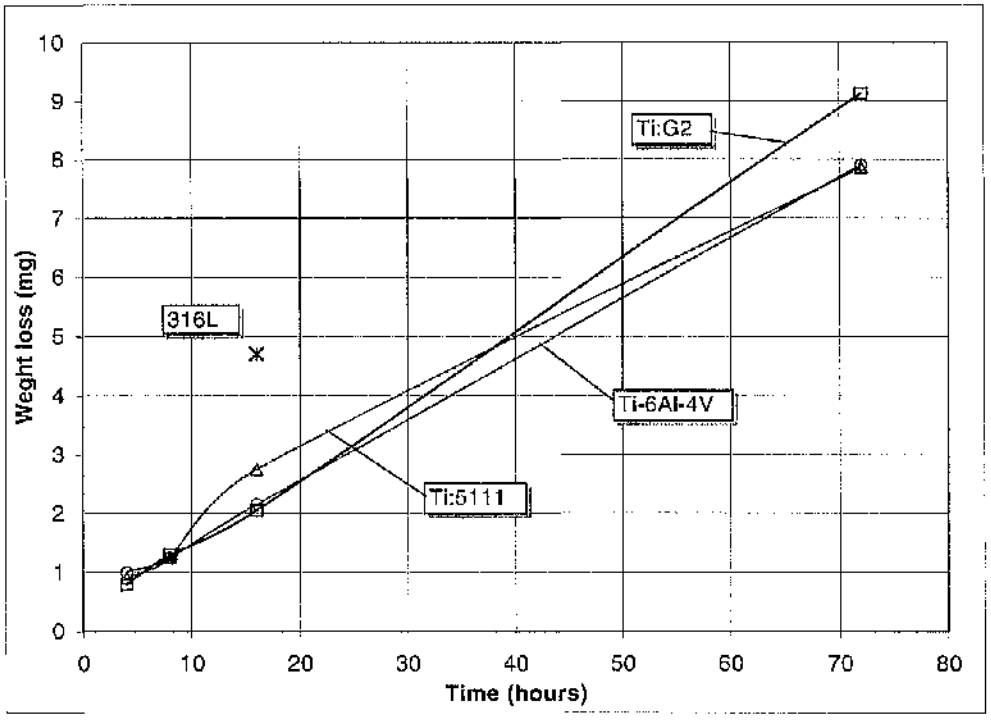

Figure 6.3.1. Weight loss versus time for Ti:G2, Ti:5111, Ti-6Al-4V and 316L under solid-liquid erosion-corrosion at 12.4 m/s and 1500-1600 ppm.

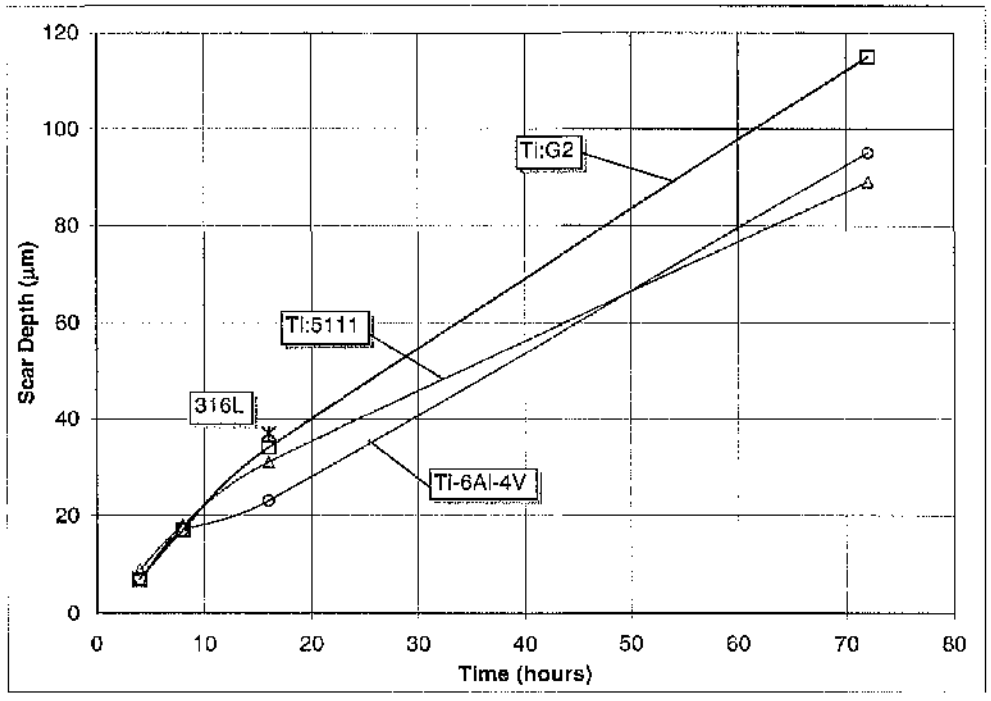

Figure 6.3.2. Scar depth versus time for Ti:G2, Ti:5111, Ti-6Al-4V and 316L under solid-liquid erosion-corrosion at 12.4 m/s and 1500-1600 ppm.

The comparison between 316L and the other materials is shown more analytically in table 6.3.5 where weight loss ratios, volume loss ratios and scar depth ratios, based on average weight losses and average scar depths at 16 hours given in tables 6.3.1, 6.3.2, 6.3.3 and 6.3.4, are presented. The mass values were converted to volume by the equation $V = m/\rho$ and the material densities are as follows:

Ti:G2 $\longrightarrow$ 4.51 g/cm^3
Ti:5111 $\longrightarrow$ 4.51 g/cm^3
Ti-6Al-4V $\longrightarrow$ 4.42 g/cm^3
316L $\longrightarrow$ 8 g/cm^3

Material	Weight loss ratio	Volume loss ratio	Scar depth ratio
Ti:G2	4.7/2.05=2.3	0.59/0.45 = 1.3	37/34 = 1.1
Ti:5111	4.7/2.75 = 1.7	0.59/0.61 = 1.0	37/31 = 1.2
Ti-6Al-4V	4.7/2.15 = 2.2	0.59/0.49 = 1.2	37/23 = 1.6

Table 6.3.5. Numerical comparison between 316L and Ti and the alloys based on weight loss, volume loss and scar depth. Each ratio represents the 316L result divided by the Ti-base material result.

Quite clearly the superiority of Ti:G2, Ti:5111 and Ti-6Al-4V to 316L in weight loss is greatly reduced when volume loss is considered. This is also essentially the case for scar depth. What these results show is only an initial indication of this interesting feature, and the results of a much more detailed comparison will be given later in this section.

Figures 6.3.3 to 6.3.5 show the surface profiles (i.e. cross-section of the wear scars) of Ti:G2, Ti:5111 and Ti-6Al-4V respectively after 72 hours of solid/liquid erosion-corrosion. The wear scars appear to be cone-shaped and quite smooth without any spikes that might denote localised damage. It is noted that for all three materials, the diameter of the scar ranges from 7 to 8 mm, although the diameter of the nozzle targeting the specimens was 4 mm in diameter.

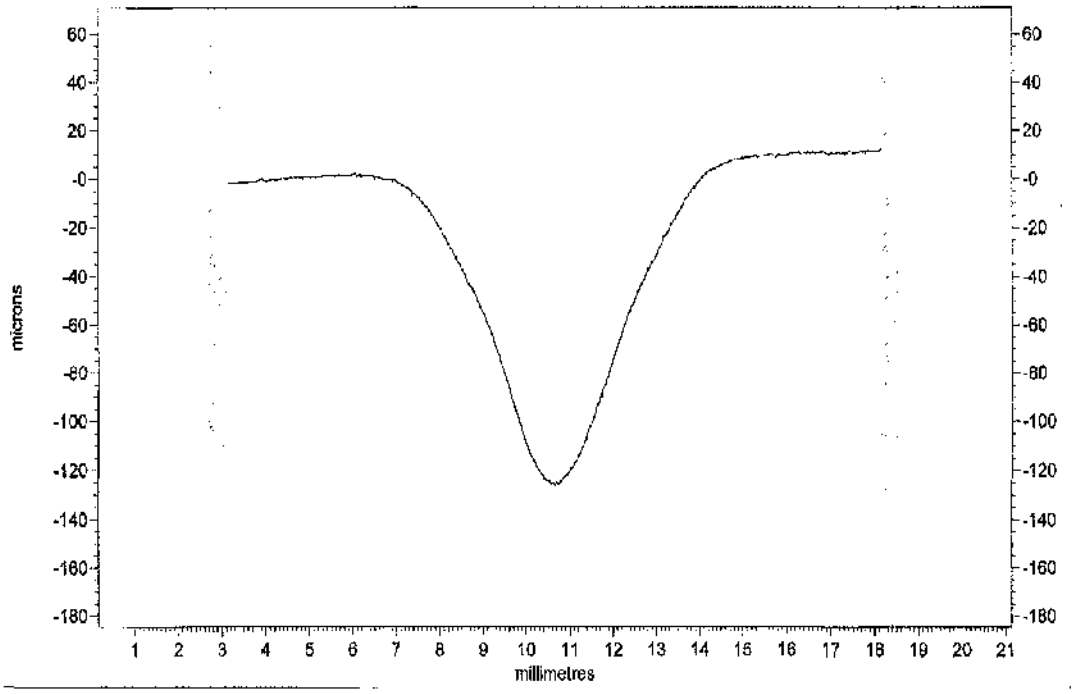

Figure 6.3.3. Surface profile of Ti:G2 after 72 hours of solid/liquid erosion-corrosion at 12.4 m/s and 1500-1600 ppm.

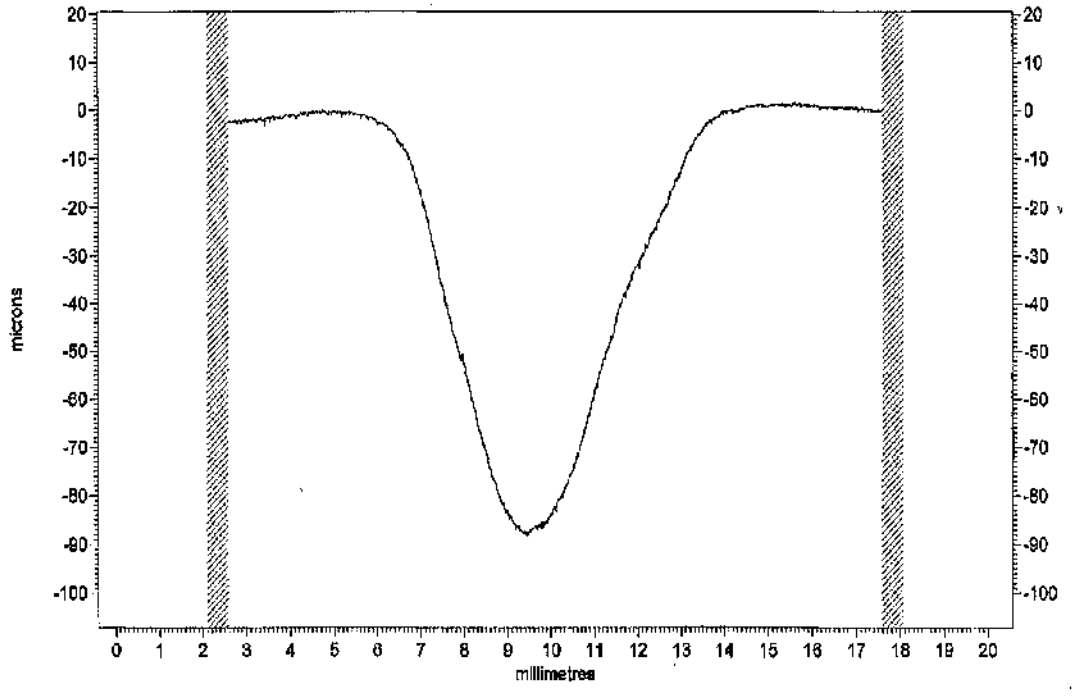

Figure 6.3.4. Surface profile of Ti:5111 after 72 hours of solid/liquid erosion-corrosion at 12.4 m/s and 1500-1600 ppm.

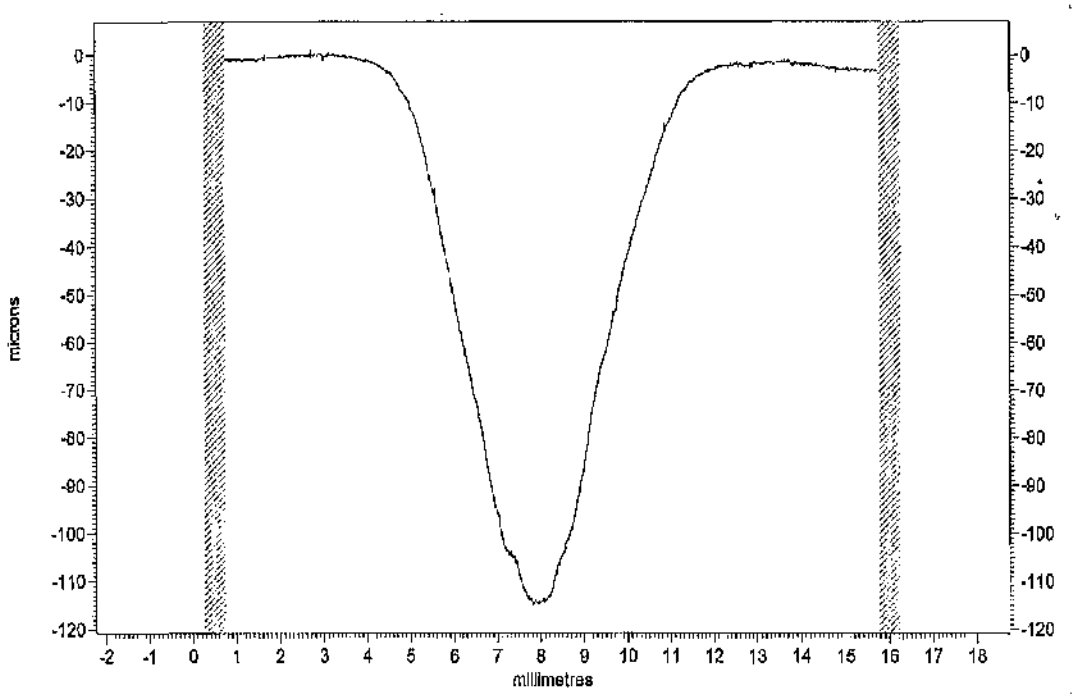

Figure 6.3.5. Surface profile of Ti-6Al-4V after 72 hours of solid/liquid erosion-corrosion at 12.4 m/s and 1500-1600 ppm.

Figures 6.3.6 to 6.3.8 show the anodic polarisation curves of duplicate experiments on Ti:G2, Ti:5111 and Ti-6Al-4V respectively, generated after 4 hours of solid/liquid erosion-corrosion at 12.4 m/s with 1500-1600 ppm sand concentration. It is noted that in the case of Ti:5111 and Ti-6Al-4V, at the beginning of the polarisation scan the current reaches an initial value of around 10 $\mu A/cm^2$ around which the current fluctuates as the potential further increases. This kind of behaviour can be attributed to the continuous and intense bombardment of silica particles, right from the start of the experiment, onto the surface of the specimen causing in this way rapid local depassivation/repassivation sequences. The particle impact frequency is apparently too rapid to allow the current densities to return to the much lower values typical of normal passive behaviour. In relation to that, since the particles hit the specimen only at its central region, this would suggest that the anodic site would be mostly concentrated in the target of the impinging jet, i.e. the centre of the specimen. This point will be examined in much more detail later in this section with reference to results using concentric specimens. Ti:G2 exhibits the same general features as Ti:5111 and Ti-6Al-4V but it did not reach as a high current density. This implies that

the passive film on Ti:G2 is slightly more resistant to rupture by particle impact and/or is more quickly repaired between impacts.

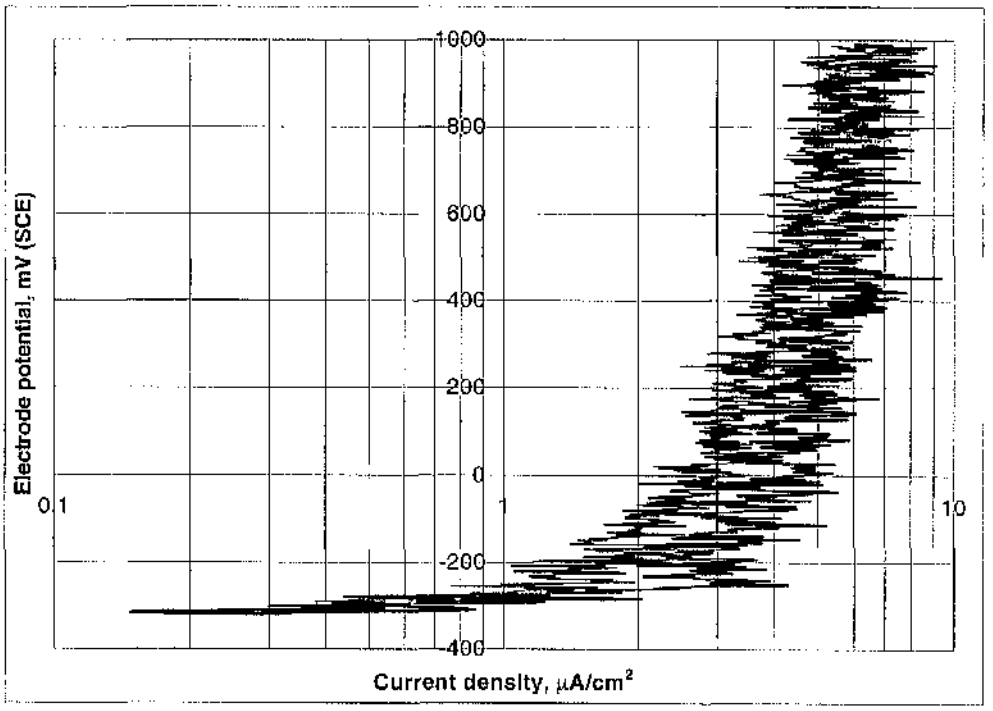

Figure 6.3.6. Anodic polarisation of Ti:G2 after 4 hours of solid/liquid erosion-corrosion at 12.4 m/s and 1500-1600 ppm.

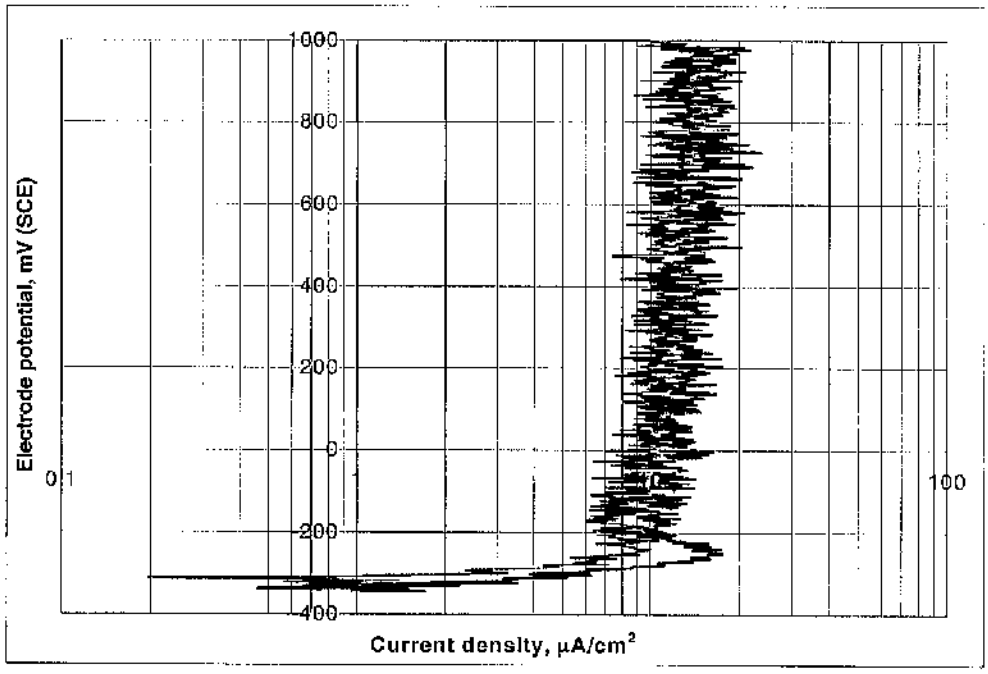

Figure 6.3.7. Anodic polarisation of Ti:5111 after 4 hours of solid/liquid erosion-corrosion at 12.4 m/s and 1500-1600 ppm.

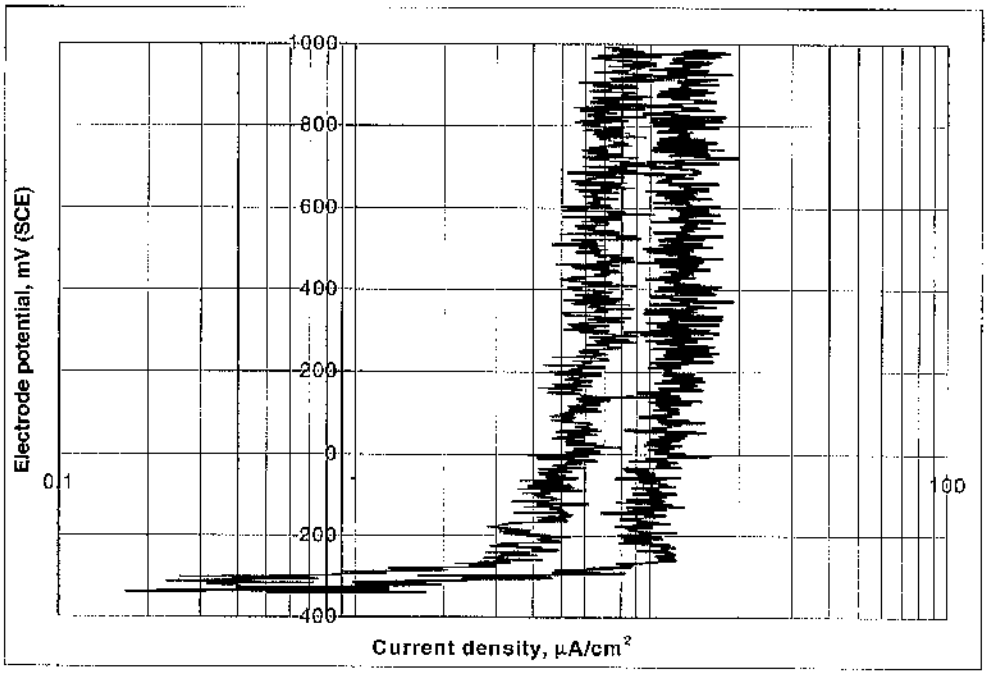

Figure 6.3.8. Anodic polarisation of Ti-6Al-4V after 4 hours of solid/liquid erosion-corrosion at 12.4 m/s and 1500-1600 ppm.

Tests of same duration

In another set of experiments, Ti:G2, Ti-6Al-4V, 316L and superduplex stainless steel ("Z100") were tested under solid/liquid erosion-corrosion at 12.6 m/s impinging velocity just for a 16 hour exposure period. It was decided that 16 hours was enough time for substantial weight losses to be obtained and, therefore, to facilitate all the required comparisons. In this group of experiments the sand concentration (1700-1800 ppm) was slightly higher than the 1500-1600 ppm in the experiments described earlier. The specimen's area was 8 cm^2 for Ti:G2, 5 cm^2 for Ti-6Al-4V and 316L and 3.8 cm^2 for Z100.

Table 6.3.6 shows all results (weight losses and wear scar depths) for each different material. Although the weight losses and scar depths are much greater than in the experiments described just earlier, the comparisons between the different materials are the same. Thus, in terms of both weight loss and wear scar depth Ti:G2 and Ti-6Al-4V are superior to 316L and Z100. Moreover Ti-6Al-4V appears to exhibit higher erosion-corrosion resistance and less damage directly under the jet (i.e. smaller scar depth) than pure Ti.

Material	Weight loss (mg)	Average weight loss (mg)	Scar depth (μm)	Average scar depth (μm)
Ti:G2	4.1, 4.0, 3.8	4.0	51.0, 46.0, 38.0	45.0
Ti-6Al-4V	2.7, 3.0	2.85	34.0, 36.0	35.0
316L	7.0	7.0	63.0	63.0
Z100	6.0, 6.7	6.35	52.0, 65.0	58.5

Table 6.3.6. Weight losses and wear scar depths for Ti:G2, Ti-6Al-4V, 316L and Z100 under solid/liquid erosion-corrosion at 16 hours exposure period.

The comparison between Ti:G2, Ti-6Al-4V and the two stainless steel alloys is shown more clearly in tables 6.3.7 and 6.3.8 where weight loss ratios, volume loss ratios and scar depth ratios, based on average weight losses and average scar depths given in table 6.3.6, are provided. Again the mass values were converted to volume by using $V = m/\rho$ and for Z100, $\rho = 7.84$ g/cm^3.

Material	Weight loss ratio	Volume loss ratio	Scar depth ratio
Ti:G2	7/4 = 1.75	0.875/0.89 = 1.0	63/45 = 1.4
Ti-6Al-4V	7/2.85 = 2.5	0.875/0.64 = 1.4	63/35 = 1.8

Table 6.3.7. Numerical comparison between Ti:G2 and 316L, and Ti-6Al-4V and 316L based on weight loss, volume loss and scar depth. Each ratio represents the 316L result divided by the Ti-base material result.

Material	Weight loss ratio	Volume loss ratio	Scar depth ratio
Ti:G2	6.35/4 = 1.6	0.81/0.89 = 0.9	58.5/45 = 1.3
Ti-6Al-4V	6.35/2.85 = 2.2	0.81/0.64 = 1.3	58.5/35 = 1.7

Table 6.3.8. Numerical comparison between Ti:G2 and Z100, and Ti-6Al-4V and Z100 based on weight loss, volume loss and scar depth. Each ratio represents the Z100 result divided by the Ti-base material result.

Quite similarly to the earlier results, the superiority of Ti:G2 and Ti-6Al-4V to 316L and Z100 in weight loss is greatly reduced when weight loss is converted to volume loss. In terms of volume loss, Ti:G2 is no better than either stainless steel alloy and Ti-6Al-4V is only 30 – 40% more resistant than 316L and Z100. In terms of wear scar depth both Ti:G2 and Ti-6Al-4V display greater resistance than 316L and Z100 directly under the jet. However, this last feature is not as much evident for Ti:G2 as for Ti-6Al-4V.

Figures 6.3.9 to 6.3.12 show the surface profiles (i.e. cross-section of the wear scars) of Ti:G2, Ti-6Al-4V, 316L and Z100 respectively after 16 hours of solid/liquid erosion-corrosion. Once more Ti:G2 and Ti-6Al-4V appeared to have developed cone-shaped and quite smooth wear scars. This is, more or less, also the case for 316L and Z100, although as can be noticed in figure 6.3.11 and figure 6.3.12 their wear scars exhibit a rather asymmetrical cross-section. Since other profiles on stainless steels (not shown) were more symmetrical, this feature could just result from some random behaviour rather than being attributable to some aspect of the metallurgical structure of stainless steels.

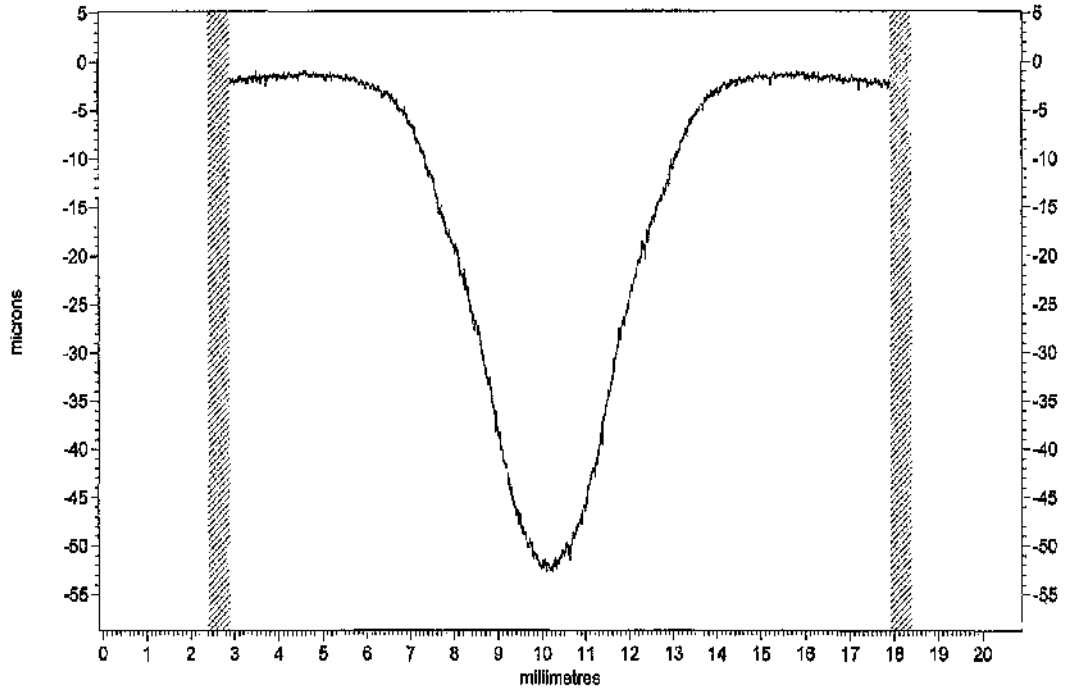

Figure 6.3.9. Surface profile of Ti:G2 after 16 hours of solid/liquid erosion-corrosion at 12.6 m/s and 1700-1800 ppm.

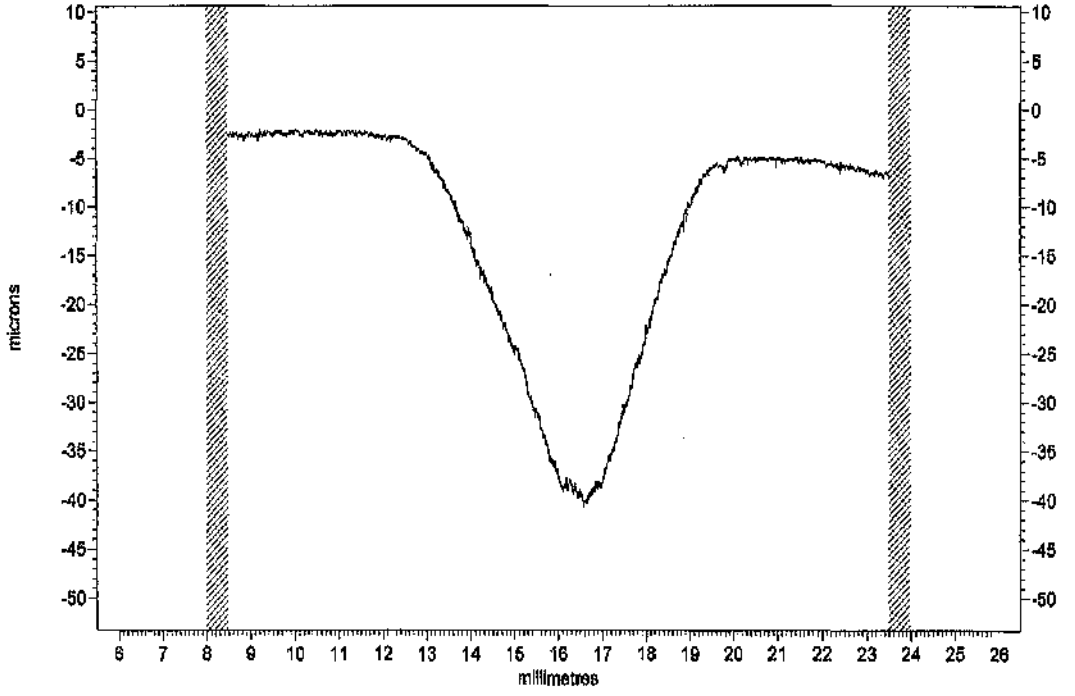

Figure 6.3.10. Surface profile of Ti-6Al-4V after 16 hours of solid/liquid erosion-corrosion at 12.6 m/s and 1700-1800 ppm.

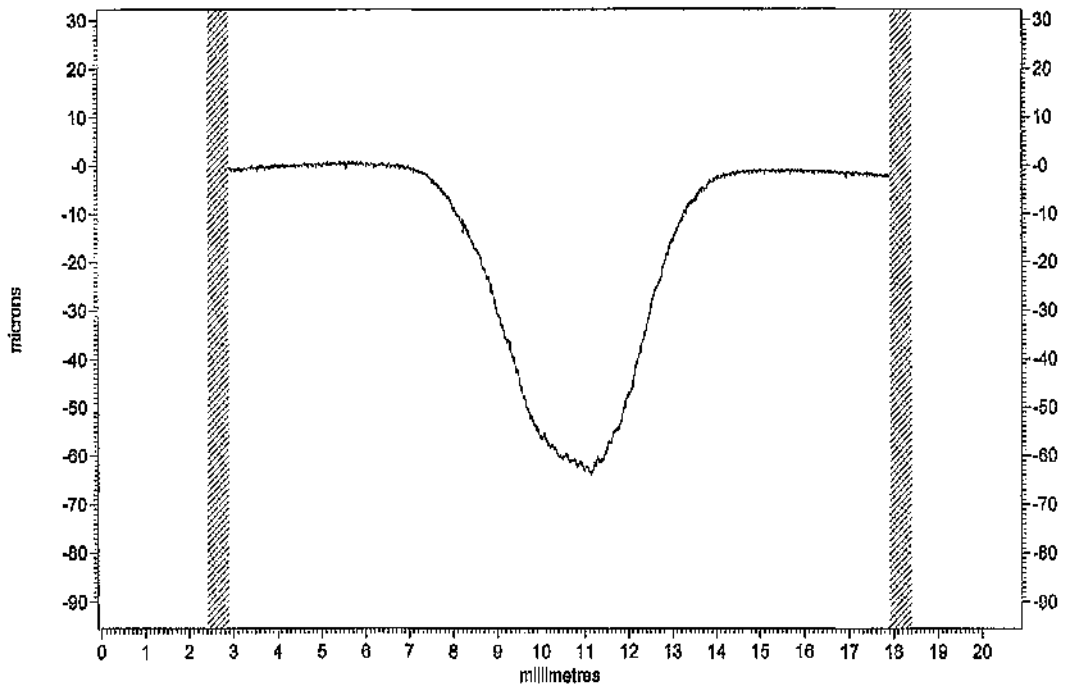

Figure 6.3.11. Surface profile of 316L after 16 hours of solid/liquid erosion-corrosion at 12.6 m/s and 1700-1800 ppm.

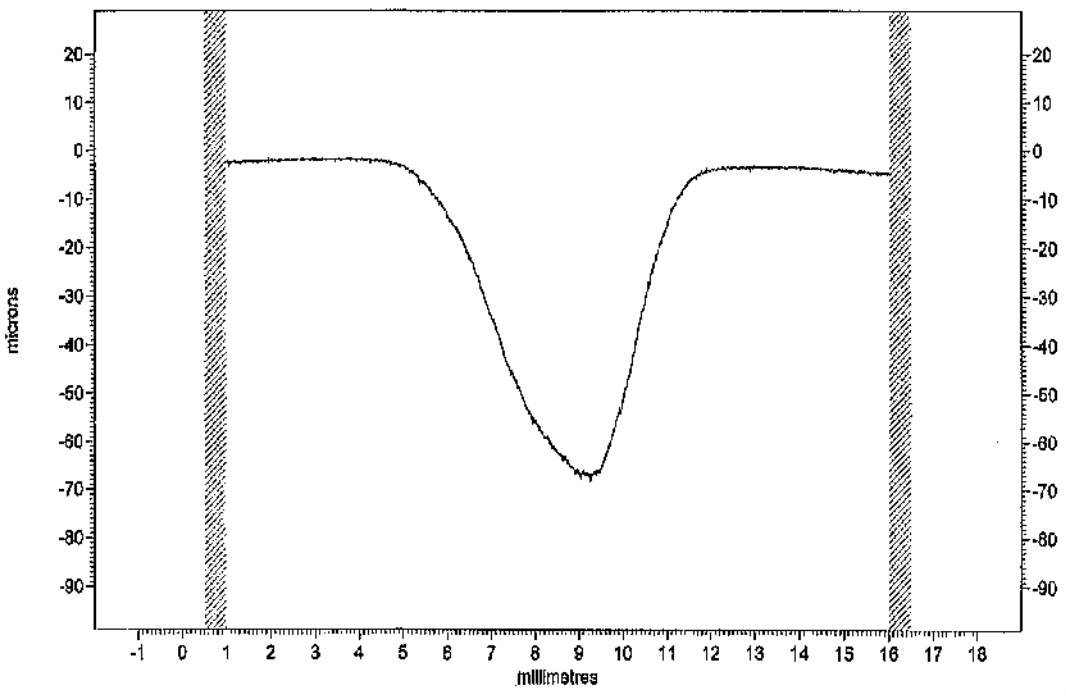

Figure 6.3.12. Surface profile of Z100 after 16 hours of solid/liquid erosion-corrosion at 12.6 m/s and 1700-1800 ppm.

It is also noted that for all four materials, the diameter of the scar again ranged from 7 to 8 mm, although the diameter of the nozzle targeting the specimens was 4 mm. The same characteristic was observed in wear scars of pure Ti and its two alloys, obtained after 3 days of solid/liquid erosion-corrosion (see figures 6.3.3 to 6.3.5) and, therefore, it very likely develops at early exposure stages and then remains constant (i.e. of same diameter). Apparently this is a common behaviour between Ti and its alloys and the two stainless steel alloys.

Ti:G2, Ti-6Al-4V and Z100 were also subjected to cathodic protection over the period of 16 hours. The weight losses and scar depths obtained are shown in table 6.3.9 and consequently represent pure erosion damage. Evidently, for Ti:G2 and Ti-6Al-4V the reduction in scar depth indicates the existence of a small but very significant contribution of corrosion to the overall erosion-corrosion damage directly under the jet.

Material	Weight loss (mg)	Average weight loss (mg)	Scar depth (μm)	Average scar depth (μm)
Ti:G2	2.9, 2.8, 2.7	2.8	35.0, 35.0, 36.0	35.0
Ti-6Al-4V	2.1, 2.1	2.1	29.0, 33.0	31.0
Z100	3.2, 3.4	3.3	36.0, 38.0	37.0

Table 6.3.9. Weight losses for Ti:G2, Ti-6Al-4V and Z100 over 16 hours of cathodic protection under solid/liquid erosion-corrosion.

Using the relation TWL = E + C + S, as explained in 2.3, and taking into account the total weight losses given in table 6.3.6, the contribution (in percentage) of 'E', and therefore (C + S), for Ti:G2, Ti-6Al-4V and Z100 is deduced (table 6.3.10).

Material	E %	(C + S) %
Ti:G2	70	30
Ti-6Al-4V	74	26
Z100	52	48

Table 6.3.10. Contribution of 'E', and (C + S) for Ti:G2, Ti-6Al-4V and Z100 after 16 hours of solid/liquid erosion-corrosion.

Taking into account the average scar depths given in tables 6.3.6 and 6.3.9, the contribution of 'E' to the overall damage directly under the jet is deduced (table 6.3.11)

Material	'E' %
Ti:G2	78
Ti-6Al-4V	89
Z100	63

Table 6.3.11. Contribution of 'E' to the overall damage directly under the jet for Ti:G2, Ti-6Al-4V and Z100 after 16 hours of solid/liquid erosion-corrosion.

Figure 6.3.13 shows the anodic polarisation curves of Ti:G2, Ti-6Al-4V, 316L and Z100 generated after 16 hours of solid/liquid erosion-corrosion at 12.6 m/s with 1700-1800 ppm sand concentration. Since not all curves in figure 6.3.13 are shown quite clearly, individual curves are presented separately in figures 6.3.14 to 6.3.16.

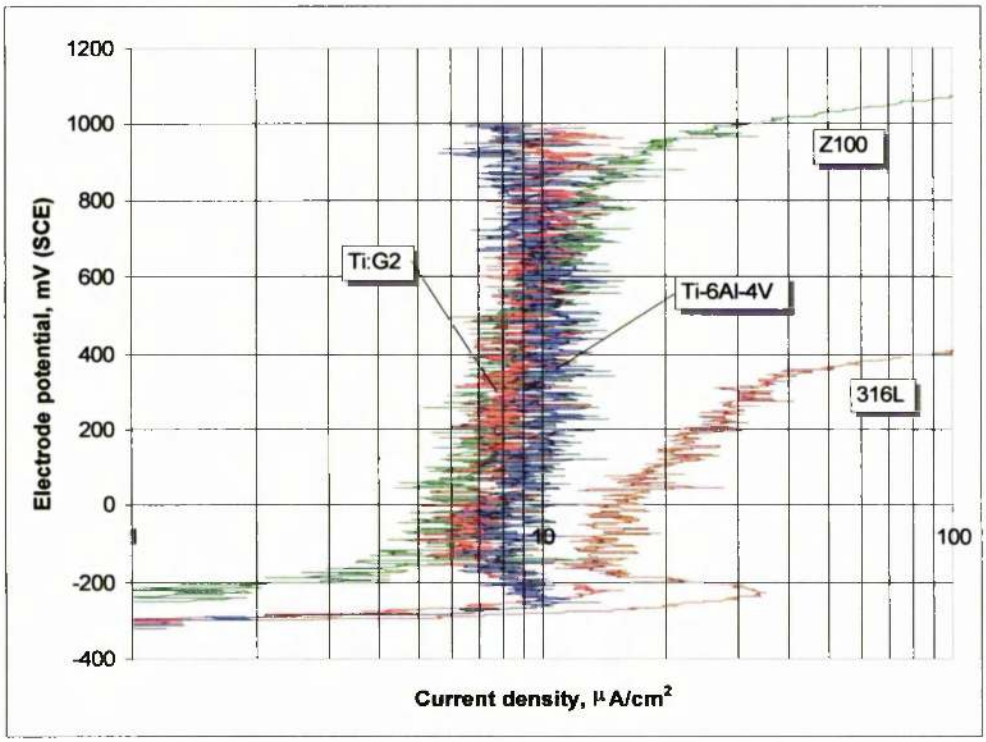

Figure 6.3.13. Anodic polarisation of Ti:G2, Ti-6Al-4V, 316L and Z100 after 16 hours of solid/liquid erosion-corrosion at 12.6 m/s and 1700-1800 ppm.

The major feature of the anodic polarisation curves for Ti:G2, Ti-6Al-4V and superduplex stainless steel alloy is of fluctuating currents around a mean current that is either almost constant or moderately increasing over a very wide (>1V) potential range. It is noted that the observed fluctuations are almost certainly 'truncated' due to passivation/repassivation events being so fast (frequent) compared to the electrochemical sampling time. The stainless steels exhibit shifts to higher rates of current increasing at about +950 mV and +350 mV respectively for the superduplex and 316L. The other remaining feature is a current peak immediately positive to Ecorr which is most distinctive for 316L and of relatively minor proportions for Ti:G2.

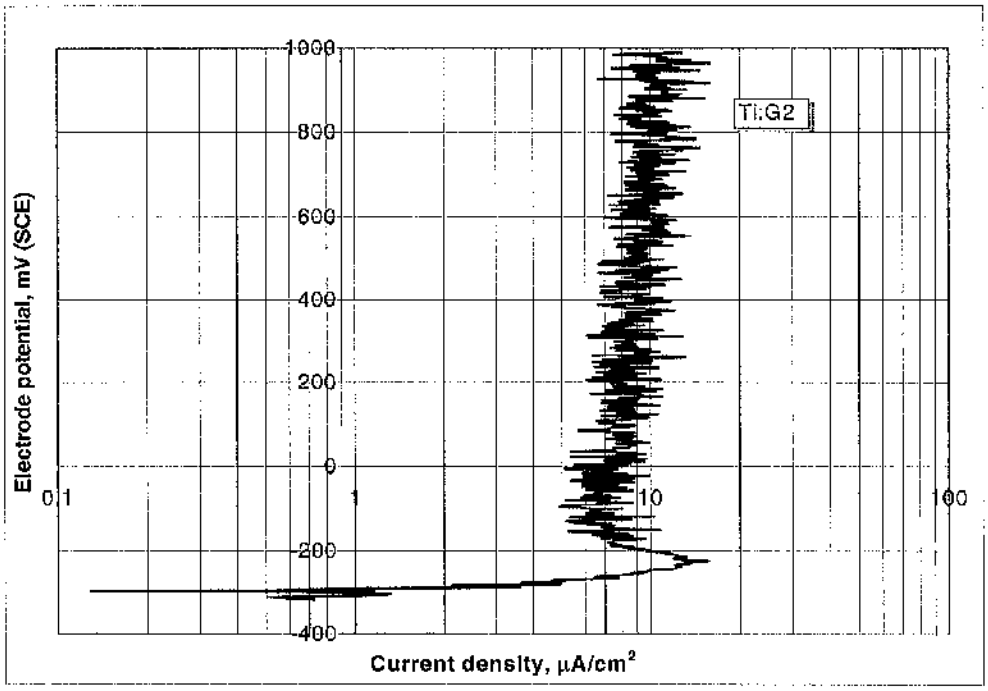

Figure 6.3.14. Anodic polarisation of Ti:G2 after 16 hours of solid/liquid erosion-corrosion at 12.6 m/s and 1700-1800 ppm.

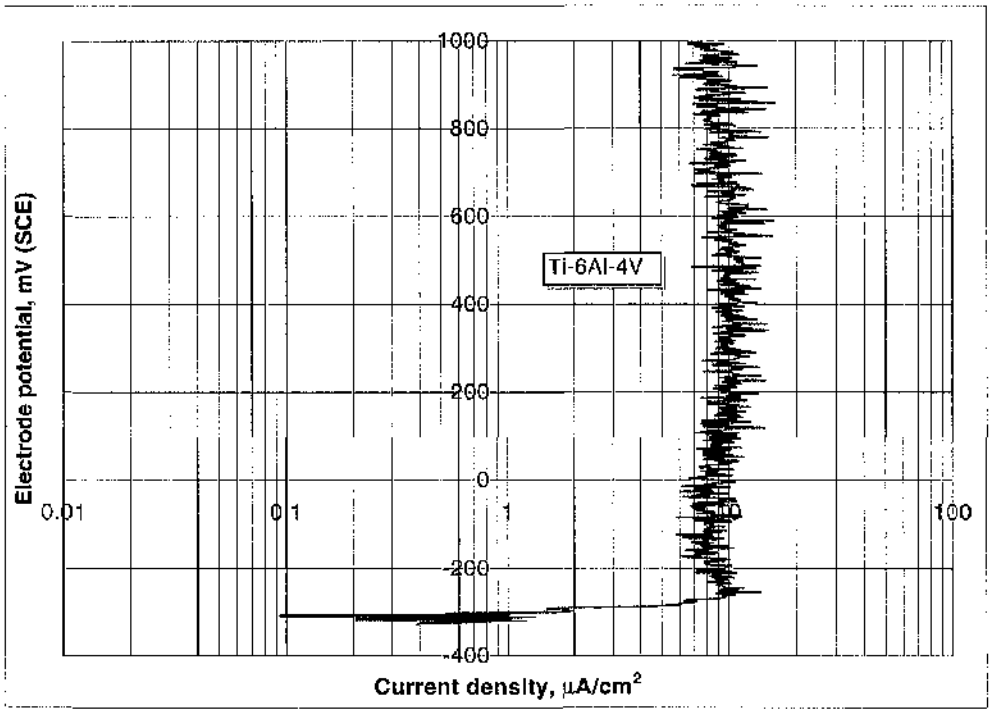

Figure 6.3.15. Anodic polarisation of Ti-6Al-4V after 16 hours of solid/liquid erosion-corrosion at 12.6 m/s and 1700-1800 ppm.

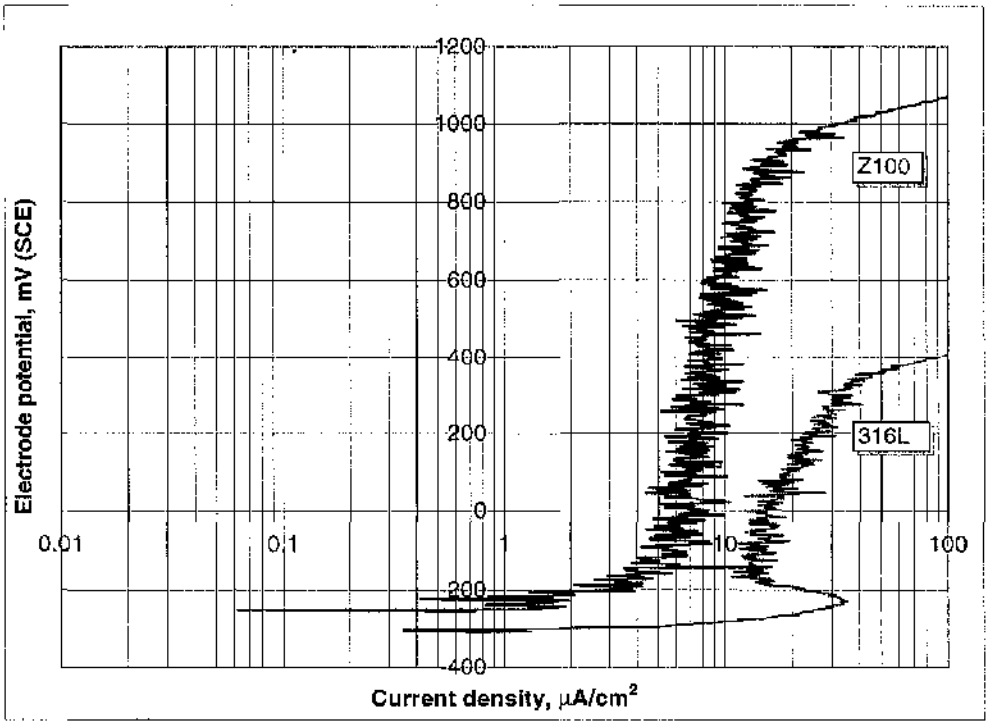

Figure 6.3.16. Anodic polarisation of Z100 and 316L after 16 hours of solid/liquid erosion-corrosion at 12.6 m/s and 1700-1800 ppm.

Figure 6.3.17 is a magnification of the current peak for Ti:G2 immediately positive to Ecorr (the full anodic scan has been given in figure 6.3.14).

In an attempt to calculate the separate 'C' and 'S' factors for Ti:G2 related to the TWL = E + C + S equation, a current flow at Ecorr (icorr) of 2 $\mu A/cm^2$ was estimated (see figure 6.3.17), and Faraday's law was used.

According to Faraday's law (see section 2.1): 96500 coulombs = 1/n moles

For Ti, atomic weight = 47.9 g/mole and valency n = 3 for higher oxidation state (note that at the observed corrosion potentials the stable state of dissolved Ti is taken to be Ti^{3+}).

$\therefore$ passage of 96500 coulomb of charge is associated with dissolution of 47.9/3 = 15.96 g of Ti.

96500 Amp. will dissolve 15.96 g/s, i.e. 2 $\mu A/8cm^2$ (note that 8 cm^2 is the area of the Ti:G2 specimen) will dissolve $(15.96 \times 2 \times 10^{-6} \times 8)/96500 = 2.65 \times 10^{-9}$ g/s = 2.65×10^{-6} mg/s = $2.65 \times 10^{6} \times 60 \times 60 \times 16$ = <u>0.15 mg/16h.</u>

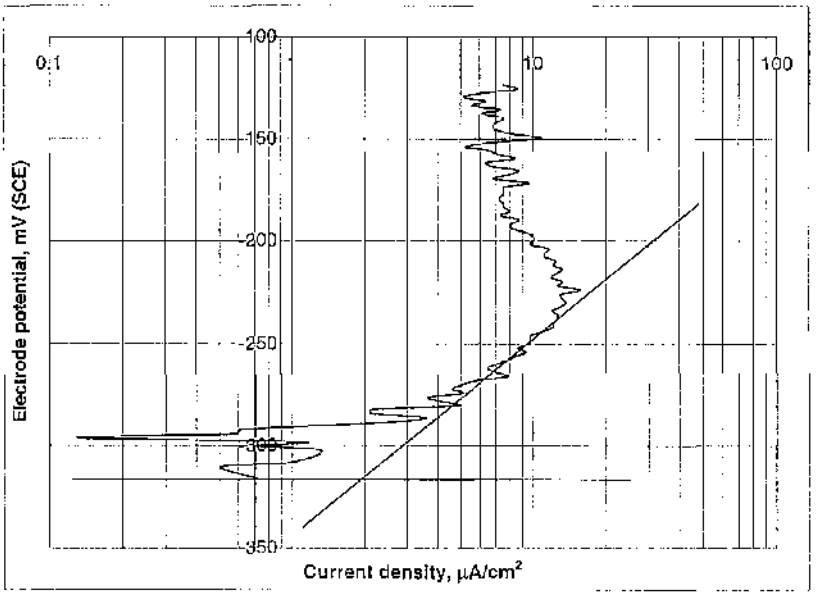

Figure 6.3.17. Magnification of Ti:G2's current peak immediately +ve to Ecorr (full anodic scan in figure 6.3.14).

For Ti:G2, 'TWL' = 4 mg (table 6.3.6), 'E' = 2.8 mg (table 6.3.9) and now 'C' = 0.15 mg. Therefore 'S' = 1.05 mg. The latter suggests that under these particular experimental conditions, erosion-corrosion damage on Ti:G2 consists of 3.75% 'C', 26.25% 'S' and as mentioned earlier 70% 'E'. Whilst the figure of 30% of total material loss for the composite specimen due to combined corrosion plus synergy is soundly based, the separation into the separate 'C' and 'S' factors is clearly distorted by the behaviour of the different parts (e.g. impinged zone and outer regions of the sample) of the composite specimen. This matter was the subject of further work with concentric specimens presented later in this section.

On account of the issue raised in the above paragraph, attempts to deduce values of icorr were not undertaken for the other materials in these tests; however the expanded anodic polarisation curves around Ecorr are shown for completeness in figures 6.3.18 – 6.3.20.

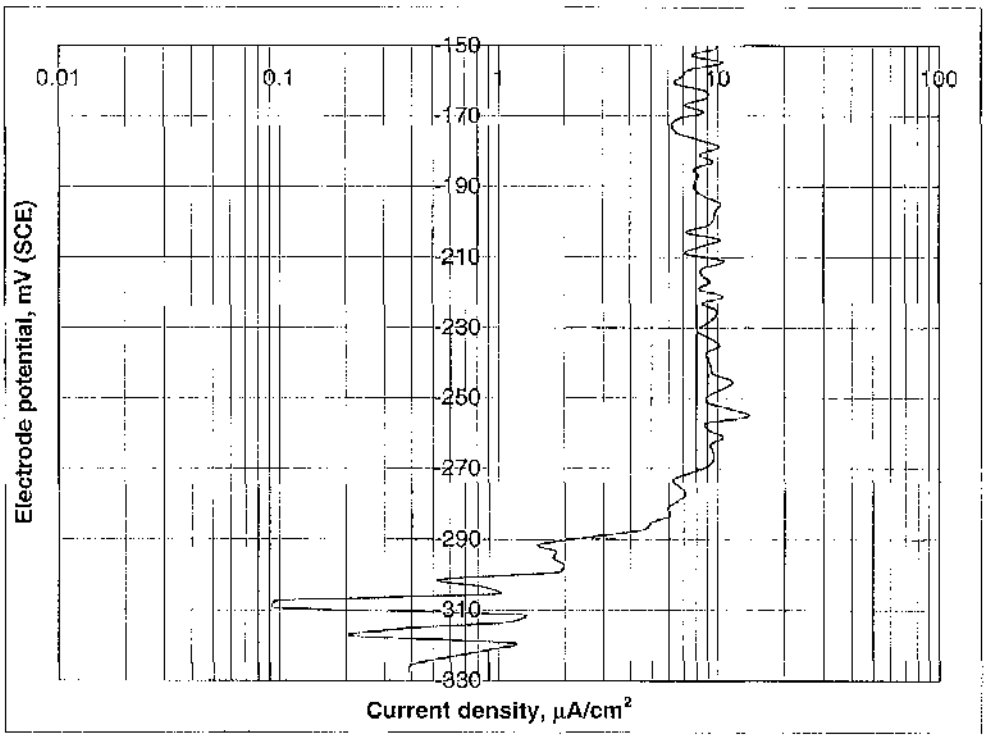

Figure 6.3.18. Magnification of Ti-6Al-4V's current peak immediately +ve to Ecorr (full anodic scan in figure 6.3.15).

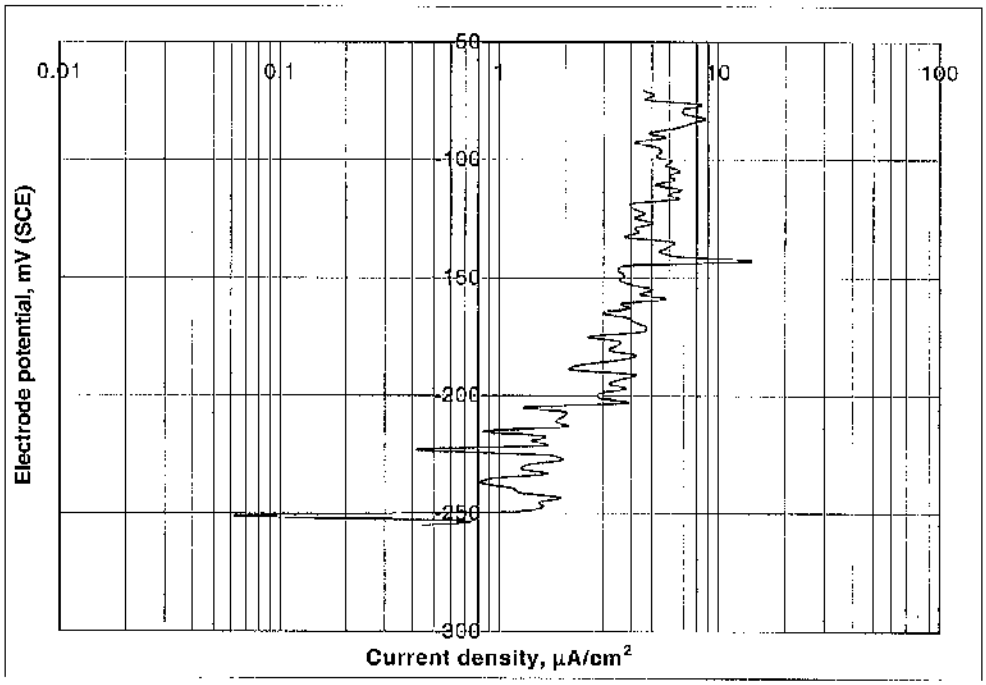

Figure 6.3.19. Magnification of Z100's current peak immediately +ve to Ecorr (full anodic scan in figure 6.3.16).

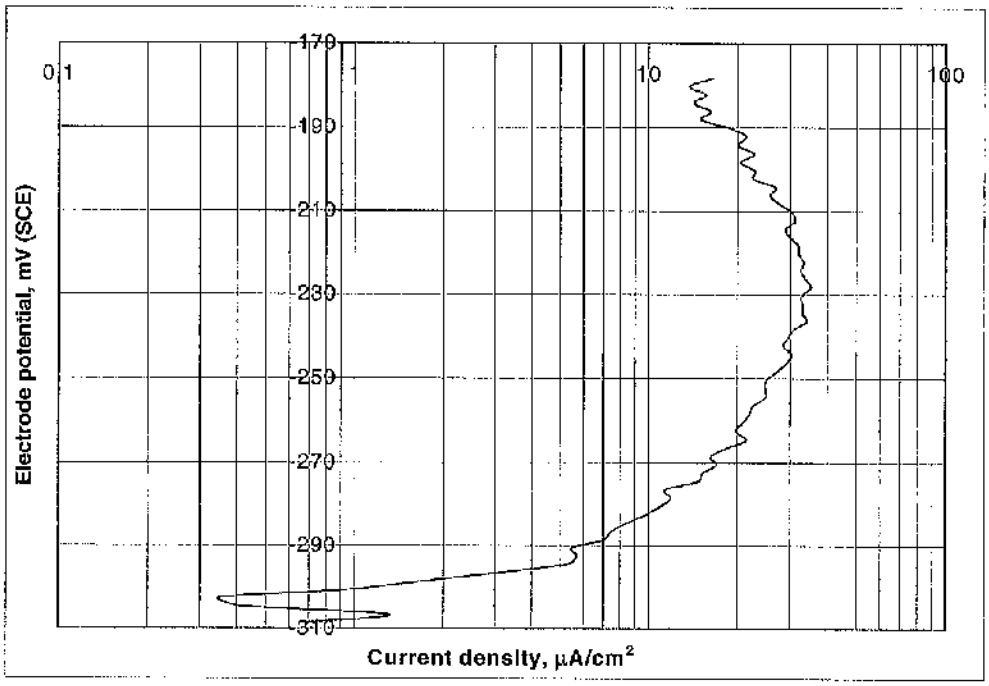

Figure 6.3.20. Magnification of 316L's current peak immediately +ve to Ecorr (full anodic scan in figure 6.3.16).

Tests in a range of particle concentrations

In the third group of experiments, Ti:G2, 316L and superduplex stainless steel ("Z100") were tested under solid/liquid erosion-corrosion with various particle concentrations. Again the velocity of the impinging jet was 12.6 m/s and the exposure period was kept at 16 hours. In order to examine the effect of different sizes of exposed surface to the weight loss of the materials, various specimen areas were used for Ti:G2 and the superduplex alloy. For Ti:G2, specimen areas studied were 8 cm^2, 5 cm^2 and 0.28 cm^2 and for superduplex 8 cm^2 and 5 cm^2.

Tables 6.3.12 - 6.3.17 show all results of each material at each different area and the results are plotted in figure 6.3.21 in which average sand loadings are used. Figure 6.3.21 clearly demonstrates for both Ti and superduplex stainless steel an increasing magnitude of erosion-corrosion damage with increasing solid loadings with some indications that the relationship may be linear. The weight loss results also demonstrate two other features: 1) Higher weight losses for the stainless steels than for titanium and 2) for both Ti:G2 and Z100, a larger surface area leads to higher weight loss. The first feature will be considered in more detail in a later part of this section of the thesis. The second feature indicates that some of the erosion-corrosion damage is well outside the central scar

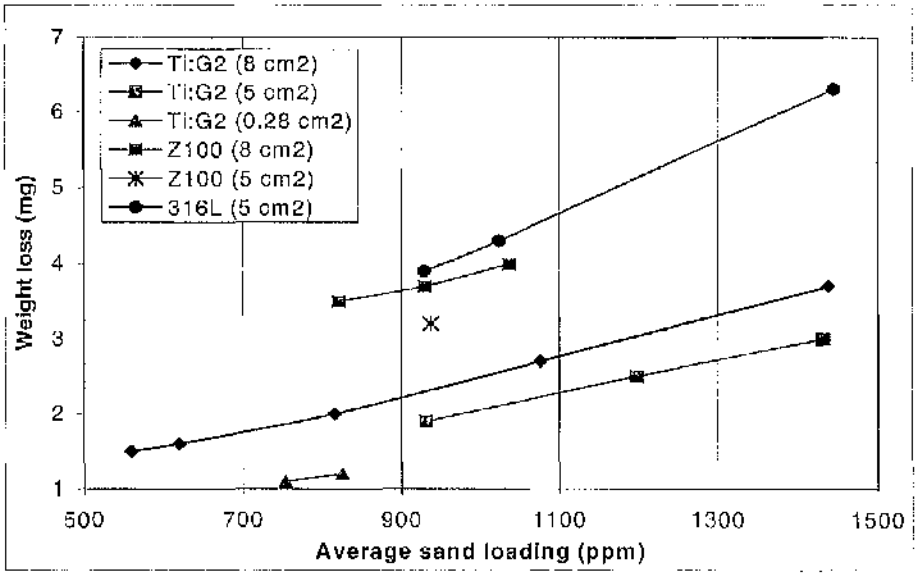

Figure 6.3.21. Weight loss versus average sand loading for 16 hour solid/liquid erosion-corrosion on Ti:G2, Z100 and 316L.

Sand loading (ppm)	Weight loss (mg)	Volume loss (mm^3)	Scar depth (μm)
1035 – 1116	2.7	0.59	49
1410 – 1465	3.7	0.82	61
804 - 827	2.0	0.44	39
608 - 631	1.6	0.35	25
532 - 588	1.5	0.33	25

Table 6.3.12. Weight losses, volume losses and wear scar depths of 8 cm^2 Ti:G2 specimens at various sand loadings, under solid/liquid erosion-corrosion after 16 hours exposure period.

Sand loading (ppm)	Weight loss (mg)	Volume loss (mm^3)	Scar depth (μm)
1387 – 1476	3.0	0.66	54
1150 – 1246	2.5	0.55	42
907 - 955	1.9	0.42	39

Table 6.3.13. Weight losses, volume losses and wear scar depths of 5 cm^2 Ti:G2 specimens at various sand loadings, under solid/liquid erosion-corrosion after 16 hours exposure period.

Sand loading (ppm)	Weight loss (mg)	Volume loss (mm^3)
742 – 765	1.1	0.24
803 – 848	1.2	0.27

Table 6.3.14. Weight losses, volume losses and wear scar depths of 0.28 cm^2 Ti:G2 specimens at various sand loadings, under solid/liquid erosion-corrosion after 16 hours exposure period.

Sand loading (ppm)	Weight loss (mg)	Volume loss (mm^3)	Scar depth (μm)
981 – 1093	4.0	0.51	53
873 – 987	3.7	0.47	46
814 – 828	3.5	0.45	41

Table 6.3.15. Weight losses, volume losses and wear scar depths of 8 cm^2 Z100 specimens at various sand loadings, under solid/liquid erosion-corrosion after 16 hours exposure period.

Sand loading (ppm)	Weight loss (mg)	Volume loss (mm^3)	Scar depth (μm)
921 – 954	3.2	0.41	44

Table 6.3.16. Weight loss, volume loss and wear scar depth of 5 cm^2 Z100 specimen, under solid/liquid erosion-corrosion after 16 hours exposure period.

Sand loading (ppm)	Weight loss (mg)	Volume loss (mm^3)	Scar depth (μm)
1403 – 1487	6.3	0.79	83
987 – 1062	4.3	0.54	57
892 – 967	3.9	0.49	49

Table 6.3.17. Weight losses, volume losses and wear scar depths of 5 cm^2 316L specimens at various sand loadings, under solid/liquid erosion-corrosion after 16 hours exposure period.

This second aspect is also demonstrated by further consideration of the surface profiles. Figures 6.3.22 and 6.3.23 show two wear scars from two different Ti:G2 specimens. Since the wear scars were quite smooth and symmetrical, they were divided into numerous small segments as both figures indicate. Each wear scar is circular and therefore all separate segments were treated as short cylinders. The volume of each cylinder was calculated by $V_c = \pi \times r^2 \times h$, where 'r' is the radius and 'h' is the height of the plate, and finally all cylinder volumes were added up to give the volume of the wear scar.

In order to reduce the errors in this approximate procedure, the cylinders were drawn in identical pairs (see '2' and'3' in figure 6.3.22). It was reasoned that this would lead to an approximate balance between the very small parts of the volume of the cylinders that were either outside the scar or were part of the scar excluded from the volume of a particular cylinder. The exception to this procedure was for the uppermost "cylinder" in figure 6.3.22, whose volume was calculated assuming it was a trapezium cone, $V_t = ½ \times \pi \times h \times (R_1^2 + r_2^2)$, where 'R' and 'r' are the large and small radii respectively of the trapezium cone.

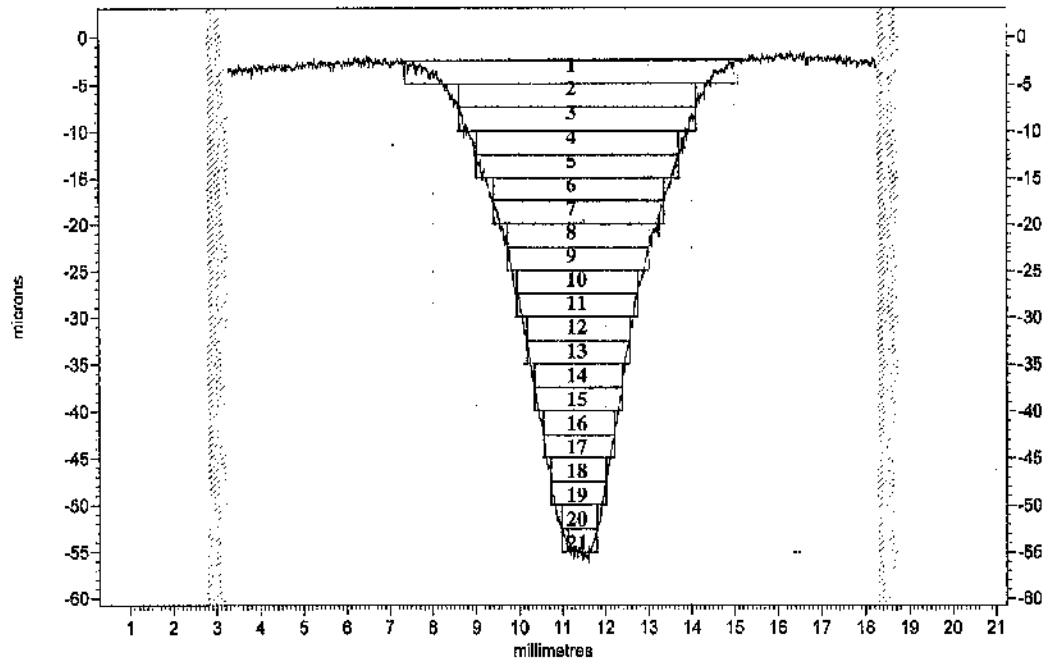

Figure 6.3.22. Surface profile, divided into numerous segments, of 5 cm^2 Ti:G2 specimen after 16 hours of solid/liquid erosion-corrosion at 12.6 m/s and 1387-1476 ppm (weight loss obtained · · › 3.0 mg).

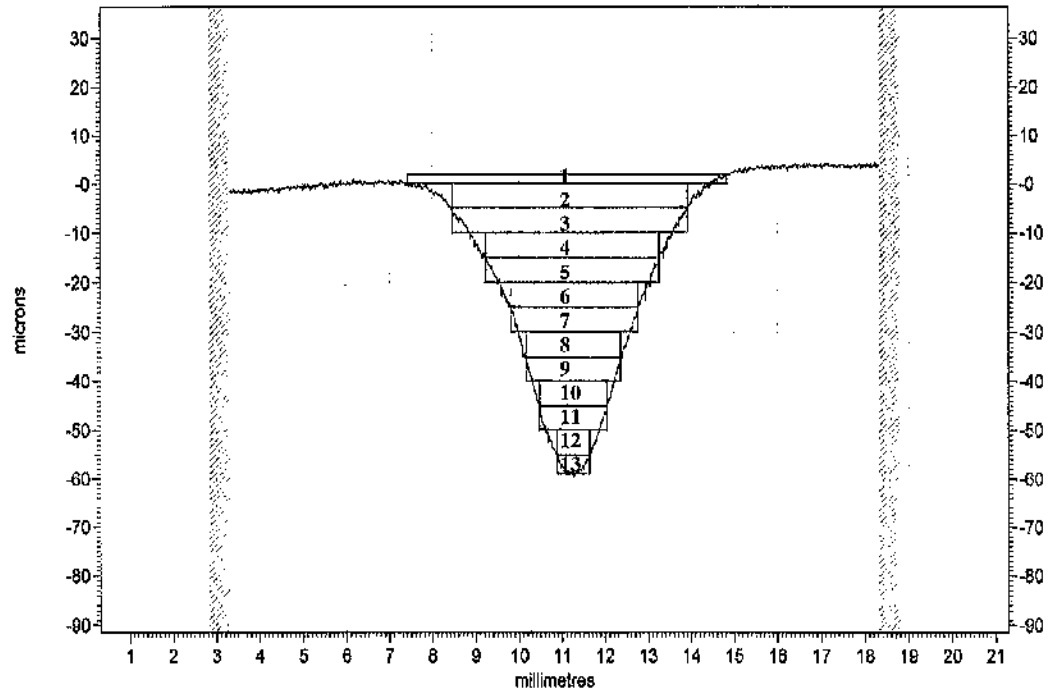

Figure 6.3.23. Surface profile, divided into numerous segments, of 8 cm^2 Ti:G2 specimen after 16 hours of solid/liquid erosion-corrosion at 12.6 m/s and 1410-1465 ppm (weight loss obtained —› 3.7 mg).

Figure 6.3.22 shows the wear scar of a 5 cm^2 area Ti:G2 specimen that exhibited a weight loss of 3.0 mg. By using $V = m/\rho = 3.0\times10^{-3}/4.51$, the overall volume loss of the specimen equals 0.7 mm^3. According to the measurements in figure 6.3.22 the volume loss inside the scar was 0.47 mm^3 (see table 6.3.18). Quite evidently, part of the overall volume loss occurred outside the wear scar. Figure 6.3.23 shows the wear scar of a 8 cm^2 area Ti:G2 specimen that exhibited a weight loss of 3.7 mg. Similarly to the first example, the calculated volume loss inside the scar was 0.56 mm^3 (see table 6.3.19) while the overall volume loss equalled 0.82 mm^3 and hence, the notion of significant material loss outside the wear scar is totally realistic.

Number of plate	Volume of plate
1	$\frac{1}{2} \times \pi \times 0.0025 \times (3.9^2 + 3.1^2) = 0.097$ mm^3
2	$\pi \times 2.65^2 \times 0.0025 = 0.055$ mm^3
3	$\pi \times 2.65^2 \times 0.0025 = 0.055$ mm^3
4	$\pi \times 2.3^2 \times 0.0025 = 0.04$ mm^3
5	$\pi \times 2.3^2 \times 0.0025 = 0.04$ mm^3
6	$\pi \times 1.95^2 \times 0.0025 = 0.03$ mm^3
7	$\pi \times 1.95^2 \times 0.0025 = 0.03$ mm^3
8	$\pi \times 1.6^2 \times 0.0025 = 0.02$ mm^3
9	$\pi \times 1.6^2 \times 0.0025 = 0.02$ mm^3
10	$\pi \times 1.4^2 \times 0.0025 = 0.015$ mm^3
11	$\pi \times 1.4^2 \times 0.0025 = 0.015$ mm^3
12	$\pi \times 1.15^2 \times 0.0025 = 0.01$ mm^3
13	$\pi \times 1.15^2 \times 0.0025 = 0.01$ mm^3
14	$\pi \times 1^2 \times 0.0025 = 0.008$ mm^3
15	$\pi \times 1^2 \times 0.0025 = 0.008$ mm^3
16	$\pi \times 0.8^2 \times 0.0025 = 0.005$ mm^3
17	$\pi \times 0.8^2 \times 0.0025 = 0.005$ mm^3
18	$\pi \times 0.6^2 \times 0.0025 = 0.003$ mm^3
19	$\pi \times 0.6^2 \times 0.0025 = 0.003$ mm^3
20	$\pi \times 0.4^2 \times 0.0025 = 0.001$ mm^3
21	$\pi \times 0.4^2 \times 0.0025 = 0.001$ mm^3
Sum (volume of scar) = 0.47 mm^3	

Table 6.3.18. Volumes of all separate plates consisting the wear scar shown in figure 6.3.22.

Number of plate	Volume of plate
1	$\pi \times 3.7^2 \times 0.002 = 0.086\ mm^3$
2	$\pi \times 2.7^2 \times 0.005 = 0.11\ mm^3$
3	$\pi \times 2.7^2 \times 0.005 = 0.11\ mm^3$
4	$\pi \times 2^2 \times 0.005 = 0.06\ mm^3$
5	$\pi \times 2^2 \times 0.005 = 0.06\ mm^3$
6	$\pi \times 1.5^2 \times 0.005 = 0.035\ mm^3$
7	$\pi \times 1.5^2 \times 0.005 = 0.035\ mm^3$
8	$\pi \times 1.1^2 \times 0.005 = 0.02\ mm^3$
9	$\pi \times 1.1^2 \times 0.005 = 0.02\ mm^3$
10	$\pi \times 0.8^2 \times 0.005 = 0.01\ mm^3$
11	$\pi \times 0.8^2 \times 0.005 = 0.01\ mm^3$
12	$\pi \times 0.4^2 \times 0.005 = 0.0025\ mm^3$
13	$\pi \times 0.4^2 \times 0.004 = 0.002\ mm^3$
Sum (volume of scar) = 0.56 mm^3	

Table 6.3.19. Volumes of all separate plates consisting the wear scar shown in figure 6.3.23.

Returning now to the matter of comparison of material loss between Ti:G2 and the stainless steels, it is important to consider the separate aspects of weight loss, volume loss and scar depth. An overall indication of such aspects is obtained by comparing figure 6.3.24 (volume loss) and figure 6.3.25 (scar depth) with figure 6.3.21 (weight loss). Note that in these three figures, the y axis scales have been chosen to represent identical proportionate sevenfold increases. This allows the clear visual conclusion that the apparent superiority of Ti:G2 over the superduplex stainless steel in weight loss terms is eliminated completely in volume loss terms and almost completely in respect of the scar depth. Precise data demonstrating these matters are presented in three separate examples at comparable sand loadings in tables 6.3.20 – 6.3.22.

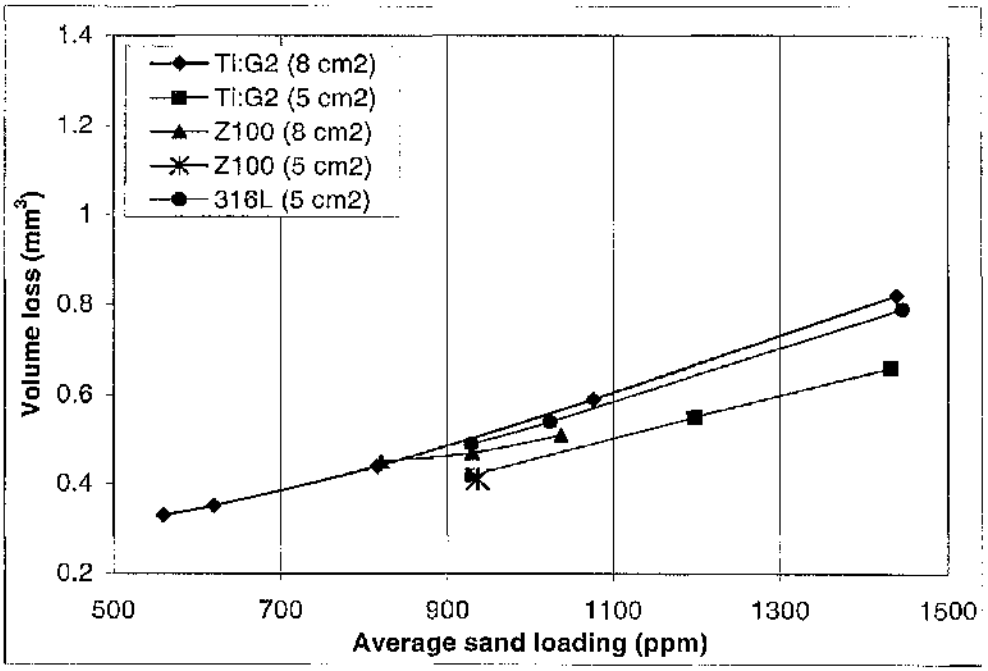

Figure 6.3.24. Volume loss versus average sand loading for 16 hour solid/liquid erosion-corrosion on Ti:G2, Z100 and 316L.

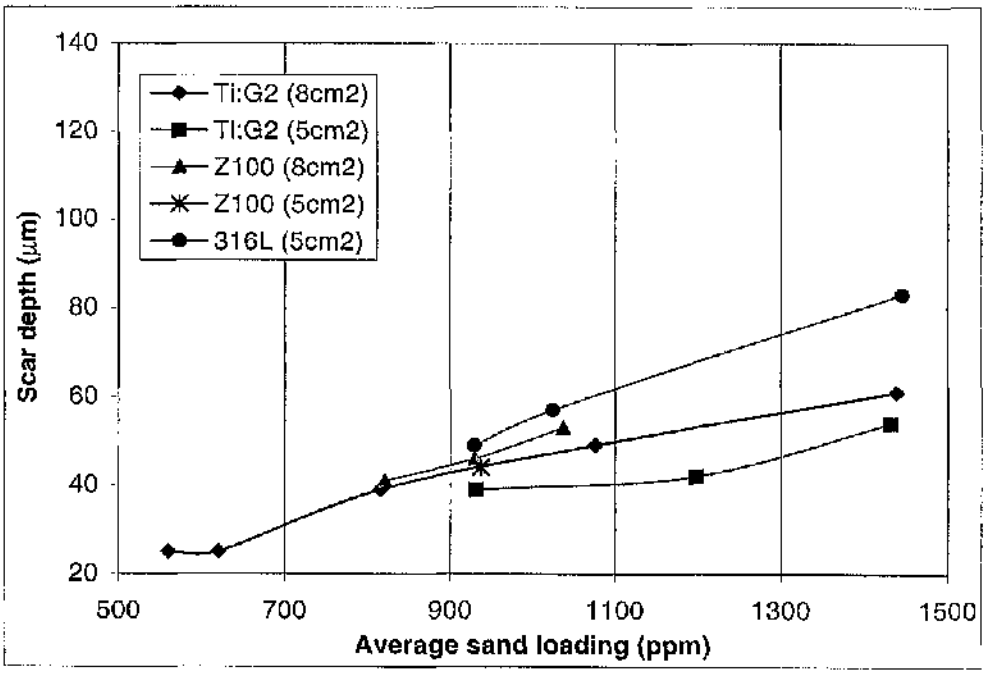

Figure 6.3.25. Scar depth versus average sand loading for 16 hour solid/liquid erosion-corrosion on Ti:G2, Z100 and 316L.

	Weight loss (mg)	Sand loading (ppm)	Scar depth (μm)
Ti:G2 (A=8cm^2)	2.7	1035 – 1116	49
Z100 (A=8cm^2)	4.0	981 - 1093	53
Weight loss ratio = 4.0/2.7 = 1.5			
Volume loss ratio = 0.5/0.6 = 0.8			
Scar depth ratio = 53/49 = 1.1			

Table 6.3.20. First numerical comparison between 8 cm^2 Ti:G2 and 8 cm^2 Z100, based on weight loss, volume loss and scar depth.

	Weight loss (mg)	Sand loading (ppm)	Scar depth (μm)
Ti:G2 (A=8cm^2)	2.0	804 - 827	39
Z100 (A=8cm^2)	3.5	814 - 828	41
Weight loss ratio = 3.5/2 = 1.75			
Volume loss ratio = 0.45/0.44 = 1			
Scar depth ratio = 41/39 = 1.05			

Table 6.3.21. Second numerical comparison between 8 cm^2 Ti:G2 and 8 cm^2 Z100, based on weight loss, volume loss and scar depth.

	Weight loss (mg)	Sand loading (ppm)	Scar depth (μm)
Ti:G2 (A=5cm^2)	1.9	907 – 955	39
Z100 (A=5cm^2)	3.2	921 - 954	44
Weight loss ratio = 3.2/1.9 = 1.7			
Volume loss ratio = 0.4/0.4 = 1			
Scar depth ratio = 44/39 = 1.1			

Table 6.3.22. Numerical comparison between 5 cm^2 Ti:G2 and 5 cm^2 Z100, based on weight loss, volume loss and scar depth.

Similarly, the impressive large superiority of Ti:G2 to 316L in weight loss drops by a great amount when volume loss and scar depth are considered (table 6.3.23). Ti:G2 remains more erosion-corrosion resistant than 316L in terms of both volume loss and scar depth but only by about 25%.

	Weight loss (mg)	Sand loading (ppm)	Scar depth (μm)
Ti:G2 (A=5cm^2)	1.9	907 – 955	39
316L (A=5cm^2)	3.9	892 - 967	49
Weight loss ratio = 3.9/1.9 = 2.05			
Volume loss ratio = 0.5/0.4 = 1.25			
Scar depth ratio = 49/39 = 1.25			

Table 6.3.23. Numerical comparison between 5 cm^2 Ti:G2 and 5 cm^2 316L, based on weight loss, volume loss and scar depth.

Effect of impingement angle

Ti:G2 specimens of 8 cm^2 area were also tested at 30° and 60° impinging angle in solid/liquid erosion-corrosion. The weight loss results obtained (tables 6.3.24 and 6.3.25) are plotted in figure 6.3.26 together with the relative results at 90° (see table 6.3.12). The evidence indicates that at 30° degrees Ti:G2 exhibits somewhat higher material loss than at 90°. One test at 60° also exhibited a higher weight loss than at 90° - experiment at comparable sand loading. The other two 60° - tests, undertaken at relatively low solid contents, yielded results which suggest (as might be expected) that any effect of impingement angle will be minimised as solid loading approaches zero.

Sand loading (ppm)	Weight loss (mg)	Scar depth (μm)
1088 – 1095	3.0	48
970 – 1068	2.8	43
867 - 949	2.4	37

Table 6.3.24. Weight losses and wear scar depths of 8 cm^2 Ti:G2 specimens at various sand loadings, after 16 hours solid/liquid erosion-corrosion at 30° impinging angle.

Sand loading (ppm)	Weight loss (mg)	Scar depth (μm)
509 – 579	1.7	36
460 – 498	1.4	34
396 - 472	1.3	26

Table 6.3.25. Weight losses and wear scar depths of 8 cm^2 Ti:G2 specimens at various sand loadings, after 16 hours solid/liquid erosion-corrosion at 60° impinging angle.

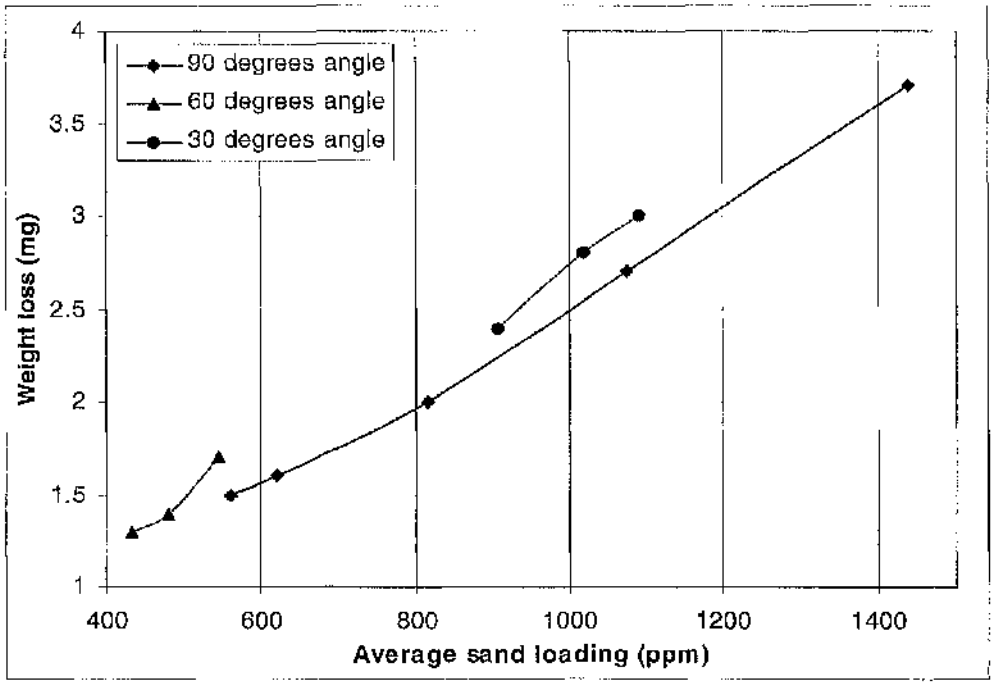

Figure 6.3.26. Weight loss versus average sand loading for 16 hour solid/liquid erosion-corrosion on 8 cm^2 Ti:G2 specimens at 90°, 60° and 30° impingement angle.

Figure 6.3.27 shows the comparison between 90°, 60° and 30° degrees impinging angle in terms of wear scar depth. The evidence is that at 90° degrees Ti:G2 suffers deeper erosion-corrosion damage directly under the jet than at 30°. On the other hand it appears that erosion-corrosion damage directly under the jet is greater at 60° than at 90°. Figures 6.3.28 and 6.3.29 show two surface profiles of Ti:G2 at 30° and 60° degrees impinging angle respectively. The wear scars are remarkably symmetrical even at the oblique angle of 30° impingement although, as would be expected, it is evident that at 30° impinging angle the diameter of the wear scar (~ 10 mm) is greater than at 90° (~ 8 mm, see figure 6.3.9). Thus the greater weight loss at 30° (despite the lower scar depth) must, at least partly, be accounted for by the apparently larger scar volume but may also involve relatively more material loss from the region outside the scar. However, 60° degrees impinging angle does not seem to have any clear effect on the width of the wear scar.

These interesting and variable effects of angle of impingement on erosion-corrosion damage are quantified in table 6.3.26 for three examples at comparative sand loading. Moreover table 6.3.27 shows the ratios of weight loss and scar depth for one 90° test and two 60° tests at lower solid loadings and tend to support the notion of deeper scar depths at 60° than 90°.

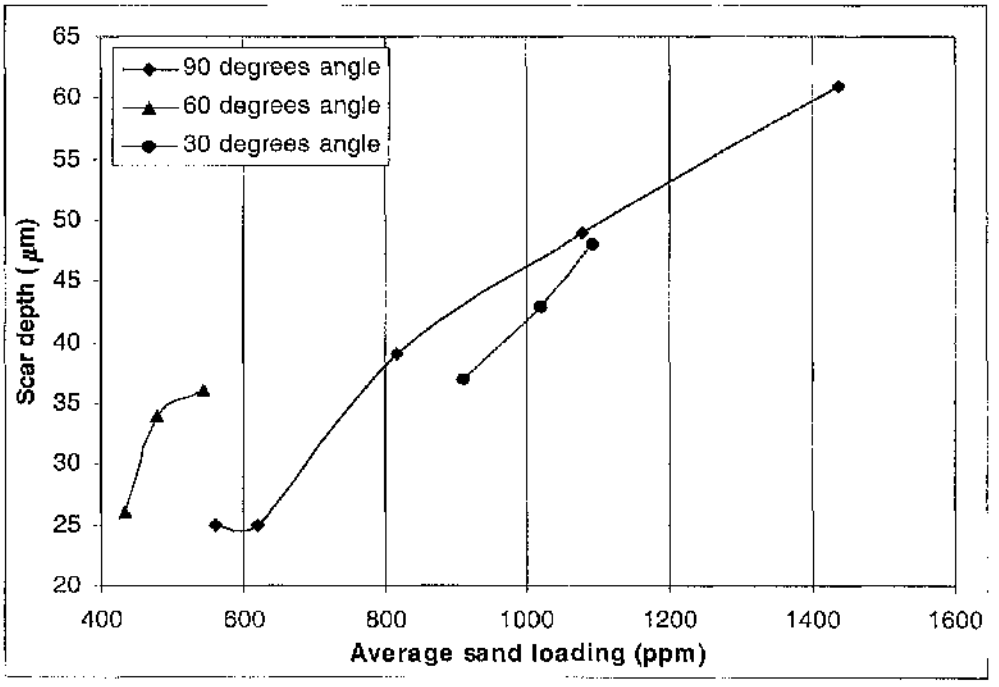

Figure 6.3.27. Scar depth versus average sand loading for 16 hour solid/liquid erosion-corrosion on 8 cm^2 Ti:G2 specimens at 90°, 60° and 30° impingement angle.

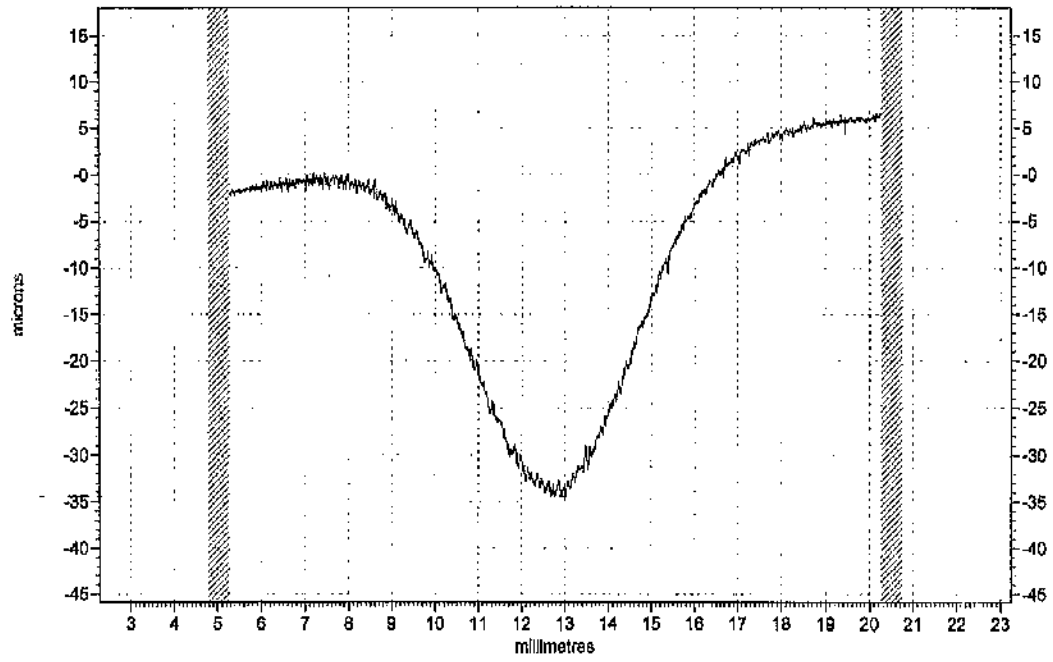

Figure 6.3.28. Surface profile of Ti:G2 after 16 hours of solid/liquid erosion-corrosion at 30° impingement angle, 12.6 m/s and 867 – 949 ppm.

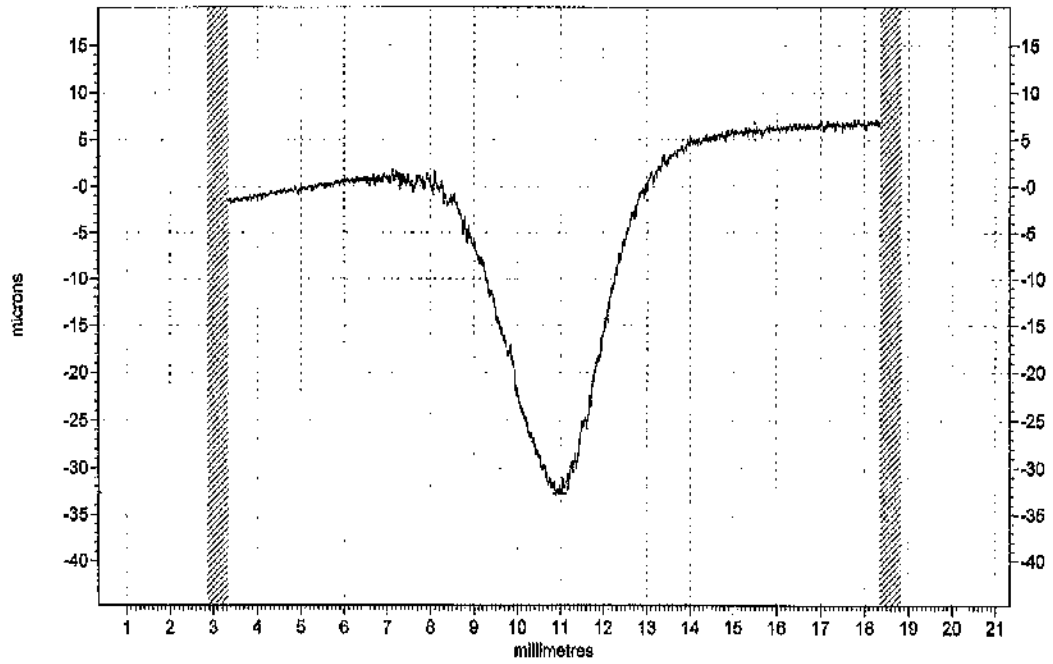

Figure 6.3.29. Surface profile of Ti:G2 after 16 hours of solid/liquid erosion-corrosion at 60° impingement angle, 12.6 m/s and 509 – 579 ppm.

	Weight loss (mg)	Sand loading (ppm)	Scar depth (μm)
90° impingement angle	2.7	1035 – 1116	49
30° impingement angle	2.8	970 – 1068	43
Weight loss ratio = 2.7/2.8 = 0.96			
Scar depth ratio = 49/43 = 1.14			
90° impingement angle	2.7	1035 – 1116	49
30° impingement angle	3.0	1088 – 1095	48
Weight loss ratio = 2.7/3.0 = 0.9			
Scar depth ratio = 49/48 = 1.02			
90° impingement angle	1.5	532 – 588	25
60° impingement angle	1.7	509 – 579	36
Weight loss ratio = 1.5/1.7 = 0.88			
Scar depth ratio = 25/36 = 0.7			

Table 6.3.26. Numerical comparison between 90° and 30°, and 90° and 60° impingement angle on 8 cm^2 Ti:G2 specimens, based on weight loss and scar depth.

	Weight loss (mg)	Sand loading (ppm)	Scar depth (μm)
90° impingement angle	1.5	532 – 588	25
60° impingement angle	1.4	460 – 498	34
Weight loss ratio = 1.5/1.4 = 1.07			
Scar depth ratio = 25/34 = 0.73			
90° impingement angle	1.5	532 – 588	25
60° impingement angle	1.3	396 - 472	26
Weight loss ratio = 1.5/1.3 = 1.15			
Scar depth ratio = 25/26 = 0.96			

Table 6.3.27. Numerical comparison between 90° and 60° impingement angle at lower solid loadings for 60° ,on 8 cm^2 Ti:G2 specimens, based on weight loss and scar depth.

Tests with concentric specimens

In addition to the main series of solid/liquid erosion-corrosion experiments using composite specimens, tests were also undertaken on concentric specimens. These were designed to enable the observation, separately and under the same experimental conditions, of the erosion-corrosion behaviour of specimen's central region directly under the jet from the erosion-corrosion behaviour of the metal matrix around the central region. The description of concentric specimens has already been given in chapter 6.

Concentric specimens were involved in two 16 hour solid/liquid erosion-corrosion tests. The main objective of these tests was to compare the anodic polarisation responses of the two specimens as a function of time. In order to do this in one experiment on the two specimens simultaneously, the anodic polarisation scans were limited to 20 mV from Ecorr (rather similar to a linear polarisation monitoring exercise). This procedure allows multiple anodic polarisation scans on the same specimen without the danger of altering the surface characteristics which is a possible feature of a full anodic polarisation scan. These small-range polarisations were carried out after half an hour, 2 hours and 16 hours in the two separate experiments (figures 6.3.30 – 6.3.35). The particle concentration was 606 – 692 ppm and 602 – 690 ppm in the first and second experiment respectively.

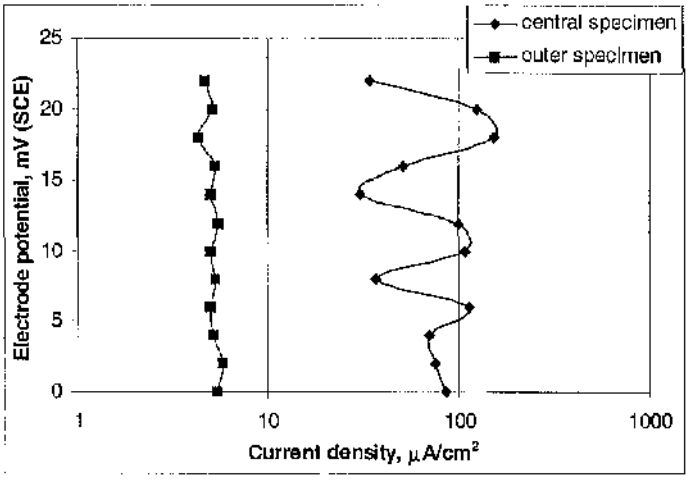

Figure 6.3.30. Linear polarisation of Ti:G2 central and outer ring specimen after half an hour solid/liquid erosion-corrosion (first test).

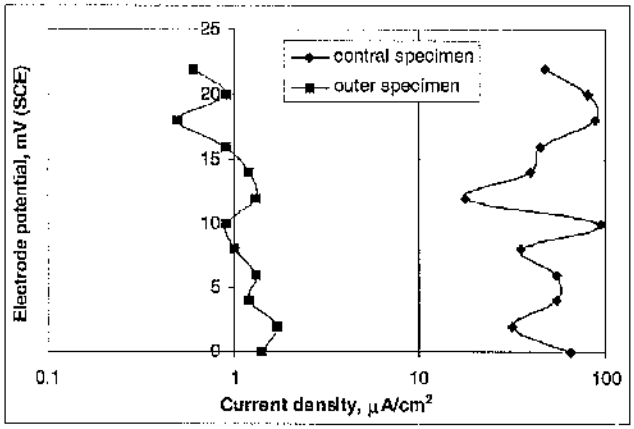

Figure 6.3.31. Linear polarisation of Ti:G2 central and outer ring specimen after 2 hours solid/liquid erosion-corrosion (first test).

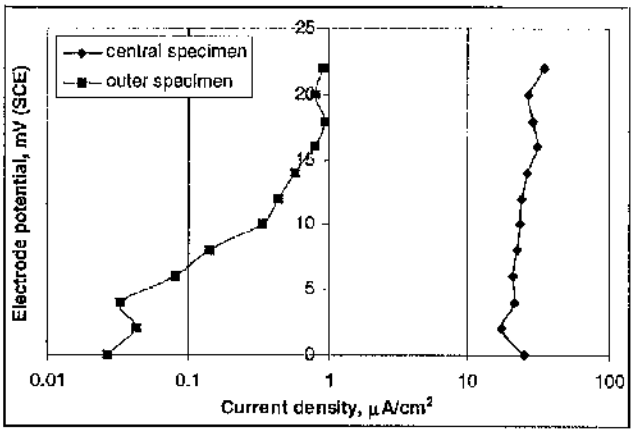

Figure 6.3.32. Linear polarisation of Ti:G2 central and outer ring specimen after 16 hours solid/liquid erosion-corrosion (first test).

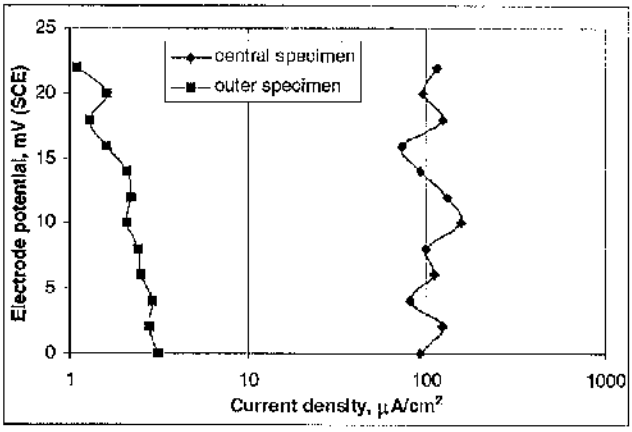

Figure 6.3.33. Linear polarisation of Ti:G2 central and outer ring specimen after half an hour solid/liquid erosion-corrosion (second test).

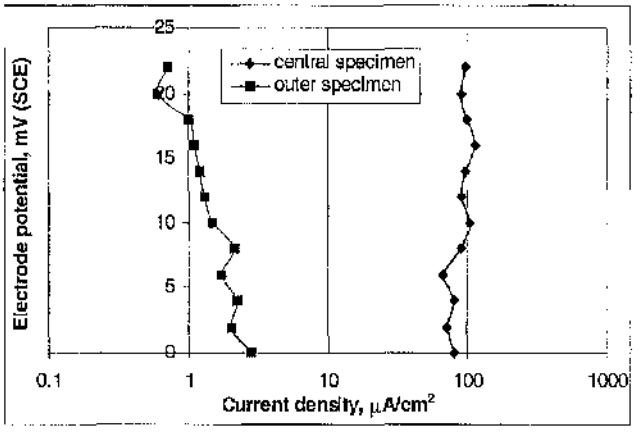

Figure 6.3.34. Linear polarisation of Ti:G2 central and outer ring specimen after two hours solid/liquid erosion-corrosion (second test).

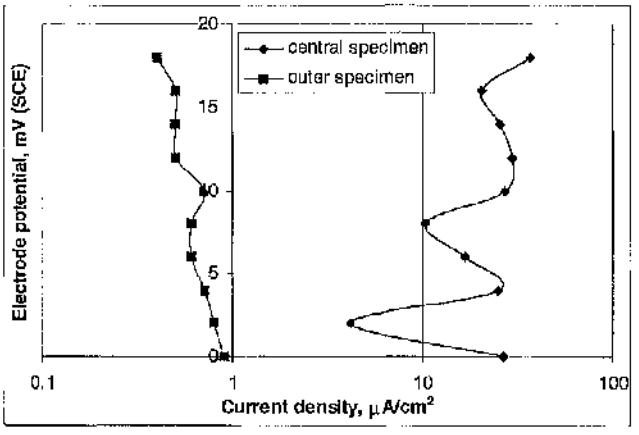

Figure 6.3.35. Linear polarisation of Ti:G2 central and outer ring specimen after 16 hours solid/liquid erosion-corrosion (second test).

Figures 6.3.30 – 6.3.35 demonstrate that the central specimen is quite clearly more electrochemically active than the outer specimen right from the very start of the 16 hour exposure and also that it exhibits continually much higher current density than the outer ring specimen. Furthermore, figures 6.3.31, 6.3.32 and 6.3.35 show that the corrosion rates decreased for both central and outer specimens with time. Note that the curves in figures 6.3.30 – 6.3.35 are normalised to Ecorr = 0.

Figure 6.3.36 shows the full anodic scans after 16 hours of solid/liquid erosion-corrosion. Evidently, the outer ring specimen gives an active ⟶ passive polarisation curve at an electrode potential somewhat higher than Ecorr whereas the central ring does not. The latter gives a more straightforward anodic polarisation plot for about 100 mV from Ecorr after which average current 'stabilises' but with rapid fluctuation of up to 100 $\mu A/cm^2$.

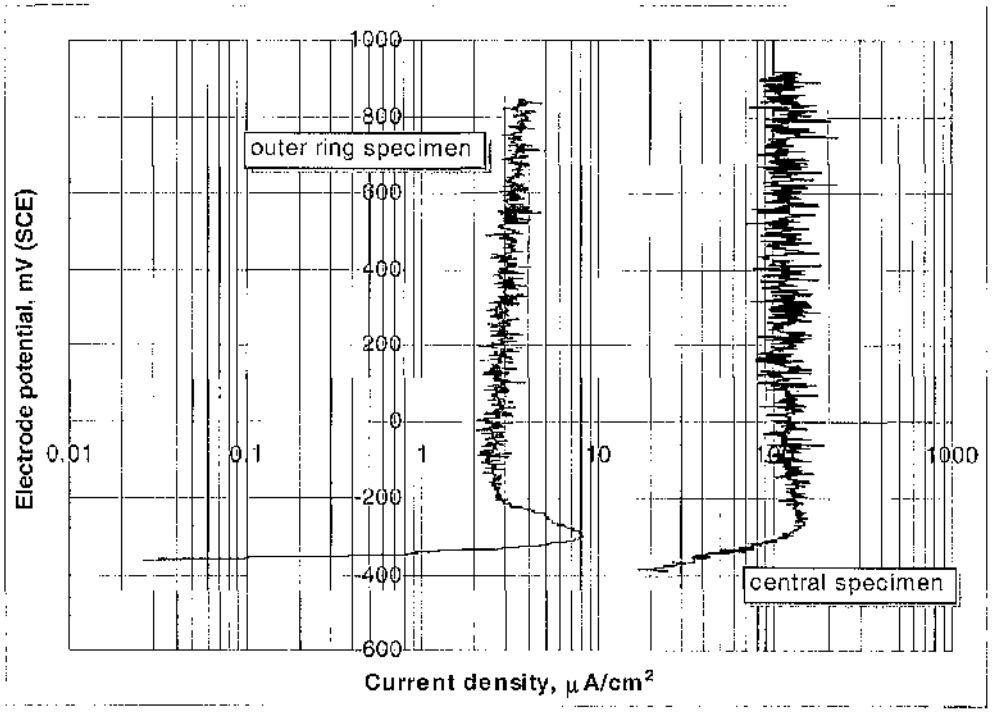

Figure 6.3.36. Anodic polarisation of Ti:G2 central and outer ring specimen after 16 hours of solid/liquid erosion-corrosion.

Figure 6.3.37 shows the first 200 mV positive from Ecorr of the anodic polarisation curves shown in figure 6.3.36. The value of i_{corr} (obtained by Tafel extrapolation of linear portion of anodic polarisation curve) for the central specimen is shown to be 20 $\mu A/cm^2$. By Faraday's law, the passage of 96500 coulombs of charge is associated with the dissolution of 47.9/3 = 15.96 g of Ti (note for Ti, atomic weight = 47.9 g/mole and valency n = 3) "dissolving" via $Ti \longrightarrow Ti^{3+} + 3e^-$,

i.e. 20 $\mu A/cm^2$ will dissolve $(15.96 \times 20 \times 10^{-6})/96500 = 3.3 \times 10^{-9}$ $g/cm^2/s = 3.3 \times 10^{-6}$ $mg/cm^2/s = 3.3 \times 10^{-6} \times 60 \times 60 \times 16 = 0.19$ $mg/cm^2/16h$.

Since the area of the central specimen = 0.28 cm^2 then $0.19 \times 0.28 =$ 0.05 mg/16h.

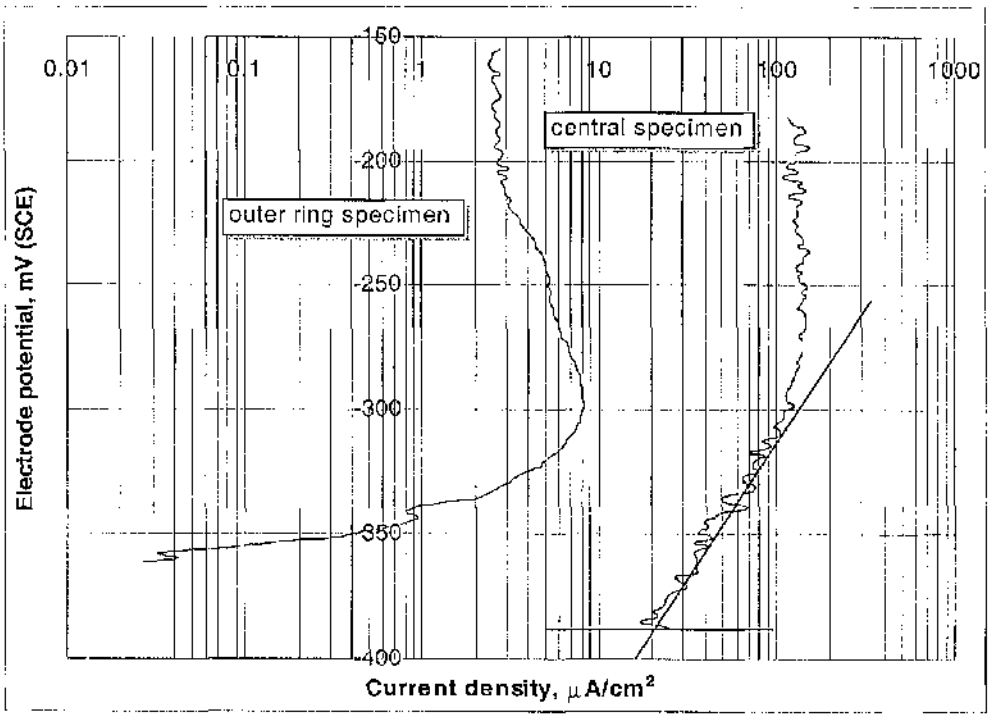

Figure 6.3.37. Magnification of Ti:G2 central and outer ring specimen's current density immediately positive to Ecorr (full anodic scans in figure 6.3.36).

After 16 hours of solid/liquid erosion-corrosion, Ti:G2 as a small specimen of area 0.28 cm^2 has given a 'TWL' of 1.1 mg at a particle concentration of 742 – 765 ppm (Table 6.3.14) and the direct corrosion rate, 'C', = 0.05 mg at 606 – 692 ppm as mentioned above. In an additional experiment, a specimen of 0.28 cm^2 area was tested under the influence of cathodic protection with a sand loading of 683 – 751 ppm and gave a weight loss of 0.8 mg after 16 hours. Since particle concentrations are more or less comparable it is approximated that erosion-corrosion damage on the central specimen consists of 72.7% 'E', 4.5% 'C' and 22.8% 'S' (above data also shown in table 6.3.28). It is presumed that the 'C' factor for the outer specimen would be negligible since the very low current exhibited would give a very small icorr.

Factor	Sand loading (ppm)	Weight loss (mg)	% of 'TWL'
'E'	683 - 751	0.8	72.7
'C'	606 - 692	0.08	4.5
'S'	-	0.22	22.8

Table 6.3.28. Sand concentration, weight loss and percentage of 'TWL' for 'E', 'C' and 'S' factors consisting a 'TWL' of 1.1 mg at 742 – 765 ppm.

Table 6.3.29 shows all Ecorr values recorded at various stages through both experiments. As soon as erosion-corrosion starts, the corrosion potential of both outer and central specimens undergoes a large shift in the negative direction apparently due to breakdown of the protective film by the bombardment of the sand particles. This is followed by a slow positive drift in the corrosion potential throughout the 16 hours of the experiment. Additionally, the Ecorr values of the central specimen are noted to be more negative than the relative Ecorr values of the outer specimen.

	1st test		2nd test	
Ecorr (mV)	Central specimen	Outer specimen	Central specimen	Outer specimen
when static	-368	-351	-288	-324
when test just started	-620	-470	-535	-420
after half an hour	-545	-440	-500	-384
After 2 hours	-480	-367	-453	-355
After 16 hours	-430	-360	-420	-344

Table 6.3.29. Ecorr values of central and outer ring specimens at various stages through both 16 hour concentric tests in solid/liquid erosion/corrosion.

Galvanic currents were also recorded (table 6.3.30). The galvanic currents were measured by temporarily connecting the two specimens via an ammeter at the times shown in table 6.3.30. The direction of current flow of all galvanic currents measured was such that the central specimen was acting as anode (as the potential readings in table 6.3.29 would imply). The recorded galvanic currents were very substantial, in relation to the anodic area of 0.28 cm^2, in the early stages of the experiment but did decline as time passed.

Galvanic current ($\mu A/0.28cm^2$)	1st test	2nd test
after half an hour	15-27	19-32
after 2 hours	9-17	14-20
after 16 hours	5-6	4-7

Table 6.3.30. Galvanic currents measured at different stages through both 16 hour concentric tests in solid/liquid erosion/corrosion. (Note that 0.28 cm^2 is the area of the central specimen.)

Microscopy

Free solid/liquid erosion-corrosion

Figure 6.3.38 shows a Ti:G2 specimen as a whole which was tested for three days in solid/liquid erosion-corrosion. It reveals an outer dark ring of approximately inner diameter 7 mm and outer diameter 12 mm, which was always the case for all materials tested in solid/liquid erosion-corrosion, and a clear inner scar. Figures 6.3.39 to 6.3.41 show at low and very high magnification the centre (region directly under the jet) of a Ti:G2 specimen after 16 hours of solid/liquid erosion-corrosion. Clearly, the surface in the wear scar is rather non-uniform on a microscale and drill holes, apparently caused by the bombardment of the sand particles, are also evident. Further out the surface looks more uniform and high magnification reveals 'skid marks' (figure 6.3.42), presumably caused by the effect of the sand particles sliding along the surface around the centre. In all of a number of Ti:G2 specimens, after different exposure periods (4, 8, 16 and 72 hours) in solid/liquid erosion-corrosion, skid marks were found to be most intense in the region just outside the wear scar, i.e. in the dark ring shown in figure 6.3.38. An example of this is shown in figures 6.3.43a and 6.3.43b. Under the same experimental conditions, 316L and Z100 demonstrated basically very similar features and equivalent sets of photos are presented in figures 6.3.44 – 6.3.52. However, in contrast to Ti:G2, 316L and Z100 developed some rather clear plastic deformation inside the wear scar (figures 6.3.46 and 6.3.50 respectively). Moreover, in the case of 316L there was evidence of damage right at the very outside of the specimen (figure 6.3.48), a feature that was not observed on all the other materials that were tested in solid/liquid erosion-corrosion. Figures 6.3.47 and 6.3.52 also reveal possible cracks along skid marks on the surface of 316L and Z100 respectively.

As figures 6.3.53 and 6.3.54 demonstrate, Ti-6Al-4V displayed more or less the same features inside the wear scar after 16 days solid/liquid erosion-corrosion as Ti:G2. Figure 6.3.55 shows the same Ti-6Al-4V specimen shown in the two previous figures with skid marks on the surface area outside the wear scar. Quite similarly to Ti:G2, skid marks were much more intense in the outer dark ring than in the surface further out (also see figures 6.3.43a and 6.3.43b). The S.E.M. photograph in figure 6.3.56

shows these skid marks at higher magnification together with possible cracks associated with them.

It was also noticed that the surface of all materials tested in free solid/liquid erosion-corrosion, but especially the surface of 316L and Z100, consisted of numerous tiny pits. These pits were present in both wear scar and outer surface (see figures 6.3.40, 6.3.42, 6.3.45, 6.3.47, 6.3.48, 6.3.50, 6.3.52, 6.3.53 and 6.3.56).

Solid/liquid erosion-corrosion under cathodic protection

After 16 hours of cathodic protection in solid/liquid erosion-corrosion, the surface of Ti-6Al-4V both inside and outside the wear scar (figures 6.3.57 and 6.3.58 respectively) looks as much affected as in free solid/liquid erosion-corrosion conditions. That was also the case for Ti:G2. After 16 hours of cathodic protection, the surface of Ti:G2 just outside the wear scar (figure 6.3.59) looks very similar to Ti:G2's surface just outside the wear scar under free solid/liquid erosion-corrosion (also see 7.3.43a) which indicates no apparent difference in the damage mechanisms. The latter implies that for Ti:G2 and Ti-6Al-4V in solid/liquid erosion-corrosion conditions, the erosion effect, in relation to the corrosion effect, is quite predominant.

Anodic polarisation after 16 hours of solid/liquid erosion-corrosion

Figure 6.3.60 shows the same outer dark ring around the wear scar of a Ti:G2 specimen that was anodically polarised after 4 hours of solid/liquid erosion-corrosion as the one developed during free solid/liquid erosion-corrosion (see figure 6.3.38). Figure 6.3.61 shows severe pitting in the centre (region directly under the jet) of a 316L specimen that was anodically polarised after 16 hours of solid/liquid erosion-corrosion. Pitting outside the centre was not as intense but certainly quite obvious (figure 6.3.62). No such pitting was observed on Ti:G2 (figure 6.3.63) or Z100 (figure 6.3.64) when anodically polarised after 16 hours of solid /liquid erosion-corrosion. This suggests that, under such conditions of exposure, the erosion corrosion behaviour of superduplex stainless steel is closer to titanium than to austenitic stainless steel. However, as shown in figure 6.3.65, in contrast to Ti:G2, Z100 after 16 hours developed small but numerous comets outside the directly impinging zone.

So far all photos presented in this section have shown specimens subjected to solid/liquid erosion-corrosion at ~ 1600-1700 ppm. Specimens exposed in solid/liquid erosion-corrosion at various other sand loadings ranging from 532 – 1487 ppm showed basically the same damage features. For example, figure 6.3.66 shows clear 'skid marks' on Ti:G2 at 907 – 955 ppm sand concentration.

Figure 6.3.38. Ti:G2 specimen as a whole after 3 days in solid/liquid erosion-corrosion (diameter of specimen 32 mm).

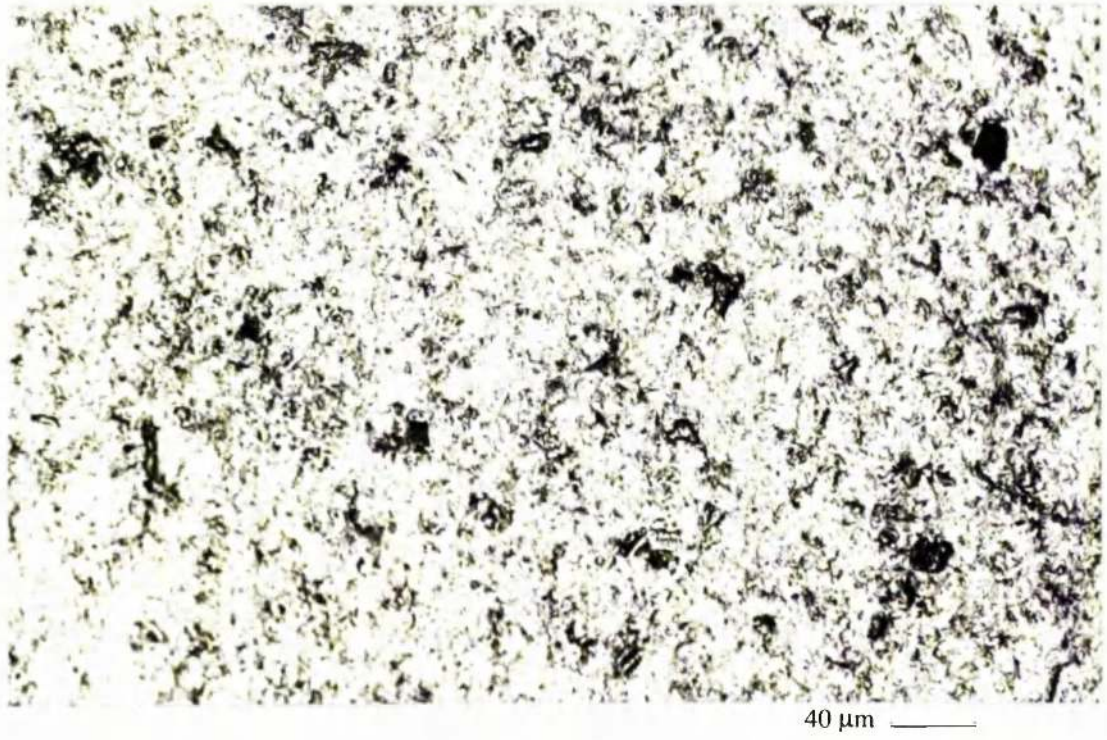

Figure 6.3.39. Centre of impingement with possible drill holes on Ti:G2 after 16 hours of solid/liquid erosion-corrosion.

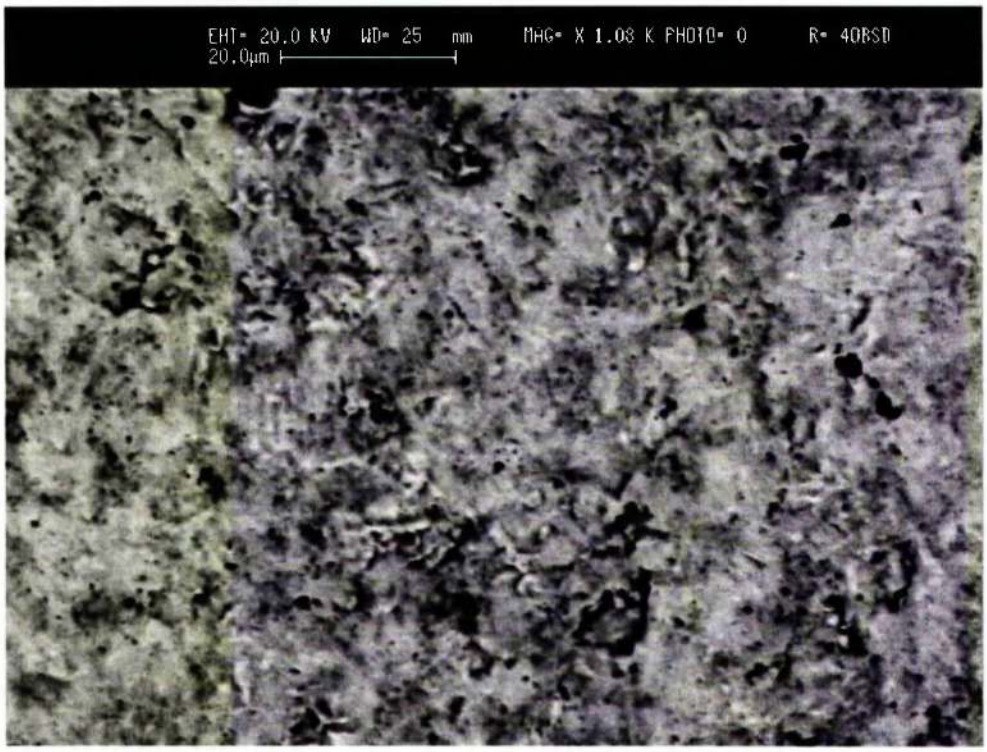

Figure 6.3.40. Centre of impingement on Ti:G2 after 16 hours of solid/liquid erosion-corrosion (S.E.M. image).

Figure 6.3.41. Centre of impingement on Ti:G2 at higher magnification after 16 hours of solid/liquid erosion-corrosion (S.E.M. image).

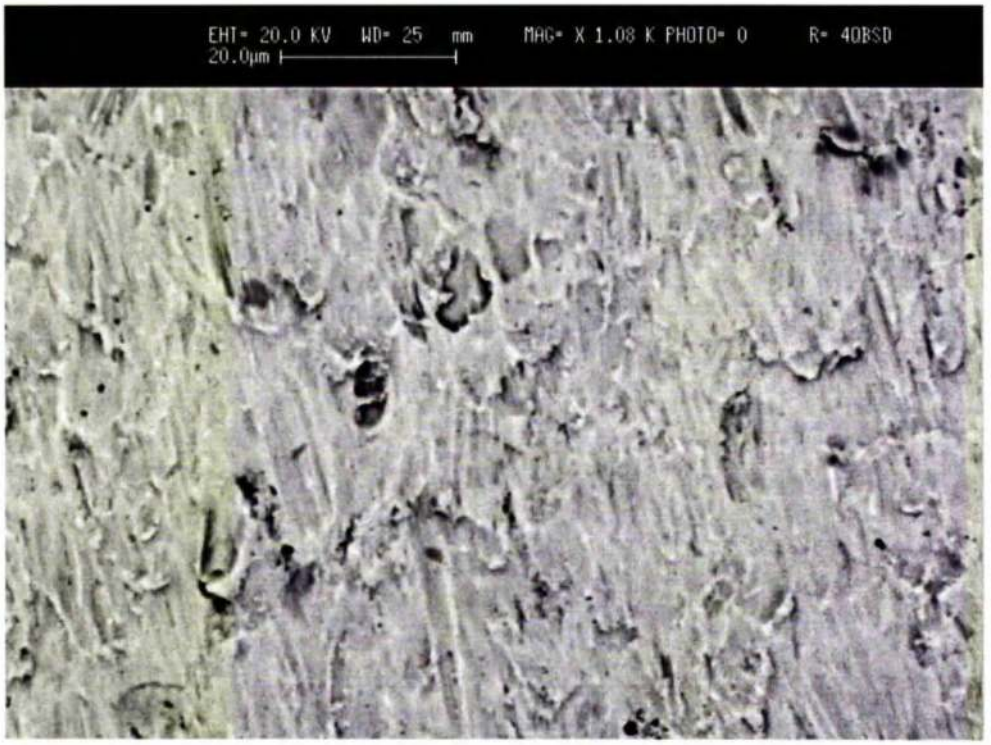

Figure 6.3.42. Skid marks outside the directly impinged zone of the same Ti:G2 specimen shown in figures 6.3.40 and 6.3.41(S.E.M. image).

Figure 6.3.43a. Quite intense skid marks in dark ring just outside the wear scar (shown in figure 6.3.38) on Ti:G2 tested in solid/liquid erosion-corrosion for 16 hours.

Figure 6.3.43b. Less intense skid marks in region further out the outer dark ring on Ti:G2 tested in solid/liquid erosion-corrosion for 16 hours.

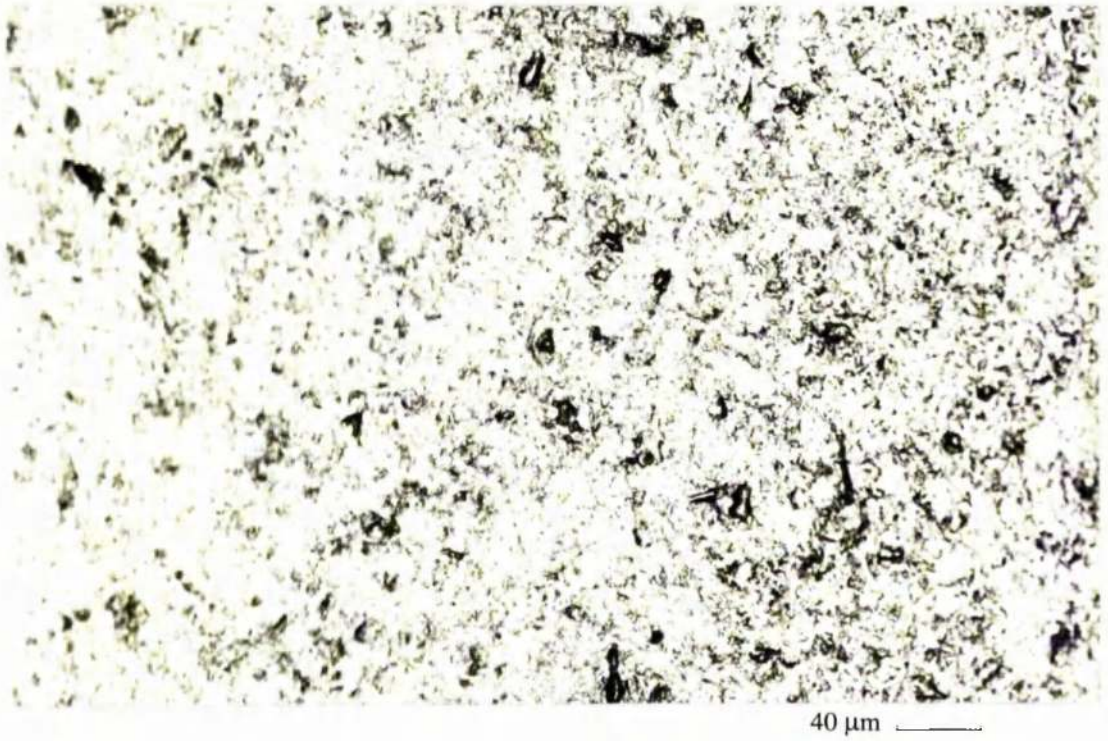

Figure 6.3.44. Centre of impingement with possible drill holes on 316L after 16 hours of solid/liquid erosion-corrosion.

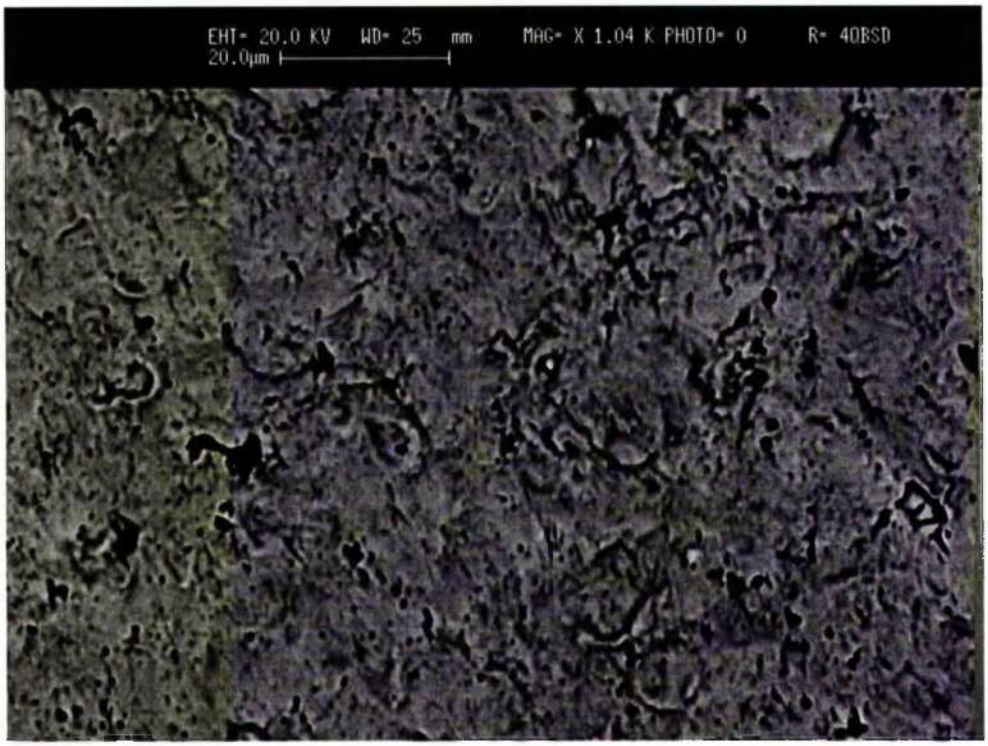

Figure 6.3.45. Centre of impingement on 316L after 16 hours of solid/liquid erosion-corrosion (S.E.M. image).

Figure 6.3.46. Centre of impingement on 316L at high magnification with possible evidence of plastic deformation after 16 hours of solid/liquid erosion-corrosion (S.E.M. image).

Figure 6.3.47. Skid marks along with numerous possible cracks outside the directly impinged zone of the same 316L specimen shown in figures 6.3.45 and 6.3.46 (S.E.M. image).

Figure 6.3.48. Evidence of damage right at the very outside of the surface of the same 316L specimen shown in figures 6.3.45, 6.3.46 and 6.3.47 (S.E.M. image).

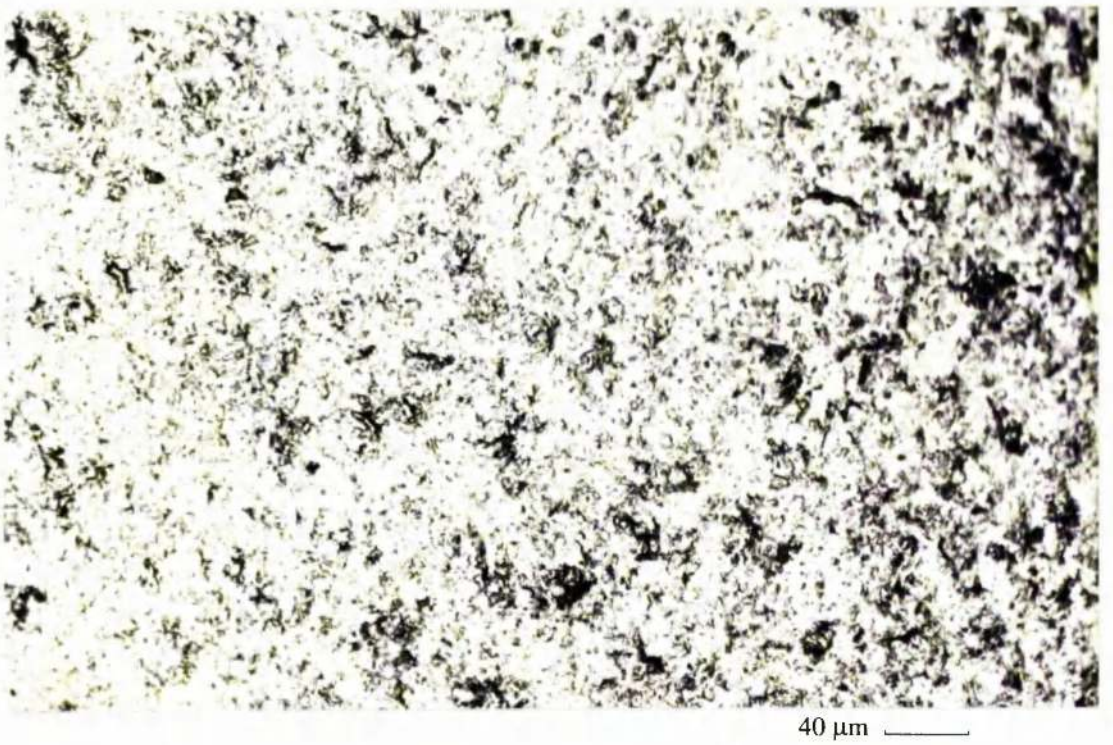

Figure 6.3.49. Centre of impingement with possible drill holes on Z100 after 16 hours of solid/liquid erosion-corrosion.

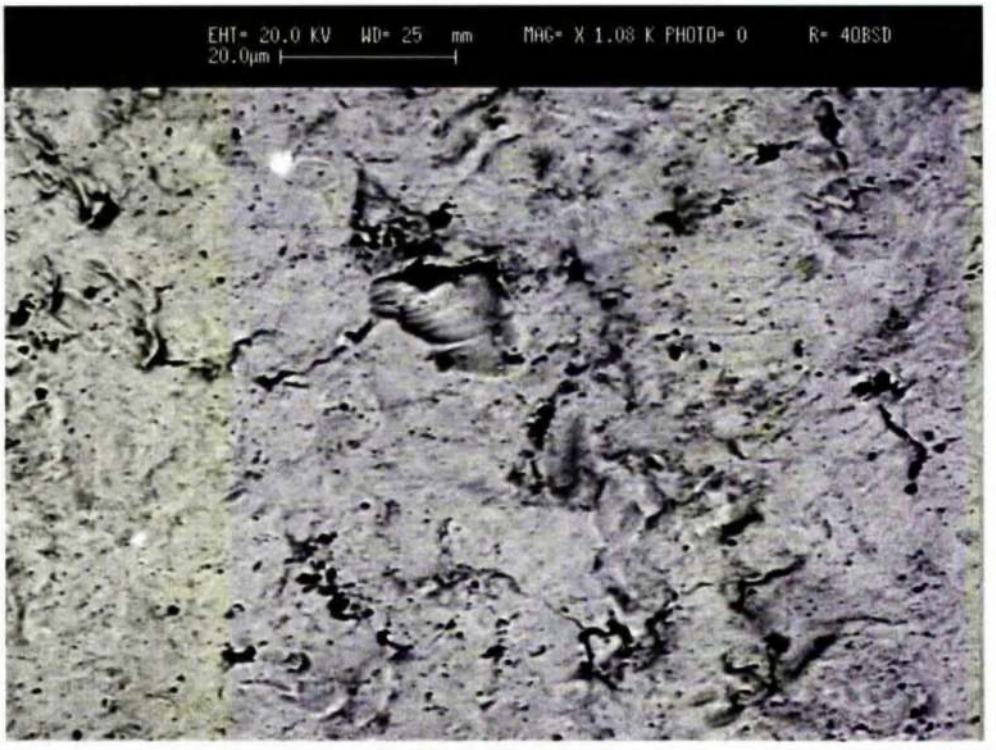

Figure 6.3.50. Centre of impingement on Z100 with possible evidence of plastic deformation after 16 hours of solid/liquid erosion-corrosion (S.E.M. image).

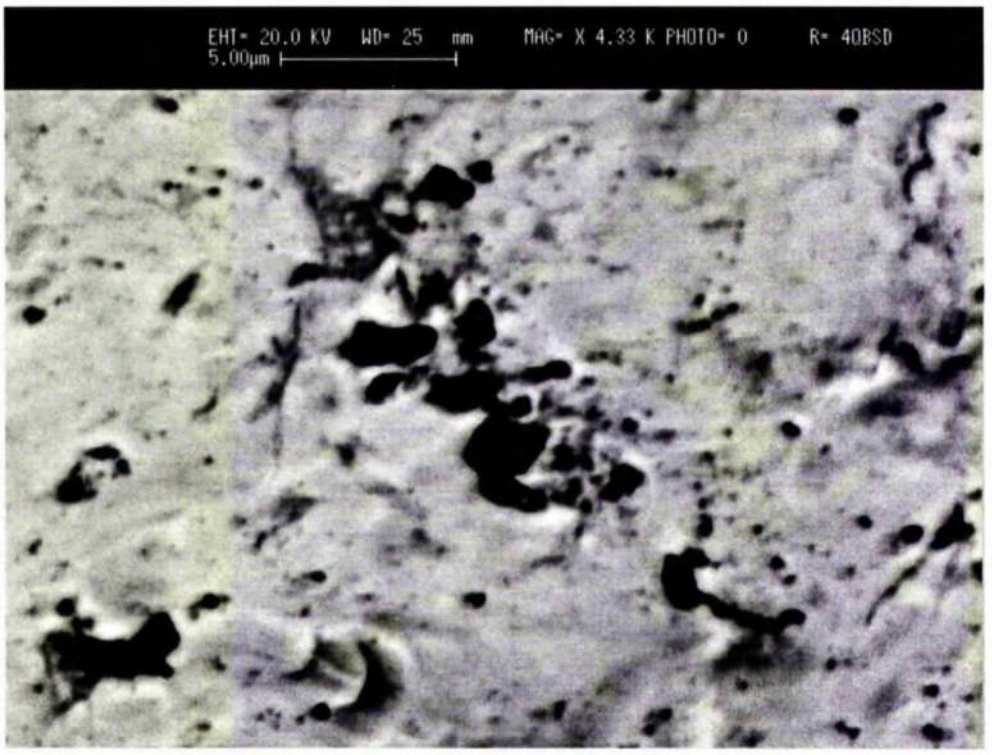

Figure 6.3.51. Centre of impingement on Z100 at very high magnification after 16 hours of solid/liquid erosion-corrosion (S.E.M. image).

Figure 6.3.52. Skid marks along with numerous possible cracks outside the directly impinged zone of the same Z100 specimen shown in figures 6.350 and 6.3.51 (S.E.M. image).

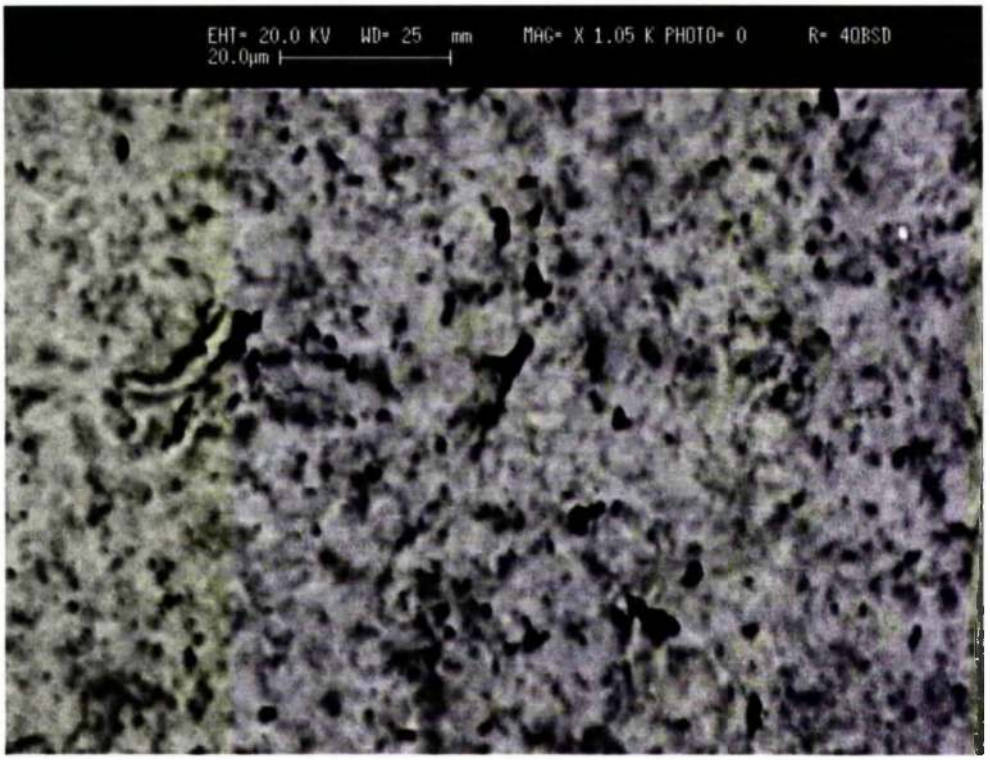

Figure 6.3.53. Centre of impingement on Ti-6Al-4V after 16 hours of solid/liquid erosion-corrosion (S.E.M. image).

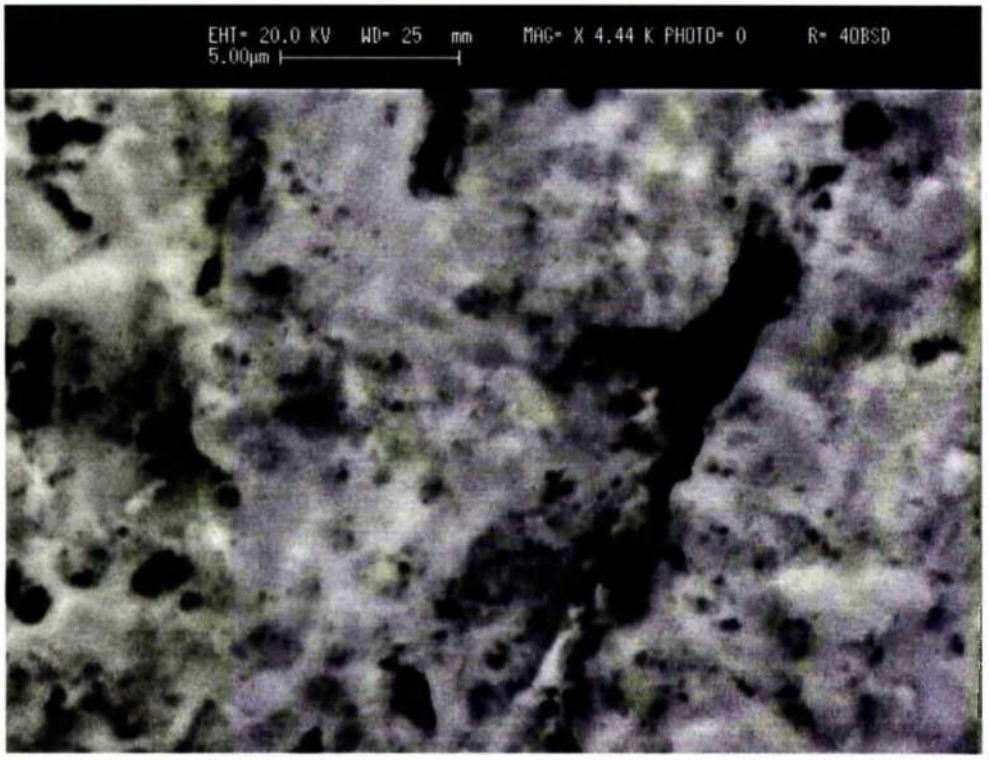

Figure 6.3.54. Centre of impingement on Ti-6Al-4V at higher magnification after 16 hours of solid/liquid erosion-corrosion (S.E.M. image).

Figure 6.3.55. Quite intense skid marks in dark ring just outside the wear scar on Ti-6Al-4V tested in solid/liquid erosion-corrosion for 16 hours.

Figure 6.3.56. Skid marks along with numerous possible cracks outside the wear scar of the same Ti-6Al-4V specimen shown in figures 6.3.53 and 6.3.54 (S.E.M. image).

Figure 6.3.57. Centre of impingement on Ti-6Al-4V after 16 hours of cathodic protection in solid/liquid erosion-corrosion (S.E.M. image).

Figure 6.3.58. Skid marks along with numerous possible cracks outside the wear scar of the same Ti-6Al-4V specimen shown in figure 6.3.57.

Figure 6.3.59. Skid marks just outside the wear scar of a Ti:G2 specimen tested in solid/liquid erosion-corrosion under cathodic protection for 16 hours.

Figure 6.3.60. Ti:G2 specimen as a whole when anodically polarised after 4 hours of solid/liquid erosion-corrosion (diameter of specimen 32 mm).

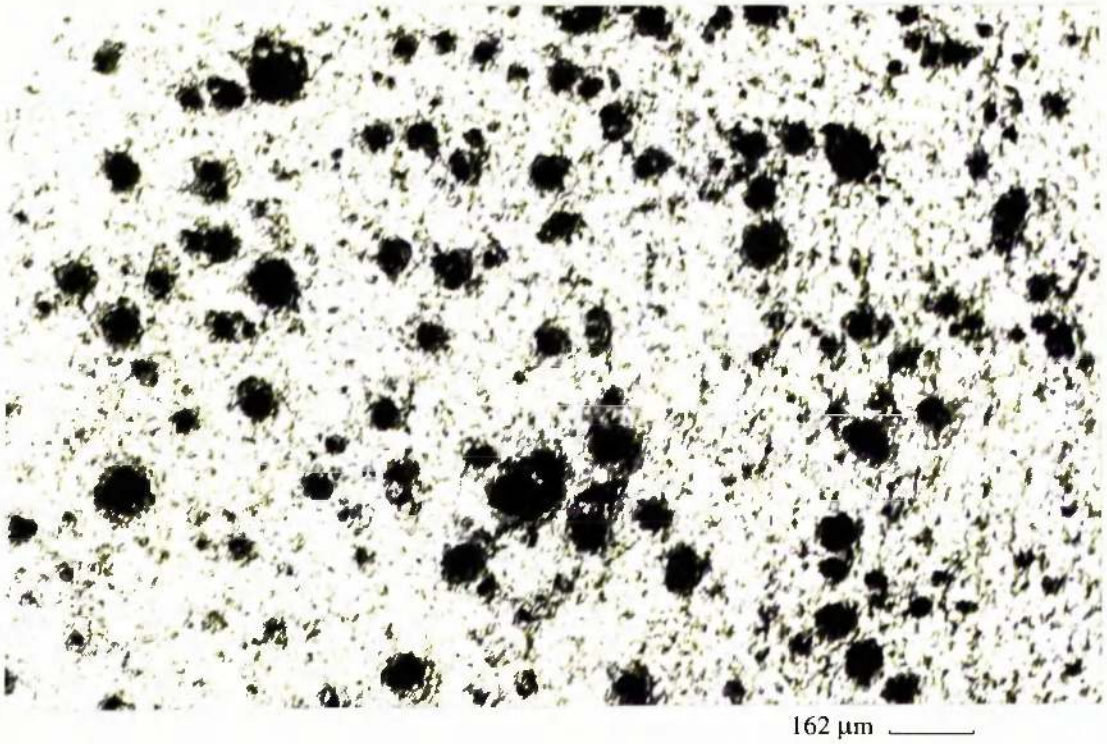

Figure 6.3.61. Severe pitting in the directly impinged region of a 316L specimen when anodically polarised after 16 hours of solid/liquid erosion-corrosion.

Figure 6.3.62. Pitting outside the directly impinged zone on the same 316L specimen shown in figure 6.3.61.

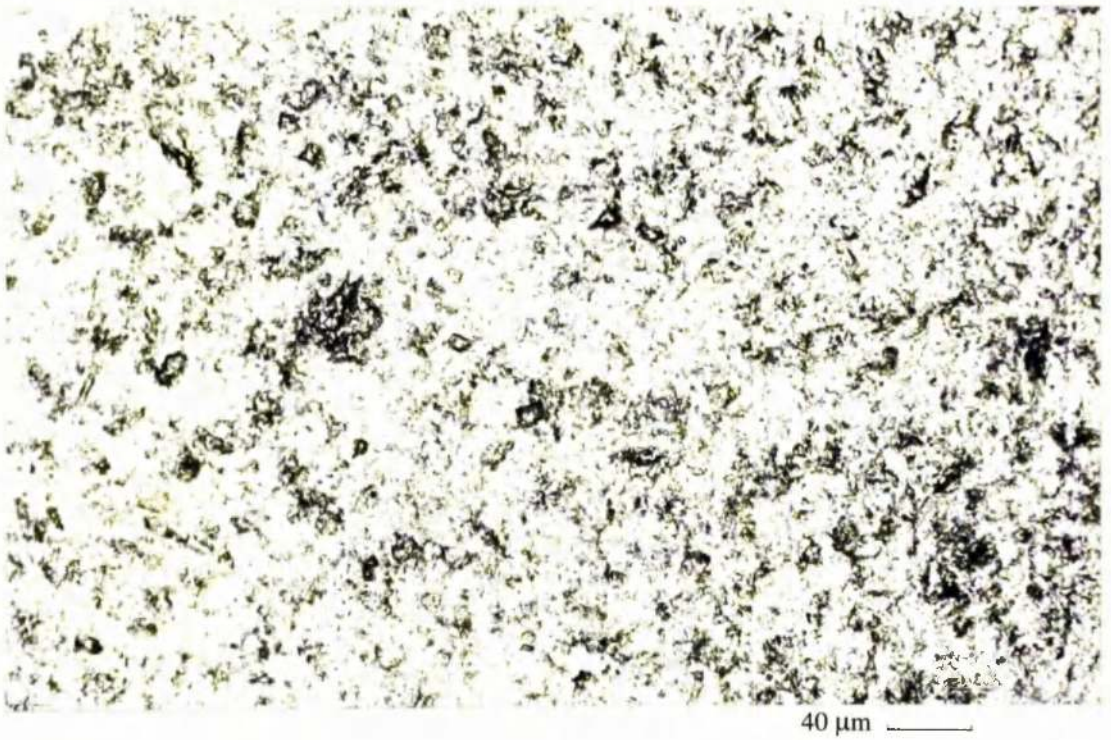

Figure 6.3.63. Centre of impingement on Ti:G2 when anodically polarised after 16 hours of solid/liquid erosion-corrosion.

Figure 6.3.64. Centre of impingement on Z100 when anodically polarised after 16 hours of solid/liquid erosion-corrosion.

Figure 6.3.65. Small comets outside the directly impinged zone on the same Z100 specimen shown in figure 6.3.64.

Figure 6.3.66. Skid marks on the surface outside the wear scar of a Ti:G2 specimen tested in solid/liquid erosion-corrosion with particle concentration 907 – 955 ppm.

7. DISCUSSION OF RESULTS ON Ti AND Ti ALLOYS ON CORROSION AND EROSION-CORROSION

7.1. Static tests

Static corrosion tests have been undertaken in this research on titanium in two environments, simulated seawater and distilled water. In the experiments in the former water, anodic polarisation tests upon initial exposure to artificial seawater at ambient temperature and 50°C demonstrated a very passive behaviour for Ti:G2, Ti:5111 and Ti-6Al-4Vconfirming that titanium and its two alloys possess excellent corrosion resistance in seawater at both temperatures. This is not at all a surprising finding given that it is well established that titanium and alloys possess excellent corrosion resistance in chloride-containing waters up to 130°C [99] (crevice corrosion resistance is limited up to 60°C [15,99,105,106,107,109,118,123]). These static tests in seawater were conducted simply to provide data within this project at one end of the erosion-corrosion spectrum.

Likewise, the experiments conducted in distilled water demonstrated excellent corrosion resistance of titanium over a range of conditions. Thus, referring back to figure 6.1.5, it is clear that after anodic polarisation upon initial exposure to distilled water, titanium over the range of distilled water conditions from 20°C to 80°C, with and without injection of CO_2, displays low current, i.e. passive, behaviour over a wide potential range. Although again this finding of excellent corrosion resistance in distilled water environments is hardly surprising, this does not appear to have been demonstrated in the literature. The stainless steel 316L, although less corrosion resistant than titanium, exhibited passive behaviour at 80°C in the presence of CO_2 for several hundred mV. Evidently, these anodic polarisation results also reveal the substantial difference in corrosion resistance between titanium and 316L on one hand and Cu-30%Ni on the other.

In relevance to the operational problems of vapour-side corrosion in some multistage flash plants [11,12,13], earlier results for Cu-10%Ni and Cu-30%Ni in this study (see chapter 4) have demonstrated the increasing severity of high temperature and CO_2 on

copper-nickel alloys. In terms of alternative materials, figure 6.1.5 provides evidence for much greater corrosion resistance in distilled water of titanium which already sees application in thermal desalination heat exchangers.

7.2. Liquid erosion-corrosion tests

Ti and its two alloys demonstrated high erosion-corrosion resistance since they exhibited no measurable weight losses after 12 hours of liquid erosion-corrosion in saline water at 71.1 m/s impinging jet velocity at both ambient temperature and 50°C. Further evidence of this high-durability performance was provided by the very passive behaviour that the three materials displayed when they were subjected to anodic polarisation at ambient temperature at the end of the 12-hour period (see figure 6.2.1). There were some current fluctuations exhibited by the Ti-base materials in the region immediately positive to Ecorr (figures 6.2.1 and 6.2.2) but they still only covered extremely low (<0.1 $\mu A/cm^2$) current density ranges and may therefore represent some influence of hydrodynamics on the formation and growth of the passive film rather than periodic de-passivation/re-passivation events.

Anodic polarisation scans at 50°C after 12 hours liquid erosion-corrosion at 71.1 m/s impinging jet velocity (see figure 6.2.3) also demonstrated protective corrosion behaviour for Ti:G2 and Ti:5111. Interestingly, under the same conditions, Ti-6Al-4V did not exhibit the same passive behaviour as Ti:G2 and Ti:5111, which implies a somewhat reduced resistance to erosion-corrosion for the Ti-6Al-4V alloy at elevated temperatures. Despite the overall similarities in the corrosion behaviour of Ti:G2 and Ti:5111 at 50°C and ambient temperature, current fluctuations were much more intense at 50°C and that indicates some possible instability in the performance of the passive film on the surface of the samples.

Without anodic polarisation at ambient temperature, stainless steel 316L also showed no evidence of measurable weight loss indicating very similar erosion-corrosion resistance to Ti and the two alloys under these particular experimental conditions. However, when anodic polarisation was applied at ambient temperature at the end of

the 12 hours, 316L exhibited a higher rate of corrosion increase with potential than Ti:G2, Ti:5111 and Ti-6Al-4V, which indicates some superiority in erosion-corrosion resistance for Ti and the two alloys in these conditions. It is also noticeable that at ambient temperature with anodic polarisation, 316L displayed fluctuation currents immediately above E_{corr} but at values of 0.1 – 2 $\mu A/cm^2$ which still represents overall passive behaviour. Breakdown of the passive film clearly occurred at ~ +250 mV and this is in good agreement with earlier work [141] at 100 m/s impinging velocity on this material. The less passive behaviour of 316L in relation to the Ti-base alloys was further and more clearly demonstrated at 50°C where the 316L stainless steel did yield a measurable weight loss (0.2 mg in each of the two tests) after 12 hours, and clear active behaviour upon anodic polarisation after 12 hours of liquid erosion-corrosion. The latter represents some difference in behaviour from a previous study [141] in similar conditions where 316L was still found to exhibit passivity at 50°C but only over a very small potential range.

It is relevant to point that the three Ti-base materials yielded no measurable weight losses, at both ambient and 50°C, under a weighing sensitivity of 0.1 mg. An "upper bound" of material loss can be calculated taking into account the density of Ti-6Al-4V and Ti:5111 (4.42 g/cm^3) and the area of their specimens used (5 cm^2). the thickness loss in mm/y was estimated as follows:

$(0.1 \times 10^{-3})/4.42 = 2.26 \times 10^{-5}$ cm^3

$(2.26 \times 10^{-5})/5 = 4.52 \times 10^{-6}$ cm thickness in 12 hours

$4.52 \times 10^{-6} \times 2 \times 365 = 3.3 \times 10^{-3}$ cm/y = 0.033 mm/y.

It is important to emphasise that the above calculations show the worst possible situation in which even at 50°C any erosion-corrosion damage on Ti-6Al-4V and Ti:5111 (and subsequently on Ti:G2 too since $\rho_{Ti:G2}$ = 4.52 g/cm^3) would be <0.033 mm/y. In other words, this present work has demonstrated the excellent durability of Ti and its two alloys in the extreme conditions of 71.1 m/s impingement at the elevated temperature of 50°C.

The sparse previous data (shown in table 7.2.1) indicated extremely low material loss of Ti and Ti-6Al-4V at the low velocity of 2.4 – 7.2 m/s with higher but still very low losses of 0.025 mm/y for Ti-6Al-4V at 45.7 m/s. This present investigation has yielded material losses certainly no greater than 0.033 mm/y at the considerably higher velocity of 71.1 m/s and the enhanced temperature of 50°C, and therefore can almost certainly be considered less than the 0.025 mm/y [131] at ambient temperature.

Velocity (m/s)	Temperature (°C)	Material	Thickness loss (mm/y)	Reference
7.2	ambient	Ti	0.0005	[129]
2.4	ambient	Ti-6Al-4V	0.0022	[132]
45.7	ambient	Ti-6Al-4V	0.025	[131]

Table 7.2.1. Previous data on liquid erosion-corrosion for Ti and Ti-6Al-4V.

The above comparisons demonstrate that this present work has produced new data on erosion-corrosion behaviour (in zero solids) of Ti and its two alloys which confirms and, more importantly, expands previous knowledge.

With reference to the 316L stainless steel tested, this investigation has shown its excellent resistance to attack under impingement conditions up to 71.1 m/s at ambient temperature. This represents a demonstration of the well known high-velocity resistance of stainless steels but does so up to an extremely high velocity of 71.1 m/s. In contrast to the Ti-base materials studied, there was evidence that the 316L stainless steel does experience somewhat lower erosion-corrosion resistance at the elevated temperature of 50°C. Even so, the measured weight losses were still small (equivalent to a thickness loss of 0.0365 mm/y).

The advanced erosion-corrosion strength of the three Ti-base materials in relevance to 316L stainless steel was supported by further evidence provided by microscopical examination on the four materials. As already mentioned in section 6.2, Ti:G2, Ti:5111 and Ti-6Al-4V did not exhibit any detectable effect on their surface either visually or under the light microscope when subjected to ambient temperature liquid

erosion-corrosion tests for 12 hours at 71.1 m/s. Anodic polarisation at the end of the 12 hours led to the formation of clearly visible fully developed protective films on the surface of Ti and the two alloys with no evident traces of any damage due to corrosion (figures 6.2.4 – 6.2.9). The 316L alloy also exhibited no significant evidence of attack after 12 hours at 71.1 m/s without electrochemical intervention and this finding is in general accord with the well known resistance of stainless steels to high-velocity conditions. However, on the 316L, there was some slight evidence of possible initiation of pitting (figure 6.2.12) which might signal that this alloy is at the margin in terms of resistance at such high velocity as 71.1 m/s. On the other hand, under the same conditions with anodic polarisation, 316L samples suffered some definite damage in the central region directly under the jet mainly consisting of minor pitting attack (figure 6.2.13). Furthermore, the surface especially around the centre of the specimen appeared to be largely non-uniform (figure 6.2.14) and further out a few comets were also present (figure 6.2.15). This pitting damage on 316L could be correlated with what appeared (figure 6.2.1) to be a 'conventional' breakdown potential at about +250 mV, i.e. a fairly abrupt transition to a rapid rate of increase of current with potential. The overall evidence, most especially from the anodic polarisation scans and resulting microscopical examination, was of an enhanced durability of the Ti-base materials in comparison with the 316L stainless steel under the conditions of high velocity liquid impingement at ambient temperature.

Also under liquid erosion-corrosion at ambient temperature and 71.1 m/s impinging jet velocity with anodic polarisation after 12 hours, the film formed on the surface of the 316L specimens (figure 6.2.15) was noted to be thinner and possibly less protective than the surface film of Ti:G2, Ti:5111 and Ti-6Al-4V samples tested under the same experimental conditions.

This trend of 316L of susceptibility to liquid erosion-corrosion at high temperature was also supported by microscopical examination. Under free liquid erosion-corrosion at 50°C for 12 hours with impinging jet velocity 71.1 m/s, the centre (directly impinged region) of the 316L samples suffered some clear pitting attack and was covered by a thin discontinuous corrosion product layer which indicated the formation of a possible protective film (figure 6.2.23). Quite clearly, no such film was present in the centre of the 316L samples that were anodically polarised at the end of the 12

hours, which is consistent with the very active behaviour that 316L exhibited under these experimental conditions, and pitting appeared to be much more severe (figure 6.2.31) than the one developed in the same conditions without anodic polarisation.

Despite the unmeasurable (<0.1 mg) weight losses after liquid erosion-corrosion tests on Ti:G2, Ti-6Al-4V and Ti:5111 for 12 hours with 71.1 m/s impinging jet velocity at 50°C, there was in fact some detrimental impact on Ti:G2 and Ti-6Al-4V but Ti:5111 did not seem, visually and microscopically, to be much affected. In detail, under free-conditions, Ti:G2 and Ti-6Al-4V displayed some minor pitting attack in the surface region directly under the jet (centre of specimen), but not as intense as in the case of 316L (figure 6.2.17 for Ti:G2 and figure 6.2.20 for Ti-6Al-4V). However the centre of Ti:5111 specimens did not exhibit any traces of pitting corrosion. After anodic polarisation was applied at the end of the 12 hours, no evidence of pitting was noted in the centre of all three materials. This suggests that the pits observed, in samples not subjected to final anodic polarisation, were rather benign, non-propagating ones. It is possible that anodic polarisation tests led to the formation of films in the centre of the Ti and Ti alloys samples which apparently obliterated any previously-formed pits. Another feature indicating the maintenance of overall resistance to high-velocity liquid impingement on the Ti-base materials was the close correspondence between the anodic polarisation plots at 50°C with these at ambient temperature (figure 6.2.3).

An interesting feature of the liquid impingement results was the very distinct films developed on the Ti-base alloys. It is important to emphasise that such films were not formed on any of the Ti-base materials when subjected under anodic polarisation up to +2000 mV in *static conditions* at both ambient temperature and 50°C. This suggests that hydrodynamics have a major contribution in the growth of these films. Furthermore, under liquid impingement at ambient temperature, those films form only with anodic polarisation and not under free conditions. A possible explanation to this could be that at ambient temperature in liquid impingement at E_{corr}, turbulence causes rapid mass transfer which tends to thin the film down, whereas in the case of anodic polarisation, high electrode potential makes the rate of Ti^{2+} ion release and therefore oxide film growth to be faster and, consequently, allows a greater film thickness on the surface of the specimen than at E_{corr}. On the other hand, under liquid impingement

at 50°C, clearly visible films form not only at high electrode potentials due to electrochemical intervention, but at Ecorr too. Presumably Ti^{2+} ions are released faster at 50°C than at ambient temperature. Similar coloured films have been obtained by others [141] too on 316L and other stainless steels after anodic polarisation during liquid impingement at ambient and elevated temperatures.

It is recognised that the zones of different colours represent different film thicknesses. Correlation between the film colours and film thicknesses using optical techniques has been undertaken by other workers [142] by means of systematic studies of the film formation phenomena. In the current research the film phenomena were not studied in such detail, hence such quantitative relationships have not been attempted. Nevertheless, an attempt has been made in this investigation to correlate in a more limited qualitative sense the location of the different films with hydrodynamics.

Referring back to the Ti:5111 specimen shown in figure 6.2.27, S.E.M. images (figures 6.2.32 – 6.2.37) have shown that zones of different colour represent zones of different roughness (and presumably different thickness). A scale of degree of roughness from 1 (very smooth) to 4 (roughest) has been given to each separate zone (table 7.2.2) to allow the graphical representation (figure 7.2.1) of the roughness variation on the surface of that particular specimen. Table 7.2.2 also gives the extent of those zones as measured on the magnified scale of figure 7.2.27.

Surface region	Degree of roughness	Extent
Centre	2, rough	r = 1.45d
1st dark ring	1, very smooth	r = 1.97d
Outer edge of 1st dark ring	4, roughest	r = 2.1d
Light-colour ring	1, very smooth	r = 4.88d
Outer edge of light-colour ring	3, rougher	r = 5.46d
Rest of outside surface	1, very smooth	

Table 7.2.2. Degree of roughness and extent of each separate zone of film on the surface of a Ti:5111 specimen that was anodically polarised after 12 hours of liquid erosion-corrosion at 50°C and 71.1 m/s (r = radius of extent from stagnation point, d = diameter of nozzle = 1 mm).

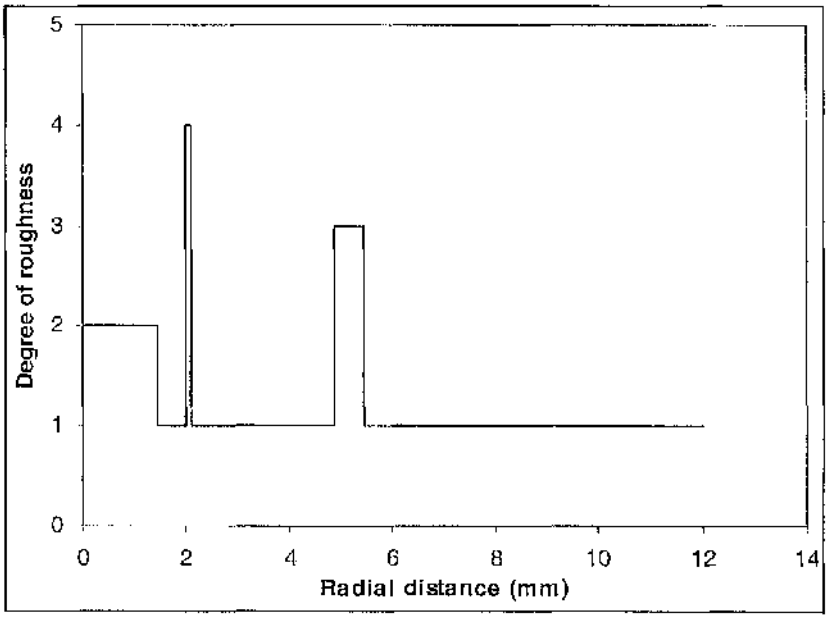

Figure 7.2.1. Graphical representation of the roughness variation on the surface of a Ti:5111 specimen that was anodically polarised after 12 hours of liquid erosion-corrosion at 50°C and 71.1 m/s.

It is obvious that any simple comparison of the extent of the hydrodynamic zones on the Ti:5111 specimen with the general literature is not easily possible (see table 2.3.1). The findings of this investigation appear to be far more complex than the simplistic theoretical view of the standard three hydrodynamic regions (stagnation, transition and wall jet regions) recommended by many authors in the literature. It is to be reminded that in the liquid erosion-corrosion tests carried out in this work, the H/d parameter (H – the distance between the nozzle and the surface of the specimen, d – diameter of the nozzle) was 5. Francesc Girald and Olev Trass et al [71] have demonstrated quite clearly that for H/d = 5 there are at least five zones of different mass transfer along the impinging target, which apparently is also the case in this work. It is also pointed out in [71] that around a height of five diameters and beyond, the maximum rate of mass transfer occurs at the stagnation point. A quite similar scenario was given in [67] according to which mass transfer is maximum at $r < 0.1d$ and between $r = 0.1d$ and the edge of the stagnation region the local mass transfer rate is constant. This perhaps explains the non-uniform surface at the very centre of the Ti:5111 specimen (figure 6.2.32) and therefore suggests that the stagnation region

extends up to $r = 1.97d$ (see table 7.2.2), the transition region is perhaps the region between $r = 1.97d$ and $r = 5.46d$ (with two peaks of high roughness which clearly emphasise the high complexity of the effect of hydrodynamics in the experimental conditions of this investigation) and, consequently, beyond that lies the wall jet region.

Finally, there follows an attempt to obtain some approximate estimates of the likely shear stresses involved in the experiments. First, use is made of the relation, mentioned in section 2.3, which provides a calculation of the maximum shear stress, $\tau_m = 0.16\ \rho\ u^2/(H/d)^2$. Actually, for the current research with $H/d = 5$, this equation is somewhat out of the range, since its use is recommended for $H/d > 8$ [81,82]. Nevertheless, it was thought to be worthwhile to undertake the calculation. Thus, for $H/d = 5$ and $u = 71.1$ m/s, the maximum shear stress was estimated to be $\tau_m = 0.03$ MPa. Next, use is made of the relation $\tau_w = 0.0447\rho u^2\ Re^{-0.182}\ (r/d)^{-2}$ [63,69] which is said to be appropriate for calculating shear stresses into the wall jet region. Taking a value of $r/d = 5.5$ as a rough indicator of the start of the wall jet region, the shear stress within the wall jet region was estimated as $\tau_w = 0.001$ MPa,

where $\rho = 1020$ kg/m^3 (density of seawater)

$u = 71.1$ m/s (velocity of jet)

$Re = (u \times d)/\gamma = 64636.4$

$d = 10^{-3}$ m (diameter of the nozzle)

$\gamma = 1.1 \times 10^{-6}$ m^2/s (kinematic viscosity of seawater).

These calculated values of shear stress are so small in magnitude that, as the literature suggests, it is hard to imagine it could cause erosion damage to a metallic surface. Mass transfer therefore is the most possible hydrodynamic mechanism, in the case of a submerged impinging jet, for the development of zones of different damage intensity on a flat metallic component.

7.3. Solid/liquid erosion-corrosion tests

The results of the solid-liquid erosion-corrosion tests demonstrate an enormous difference in severity between solid-free liquid erosion-corrosion and solid-liquid erosion-corrosion conditions. This is easily indicated by the zero-weight losses that the three Ti-base alloys exhibited in liquid erosion-corrosion conditions at both ambient temperature and 50°C, in contrast to solid-liquid erosion-corrosion conditions where all Ti-base alloys suffered material degradation even at low sand concentrations (e.g. 1.5 mg loss after 16 hours for Ti:G2 at 532 – 588 ppm). Quite obviously, the addition of sand particles in the liquid jet plays the governing role in the total material loss of the Ti-base alloys. This increase in material deterioration due to the sand particles is directly linked to increased corrosion by local breakdown of the protective film due to the continuous bombardment of the sand particles, and also to direct erosion damage.

Solid-liquid erosion-corrosion tests have demonstrated that, for both titanium and stainless steels 316L and Z100, erosion-corrosion damage increases with increasing solid loadings with some indications that the relationship may be linear (figure 6.3.21). A meaningful comparison of the different materials is facilitated by conversion of the measured weight loss data to volume loss which reveals much closer material losses between the Ti-base materials and the two stainless steel alloys (this characteristic will be described in much more detail later in the detailed comparison of materials section). As would be expected, for all materials studied, damage is particularly concentrated in the directly impinged zone (as indicated by the surface profiles). Undertaking an extrapolation from the 72-hour results for Ti:G2, one can estimate a maximum penetration rate of 14.6 mm/y assuming that the rate of material loss remains constant.

Notwithstanding the fact that the damage is locally much more severe under the impinging jet, this work has demonstrated that there is significant erosion-corrosion damage outside the directly impinged zone. This characteristic is demonstrated by:

1. Further consideration of the surface profiles. Figures 6.3.22 and 6.3.23 show two typical examples of the wear scar developed on Ti:G2 specimens after 16 hours of solid/liquid erosion-corrosion. In the first example where the overall volume loss was 0.70 mm^3, calculations showed that 0.47 mm^3 was the volume loss inside the wear scar. Similarly in the second example 0.56 mm^3 was the volume loss inside the wear scar while the overall volume loss was 0.82 mm^3. Quite clearly, a significant proportion of material loss originates from the surface outside the wear scar. Nevertheless, the knowledge that the material loss is mostly concentrated under the jet shows that the direct impinged zone is the most vulnerable region.
2. Different specimen sizes. Ti:G2 specimens of area 0.28 cm^2 (which is basically the surface region directly under the jet) and 8 cm^2 exhibited weight losses of 1.2 mg and 2.0 mg respectively at 803-848 ppm. It is obvious that the difference between the two weight losses represents material loss due to erosion-corrosion damage outside the wear scar. Another example at comparable sand loadings (1387-1476 ppm) was given by Ti:G2 specimens of area 5 cm^2 and 8 cm^2 that exhibited weight losses of 3.0 mg and 3.7 mg respectively.

In addition to this effect of the specimen size on the total material loss, the measurements also indicate that a larger specimen leads to a somewhat deeper attack under the jet but this will be discussed in more detail later in relation to Table 7.3.2.

The separation of the 'T.W.L.' into the three separate components ('C', 'E' and 'S') clearly demonstrates the complex features of erosion-corrosion with significant pure corrosion, pure erosion and synergistic contributions. As described in section 6.3, in the case of composite Ti:G2 specimens, cathodic protection tests of 16 hours of solid/liquid erosion-corrosion (see table 6.3.9) showed that the contribution of 'E' to the 'T.W.L.' was 70%. The 'C' and 'S' factors, approximated by using Faraday's law on an anodic polarisation curve of a Ti:G2 composite specimen (see figure 6.3.17), were 3.75% and 26.25% respectively. Clearly, the largest single factor affecting the overall erosion-corrosion damage is 'E'. However, the total influence (direct and indirect) of corrosion (~30%) is far from insignificant. A similar result as far as the 'E' component is concerned was presented in [95] where under slurry conditions (10% particle concentration) and jet velocity 12.8 m/s (quite similar to the 12.4 m/s jet velocity used in this work) the contribution of 'E' to the overall erosion-corrosion rate

of commercial α-Ti alloy (detailed composition not specified) was 88%. It is to be emphasised that in this work the very high 'E' (70% of the 'T.W.L.') was obtained at a much lower sand concentration (1700-1800 ppm) which demonstrates that, even at relatively low solid loadings, the influence upon total material deterioration of corrosion is not as significant as that of erosion. Nevertheless, it would be interesting to conduct investigations to discover whether this predominant contribution from pure erosion continues down to even lower (say 100 mg/l) solid loadings.

Pure erosive effects under solid-liquid erosion-corrosion

In terms of erosion mechanisms, the microscopical evidence was that the material deterioration, for both Ti-base and stainless steel alloys, in the region directly under the jet is associated with microdrilling of the sand particles into the surface. As the sand particles impact the surface, the surface becomes rougher due to the formation of tiny drillholes (for example see figures 7.3.39-7.3.41) which will eventually form the central wear scar. However, it is possible that an additional erosion mechanism involved plastic deformation from repeated particle impacts leading to eventual local fracture incidents.

In the surface area outside the wear scar, microscopical evidence has shown that material removal involves a cutting process plus plastic deformation mechanisms (see for example figure 7.3.42) apparently due to the continuous shear stress of the sand particles sliding along the metallic surface. For all materials studied, the cutting and plastic deformation were found to be most intense in the region just outside the wear scar, possibly due to turbulence associated with the system's hydrodynamics, i.e. in the dark ring (for example see figures 6.3.43a and 6.3.43b) and this very likely explains the difference in visual appearance between the dark ring and the rest of the specimen's surface.

Microscopical examination showed that under cathodic protection the surface of Ti:G2 (figure 6.3.59) and Ti-6Al-4V (figures 6.3.57 and 6.3.58) looks similar to that in free solid/liquid erosion-corrosion conditions which indicates no apparent

difference in the damage mechanisms. The latter implies that for Ti:G2 and Ti-6Al-4V, in solid/liquid erosion-corrosion the erosion effect, in relation to the corrosion effect, is quite predominant. This trend was supported by the cathodic protection tests which showed that for Ti:G2 and Ti-6Al-4V, pure erosion represents 70% and 74% respectively of the total weight loss.

Pure corrosive effects under solid-liquid erosion-corrosion

As indicated earlier in section 7.2, corrosion processes in solid-free/liquid erosion-corrosion conditions were negligible, on account of the continual stability of the passive film at extremely high velocities, on the three Ti-base alloys. In contrast, under solid-liquid erosion-corrosion a substantial contribution of the corrosion processes was detected. The anodic polarisation plots (Figures 6.3.6 – 6.3.8, 6.3.14 and 6.3.15) clearly demonstrate that this is due to the occurrence of active corrosion as a result of rupture of the protective film resulting from the continuous impact of the sand particles. Moreover the oscillating currents detected during the anodic polarisation scans are indicative of a continuous sequence of local film rupture and re-passivation.

Similar corrosion behaviour on the addition of solids was also found on the superduplex stainless steel alloy Z100 (Figure 6.3.16). It is of interest to know that the anodic polarisation results for the superduplex stainless steel were very similar to the findings of a concurrent study [142] on SAF 2205 duplex stainless steel (22%Cr, 5%Ni, 3%Mo). This other work [142] involved impingement at up to 8.6 m/s of saline solution containing solid loading at around the same level as in the present study. A rise in current above E_{corr} was observed, followed by a potential range with oscillating currents about a steady mean of about 7 $\mu A/cm^2$ – which is very close to the values shown in Figure 6.3.16.

The corrosion current densities found on Ti:G2, when translated into weight losses only contribute to a small, but nevertheless significant part of the total weight loss in solid/liquid erosion-corrosion conditions, counting up to a maximum of 3.75%. This

contribution of corrosion was determined from a composite specimen where the corrosion rate was found over the specimen's entire surface. Much more useful information on the involvement of the corrosion phenomena in the overall erosion-corrosion process were obtained from concentric specimens. Subsequent tests on Ti:G2 concentric specimens, with a central specimen with an area which was directly under the impinging jet, containing all the damage from direct solid/liquid impact, and the outer area, which was unaffected from direct solid/liquid erosion, were monitored separately. These tests showed that a much higher corrosion rate on the central impinging zone existed than on the outer regions (see figures 6.3.30 – 6.3.35).

Tests on concentric specimens also showed a definite active corrosion behaviour of the central specimen which allowed for Tafel extrapolation (see figure 6.3.37).

Table 7.3.1 compares the icorr values and also the current density values in the oscillating/steady mean region for the various specimens (see figures 6.3.14 for composite specimen and 6.3.37 for inner and outer specimens) and demonstrates similar ratios between the inner and the other specimens and also between inner and composite samples when using either i_{corr} or the oscillating current density.

Specimen	i_{corr} ($\mu A/cm^2$)	**Oscillating/steady mean current density positive to E_{corr} ($\mu A/cm^2$)**
Inner concentric	20	100
Outer concentric	0.5	3
Composite	2	9
Ratio inner/outer	40	33
Ratio inner/composite	10	11

Table 7.3.1. i_{corr} values and oscillating/steady mean current density values for inner concentric, outer concentric and composite specimen (note that the 0.5 $\mu A/cm^2$ is the i_{corr} of the outer specimen as approximated on the anodic polarisation curve of the outer specimen in figure 6.3.37).

The current densities at i_{corr} of the inner and outer specimens signify the corrosion rate as 40 times greater in the central region than on the outer surface. However, it would

be incorrect to conclude that the corrosion activity outwith the directly impinged zone is negligible. Figure 7.3.1 shows some clear indication of active corrosion behaviour positive to E_{corr} on the outer concentric specimen when compared with the very passive behaviour of a composite Ti:G2 specimen in static conditions.

Using the estimate of i_{corr} = 0.5 $\mu A/cm^2$ and Area = 7.5 cm^2 for the outer concentric specimen, Faraday's law shows that the weight loss due to 'C' on the outer concentric specimen is 0.036 mg (note that the weight loss due to 'C' on the inner concentric specimen is 0.05 mg).

Weight loss measurements were not made on the outer concentric specimen but an estimate of this weight loss can be obtained from the difference, 0.7 mg, between the weight losses of composite and central concentric specimens (1.8 and 1.1 mg respectively at comparable sand loadings. Thus, the contribution of 'C' on the surface outwith the central wear scar was estimated as 5.1% (i.e. 0.036×100/0.7). Despite this approximate nature of estimation of the value of the 'C' component for the outer surface, it is evident that corrosion on the surface outside the wear scar is quite significant.

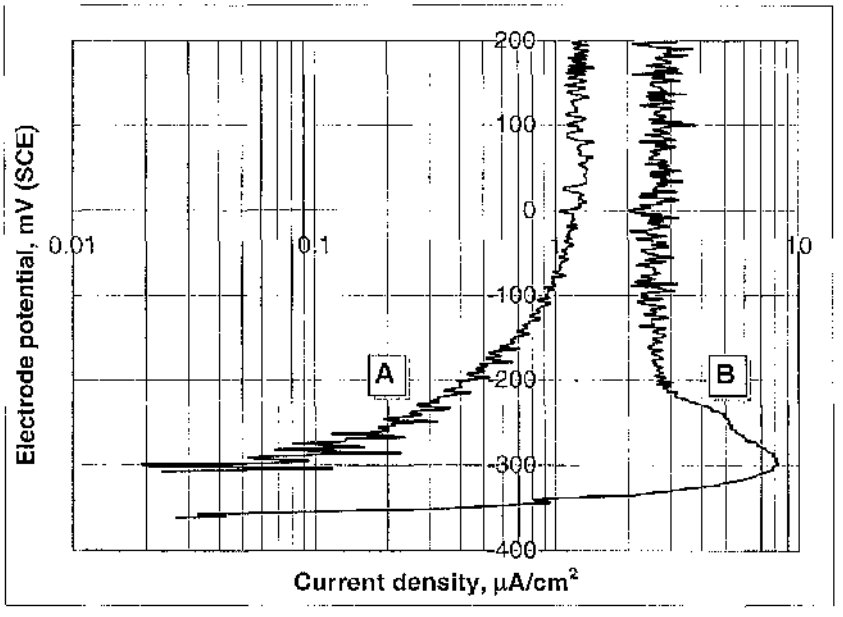

Figure 7.3.1. Anodic polarisation curve of a composite Ti:G2 specimen under static conditions (**A**), compared to the anodic polarisation curve of the outer concentric Ti:G2 specimen under solid/liquid erosion-corrosion (**B**).

An interesting feature of the anodic polarisation curves for the three Ti-base materials and the superduplex stainless steel alloy is of fluctuating currents around a mean current that is either almost constant or moderately increasing over a very wide (>1V) potential range. Levelling off of the corrosion rate at positive potentials during anodic polarisation implies that the corrosion rate is being controlled by some factor which restricts the removal rate of the products of the anodic reaction. In any case, what is happening at potentials more than 100 mV away from E_{corr} is not likely to be of crucial importance in rationalising corrosion mechanisms under free erosion-corrosion conditions at E_{corr}. However, the fluctuating currents are a strong indication of continuous de-passivation/re-passivation sequences associated with the impacting sand particles. This feature has been found previously on stainless steel alloys [91] but it is the first time it is noted on Ti. This shows that the passive film on Ti (generally considered to be more protective than the one on stainless steel alloys) can be vulnerable in erosion-corrosion conditions with the presence of solids.

It is important to note that the central specimen is more electrochemically active than the outer specimen right from the start of the 16 hour exposure and exhibits continually much higher current density than the outer ring specimen (see figures 6.3.30 – 6.3.35). Although the central zone was still clearly actively corroding after 16 hours (figure 6.3.36), it is interesting that the corrosion rate of both central and outer specimen decreased with time (see figures 6.3.30 – 6.3.35) which apparently is directly linked to the slow positive drift in the corrosion potential of both central and outer specimen (see table 6.3.29) throughout the 16 hours of the experiment. This trend might be an indication of less-severe conditions with time due to eventual smoothing out of the particles hitting the specimen. However, if the sand particles were becoming less damaging to corrosion, it might be expected that they would also be less erosive and yet the data in figure 6.3.1 do not provide any evidence that the total weight loss was decreasing significantly with time. It is thus apparent that any changes in sand particle characteristics during the experiments were not making the overall erosion-corrosion conditions significantly less severe. It might be that angular particles are more damaging in corrosion terms (e.g. on passive film) than in producing erosion damage. Another possible explanation for the reducing corrosion rates in the directly impinged zone is that, as the wear scar develops, corrosion rates become somewhat reduced by mass transfer effects within the scar.

It is also noticeable that the corrosion potential difference between the central and outer specimen reduced with time (see table 6.3.29) clearly because the corrosion potential of the inner specimen drifted positive at a faster rate than the outer specimen. This could be attributed to the fact that the outer specimen was more passive all the time over the 16 hour exposure, whereas the central specimen was very active initially and became less active with time.

Galvanic currents

A short study in the latter stages of this research investigated the galvanic interactions resulting from the concentric specimens under the solid/liquid impinging jet. The recorded E_{corr} values (see table 6.3.29) were constantly more negative for the central specimen than the outer specimen over the 16 hours of the tests. Thus, a galvanic current exists with flow of current between the two regions such that the central region directly under the jet acts as anode, while the rest of the surface is the cathode, in which case the surface outside the wear scar may be partially cathodically protected by the galvanic current, while the region under the jet corrodes at a faster rate. Measured galvanic currents found between the inner and outer concentric specimens (table 6.3.30) were substantial. These galvanic currents indicate that the I_{corr} value measured on the inner specimen (20 $\mu A/cm^2$) is an underestimate of the actual dissolution rate that would occur on a composite specimen. As shown in figures 6.3.30 – 6.3.35, corrosion is predominant in the inner section of the specimen while corrosion in the outer section is relatively negligible. In addition to the currents measured on the separate inner specimen, the inner part of a composite specimen will corrode at a higher rate due to the internal galvanic couple.

Galvanic interactions are focused quite extensively in literature on the more general situation of galvanic corrosion involving two different materials in the same environment. An expansion of this idea leads to the present situation of galvanic interaction between two areas of the same material exposed to different environments.

This situation means that the 'C' and 'S' components in the TWL = E + C + S equation are more complicated than originally thought. Not only do they include interactions involving an increase in the erosion rate due to corrosion ('S'), but in a

system such as this study, the components also include galvanic currents. The extent of these galvanic currents will be greatly dependent on the area ratio of the outer and inner area (A_{outer}/A_{inner}). Evidence towards this trend was provided by the surface profiles of the wear scars of specimens of different size. Table 7.3.2 shows two cases of deeper wear scar on 8 cm^2 Ti:G2 specimens than on 5 cm^2 Ti:G2 specimens at comparable sand loadings. It is obvious that with a bigger specimen the material loss under the jet is increased, possibly due to a larger galvanic interaction between the inner and outer concentric specimens. Consequently, the larger the area ratio, the more damage under the impinging jet, i.e. deeper wear scar.

Specimen size (cm^2)	Scar depth (μm)	Sand loading (ppm)
5	54	1387 – 1476
8	61	1410 - 1465
5	42	1150 – 1246
8	49	1035 - 1116

Table 7.3.2. Scar depths of 5 cm^2 and 8 cm^2 Ti:G2 specimens after 16 hours of solid/liquid erosion-corrosion at comparable sand loadings.

Although the measured galvanic currents found between the inner and outer concentric specimens (table 6.3.30) were initially quite substantial, they did decline as time passed. This drop in galvanic interaction is presumably directly linked to the drop in corrosion potential difference between the inner and outer specimen and is therefore also associated with the possibility of less severe conditions developing with the passage of time as discussed in detail in the previous section.

Taking into consideration the observations from this study, it is obvious that calculation of the 'C' component as a percentage of the total weight loss is complex and corrosion processes (and hence overall material loss) can be accentuated in the region under a solid/liquid impinging jet by galvanic interactions.

Erosion-corrosion and synergy

Effects from the deleterious mechanical actions of the entrained solid particles within the aqueous liquid jet are twofold. The pure mechanical effects of erosion, 'E', can be assessed by experiments employing cathodic protection , and accounts for 70% of the total material loss for Ti:G2. When the effects of corrosion and erosion are combined, the material loss increases and therefore a third component, synergy, is introduced which arises from the effects of corrosion enhancing the erosion.

This synergistic effect has been found to be in excess of 26% of the total weight loss of Ti:G2 under solid/liquid erosion-corrosion. This is a considerable amount of material loss and signifies that the interaction of the erosion and corrosion mechanisms are very important in identifying the cause of material wear.

Whilst the presence of a significant synergism has been clearly demonstrated in this research, the detailed synergistic mechanisms have not been unambiguously identified. It is likely that the absence of a stable passive film on Ti due to the continuous bombardment of the sand particles may contribute to the high synergism 'S' observed by facilitating enhanced metal loss on the bare-metal surface. More specifically, the 'S' factor may involve enhancement of erosion damage by roughening of the unfilmed Ti surface on a microscale due to corrosion followed by faster removal of 'unsupported protruding material' by sand particles. There was evidence from microscopy of such roughened surface consisting of micro drillholes within the central wear scar. Another possible mechanism of synergy is the effect of corrosion in reducing the extent of any work hardened layer caused by the impacting particles and hence facilitating more rapid erosion damage. A different scenario of the synergy mechanism might be the action of corrosive attack along the grain boundaries, thus causing easier dislodgement of the crystals. This mechanism would be more likely on two-phase materials like the duplex stainless steel and α/β Ti alloys.

Outside the wear scar the surface was plastically deformed (with skidding tracks as the main feature) but still much smoother than the surface inside the wear scar and

since corrosion is mostly concentrated directly under the jet as described earlier, synergism outside the wear scar can not be of vital importance towards the total material loss.

Notwithstanding the above tentative speculations, it has to be said that further work is required to facilitate more definitive notions on the synergy mechanisms during erosion-corrosion of Ti and its alloys.

Effect of impingement angle

A brief study on the effect of impinging angle on the erosion-corrosion damage of Ti:G2 provided some indications that material loss is greater at both 60° and 30° than at 90°. This is in broad accord with the well-established scenario of erosion damage on ductile materials being greater at oblique angles than at perpendicular incidence and is perhaps not surprising given the high proportion of pure erosion in the total material loss of Ti under the erosion-corrosion conditions studied herein. The wear scar geometry was altered somewhat at 30° incidence but the difference was not as substantial as might have been expected. Nevertheless, the wear scars were less deep at 30° than at 90° incidence and this demonstrates that:

- 30° impingement appears to be less damaging if maximum depth of penetration is the key aspect in terms of erosion-corrosion damage.
- Assessment of erosion-corrosion damage simply in terms of weight loss can in some circumstances represent an oversimplified and misleading strategy.

It has been stated earlier that there are very few other research investigations with which the findings of the current project can be compared. However, in the final stages of writing up this thesis, a paper [143], which describes some studies on Grade 2 titanium and the alloy 5111, was published. The scope of the paper is much narrower than the research undertaken in this PhD project in that:

- It does not cover any investigations on the Ti-6Al-4V alloy.
- The maximum tests times are 8 hours and most of the presented data appears to relate to 4 hour experiments.
- It includes data on experiments solely at 90° impingement angle.
- It does not include any experiments on, or consideration of, interactions between the directly-impinged zone and zones outside this region.
- It does not consider any galvanic interactions between the two regions and does not describe any experiments in which the two zones are "de-coupled" say by the use of concentric specimens.
- It does not include any comparisons of the overall erosion-corrosion behaviour of titanium and other competitive materials such as stainless steel.

Moreover, comparison of the findings presented in [143] and those in this PhD thesis is to a large extent precluded on account of relevant experimental details that are omitted from the paper [143]. Thus, in [143],

- weight losses are plotted without providing anywhere the specimen dimensions,
- wear scar depths are quoted without stating the associated test times,
- no mention is given of the methodology of the determination of the pure erosion components in the overall material loss and
- estimates of some of the corrosion rate (i_{corr}) data are questionable.

Despite the above mentioned difficulties, the paper [143] does clearly demonstrate that titanium and the 5111 alloy suffer significant erosion-corrosion damage when subject to an impinging stream at 17 m/s of 3.5% NaCl containing 500-1000 mg/l sand particles, and the weight losses are greater at the higher solid loading and continue at high rates for the entire 8 hour test times. These observations are in broad

accord with the concurrent research undertaken, at the rather lower velocities of 12.4 – 12.6 m/s, in this PhD project. Another common feature of the two investigations relates to the findings [143] of high corrosion rates involving fluctuating currents when titanium is subject to such impingement attack.

Detailed comparison of materials

Overall erosion-corrosion damage

The negligible erosion-corrosion damage at extremely high velocities of the three Ti-base materials in the absence of solids even at 50°C clearly demonstrates the technical benefits of using Ti in such conditions. However, what this work has more importantly shown is that whilst Ti and its two alloys have superb resistance to erosion-corrosion, including at elevated temperatures, in the absence of solids, they are vulnerable in the presence of significant solid burdens. This is also the case with other high grade materials such as high alloy stainless steels [90,91]. Indeed it is useful to compare the performance of the three Ti-base materials with stainless steel alloys in severe erosion-corrosion conditions. Previous work [132] has reported very substantially lower material loss (21 times less) of the Ti-6Al-4V alloy compared to C4340 ferritic steel under slurry conditions with 16% solids, 2.4 m/s jet speed and 90° angle of impingement. Also T. Lindheim [135] demonstrated in slurry conditions a 40% higher volume loss for 6Mo steel (ASTM B625-19A) in comparison to pure titanium (40-45% particle concentration, 8 m/s jet speed, 45° angle of impingement). The present work has also provided direct comparisons between Ti-base materials and stainless steels from experiments in the same rigs and conditions. Such comparisons are more likely to be more reliable than comparing performances of different materials in nominally similar conditions but from different experimental programs.

Initial examination of the behaviour of pure Ti and the two alloys under solid/liquid erosion-corrosion at ambient temperature showed that, at short time periods of exposure (4 and 8 hours), it is difficult to differentiate between the three Ti-base materials in terms of total weight loss or scar depth. Nevertheless, after 16 hours and

more clearly after 72 hours, it appears as though both alloys are somewhat superior to pure Ti in terms of both weight loss and wear scar depth (figures 6.3.1 and 6.3.2).

Straight comparison based on weight losses over 16 hour exposure tests indicated quite clearly that 316L stainless steel exhibits higher weight losses than pure Ti and the alloys (see table 6.3.4). More meaningful comparisons of the different materials is facilitated by conversion of the weight loss data to volume loss. Quite clearly, the superiority of Ti and the two alloys to 316L and Z100 in weight loss is greatly reduced when volume loss is considered (see tables 6.3.5, 6.3.7 and 6.3.8). In terms of volume loss, Ti:G2 is better than 316L but no better than Z100 and Ti-6Al-4V is only 30 – 40% more resistant than 316L and Z100.

Further experiments based on various particle concentrations provided supporting evidence towards the trend that the erosion-corrosion resistance of Ti:G2 is not any better than the one exhibited by the superduplex stainless steel ("Z100") under solid/liquid erosion-corrosion conditions. The weight loss results of those experiments demonstrated higher weight losses for both stainless steels than for titanium. However, the comparison of figures 6.3.24 and 6.3.25 with figure 6.3.21 allows the clear visual conclusion that the apparent superiority of Ti:G2 over the superduplex stainless steel in weight loss is eliminated completely when volume loss is considered. This is also demonstrated by precise data in three separate examples at comparable sand loadings in tables 6.3.20 – 6.3.22. Ti:G2 remains clearly more erosion-corrosion resistant than stainless steel 316L in terms of volume loss but only by about 25%.

As expected, the attack on specimens was most severe in the directly-impinged region as shown by the surface profiles. The wear scars were of similar smooth profile for all materials. The maximum depth of wear scars is plotted against solid loading in Figure 6.3.25 and reveals a generally similar comparison between the materials as do the overall-specimen volume loss data described earlier. The precise data in tables 6.3.20 – 6.3.22 show that the ratio of scar depth 316L/Ti:G2 is about 1.25/1 whilst for Z100/Ti:G2 it is close to unity.

In other words, the erosion-corrosion resistance of Ti:G2 under solid/liquid erosion-corrosion is only slightly superior to that of the conventional austenitic stainless steel,

316L, and is no better than that of the superduplex stainless steel Z100. Limited tests comparing the Ti-6Al-4V alloy against 316L and Z100 (see Tables 6.3.5, 6.3.7 and 6.3.8) yielded volume loss ratios, 316L/Ti-6Al-4V of (1.2-1.4)/1 and Z100/Ti-6Al-4V of 1.3/1, and wear scar depth ratios, 316L/Ti-6Al-4V of (1.6-1.8)/1 and Z100/Ti-6Al-4V of 1.7/1. This indicates that the Ti-6Al-4V alloy does not produce significant increases in overall erosion-corrosion resistance compared to Ti:G2 as measured by volume loss but is apparently beneficial in reducing the depth of attack in the directly impinged zone. It is possible that the somewhat superior erosion-corrosion resistance, especially under the jet, exhibited by the Ti-6Al-4V alloy relative to pure Ti is due to the higher strength and hardness (see Table 3.1.2) of the alloy. This notion is particularly plausible given the predominant contribution of pure erosion in the overall erosion-corrosion damage.

This latter partial benefit that Ti-6Al-4V offers, has to be set against the increased cost of fabricated components in the Ti-6Al-4V alloy compared with Ti:G2. Enquiries on the cost of Ti:G2 and Ti-6Al-4V have indicated that the cost differential of the two materials can be anything between 1.1 – 2.0 [144] or between 1.5 – 7.0 [145]. Within each case, the lower figures relate to bar product and the higher figures relate to thin sheet. There may be very little difference in cast products (e.g. valves) between the two materials [90] since casting process is quite similar for both of them.

It is relevant to indicate at this point that taking into account the results of this investigation and the cost differentials between Ti and stainless steel alloys, the benefits of replacing advanced stainless steels by titanium alloys are questionable.

Similarly to Ti:G2, superduplex stainless steel Z100 also suffers significant material loss outside the wear scar. This is demonstrated by the different size effect, i.e. a larger surface area leads to higher weight loss. For example, Z100 specimens of area 5 cm^2 and 8 cm^2 exhibited weight losses of 3.2 mg and 3.7 mg respectively at comparable sand concentration. Furthermore, the difference in scar depth between the two specimens (44 μm for 5 cm^2 specimen and 46 μm for the 8 cm^2 specimen) might indicate the existence of galvanic interactions on the superduplex stainless steel too

since the specimen with the bigger outer surface (i.e. bigger cathode) exhibits a somewhat deeper wear scar.

The mechanisms of erosion-corrosion damage under free conditions, i.e. at E_{corr}, observed by light microscopy were found to be substantially similar between all five materials studied. Thus directly under the jet the attack comprises numerous tiny "pits" (drillholes) of very limited depth presumably at points of direct sand particle impact, whereas in the region outwith the directly-impinged zone, the damage involves more of an abrasive cutting attack as the particles skid along the surface.

Erosion component

The results of the cathodic protection tests on Ti:G2, Ti-6Al-4V and Z100 reveals two interesting points:

1. For all three materials, pure erosion proportion is greater under the jet than on the rest of the specimen's surface (see table 6.3.11).
2. Pure erosion damage represents a smaller proportion of total damage for the superduplex stainless steel than for the two Ti materials (70%, 74% and 52% 'E' for Ti:G2, Ti-6Al-4V and Z100 respectively) and therefore the total (direct, 'C', plus indirect, 'S') corrosion is bigger on the superduplex stainless steel than on the two Ti materials (30%, 26% and 48% of total corrosion for Ti:G2, Ti-6Al-4V and Z100 respectively). This might imply that the erosion-corrosion resistance of Ti and the two alloys may be proportionally better than the superduplex stainless steel at low sand loadings but perhaps inferior at higher solid loadings than these employed in this research study.

Corrosion component

All the Ti-base materials and the stainless steels displayed the same characteristic of passive behaviour under solid-free liquid impingement but active corrosion under solid/liquid conditions. Ti:G2 displayed a slightly smaller current density than Ti:5111 and Ti-6Al-4V when anodically polarised after 4 hours of solid/liquid erosion-corrosion (figures 6.3.6-6.3.8). This implies that the passive film on pure titanium is slightly more resistant to rupture by particle impact and/or is more quickly repaired between impacts. This slight superiority of Ti:G2 was not apparent after 16

hours (figure 6.3.13). The anodic polarisation scans after 16 hours erosion-corrosion indicated that the corrosion on the superduplex alloy Z100 was similar to that of Ti:G2 and Ti-6Al-4V. However (Figure 6.3.13), 316L displayed a higher active corrosion rate immediately positive to E_{corr} and a greater tendency for more complete passive film breakdown than the superduplex stainless steel and the two Ti-base materials.

Microscopical examination on Ti:G2 specimens did not reveal any further erosion-corrosion damage due to anodic polarisation under solid/liquid erosion-corrosion (see figures 6.3.60 and 6.3.63) than the one that Ti:G2 suffered under free solid/liquid erosion-corrosion. On the other hand, 316L exhibited severe pitting corrosion in the surface region directly under the jet (figure 6.3.61) when anodically polarised after 16 hours. This supports the shift to higher current that 316L displayed, in contrast to all the other materials, over the anodic polarisation shown in figure 6.3.16. Pitting was also present on the surface outside the wear scar of the same 316L specimen but not as intense (figure 6.3.62). Under the same experimental conditions, no such pitting was observed on Z100 (figure 6.3.64) but numerous small comets were evident outside its directly impinged zone. This represents corrosion behaviour under impingement conditions of Z100 intermediate, between that of Ti and the lower-alloyed 316L stainless steel.

Summarising comments on industrial relevance of the study

The findings of this study do not in themselves provide a strong case for the use of Ti alloys in marine components subjected to solid-liquid erosion-corrosion conditions. In such circumstances, these materials do not seem to yield any substantial benefits in relation to superduplex stainless steels. Moreover, the high proportion of damage due to the pure erosion component precludes any large benefit associated with the use of cathodic protection. It is recognised that the above comments are based on the results involving just one velocity and a fairly narrow range of solid loadings. Consequently, a more comprehensive assessment of the potential of Ti-base materials would be possible from experimental programs covering a wider range of environmental conditions. Even in the absence of such studies, it is probably safe to assume that the

superb durability of these materials under solid-free/liquid erosion-corrosion would be carried through to aqueous environments with only small levels of solid loadings.

To focus on just one specific application to which the present research has been partially targeted, namely MSF desalination plants, the findings imply that titanium is extremely suitable as heat-exchanger tubes in the brine heater and heat-recovery section where resistance to flowing brine at elevated temperatures is required. The excellent resistance to crevice corrosion obtained in this project up to 80°C is another crucial attribute of Ti in this project. The heat rejection section receives cold seawater which can contain suspended solids and marine organisms; thus titanium might be susceptible to erosion-corrosion damage if (e.g. after stormy weather) a high burden of sand was processed in the feed (but so would competitive materials such as Cu-Ni alloys).

8. CONCLUSIONS AND RECOMMENDATIONS FOR FUTURE WORK

8.1. Conclusions

- The Cu-30%Ni possesses greater corrosion resistance than Cu-10%Ni alloy in distilled water and seawater at 20°C but the extent of superiority of the higher-nickel alloy is reduced in distilled water at 50°C making the distinction between the two alloys much reduced.
- Both alloys are susceptible to pitting attack in distilled water at ambient temperature even after exposure for many weeks at ambient temperature.
- The presence of carbon dioxide in the distilled water makes the water more aggressive to both copper-nickel alloys and, certainly for short exposures, results in apparently lower corrosion resistance of the Cu-30%Ni alloy in comparison with the Cu-10%Ni material at both ambient temperature and 50°C.
- Cu-30%Ni is more vulnerable to pitting attack than Cu-10%Ni in the presence of CO_2 in distilled water.
- For both copper-nickel alloys, distilled water at 80°C represents a much more corrosive environment than at 20°C but the injection of CO_2 does not appear to act as an additionally aggressive agent at 80°C.
- Titanium provides a marked improvement in corrosion resistance compared to the copper-nickel alloys over the whole range of distilled water conditions studied and also in seawater at ambient temperature.
- In the absence of solids, Ti:G2, Ti-6Al-4V and Ti:5111 possess excellent erosion-corrosion resistance in 3.5% NaCl solution at both ambient temperature and 50°C.
- In the absence of solids at ambient temperature, austenitic stainless steel 316L also possesses excellent erosion-corrosion resistance. However, at 50°C, 316L exhibits lower erosion-corrosion resistance than the three Ti-base materials.
- Films on the Ti-base materials in liquid erosion-corrosion are most likely the result of mass transfer due to the effect of hydrodynamics.

- In solid/liquid erosion-corrosion conditions, Ti-base materials and stainless steel alloys suffer material degradation even at sand concentrations in the range 532 – 1800 mg/l.
- Detailed studies on Ti:G2 and superduplex stainless steel Z100 demonstrated that, although erosion-corrosion damage is much more severe under the impinging jet, there is significant material loss outside the directly impinged zone.
- For both Ti and stainless steel alloys, erosion-corrosion damage increases with increasing solid loadings with some indications that the relationship may be linear.
- In solid/liquid erosion-corrosion, pure erosion accounts for generally 70%, 74% and 52% of the overall weight loss of Ti:G2, Ti-6Al-4V and Z100 respectively, and therefore the total contribution of corrosion is larger on the superduplex stainless steel than on the two Ti materials (30%, 26% and 48% of total corrosion for Ti:G2, Ti-6Al-4V and Z100 respectively).
- For Ti:G2, Ti-6Al-4V and Z100, pure erosion proportion is greater under the jet than on the rest of the specimen's surface.
- Corrosion enhances the erosion process through synergism which can account for up to 26% of the total weight loss of a composite Ti:G2 specimen.
- The process of damage mechanisms under a solid/liquid impinging jet is thought to be one where corrosion dissolves the metal due to local breakdown of the protective film from the sand particles impact, and erosion mechanisms involve the action of plastic deformation outside the impinged centre and the solid particles drilling into the centre of impingement. The mechanism of damage due to synergy mechanisms has not been clearly identified.
- Calculation of the corrosion rate on a composite specimen underestimates the actual damage due to corrosion in the region directly under the impinging jet.
- The result of the solid/liquid impinging jet being focused on only the central part of the specimen introduces higher corrosion rates within the central region and lower corrosion rates for the outer regions. However, the corrosion activity outwith the directly impinged zone is not negligible.
- Internal galvanic currents between the region directly under the jet and the outer surface are quite substantial. These galvanic currents indicate accelerated corrosion in the directly impinged region due to galvanic effects.

- The extent of the galvanic currents is dependent on the area ratio of the outer and inner area (A_{outer}/A_{inner}). A larger area ratio leads to increased damage under the impinging jet, i.e. deeper wear scar.
- At 30° degrees impinging angle material loss is greater but scar depth is smaller than at 90°.
- At 60° degrees impinging angle scar depth is greater than at 90°.
- Ti:5111 and certainly Ti-6Al-4V are somewhat superior to pure Ti in terms of both weight loss and wear scar depth.
- In terms of volume loss, Ti:G2 is no better than Z100 and only 25% better than 316L, and Ti-6Al-4V is only 30 – 40% more resistant than 316L and Z100. In terms of wear scar depth, Ti:G2, Ti:5111 and Ti-6Al-4V display greater resistance than 316L and Z100, although this is not as much evident for Ti:G2 and Ti:5111 as for Ti-6Al-4V.
- The benefit of alloying titanium has been seen in Ti-6Al-4V since it displays greater resistance in overall material loss and also exhibits less erosion-corrosion damage directly under the jet than Ti:G2.

8.2. Recommendations for future work

- It would of great interest to MSF desalination plants to study the erosion-corrosion behaviour of the two copper-nickel alloys in distilled water.
- Further investigation into the effect of hydrodynamics due to a submerged impinging jet striking on a flat component and to better identify the hydrodynamic zones on Ti and its alloys.
- To study the effect of velocity in solid/liquid erosion-corrosion.
- To study the effect of elevated temperature in solid/liquid erosion-corrosion.
- It would be quite important to expand on the findings of galvanic interactions between the inner and outer regions of specimens by a more detailed study of the behaviour of the concentric type specimens.
- To better identify the mechanisms of the process of corrosion enhancing erosion on Ti under solid/liquid erosion-corrosion.

- To study the solid/liquid erosion-corrosion behaviour of the Ti-base materials at lower solid loadings to ascertain if the pure erosion component is predominant at very low solid loadings.

LIST OF REFERENCES

[1] Arthur H. Tuthill, "Guidelines for the use of copper alloys in seawater", Materials Performance, NACE September 1987, 12-22.

[2] Peter T. Gilbert, "A review of recent work on corrosion behaviour of copper alloys in seawater", Materials Performance, NACE, February 1982, 47-53.

[3] Ralph W. Ross JR, David B. Anderson, "Hot seawater corrosion of copper-base alloys", Materials Performance, September 1975, 27-32.

[4] D. J. Godfrey, B. Angell, A. F. Taylor, "Present and feature full-scale land-based corrosion/erosion studies of ships' seawater piping systems", Copper and its alloys. Proceedings of international conference organised by the Institute of Metals. Amsterdam, 21-25 September 1970, 339-344.

[5] Anna Maria Beccaria et al, "A study of the de-alloying of 70Cu-30Ni commercial alloy in sulphide polluted and unpolluted seawater", Corrosion Science, 32, 1263-1275, 1991.

[6] A. M. Beccaria, J. Crousier, "Dealloying of Cu-Ni alloys in natural seawater", Br. Corrosion J. (1989), 24, 49-52.

[7] J. N. Alhajji, M. R. Reda, "The conflicting roles of complexing agents on the corrosion of copper-nickel alloys in sulphide polluted seawater", J. Electrochem. Soc. (1994), 141, 1432-1439.

[8] J. N. Al Hajji, M. R. Reda, "The corrosion of copper-nickel alloys in sulphide-polluted seawater: The effect of sulphide concentration", Corrosion Science (1993), 34, 163-177.

[9] J. N. Al Hajji, M. R. Reda, "Deleterious role of complexing agents in corrosion of copper-nickel alloys in sulphide polluted seawater", Br. Corrosion J. (1995), 30, 56-62.

[10] D. C. Vreeland, "Review of corrosion experience with copper-nickel alloys in seawater piping systems", Materials Performance (1976), 15, 38-50.

[11] Ian D. McGregor, Shamsui Karim, "Tube corrosion in high temperature stages of MSF distillers", Proceedings of IDA World Congress on desalination and water re-use, Abu Dhabi, (1995), 5, 301-307.

[12] E. A. Al Sum et al, "Vapour-side corrosion of copper base condenser tubes of the MSF desalination plants of Abu Dhabi", Desalination, (1994), 97, 109-119.

[13] Nausha Asrar et al, "Early failure of cupro-nickel condenser tubes in thermal desalination plant", Desalination, (1998), 116, 135-144.

[14] A. M. Shams El Din, R. A. Mohammed, "Contribution to the problem of vapour-side corrosion of copper-nickel alloys tubes in MSF distillers", Desalination, (1998), 115, 135-144.

[15] Ronald W. Shutz, Milton R. Scaturro, "Titanium outperforms rivals for improving seawater systems", Sea Technology, (1988), 29, 49-57.

[16] Moroishi T., "Present status of titanium market and technology", Sumitomo Metals, (1997), 49, 11-19.

[17] N. A. Najm-Mohammed, PhD thesis. University of Glasgow, 1997.

[18] Adil Al Radif et al, "Selection of materials for Taweelah B MSF desalination plant project (6×10-12.7 migd)", Desalination, (1994), 97, 3-16.

[19] N. T. Hanbury, T. Hodgkiess, "Desalination Technology 98", course notes of 1998.

[20] A. M. Shams El Din, "Copper alloys for desalination plants", Desalination, (1993), 93, 499-516.

[21] L. Grasjo et al, "In situ measurements of oxygen consumption and hydrogen evolution in corrosion of some metals in liquid water", Materials Science Forum (1995), Vol. 185-188, 703-712.

[22] T. Hodgkiess, J. Akhtar, "Observations on the corrosion behaviour of copper in Glasgow tap water", Proceedings of a conference held at the Society of Chemical Industry, London, 8-9 December 1992.

[23] H. Siedlarek et al, "Effects of water composition and operating conditions on the corrosion behaviour of copper in potable water", Proceedings of a conference held at the Society of Chemical Industry, London, 8-9 December 1992.

[24] T. Kaunisto, "Corrosion in potable water systems – the situation in Finland", Proceedings of a conference held at the Society of Chemical Industry, London, 8-9 December 1992.

[25] H. S. Campbell et al, "An unusual form of microbially induced corrosion in copper water pipes", Proceedings of a conference held at the Society of Chemical Industry, London, 8-9 December 1992.

[26] A. Sakamoto et al, "Erosion-corrosion tests on copper alloys for water tap use", Wear, (1995), 186-187, pp. 548-554.

[27] E. A. Culpan, G. Rose, "Corrosion behaviour of cast nickel aluminium bronze in seawater", Br. Corrosion J. (1979), 14, 160-166.

[28] Robert J. Ferrara, Thomas E. Caton, "Review of dealloying of cast aluminium bronze and nickel-aluminium bronze alloys in seawater service", Materials Performance, NACE, February 1982.

[29] Dipendra Narth Roy, Ashwini K. Sinha, "Aspects of localised corrosion of condenser tube materials in chloride media", 10th International Congress of Metallic Corrosion, Madras, India, November 1987.

[30] G. A. Bokov et al, "Corrosion resistance of copper-nickel alloys and stainless steel in cooling industrial-domestic wastewaters", Khimiya i Tekhnologiya Vody, (1994), 16, 295-300.

[31] Bostwick, T. W. Corrosion, 1961, 17, 12.

[32] P. T. Gilbert, "Use of ferrous sulphate treatment for combating condenser tube corrosion", Supplement to Chemistry and Industry, 2 July 1977.

[33] North R. F., Pryor M. J. Corrosion Science (1968), 8, 149-157.

[34] Barry C. Syrett, "Erosion-corrosion of copper-nickel alloys in seawater and other aqueous environments – a literature review", Corrosion-NACE, (1976), 32, 242-252.

[35] D. H. Foxall, P. T. Gilbert, G. Wildsmith, "Some aspects of the use of alloys for seawater cooling systems", I Mech E 1979.

[36] P. T. Gilbert, "Corrosion resisting properties of 90/10 copper-nickel-iron alloy with particular reference to offshore oil and gas applications", Br. Corrosion J. (1979), 14, 20-25.

[37] Keith Bendall, "A longer life in the ocean waves", Materials World, December 1997, 711-713.

[38] F. P. Ijsseling et al, "Influence of temperature on corrosion product film formation on CuNi10Fe in the low temperature range", Br. Corrosion J. (1982), 17, 162-167.

[39] Arthur H. Tuthill et al, "Experience with copper alloy tubing, waterboxes and iping in MSF desalination plants", Proceedings of World Congress on Desalination and Water re-use, Madrid October 1997.

[40] F. Mansfeld et al, "The corrosion behaviour of copper alloys, stainless steels and titanium in seawater", Corrosion Science (1994), 36, 2063-2095.

[41] Reda M. R., Alhajji J. N. "Comparison of current reversal chronopotentiometry (CRC) and small amplitude cyclic voltammetry (SACV) method to determine the long-term corrosion tendency of copper-nickel alloys in polluted and unpolluted seawater under jet-impingement conditions", Corrosion Testing in Naturals Waters: Second Volume, ASTM STP 1300, Robert M. Kain, Walter T. Young, Eds., 1997, 143-158.

[42] W. E. Heaton, "Condenser tube corrosion in CEGB seawater cooled plant: Recent service and research experience", Industrial Corrosion, October 1988, 6, 7-10.

[43] Anees U. Malik et al, "Materials performance and failure evaluation in SWCC MSF plants", Desalination, (1994), 97, 171-187.

[44] L. Giuliani, "Corrosion problems of copper alloys in desalination plants", Desalination, (1977), 22, 379-384.

[45] Arthur Cohen, P. F. George, "Copper alloys in the desalting environment-final report", Materials Performance, (1974), 13, 26-31.

[46] T. Hodgkiess, D. Mantzavinos, "Corrosion of copper-nickel alloys in pure water", Desalination, (1999), 126, 129-137.

[47] McGregor, H. Moore, "Improvement in distillate production and performance after modification of the stage venting system", DESAL – 92 – Arab. Gulf Regional Symposium.

[48] E. Heitz, "Chemo-mechanical effects of flow of corrosion", Corrosion-NACE (1991), 47, 135-145.

[49] Gabriel Silva, "Wear generation in hydraulic pumps", SAE Technical paper series, International Off-Highway and Powerplant Congress and Exposition, Milwaukee, Wisconsin, September 10-13, 1990.

[50] B. Todd, "Corrosion and materials selection in seawater systems", I Mech E 1979.

[51] T. J. Glover, "Recent developments in corrosion-resistant metallic alloys for construction of seawater pumps", Materials Performance, (1988), 27, 51-56.

[52] J. Madadnia, I. Owen, "Accelerated surface erosion by cavitating particle-laden flows", Wear, (1993), 165, 113-116.

[53] Chandler K. A. (1985) Marine and offshore corrosion, Butterworths Ltd.

[54] Engel. L. and Klinegele H. (1981), "An atlas of metal damage", translated by Murray S, Wolfe Publishing Ltd. London and Carl Hanser Verlag.

[55] J. R. Zhou, S. Bahadur, "Effect of blending of silicon carbide particles in varying sizes on the erosion of Ti6Al-4V", Wear (1989), 132, 235-246.

[56] S. Yerramareddy, S. Bahadur, "Effect of operational variables, microstructure and mechanical properties on the erosion of Ti-6Al-4V", Wear, (1991), 142, 253-263.

[57] M. Emiliani, R. Brown, "The effect of microstructure on the erosion of Ti-6Al-4V by spherical particles at 90° impact angles", Wear, (1984), 94, 323-338.

[58] Taishi Omote et al, "Interaction between impingement angles and materials on sand erosion", 27th International SAMPE Technical Conference October 9-12, 1995.

[59] A. Venugopal Reddy, G. Sundararajan, "The influence of grain size on the erosion rate of metals", Metallurgical Transactions A (1987), 18A, 1043-1052.

[60] R. L. Howard, A. Ball, "The effect of test temperature on the particle erosion performance of titanium aluminide alloys", Wear, (1997), 205, 11-14.

[61] J. A. C. Humphrey, "Fundamentals of fluid motion in erosion by solid particle impact", Int. J. Heat and Fluid Flow (1990), 11, 170-195.

[62] M. Bjordal et al, "Erosion and corrosion properties of WC coatings and duplex stainless steel in sand-containing synthetic seawater", Wear, (1995), 186-187, 508-514.

[63] Francesc Giralt, Olev Trass, "Mass transfer from crystalline surfaces in a turbulent impinging jet part 2: Erosion and diffusional transfer", Canadian Journal of Chemical Engineering, (1976), 54, p.148.

[64] D. C. Silverman, "Rotating cylinder electrode – geometry relationships for prediction of velocity – sensitive corrosion", Corrosion – NACE (1987), 44, P. 42.

[65] Frederick G. Hammit, Frank J. Heymann, "Liquid erosion failures", in ASM Metals Handbook, Vol. 10, 8th ed. P160-167.

[66] J. T. Davies, "Turbulence phenomena", (1972), Academic press, New York and London.

[67] D. T. Chin, C. H. Tsang, "Mass transfer to an impinging jet electrode", J. Electrochem. Soc., (1978), 125, 1461-1470.

[68] N. Rajaratnam, "Turbulent jets – developments in water science, Elsevier, 1976.

[69] Francesc Giralt, Olev Trass, "Mass transfer from crystalline surfaces in a turbulent impinging jet part 1: Transfer by erosion", Canadian Journal of Chemical Engineering, (1975), 53, p.505-511.

[70] Carolyn M. Preece, "A comparison of liquid impact erosion and cavitation erosion", Wear, (1980), 60, 269-284.

[71] Chu-Jen Chia et al, "Mass transfer in axisymmetric turbulent impinging jets", Ind. Eng. Chem. Fundam., (1977), 16, 28-35.

[72] U. Meyer et al, "A new impinging jet test rig used to identify the important parameters in service erosion-corrosion in Bayer liquor and to study the damage morphology", Wear, (1994), 176, 163-171.

[73] J. M. Esteban et al, "The impinging jet electrode: Measurement of the hydrodynamic constant and its used for evaluating film persistency", Corrosion, (1990), 46, 896-901.

[74] J. L. Dauson et al. Corrosion-NACE 87, pp. 453.

[75] K. D. Effird et al, "Correlation of steel corrosion in pipe flow with jet impingement and rotating cylinder tests", Corrosion Engineering-NACE, (1993), 49, 992-1003.

[76] Bryan Poulson, "Electrochemical measurements in flowing solutions", Corrosion Science, (1983), 23, 391-430.

[77] H. Q. Becerra et al, Corrosion Science (2000), 42, 561-575.

[78] R. C. Woolam et al, "Electrochemical methods of corrosion research", Ed. By M. Duprat, Materials Science Forum (1986), 8, 53-68.

[79] Bryan Poulson, "Complexities in predicting erosion-corrosion", Wear (1999), 233-235, 497-504.

[80] Bryan Poulson, "Advances in understanding hydrodynamic effects on corrosion", Corrosion Science (1993), 35, 655-665.

[81] B. T. Ellison, C. J. Wen, "Hydrodynamic effects on corrosion", The American Institute of American Engineers (1981), 77, 161-169.

[82] K. D. Effird, "Effect of fluid dynamics on the corrosion of copper-base alloys in seawater", Corrosion-NACE (1977), 33, 3-8.

[83] G. Hoff et al, "Rain and sand erosion, phenomena of material destruction caused by repeated loads", Characterisation and determination of erosion resistance, ASTM STP 474, American Society for Testing and Materials, (1970) 353-382.

[84] Kozyrev, S. P., "The genesis of cavitation wear", Trenie Iznos (1980), 1, 793-808.

[85] Iain Finnie, "Erosion of surfaces by solid particles", Wear (1960), 3, 87-103.

[86] Hector Mcl. Clark, "The influence of the flow field in slurry erosion", Wear (1992), 152, 223-240.

[87] A. A. Grant, "Wear in slurry pumps", Technical Bulletin, Warman Group Development No 9, May 1991.

[88] S. Zhou et al, "Electrochemical studies of anodic dissolution of mild steel in a carbonate-bicarbonate buffer under erosion-corrosion conditions", Corrosion Science (1996), 38, 1-14.

[89] M. M. Stack et al, "Some thoughts on the construction of erosion-corrosion maps for PVD coated steels in aqueous environments", Surface and Coatings Technology (1999), 113, 52-62.

[90] T. Hodgkiess et al, "Electrochemical and mechanical interactions during erosion-corrosion of a high velocity oxy-fuel coating and a stainless steel", Wear (1999), 233-235, 623-634.

[91] A. Neville, T. Hodgkiess, J. T. Dallas, "A study of the erosion-corrosion behaviour of engineering steels for marine pumping applications", Wear (1995), 186-187, 497-507.

[92] T. Hodgkiess, "The role of advanced materials to combat erosion-corrosion in aqueous environments", Stainless Steel World, July/August 1999, 39-42.

[93] R. J. Wood, S. P. Hutton, "The synergistic effect of erosion and corrosion: trends in published results", Wear (1990), 140, 387-394.

[94] X. X. Jiang et al, "Accelerative effect of wear on corrosion of high-alloy stainless steel", Corrosion-NACE (1993), 49, 836-841.

[95] J. P. Tu, "The effect of TiN coating on erosion-corrosion resistance of α-Ti alloy in saline slurry", Corrosion Science (2000), 42, 147-163.

[96] H. McI. Clark, L. C. Burmeister, "The influence of squeexe film on particle impact velocities in erosion", Int. J. Impact Eng. (1992), 12, 415-426.

[97] "Titanium alloys", DERA 1997, Structural Materials Centre, Farnborough GU14 0XL, Hampshire UK.

[98] "Surface treatment of titanium – a designers and users handbook", TIG (the Titanium Information Group), NASURF, March 1998.

[99] C. P. De, "Use of titanium and its alloys in seawater service", High Temperature Materials and Processes (1993), 11, pp.61.

[100] K. Kohsaka et al, "Light gauge welded titanium tubes for seawater desalination plants", Desalination (1989), 73, 429-446.

[101] Shozo Yakamoto et al, "Galvanic corrosion of copper alloys coupling with titanium in desalination plants and its cathode", Hitachi Zosen Technical Review (1983), 44, 77-82.

[102] C. D. Hornburg et al, "Heat transfer tubing selection for MSF desalination plants", Proceedings of the IDA World Congress on Desalination and Water Sciences, Abu Dhabi, UAE, November 18-24 1995.

[103] C. Sommariva et al, "Titanium exchange tubes for MSF desalination plant. A study on the aspects relevant to the adoption of this material", Desalination (1994), 97, 53-65.

[104] S. Narain, Sami H. Asad, "Corrosion problems in low-temperature desalination units", Materials Performance (1992), 31, 64-67.

[105] Makoto Yamada, "Guidelines for use of titanium in seawater heat exchanger", Proceedings of the IDA World Congress on Desalination and Water Sciences, Abu Dhabi, UAE, November 18-24 1995.

[106] D. K. Peacock, "Effective design of marine high performance corrosion resistant systems using titanium", Trans IMarE (1998), 110, 155-170.

[107] John A. Mountford, Jr., "Titanium for condenser and heat exchanger service", American Society of Mechanical Engineers, Power Division (Publication) PWR , 1996, 30, 63-75.

[108] TIG (the Titanium Information Group), Data sheets No.3 (1996), No.6 (1997), No.7 (1998).

[109] David K. Peacock, "Experience with titanium alloys for control of corrosion in advanced environmental protection processes", Titanium Information Group, TIMET UK, Witton, Birmingham, England.

[110] L. H. Boulton, A. J. Betts, "Corrosion performance of titanium and titanium stabilised stainless steels", Br. Corrosion J. (1991), 26, 287-292.

[111] A. M. Shams El Din et al, "Titanium hydride formation from Arabian Gulf water", Desalination (1996), 107, 265-276.

[112] Margaret Hunt, "Titanium: the right stuff for land, air and sea", Materials Engineering (Cleveland) 1988, 105, 45-49.

[113] H. Dong et al, "Oxygen thermochemical treatment combined with DLC coating for enhanced loadbearing capacity", Surface Engineering (1998), 14, 505-512.

[114] Fayyaz Muddassir, "Materials for desalination processes: Titanium", Desalination and Water Reuse, February/March 1996, Vol. 5/4, 38-41.

[115] J. R. B. Gilbert, "The uses of titanium", Materials Science and Technology (1985), 1, 257-262.

[116] Masayuki Yamamoto et al, "Commercial test results of the light guage (.04 Mm wall thickness) titanium tube and considerations thereof", Proceedings of the IDA World Congress on Desalination and Water Sciences, Abu Dhabi, UAE, November 18-24 1995.

[117] G. Stern et al, "Choosing materials for desalting by distillation", Materials Engineering Forum, Chemical Engineering, September 22, 1980, 171-176.

[118] T. Hodgkiess, A. Asimakopoulos, "Studies of the localised-corrosion behaviour of some stainless steels, incoloy 825 and titanium in seawater", Desalination (1981), 38, 247-256.

[119] A. N. Lebedev, "Corrosion of heat exchanger tubes in hot seawater, according to experience in the operation of desalination distillation plant", Protection of Metals, May0June 1982, 18, 325-327.

[120] Andrew Bacon, "Oil and gas industry are poorly informed about titanium properties", Anti-Corrosion Methods and Materials (1996), 43, 5-8.

[121] Xiangrong Zhu et al, "Study on galvanic corrosion of titanium alloys in seawater", Memoires et Etudes Scientifiques Revue de Metallurgie (1989), 86, 667-670.

[122] Bruce E. Liebert, "Corrosion of aluminium and titanium at Keahole Point over an eight month period", Proceedings of the Ocean Therm. Energy Convers. (OTEC) Biofouling, Corros. And Mater. Workshop, Rosslyn, Va, January 8-10 1979, 189-196.

[123] Gene Baker, James S. Grauman, "Solving some seawater corrosion problems with titanium", Sea Technology (1991), 32, 70-74.

[124] Ali Al Odwani et al, "Performance of high chromium stainless steels and titanium alloys in Arabian Gulf seawater", Desalination (1998), 120, 73-81.

[125] M. A. Khan et al, "Titanium alloys – corrosion and wear studies in-vitro", Fifth World Biomaterials Congress, May 29 – June 2, Toronto, Canada, pp.480.

[126] Xiaoxia Jiang et al, "The effect of hydrogen on wear resistance of a titanium alloy in corrosive medium", Lubrication Engineering (1990), 46, 529-532.

[127] Gasser B., Frenk A., "Anodising medical titanium implants", Metalloberflache (1997), 51, 88-91.

[128] Rodney Boyer, Gerhard Welsch, E. W. Colings, "Materials properties handbook: titanium alloys" 1994.

[129] "Titanium heat exchangers for service in seawater, brine and other natural aqueous environments: The corrosion, erosion and galvanic corrosion characteristics of titanium in seawater, polluted inland waters and in brines", Titanium Information Bulletin. Imperial Metals Industries (Kynoch) Ltd., May 1970.

[130] Bezzam C. S. Rao, Donald H. Buckley, "Characterisation of erosion of metallic materials under cavitation attack in a mineral oil", NASA Technical Memorandum (1985), No.86934, p.23p.

[131] A. E. Hohman, W. L. Kennedy, "Corrosion and materials selection problems on hydrofoil craft", Materials Protection September 1963, 56-68.

[132] J. Yang, J. H. Swisher, "Erosion-corrosion behaviour and cathodic protection of alloys in seawater-sand slurries", Journal of Materials Engineering and Performance (1993), 2(6), 843-850.

[133] "Corrosion resistance of titanium", TIMET, Pittsburgh, Pennsylvania 15230 400 Rouser Road, P.O. Box 2824.

[134] "Titanium for refinery use", TIMET, Bulletin RT-2, March 1984.

[135] T. Lindheim, "Erosion performance of Glass Fibre Reinforced plastics (GRP)", Revue De Institut Francais du Petrole, 50, N 1, Janvier Fevrier 1995, 83-95.

[136] M. H. Ali El-Saie et al, "Sea water intake and its effect on heat rejection design and material for flash distillation plant", Desalination (1981), 38, 257-267.

[137] Nagao Iwai et al, "Steam-side condenser tube erosion by droplet impingement", PWR-Vol.19, Practical Aspects and performance of Heat Exchanger Components and Materials, ASME 1992.

[138] Jan Olsson, "UNS S32654 a stainless steel for condenser tubes", Proceedings of the IDA World Congress on Desalination and Water Sciences, Abu Dhabi, UAE, November 18-24 1995.

[139] D. H. Buckley, B. C. S. Rao, "The mechanism of erosion of metallic materials under cavitation attack", NASA Technical Memorandum (1986), No.87133, p.17p.

[140] D. Mantzavinos, T. Hodgkiess, S. L. C. Lai, "Corrosion of condenser tube materials in distilled water", Desalination (2001), 138, 365-370.

[141] T. Hodgkiess, A. Neville, Corrosion Science 38 (1996) 927-956.

[142] E. A. M. Hussain, "An electrochemical investigation of erosion-corrosion of duplex stainless steel in seawater containing sand particles", PhD thesis, Cranfield 2001.

[143] A. Neville, B. A. B. McDougall, "Erosion-corrosion of titanium and its alloys", Corrosion Odyssey 2001, Institute of Corrosion, Edinburgh, September 2001, Session 8, Paper 3.

[144] Simon Ford, TIMET Ltd. Private communication.

[145] Nigel Hoskison, Titanium International Ltd. Private communication.

[146] Trevor Hodgkiess, lecture notes, University of Glasgow.